Chiral organisations expressed by biomolecules at the Cu(110) surface

UNIVERSITY OF LIVERPOOL

Thesis submitted in accordance with the requirements of
the University of Liverpool for the degree of Doctor in Philosophy
by

Tommaso Sgrilli

Supervisor: Prof. Rasmita Raval

Surface Science Research Centre
Department of Chemistry

August 2015

Abstract

This thesis aims at understanding the manifestations of chirality that are expressed by selected organic molecules of biochemical relevance when adsorbed on a copper single-crystal exposing the (110) face. All the experiments described in this thesis are carried out in Ultra High Vacuum (UHV) environment by means of complementary surface science techniques. In some circumstances, the experimental results are interpreted on the basis of theoretical calculations that have been performed by collaborators.

The adsorption of enantiopure amino acid R-serine on Cu(110), previously reported to give rise to a symmetry-breaking organisational arrangement, is studied with the aim of establishing the geometry of the single conformers populating the organic adlayer. While theoretical calculations on this system indicate two energetically preferred geometries, on the basis of a direct comparison between experimental and simulated Scanning Tunneling Microscopy (STM) investigations a single geometry is proposed. This features homochirality at the footprint level, with the stereo-distribution of the molecular atoms coordinated with the surface possessing uniform chirality. Furthermore, the hydrogen bonds that give stability to the proposed molecular assembly are discussed, and are suggested to play a symmetry-breaking role in the characteristic chiral direction of elongation of R-serine islands on Cu(110).

The behaviour of serine in racemic proportion on Cu(110) is characterised by two main phenomena. The tendency of the two enantiomers to segregate into domains with homogeneous chirality is accompanied by a second effect, which sees interactions between molecules with differing chirality. The latter phenomenon takes place principally when the surface coverage is high and tends to disappear once the sample is annealed, thus is proposed to possess a metastable nature. By means of high-resolution STM images, the metastable state is investigated and the chirality of the single molecules can be tracked. As a result, the occurrence of serine trimers, constituted by a homochiral serine dimer and a serine molecule with opposite chirality, is revealed. These trimers represent a recurrent manifestation of heterochiral recognition when racemic serine is adsorbed on Cu(110).

The study of enantiopure S-valine on Cu(110) reveals a temperature-dependent chiral-achiral phase transition at the organisational level. The achiral high-temperature phase is found, by means of STM and Low Energy Electron Diffraction (LEED) to possess a (3x2) periodicity with alternating footprint chirality, as corroborated by theoretical calculations. The interruptions and irregularities that occur within the (3x2) structure are discussed on the basis of previous studies conducted on the alanine/Cu(110) system, and are proposed to be originated by the presence of rotational domains, by the local occurrence of different molecular conformations or a bigger unit cell.

Finally, the adsorption of the achiral nucleobase adenine on Cu(110) is investigated exclusively with STM. Given the characteristics of the probing technique, the complete understanding of the molecular geometry of the adsorbed molecules is not attempted. However, the nucleation of chirality at the supramolecular level is followed and a proposed mechanism of formation of the previously reported long-range chiral assembly on Cu(110) is presented. It is shown in fact that, despite the formation of diverse temperature-dependent molecular phases, a key role in the break of the surface symmetry is played by the on-surface formation of chiral adenine dimers, which can interact laterally to give rise to chiral 1D chains and 2D domains when the sample is annealed further.

Contents

Acknowledgements

I am grateful for the support from the FP7 Marie Curie Actions of the European Commission, via the Initial Training Network SMALL (MCITN-238804), through which my PhD has been funded.

I would like to thank my supervisor, Prof Rasmita Raval, for having given me the opportunity to undertake this research project in her group and for her precious guidance throughout my PhD. I want to express my gratitude to Dr Sam Haq, with whom I am hugely indebted for his help during the experimental work and for the useful discussions. His generosity and unselfishness are unique. I thank Dr Alexandre Tkatchenko, Dr Wei Liu and Nicola Ferri, from the Fritz Haber Institut in Berlin, and Dr George Darling, who have carried out theoretical calculations that complement the experimental work of this thesis. Special thanks go to Fiona, who has carefully proof-read my thesis with a lot of patience, and Matthew, who has spent time training me with the instruments and also helped me with the drafting of some chapters and a paper after having left the group. All the people that have been part of the group in the last four years have provided me with help and inspiration. For this reason I thank Andrew and Chi for the initial training. I thank my fellow PhD students Dexter, Gary and Bart, who have shared with me the difficulties and the joys of this adventure for a long time. I also thank the PhD students with whom I have shared a shorter period, like Geoff, Takuma and María. The group has seen a big expansion during the last year. These new members have always supported me in a lot of different ways during the writing up of my thesis. I would like to thank all of them, in particular Yuri and Arturo, for the useful support and advices in the *latino* way, Edidiong, the real *Don*, Alan, for the nice discussions on scientific and non-scientific matters, Ed, Gareth, Paul and Emma. Special thanks go to Ioritz, with whom I have established a partnership that has improved my language skills in Spanish and my performances in *palestra*.

The amazing people that I have met during these years are so many! Sergio is my life mentor, as simple as that. The deep and inspiring *beer and chats* sessions with Emiliano on Fridays have always been something to look forward to. Enzo, the *President*, is an icon. I also want to thank Ivan, one of the wisest persons that I have met, Elena, with whom I have discovered the importance of having a woman's perspective in the matters of life, Salvatore, one of the first friends that I have made in

Liverpool, Luigi, my *bianconero* buddy, Gilberto, Ilaria, Giulia, Diego, Paolo, Marika, Covi, Chiara, Andrea, Massimo and Mattia. With all of them it has always been fun to have a laugh. In the last period of my PhD I have met a lot of new people, the *Stephenson lads*: it is nice to have a crazy party, or just a coffee, with them. I want to mention Silvia, Paula, Pepe, Giorgos, Nikolas, Marios, Eva, Marta, Lorena, Josh, Maria, Felipe, Laura, Ebénézer and Jokin.

I am not forgetting all the support and help that I have received from Italy during this period, notwithstanding the distance. For this, I would like to thank my life-long friends Walter, Giacomo, Antonio, Stefano, Andrea C, Andrea B and Silvia, but also Valentina, Irene, Celenia, Federico, Antony and Julia: whenever I meet them, it seems like I have never left. I also thank Dr Franco Dinelli and Dr Pasquale Pingue, with whom I have worked during my MSc project at the University of Pisa and who have always been available for important advices ever since.

Naturally, I wish to thank my parents Paolo and Laura, whose infinite support and love are invaluable. I also want to mention my dog Argo, the best dog ever, that accompanied me for a long period of my life and passed away a few months ago. And of course I thank my loved Clara, for the beautiful moments spent together: what we are building is the basis for a bright and happy future.

Finally, my thanks go to Liverpool and its people, for having made me feel at home. I believe that after this adventure I will be a stronger and, hopefully, a better man.

Chapter 1

Introduction

1.1 Thesis aims

The nanoconfinement of biomolecules in environments with restricted dimensionality, such as when they are adsorbed at surfaces, is a subject that has received a great interest from the scientific community, since the intermolecular interactions are significantly influenced by their interfacial positioning and by the substrate itself.

Chirality, in particular, is a property that is generally amplified when molecules are adsorbed at surfaces, and its expressions have been categorised recently [1–3]. On this basis, the role that surfaces may have played in the prebiotic development of a single-handed form of life, a phenomenon that is not understood [4], has been proposed to have been significant [5, 6]. Amongst all the systems of interest, the adsorption of amino acids on copper surfaces possessing a (110) cut has been the subject of different studies, and, interestingly, a new form of chirality, induced by the molecular adsorption and termed *footedness*, has been introduced [7]. This property is autonomous from the molecular chirality of any adsorbed molecule.

The behaviour of the amino acids glycine [8–16], alanine [17–26] and proline [7, 27–32] on the Cu(110) surface, in particular, has been thoroughly investigated. The combination of experimental and theoretical tools has allowed one to characterise these systems in terms of the footprint distribution when enantiopure systems are considered, and in terms of footprint distribution and chiral recognition phenomena at the molecular level when the racemic mixtures are studied.

This work aims at extending the database of knowledge upon the behaviour of selected amino acids on the Cu(110) surface.

The enantiopure amino acid serine, which has been shown to possess local and global chiral organisational properties [33], is the subject of chapter 4. By means of high-resolution Scanning Tunneling Microscopy (STM) data supported by theory, the distribution of chirality at the footedness level is intended to be investigated. The outcomes of this chapter constitute the basis for the investigation on the adsorption of racemic serine on Cu(110). This system has been shown to lean towards a state

in which the serine enantiomers are separated on the surface [33], which thus acts as a medium for chiral resolution. In chapter 5 the mechanisms that lead to the chiral resolution of the serine enantiomers will be proposed and further chiral recognition properties will be presented.

The adsorption of the enantiopure amino acid valine on Cu(110) is studied in chapter 6. This system has been shown to undergo a phase transition at the organisational level, from chiral to achiral, upon thermal treatment [34]. The achiral organisation will be investigated, with a particular attention to the distribution of chirality at the footprint level that is created.

Finally, in chapter 7 the adsorption of the achiral nitrogenous base adenine on Cu(110) is investigated by means of STM. It is shown that the previously published [35] two-dimensional chiral organisation adopted by this molecule is achieved after a thermal treatment of the sample. It is also presented that, before this long-range chiral organisation is achieved, a complex mixture of supramolecular phases coexist on the surface. Amongst these, the direct observation of individual isolated adenine dimers, which are considered the manifestation of the on-surface chiral nucleation at the supramolecular level, permits to propose a pathway for the formation of the long-range chiral organisation of adenine on Cu(110).

1.2 Chirality

Chirality is the fascinating property of an object to be not superimposable, via translational or rigid rotational operations, to its mirror image. The adjective *chiral* was coined by Lord Kelvin in 1894 [36, 37] and takes its origin from the Greek word for "hand", $\chi\epsilon\iota\rho$. Human hands are certainly the most iconic examples of chiral objects, to the extent that the word *handedness* is widely used as a synonym for chirality. Chirality, however, is expressed ubiquitously, from the macroscopic world to the nanoscale. In nature, there are countless examples of chiral objects. Most gastropod shells, for instance, are coiled in a spiral manner with either dextral or sinistral helicities, and heterochiral individuals are rarely present in the same species [38]. In the inanimate world, chiral shapes are also widely present. For instance, screws, springs and propellers are all helix-shaped objects with an intrinsically defined chirality. As an example, a coil-shaped boat propeller produces a rotational and a translational movement, and is an example of dynamic chirality [39]. In this case, a clockwise rotation forward or a counterclockwise rotation backward would both result in the boat moving in the same direction.

It is at the molecular level, however, that the importance of chirality has its maximum expression. Historically, Jean-Baptiste Biot [40] was the first to observe optical activity, consisting in the ability possessed by certain liquid solutions of rotating the light polarisation plane. The connection between this macroscopic physical property

and the molecular nature of the substance used was made by Louis Paster in 1848 [41]. He was able to manually separate crystals of ammonium sodium tartrate on the basis of their (chiral) shapes. He also showed that these diverse substances, once in solution, manifested equal optical activities in absolute values, but with opposite directions. Optical activity is, in fact, the sole physical property that differs in substances possessing mirror-image molecular structure [42].

1.3 Chirality at the molecular level

In organic chemical compounds, a widely available source of asymmetry is the sp^3 hybridised carbon atom. When this is bound to four different substituents, it gives rise to two possible mirror-image asymmetric structures, with their chiralities depending on the stereodistribution of the substituents (*configuration*). Each asymmetric carbon atom is termed a *stereogenic centre* or *stereocentre*. Thus, molecules that possess the same molecular formula and the same constitution can be distinguished on the basis of the configuration of their stereocentres. This class of molecules are called *stereoisomers*, of which a particular subcategory is represented by couples of *enantiomers*, i.e. two molecular structures that are the mirror images of each other. In rare circumstances, when an asymmetric centre possesses two achiral substituents and two substituents that are mirror images of each other, the stereocentre does not give rise to mirroring asymmetry, despite its asymmetrical configuration: molecules that possess one or more of these asymmetric centres are called *pseudochiral*.

Stereogenic atoms are not, however, the sole cause of asymmetry at the molecular level. A molecule can, in fact, possess chirality on the basis of its geometrical structure. Examples of the latter situation are described with the term *inherent chirality* [43, 44], a characteristic of those molecules that possess a curvature in their structure. *Axial chirality* or *helicity* are used to describe molecules with a helical spatial arrangement. Finally, molecules constituting two different non-coplanar rings that are not able to rotate about the chemical connection between them are said to possess *planar chirality* [45].

1.4 Nomenclature of enantiomers and stereocentres

Enantiomers can be classified on the basis of their ability to rotate the polarisation plane of polarised light in either a clockwise or a counterclockwise direction, as viewed from an observer towards whom the light is directed. On the basis of this property, enantiomers are labelled with the prefixes (+) and (-), respectively. Alternatively, the labels d- and l-, standing for *dextrorotatory* and *levorotatory* respectively, are used.

This system relies on the experimental determination of optical activities of defined compounds and is thus not helpful when chirality has to been assigned, for instance, to a newly discovered molecule. Furthermore, it is not accurate for molecules possessing more than one stereogenic centre.

In biochemical practice, the D-/L- nomenclature is extensively utilised. In this historical system the configuration of enantiomers is related to that of either optical isomers of glyceraldehyde, thus the prefixes D- or L-, based on the Latin words for right, *dexter*, and left, *laevus*, are assigned. The need of a reference molecule for the D-/L- system has made it unsuitable for compounds not related to biochemistry, and the development of a universal nomenclature has become necessary.

This reference system, established in the 50s, is named *the sequence rule* or *CIP system*, from the initials of its inventors [46–48]. In this convention, priorities are attributed to the four substituents of an asymmetric atom on the basis of arbitrary rules that take into account, amongst other factors, the atomic mass and the position of the atoms constituting each substituent. Once the priorities, indicated with the Roman numerals in figure 1.1, where the lowest number denotes the highest priority, are assigned, their stereodistribution is considered. Placing the group with lowest priority (IV) away from the observer, it is possible to draw an imaginary circle joining the remaining three groups in the order of decreasing priorities (I-II-III). If the direction of the path appears counterclockwise or clockwise to the observer, the stereocentre is denoted with the stereodescriptors (R) or (S), respectively (figure 1.1). Again, the origin of this denotation comes from the Latin words to indicate right, *rectus*, and left, *sinister*.

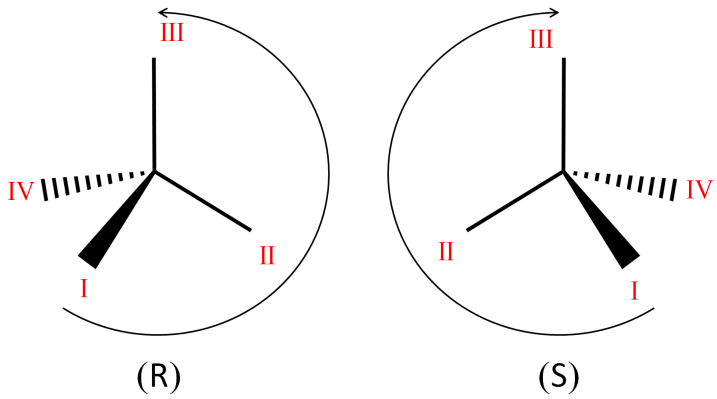

Figure 1.1: Scheme of the Cahn-Ingold-Prelog convention [47] for the attribution of chirality to a tetrahedral stereogenic centre. The Roman numerals I-IV indicate substituents with decreasing priorities.

1.5 True and false chirality: the parity violating weak interactions

A complete understanding of the manifestations of chirality at the molecular level needs to take into account the symmetry-breaking factors that take place at a subatomic scale. Considering the symmetries that underpin all the fundamental physical quantities, these are distinguishable on the basis of their behaviour upon three basic symmetry operations, namely parity (P), time reversal (T) and charge conjugation (C). For instance, *scalars* and *axial vectors* are invariant upon inversion of the spatial coordinates, whereas *pseudoscalars* and *polar vectors* change sign. Analogously, physical quantities are divided into *time-even* or *time-odd*, depending upon their behaviour upon a time-reversal operations [49]. Although a physical quantity might break the symmetry within a single operation, it has to show invariance upon the composition of the three fundamental symmetries (CPT) [50–52]. This theorem, known as CPT or Lüders-Pauli theorem [53–55], is based on the Lorentz covariance of the Hamiltonian of a given system [56]. Taking into account the fundamental interactions, it is acknowledged that electromagnetic and strong nuclear forces are parity-invariant, whereas the weak interactions mediated by bosons, as in the β-decay processes of radioactive nuclei, are not [4]. This fundamental and perhaps surprising concept was hypothesised theoretically by Lee and Yang in 1956 [57], and was confirmed experimentally shortly afterwards by Wu and collaborators [58]. The authors studied the β-decay of a neutron from ^{60}Co into a proton, an electron and an electron antineutrino:

$$^{60}\mathrm{Co} \longrightarrow {}^{60}\mathrm{Ni} + e^{-} + \bar{\nu}_e \tag{1.1}$$

The spin polarisation of the electron emitted was found to have a given chirality (helicity) [58]. The electron with opposite chirality would be emitted as a product of the reaction with constituents made of antiparticles. The symmetry is thus recovered upon parity combined with charge conjugation (CP) [59]. This finding is at the basis of the concept of *true chirality*. Hence, a *true enantiomer* of a given chiral molecule is that molecule with mirror-image constitution composed of antiatoms (figure 1.2). It is noted that in the body of this work, for simplicity, the term *enantiomers* refers to *P-enantiomers*, i.e. molecules that are superimposable through the sole inversion of spatial coordinates.

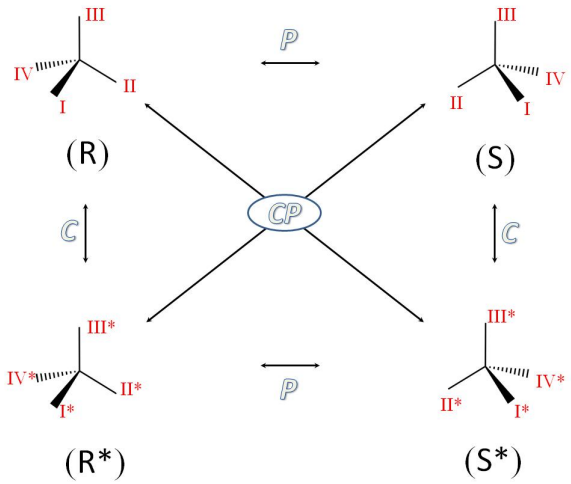

Figure 1.2: Diagram showing the effect of parity (P), charge conjugation (C) and their combination (CP) on a stereogenic centre. The priorities of the substituents and the stereodescriptors of the centres according to the CIP system are indicated. Asterisks denote antimatter. The diagram is inspired by [49].

1.6 Chirality in the biosphere

The environment in which chirality is expressed at its utmost degree is represented by the living world. This was suggested for the first time by Pasteur's famous experiment [41], in which he showed that natural samples of sodium ammonium tartrate showed different optical activities compared to the synthesised ones. The key molecules involved in life constitution and reproduction present, in fact, an intrinsic chiral homogeneity. This is the case of D-sugars forming the backbone of nucleic acid chains and of L-amino acids, the building blocks of proteins. As a macroscopic effect of this, it is noteworthy that, in some cases, mirror image molecules are perceived by the human body in deeply different ways. For instance some pharmaceuticals are active in just one enantiomeric form, with the mirror-image molecules having toxic effects on the human body, resulting in the consequent development of targeted single-enantiomer pharmaceutical research in the last decades [60–62]. One of the most notorious examples of enantiospecific bioactivity is represented by the thalidomide tragedy. While the R-enantiomer has the property of alleviating morning sickness and nausea, the S-enantiomer is found to have teratogenic effects. However, in this case the exclusive administration of the non-toxic enantiomer would not have prevented the calamity, since in vivo racemisation processes of thalidomide have been demonstrated to take place [63]. Furthermore, the gustatory sensations towards specific chiral substances have also been studied. For instance, the amino acid serine is perceived as sweet or sweet/umami if ingested in its D- or L- form, respectively [64]. These examples are direct manifestations of the fact that the human

body, like that of all living organisms, is a truly chiral environment, in which molecules with the same chemical constitution but diverse chirality show differing reactivities. The latter property, a different reactivity in chiral environments, is in fact a specific characteristic of stereoisomers.

1.6.1 Theories on the origin of the homochirality of life

The dilemma concerning the origin of chiral homogeneity in biological matter is far from being resolved, despite the great number of experimental works that have been performed and the numerous theories proposed in this field. The theories approaching this issue can be classified as biotic or abiotic [4]. Biotic theories postulate that a symmetry-breaking event occurred after the appearance of life on Earth, caused by a natural selection process in which one of the two mirror-image possible life forms eventually ceased to exist. Conversely, abiotic approaches, widely acknowledged today [65], place that event before the biological era and consider it a prior condition for life development. In the latter hypothesis, external causes are alleged to have introduced a chiral bias in organic building blocks. A fact in favour of this hypothesis was the finding of the famous Murchison meteorite, in which traces of modified amino acids with a slight predominance of the L-form were retrieved [66–68].

Amongst these external factors, circularly polarised light (CPL) originating from cosmic background radiation [69, 70] has been proposed as a cause for the introduction of asymmetry in organic molecules [71, 72]. Research in this field includes examples of experiments conducted on the amino acids alanine, glutamic acid [71] and leucine [73], which have been shown to undergo asymmetric decomposition upon radiation with CPL, yielding enantiomeric excesses (*ee*) up to 2.5%. Parity violating energy differences (PVED) between enantiomers have also been proposed as a source of chiral bias [74, 75]. PVED consist in minuscule differences in the binding energies of mirror-image molecules. The rationale underlying this concept takes origin from the parity-violating weak interactions that determine the idea of true and false chirality (see section 1.5). PVEDs have been calculated theoretically, but experimental evidence of an energetic imbalance between two enantiomers has not been hitherto achieved [49, 76]. PVED for amino acid enantiomeric couples have been calculated to be in the order of $10^{-14} kJ/mol$ [77]. Successive calculations have also taken into account D-sugars [78]. In both cases, naturally occurring biomolecules, such as L-amino acids and D-sugars, have shown to be energetically favoured [75].

Additional symmetry-breaking processes of terrestrial origin have been proposed, including asymmetric crystallization processes that lead, locally, to one-handed conglomerates [79, 80]. Processes of enantioenrichment have been suggested on the basis of asymmetric autocatalysis [81], which could have created enantiopure systems starting from small *ee*s, following nonlinear stereochemical processes [82–84]. Finally, another

terrestrial hypothesis sees the involvement of interactions between mineral surfaces and organic molecules in the creation of enantiomeric imbalances. Diverse experimental studies have shown the preferential adsorption/desorption of specific enantiomers of amino acids and peptides on intrinsically chiral surfaces of geologic relevance [85–88].

The emergence of novel types of chirality arising from the restricted dimensionality of surfaces are briefly described in the following section.

1.7 Chirality at surfaces

The creation of chirality in two dimensions can be grouped into two different categories. Surfaces can, in fact, be intrinsically chiral or rendered so via the adsorption of molecular systems. To the first scenario belong high-Miller index surfaces, in which the reduced symmetry favours the formation of regions in which the interfacial atomic arrangement presents local chirality, given by sense of rotation of microfacets with decreasing atomic density [5, 89]. An alternative way consists in employing adsorbates as chiral modifiers on an achiral interface, able to locally break the symmetry of the underlying substrate and create a chiral environment. The latter field of research, in which this work is included, has seen a considerable expansion in recent times [1, 2, 90–93].

The expressions of chirality at surfaces upon adsorption of molecular overlayers are multiple and manifold, mainly as a result of the low dimensionality that the system surface-molecules experiences. In fact, in terms of point group symmetry, the 32 crystallographic point groups in 3D are reduced to 10 in 2D, of which 5 are chiral. In terms of molecular organisation at surfaces, 17 space group are allowed, of which 5 are chiral, compared to the 230 possible space groups in 3D [2]. Furthermore, chirality at surfaces has been categorised in terms of the symmetry-breaking effects that the molecular adsorption implies [1, 90]. The adsorption of a chiral molecule on a surface always bestows chirality at the adsorption site, since mirror-image environments cannot be created due to the intrinsic molecular chirality of the adsorbate. This situation is termed *global point chirality* (figure 1.3c). However, adsorption of achiral molecules can also occur in a chiral manner, i.e. the interaction with the surface can occur in two different mirror-image ways. In these cases molecules are termed *prochiral*, and give rise to *local point chirality* (figure 1.3a,b). If no preference between the two mirroring adsorption geometries is expressed, the system remains racemic overall, but with local chiral environments. When adsorbed molecules self-assemble in extended 2D networks, organisational chirality can be categorised. *Local organisational chirality* (figure 1.3d) takes place when achiral molecules assemble in two possible mirror-image domains (e.g. with mirroring unit cells or along mirroring surface directions). Again, in the absence of a bias towards the creation of either of the two kinds of chiral domains the system is overall racemic. In addition, chiral molecules may assemble in extended achiral do-

mains, and this is the case in which *global point* and *local organisational chirality* coexist (figure 1.3e). Finally, the maximum chiral expression at surfaces is manifested when chiral molecules are organised in chiral domains (figure 1.3f). In the latter situation the system possesses *global point* and *global organisational chirality*.

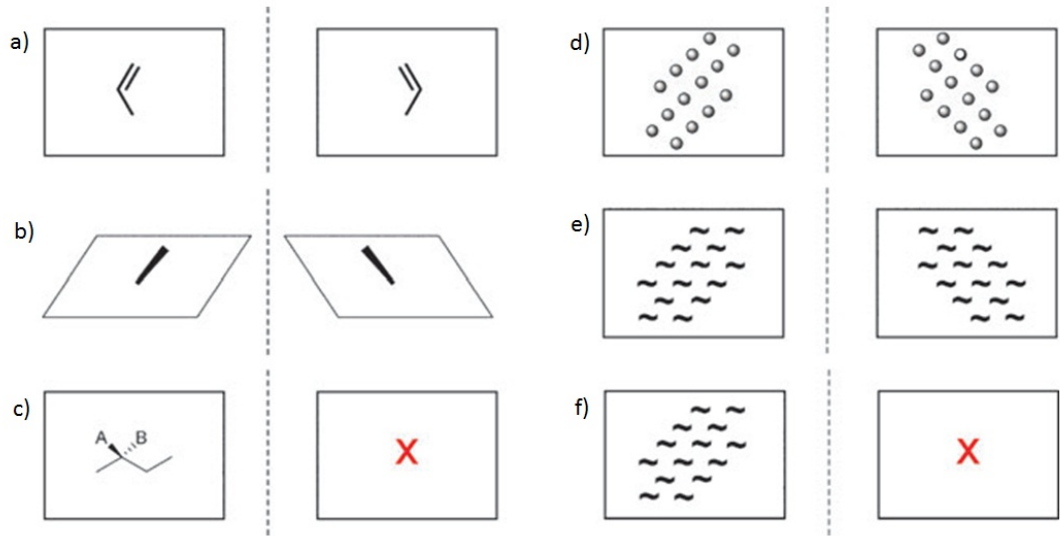

Figure 1.3: Schematic representation of the types of local point (a-c) and organisational (d-f) chirality that molecules can introduce upon adsorption of an achiral surface. Mirroring planes normal to the surface are represented by dashed lines. a-b) Local point chirality upon adsorption of an achiral (prochiral) molecule in a flat or tilted geometry, respectively. c) Global point chirality upon adsorption of a chiral molecule. d) Local organisational chirality, created by the assembly of achiral molecules in chiral domains. e) Global point and local organisational chirality, which describes the achiral organisation of chiral molecules. f) Global point and global organisational chirality, situation achieved when chiral molecules self-assemble in chiral domains. After [1].

The extension at which chirality is conferred to an achiral surface upon molecular adsorption can be categorised further on the basis of the dimensionality of the chiral regions that are created [2]. *0D chirality* refers to the chirality induced upon the adsorption of an individual molecule in isolated state, which means without the creation of an organisational chirality. The formation of molecular-wide lines or stripes with a given chiral direction belongs to the case of *1D chirality*. When, finally, chirality is bestowed in long-range domains, a proper organisational chirality is created and classified as *2D chirality* [2].

The amplification of chiral phenomena has also been observed at surfaces through the use of chiral adsorbates [6]. The most noticeable effects, which are named after similar mechanisms studied in stereoregular polymeric systems [94, 95], are called *sergeant and soldier* and *majority rules*. The former mechanism sees the surface chirality led by the adsorption of a chiral molecule (the *sergeant*) which forces a coadsorbed prochiral molecule (the *soldier*), which would otherwise adopt two energetically degen-

erate mirror-image geometries, to adsorb in a homochiral way [96–100]. A landmark study in this regard is represented by the coadsorption of tartaric acid and succinic acid on Cu(110), that gives rise to a single-handed surface organisation depending on the chirality of the *sergeant* molecule, in this case tartaric acid [98, 101]. In the *majority rules* mechanism, a small enantiomeric disproportion in the adsorbates determines an extended on-surface homochirality [102–105]. Also in this case, the study of the adsorption of tartaric acid on Cu(110) is instructive: introducing a small *ee* of tartaric acid in the adlayers yields the formation of extended homochiral 2D structures whose chirality is governed by the enantiomer in excess [106].

1.7.1 Amino acids on the Cu(110) surface

The adsorption of naturally chiral biomolecules such as amino acids on defined single-crystal metal surfaces has attracted huge attention in the last few decades [7–15, 17–23, 27–33, 107–124], thanks to their wide availability and to their property of facile sublimation in vacuum [125, 126]. Moreover, surface-supported amino acids and derivatives have been shown to introduce enantioselectivity in heterogeneous catalysis. This is the case, for example, of the amino acid alanine in the hydrogenation of β-ketoesters on Ni catalysts [127], and of modified proline on carbon [128, 129]. Amongst the surfaces involved in the coordination of amino acids, copper has represented the most studied substrate, due to its intermediate reactivity towards organic biomolecules. In fact, while most organic molecules do not undergo dissociative adsorption processes on copper surfaces, maintaining their chemical form upon adsorption, the outermost copper atoms on the surface usually establish a strong interaction with the organic overlayer. In this manner, 2D confinement effects are manifested, in coexistence with those originated by the intermolecular interactions between adsorbed molecules, which commonly lead to their self-assembly on copper surfaces. With regards to the surface crystallography, the (110) face of copper has been proven to be the most suitable for highlighting surface-induced chiral effects, in terms of point chirality and organisational chirality, in a variety of systems [2], plausibly as a consequence of its rectangular unit cell possessing a two-fold symmetry.

On the Cu(110) surface, amino acids adsorb preferentially in their anionic form, with deprotonation occurring at the carboxylic moiety. The coordination with the copper surface is usually mediated via the two oxygen atoms of the carboxylate group, that are placed along the close-packed surface direction, and the nitrogen atom of the amino group, giving rise to a tridentate adsorption geometry that has been named μ_3 [116]. This adsorption geometry gives rise to two different footprints, depending on the position of the nitrogen atom in comparison to the carboxylate bonding. If the nitrogen coordination occurs at the bottom-left or at the bottom-right if an observer looks at the carboxylate bonding scaffold, the two adsorption footprints are termed *lambda* (λ) or

delta (δ), respectively (figure 1.4). In this manner, a new type of chirality is implicitly introduced, referring solely to the stereodistribution of the atoms coordinated with the surface and generally independent from the molecular chirality, or *handedness*. For this reason it has been named *footedness* [7].

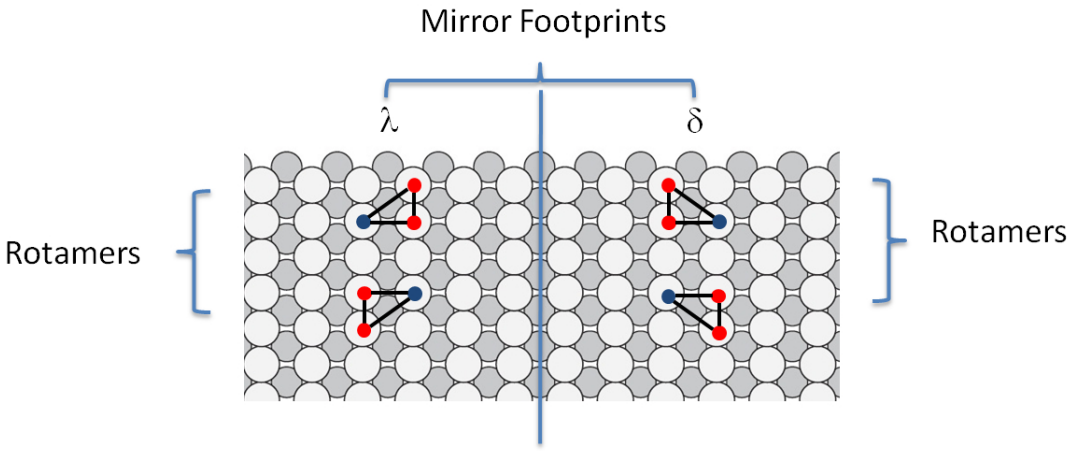

Figure 1.4: The two mirroring footprints that a μ_3 adsorption geometry of an amino acid on Cu(110) allows. Molecules are schematically represented with right-angled triangles, at whose vertices the atoms in coordination with the surface are placed, i.e. the carboxylate oxygen atoms (red) and the amino nitrogen atom (blue). The two footprints are named λ or δ depending on the position of the nitrogen atom with respect to the carboxylate bonding (see text for details). Each footprint allows two rotamers, both sketched in the figure.

1.7.2 Case studies: glycine, alanine and proline on Cu(110)

Surface science studies of amino acids adsorbed on a metallic surface present significant challenges. In order to achieve a complete structural study of an amino acid-metal system, in fact, it is essential to probe various characteristics of the adsorbed molecules: these include chemical forms of the molecules, their bonding geometries, their possible long-range organisation and their conformation in terms of footprint chirality. When racemic adsorbates are taken into account, further aspects need to be characterised, namely the chiral recognition phenomena that are established at the molecular and the footprint levels. Averaging investigating techniques, of which vibrational and X-ray spectroscopies represent examples, are not able to distinguish conformers having different footprints. The small size of amino acids and their residual groups renders them, on the other hand, very difficult to be recognised through local-probe techniques. Due to, and perhaps notwithstanding, these reasons, the studies on the adsorption of glycine [8–16], alanine [17–26] and proline [7, 27–32] on the Cu(110) surface have produced a wealthy literature.

Glycine is the sole naturally occurring amino acid that is not chiral, possessing just a hydrogen atom as residual group. However, two different mirroring footprints are possible. In this case, the creation of mirror-image footprints yields the formation of two possible real mirror-image structures. Glycine molecules self-assemble on the Cu(110) surface with a (3x2) unit cell, as shown via Scanning Tunneling Microscopy (STM) [10]. The authors of this study proposed a coexistence of homochiral and heterochiral arrangements on the surface. This suggestion has been confirmed to an extent by successive theoretical calculations [12, 13]. However, only recently an experimental study based on Low Energy Electron Diffraction with quantitative analysis (LEED-IV) has ruled out a homochiral arrangement, proposing a strict heterochiral footedness for glycine molecules on Cu(110) [16].

The prototype of the complexities that can arise in the investigations of amino acids at surfaces is represented by the alanine/Cu(110) system. Despite its simplicity, alanine being the smallest chiral amino acid, possessing a methyl residual group, it shows a surprising variety of adsorption patterns on the Cu(110) surface. The polymorphism displayed by S-alanine is summarised in figure 1.5 [116, 117]. At low coverages, a disordered mobile structure (phase I), with molecules possessing a μ_3 adsorption geometry is observed [19]. Increasing the coverage, the emergence of two-contact (μ_2) adsorption is detected. This has been inferred from the appearance of a vibrational band at 1626 cm^{-1} in Reflection Absorption Infra-Red Spectroscopy (RAIRS) studies, attributed to the asymmetric stretching mode of the carboxylate group ν_{as}(OCO), which indicates that one of the carboxylate oxygen atoms has moved away from the surface (phase II) [17, 19]. The coexistence of this μ_2 geometry is associated with the emergence of a chiral organisation with unit cell (2 -2, 5 3), which appears when the high-coverage sample is annealed to 430 K (phase III), as shown via STM [18]. Further annealing yields the formation of an achiral (3x2) arrangement, with the recovery of the μ_3 geometry (phase IV) [19]. Theoretical calculations that have been carried out on the (3x2) alanine structure have put forward a heterochiral footedness arrangement in the unit cell [24].

A similar phase diagram has been observed for the adsorption of racemic alanine on Cu(110), with a high-temperature (3x2) organisation [23]. This LEED and STM-based study has however highlighted some differences with respect to the enantiopure species. While the latter always shows a mismatched, or "distorted",(3x2) organisation with the surface lattice, racemic alanine is able to reach a "true" (3x2) organisation at high coverages [23] (figure 1.6). STM images however are not able to determine the chirality at the molecular and footprint levels of racemic alanine adlayers. Theoretical calculations performed on this system have predicted a strict heterochiral footedness, whereas the molecular chirality is randomly organised, with no enantiospecific recognition phenomena taking place [24].

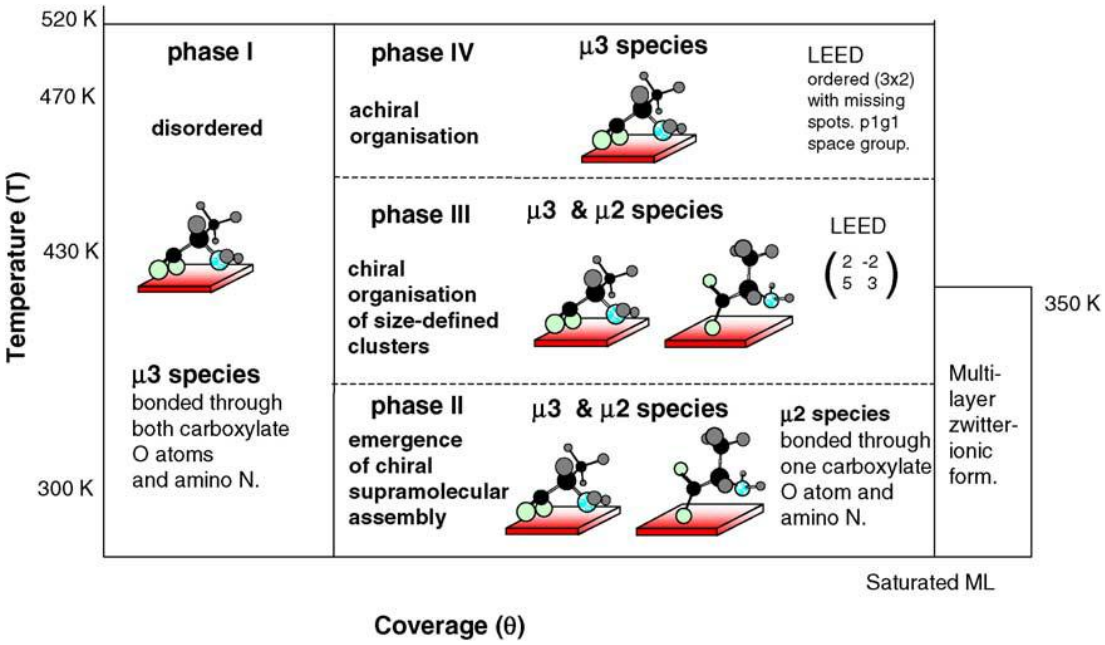

Figure 1.5: The complex phase diagram that enantiopure S-alanine manifests on the Cu(110) surface, depending on the coverage and temperature of annealing. Figure reproduced from [117].

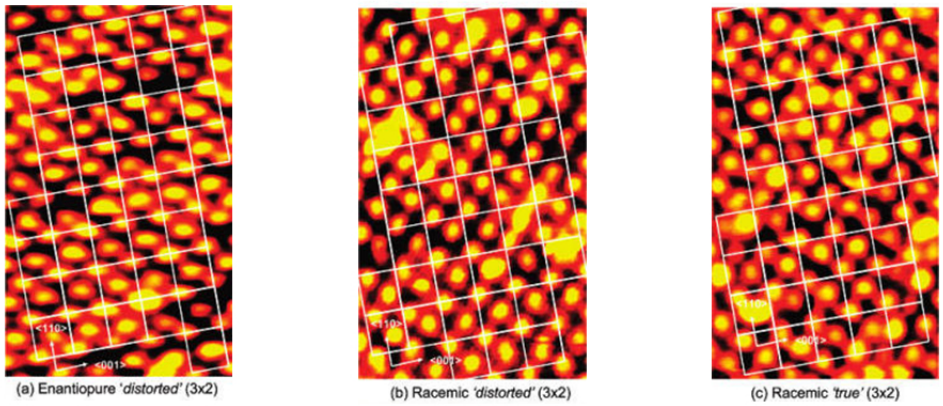

Figure 1.6: STM images of alanine on Cu(110). a) "Distorted" (3x2) phase IV for S-alanine on Cu(110). b) "Distorted" (3x2) phase for RS-alanine on Cu(110). c) "True" (3x2) phase for RS-alanine on Cu(110). In each image, a (3x2) net is superimposed to the STM signal. Images reproduced from [23].

A significantly deeper understanding of the insights of chiral ordering in terms of handedness and footedness has been achieved for the adsorption of the amino acid proline on Cu(110) [7, 28–32]. This has been somehow facilitated by a peculiar property of this amino acid, whose amino group is incorporated within a pyrrolidine ring, that confers to the molecule an enhanced structural rigidity with respect to other amino acids. An STM study, combined with Density Functional Theory (DFT) calculations and STM simulations [28] has been able to structurally resolve the enantiopure S-proline adlayer within the previously reported (4x2) arrangement [27]. The λ and δ footprints of S-proline have been shown to possess the pyrrolidine ring tilted and planar respect to the surface, respectively. These arrangements give rise to two geometries that are clearly recognisable via STM (figure 1.7b). The simulated images (figure 1.7a) attribute the production of a higher STM intensity to a proline conformer with its ring tilted away from the surface, whereas a proline molecule with a planar ring would originate a weaker STM signal. As a consequence, a stringent heterochirally footed organisation is found, with alternate rows featuring high- and low-intensity STM signals dictated by the molecular footprint, as shown in figure 1.7c, where S-proline molecules adopting λ and δ footprints are sketched with filled and empty triangles, respectively [28].

The ability of correlating STM intensities with adsorption footprints has proven subsequently useful in determining the chiral ordering of racemic proline on Cu(110), with an STM study supported by DFT calculations and simulations [30]. Along with two distinct manners of appearance of proline molecules, with bright and weak STM signals, a slight elongation of the features, indicated with white triangles in figure 1.8a, is visible. This has been attributed to the conformation of the molecules at the footprint level, which is then probed directly via STM for the first time. These two aspects allow a complete structural determination in terms of the chirality distribution at molecular and footprint levels. Whereas the strict heterochiral footprint organisation is maintained in the achiral (4x2) structure, R- and S-proline are randomly distributed in the adlayer (figure 1.8b), constituting a random solid solution with no chiral recognition properties present at the molecular level [30]. In the schemes of figures 1.8c-e the random distribution of conformers and molecular chirality (figure 1.8c,d), accompanied with a strict heterochiral footprint arrangement (figure 1.8e), is highlighted.

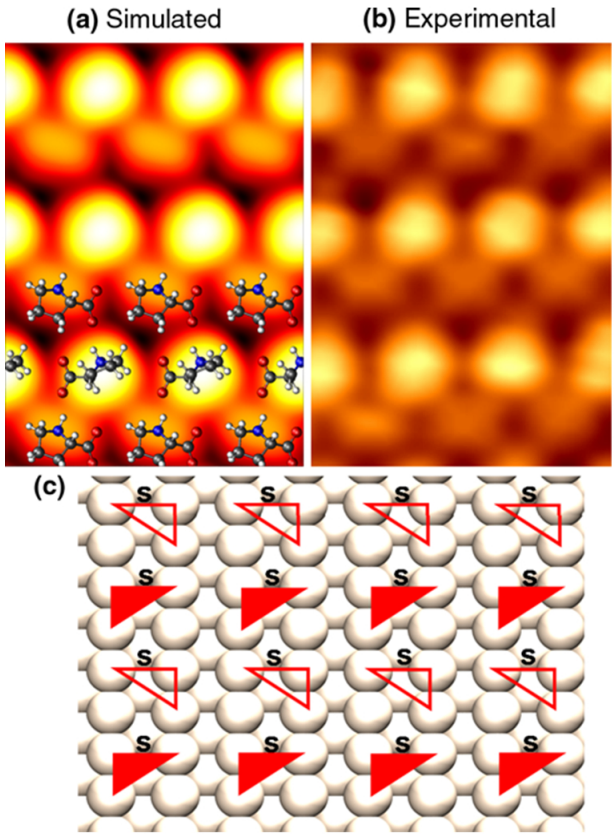

Figure 1.7: a-b) Simulated and experimental STM images of S-proline on Cu(110), respectively. In a) the molecular geometry of each conformer resulting from DFT calculations is superimposed to the simulated image. c) Scheme representing the distribution of chirality at the footedness level, which is denoted with filled and empty triangles, to indicate λ and δ conformers, respectively. Image reproduced from [31].

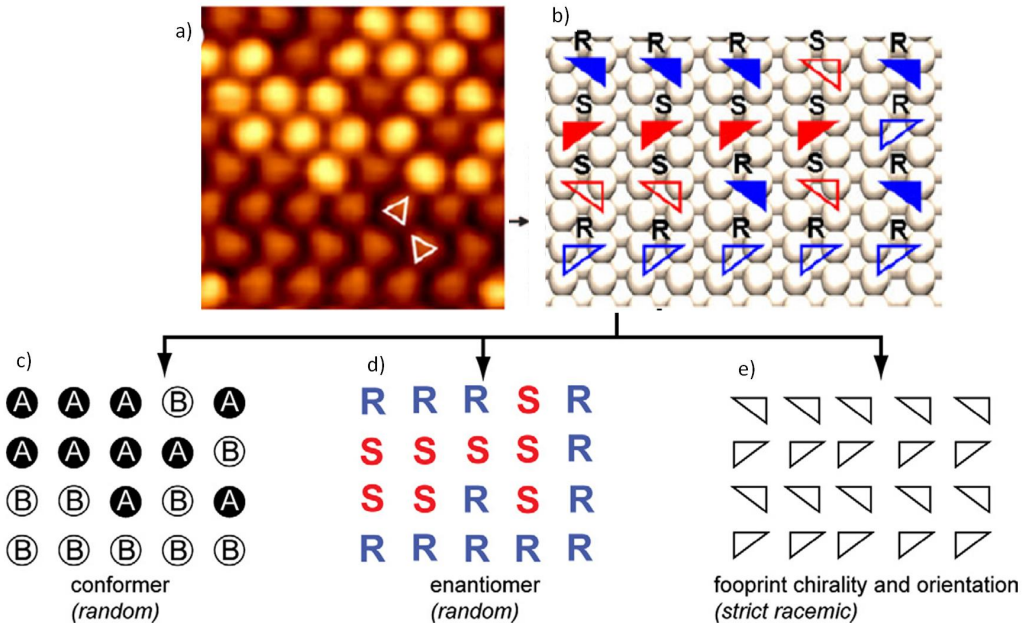

Figure 1.8: a) STM image of racemic proline on Cu(110). Faint and bright intensities are clearly visible. Superimposed triangles indicate the possibility of tracking the organisation at the footprint level. b) Scheme indicating the distribution of handedness, with the letters R and S, and footedness, with filled and empty triangles for λ and δ conformers. c) Sketch of the random conformational organisation. The letters A and B denote a proline molecule with a tilted and planar pyrrolidine ring, respectively. d) Sketch of the random distribution of molecular chirality. e) Sketch of the strict racemic organisation in the chiral recognition at the footprint level. Images and diagrams adapted from [29].

1.7.3 Considerations upon the chiral recognition events in the amino acid organisation on Cu(110)

In summary, in the previous section it has been shown that the tridentate adsorption geometry (μ_3) through the carboxylate and the amino groups that amino acids like glycine, alanine and proline adopt on the Cu(110) surface yields a symmetry-breaking effect that allows us to define an adsorption-induced chirality, or footedness, in these systems. The μ_3 geometry is also associated to molecular assemblies with (nx2) periodicity, and chirality is thus not expressed at the organisational level. In the case of glycine, the (3x2) organisation features a racemic footprint distribution, that renders the adsorbed glycine molecules mirror-image conformers, as an example of local point chirality. A heterochiral footprint distribution is also observed in the (3x2) and (4x2) arrangements adopted by enantiopure alanine and proline on Cu(110), respectively, which corresponds to the creation of global point chirality. The depositions on Cu(110) of alanine and proline in their racemic form do not cause changes in the organisational assembly, which remains achiral. However, the heterochirality in the footedness distribution is maintained. The importance of alternating footprints renders the intrinsic molecular chirality of the adsorbers immaterial in terms of the positioning on the surface. This phenomenon, i.e. the on-surface formation of a solid solution, is particularly instructive with regards to the importance of surfaces in the organisation of molecular chirality. In order to understand this effect, it is important to consider the aggregation states of racemic compounds in three-dimensional crystals. Typically, the convolution of thermodynamic and kinetic mechanisms underpin the bias that lead to either homochiral or heterochiral recognition events in 3D [130], fact that renders the theoretically predicted chiral behaviour of a racemate challenging. Empirically, it has been observed that the dominant form (circa 90%) in crystalline structures is the racemic organisation, whereas about 10% of compounds undergo segregation in enantiopure conglomerates. The form of the random solid solution, in which molecules are distributed independently of their molecular chirality, accounts for a fraction smaller than 1% [92, 131, 132]. The examples provided by the adsorption of racemic alanine and proline on the Cu(110) surface are thus extremely informative on the ability of surfaces to induce not only a new form of adsorption-induced chirality, but also randomisation effects of the molecular chirality that are hardly observed in three dimensions.

In this thesis the behaviour on the Cu(110) surface of the amino acid serine, in its enantiopure (chapter 4) and racemic (chapter 5) forms, will be investigated. The study of both these systems will allow to expand the knowledge on the distribution of chirality of this amino acid at the footprint level, and the effect of the surface on the recognition effects taking place between the two enantiomers, in the case of the racemic mixture.

The enantiopure amino acid S-valine undergoes a phase transition at the organisational level on Cu(110), from chiral to achiral, upon annealing. The achiral high-temperature phase will be investigated, and a correlation between its achiral organisation with the footprint chirality of the conformers populating this molecular assembly will be attempted (chapter 6).

Finally, the chiral expressions manifested at the Cu(110) surface are complemented by the STM study on the adsorption of the achiral nucleobase adenine (chapter 7). It will be illustrated that adsorption-induced forms of chirality with different dimensionality, as described in section 1.7, are present on the surface, and the formation of chiral nuclei, then able to give rise to extended chiral networks, will be particularly highlighted.

References for chapter 1

[1] J. Elemans, I. De Cat, H. Xu, and S. De Feyter, "Two-dimensional chirality at liquid-solid interfaces," *Chemical Society Reviews*, vol. 38, no. 3, pp. 722–36, 2009.

[2] R. Raval, "Chiral expression from molecular assemblies at metal surfaces: insights from surface science techniques," *Chemical Society Reviews*, vol. 38, no. 3, pp. 707–21, 2009.

[3] K.-H. Ernst, "Molecular chirality in surface science," *Surface Science*, vol. 613, pp. 1–5, 2013.

[4] W. Bonner, "The origin and Amplification of Biomolecular Chirality," *Origins of Life and Evolution of the Biosphere*, vol. 21, p. 59, 1991.

[5] R. M. Hazen and D. S. Sholl, "Chiral selection on inorganic crystalline surfaces," *Nature Materials*, vol. 2, no. 6, pp. 367–74, 2003.

[6] K.-H. Ernst, "Amplification of chirality at solid surfaces," *Origins of Life and Evolution of the Biosphere*, vol. 40, no. 1, pp. 41–50, 2010.

[7] A. G. Mark, M. Forster, and R. Raval, "Recognition and ordering at surfaces: the importance of handedness and footedness," *Chemphyschem*, vol. 12, no. 8, pp. 1474–80, 2011.

[8] S. Barlow, K. Kitching, S. Haq, and N. Richardson, "A study of glycine adsorption on a Cu{110} surface using reflection absorption infrared spectroscopy," *Surface Science*, vol. 401, no. 3, pp. 322–335, 1998.

[9] N. Booth, D. Woodruff, O. Schaff, T. Gießel, R. Lindsay, P. Baumgärtel, and A. Bradshaw, "Determination of the local structure of glycine adsorbed on Cu(110)," *Surface Science*, vol. 397, no. 1-3, pp. 258–269, 1998.

[10] Q. Chen, D. Frankel, and N. Richardson, "Chemisorption induced chirality: glycine on Cu{110}," *Surface Science*, vol. 497, no. 1-3, pp. 37–46, 2002.

[11] J.-H. Kang, R. L. Toomes, M. Polcik, M. Kittel, J.-T. Hoeft, V. Efstathiou, D. P. Woodruff, and A. M. Bradshaw, "Structural investigation of glycine on Cu(100) and comparison to glycine on Cu(110)," *The Journal of Chemical Physics*, vol. 118, no. 13, p. 6059, 2003.

[12] M. Nyberg, M. Odelius, A. Nilsson, and L. G. M. Pettersson, "Hydrogen bonding between adsorbed deprotonated glycine molecules on Cu(110)," *The Journal of Chemical Physics*, vol. 119, no. 23, p. 12577, 2003.

[13] R. B. Rankin and D. S. Sholl, "Assessment of heterochiral and homochiral glycine adlayers on Cu(110) using density functional theory," *Surface Science*, vol. 548, no. 1-3, pp. 301–308, 2004.

[14] S. Blankenburg and W. G. Schmidt, "Steric effects and chirality in the adsorption of glycine and phenylglycine on Cu(110)," *Nanotechnology*, vol. 18, no. 42, p. 424030, 2007.

[15] M. L. Clegg, L. Morales de la Garza, S. Karakatsani, D. A. King, and S. M. Driver, "Chirality in Amino Acid Overlayers on Cu Surfaces," *Topics in Catalysis*, vol. 54, no. 19-20, pp. 1429–1444, 2011.

[16] Z. V. Zheleva, T. Eralp, and G. Held, "Complete Experimental Structure Determination of the p(3 x2)pg Phase of Glycine on Cu{110}," *The Journal of Physical Chemistry C*, vol. 116, pp. 618–625, 2012.

[17] J. Williams, S. Haq, and R. Raval, "The bonding and orientation of the amino acid l-alanine on Cu{110} determined by RAIRS," *Surface Science*, vol. 368, no. 1-3, pp. 303–309, 1996.

[18] S. M. Barlow, S. Louafi, D. Le Roux, J. Williams, C. Muryn, S. Haq, and R. Raval, "Supramolecular assembly of strongly chemisorbed size- and shape-defined chiral clusters: S- and R-alanine on Cu(110)," *Langmuir*, vol. 20, no. 17, pp. 7171–6, 2004.

[19] S. Barlow, S. Louafi, D. Le Roux, J. Williams, C. Muryn, S. Haq, and R. Raval, "Polymorphism in supramolecular chiral structures of R- and S-alanine on Cu(110)," *Surface Science*, vol. 590, no. 2-3, pp. 243–263, 2005.

[20] R. B. Rankin and D. S. Sholl, "Structures of glycine, enantiopure alanine, and racemic alanine adlayers on Cu(110) and Cu(100) surfaces," *The Journal of Physical Chemistry B*, vol. 109, no. 35, pp. 16764–73, 2005.

[21] D. Sayago, M. Polcik, G. Nisbet, C. Lamont, and D. Woodruff, "Local structure determination of a chiral adsorbate: Alanine on Cu(110)," *Surface Science*, vol. 590, no. 1, pp. 76–87, 2005.

[22] G. Jones, L. Jones, F. Thibault-Starzyk, E. Seddon, R. Raval, S. Jenkins, and G. Held, "The local adsorption geometry and electronic structure of alanine on Cu{110}," *Surface Science*, vol. 600, no. 9, pp. 1924–1935, 2006.

[23] S. Haq, A. Massey, N. Moslemzadeh, A. Robin, S. M. Barlow, and R. Raval, "Racemic versus enantiopure alanine on Cu(110): an experimental study," *Langmuir*, vol. 23, no. 21, pp. 10694–700, 2007.

[24] R. B. Rankin and D. S. Sholl, "Structure of enantiopure and racemic alanine adlayers on Cu(110)," *Surface Science*, vol. 574, no. 1, pp. L1–L8, 2005.

[25] J. Seifert, M. Busch, E. Meyer, and H. Winter, "Surface Structure of Alanine on Cu(110) Studied by Fast Atom Diffraction," *Physical Review Letters*, vol. 111, no. 13, p. 137601, 2013.

[26] J. Seifert, M. Busch, E. Meyer, and H. Winter, "Surface structure of alanine on Cu(110) via grazing scattering of fast atoms and molecules," *Physical Review B*, vol. 89, no. 7, p. 075404, 2014.

[27] E. Mateo Marti, S. Barlow, S. Haq, and R. Raval, "Bonding and assembly of the chiral amino acid S-proline on Cu(110): the influence of structural rigidity," *Surface Science*, vol. 501, no. 3, pp. 191–202, 2002.

[28] M. Forster, M. S. Dyer, M. Persson, and R. Raval, "Probing conformers and adsorption footprints at the single-molecule level in a highly organized amino acid assembly of (S)-proline on Cu(110)," *Journal of the American Chemical Society*, vol. 131, no. 29, pp. 10173–81, 2009.

[29] A. G. Mark, M. Forster, and R. Raval, "Direct visualization of chirality in two dimensions," *Tetrahedron*, vol. 21, no. 9-10, pp. 1125–1134, 2010.

[30] M. Forster, M. S. Dyer, M. Persson, and R. Raval, "2D random organization of racemic amino acid monolayers driven by nanoscale adsorption footprints: proline on Cu(110)," *Angewandte Chemie (International ed. in English)*, vol. 49, pp. 2344–2348, 2010.

[31] M. Forster, M. S. Dyer, M. Persson, and R. Raval, "Assembly of Chiral Amino-Acids at Surfaces from a Single Molecule Perspective: Proline on Cu(110)," *Topics in Catalysis*, vol. 54, no. 1-4, pp. 13–19, 2011.

[32] M. Forster, M. S. Dyer, M. Persson, and R. Raval, "Tailoring homochirality at surfaces: going beyond molecular handedness," *Journal of the American Chemical Society*, vol. 133, no. 40, pp. 15992–16000, 2011.

[33] T. Eralp, A. Shavorskiy, Z. V. Zheleva, G. Held, N. Kalashnyk, Y. Ning, and T. R. Linderoth, "Global and local expression of chirality in serine on the Cu{110} surface," *Langmuir*, vol. 26, no. 24, pp. 18841–51, 2010.

[34] M. L. Támara, *Factors controlling enantiomer-selective amino acid adsorption on mineral and metal surfaces*. PhD thesis, University of Liverpool (UK), 2009.

[35] Q. Chen, D. J. Frankel, and N. V. Richardson, "Self-Assembly of Adenine on Cu(110) Surfaces," *Langmuir*, vol. 18, no. 8, pp. 3219–3225, 2002.

[36] W. T. B. Kelvin, *The Molecular Tactics of a Crystal*. Robert Boyle lecture, Oxford: Clarendon Press, 1894.

[37] R. Bentley, "Chiral: a confusing etymology," *Chirality*, vol. 22, no. 1, pp. 1–2, 2010.

[38] M. Schilthuizen and A. Davison, "The convoluted evolution of snail chirality," *Die Naturwissenschaften*, vol. 92, no. 11, pp. 504–15, 2005.

[39] G. H. Wagnière, *On chirality and the universal asymmetry: reflections on image and mirror image*. Zürich, Weinheim: VHCA, Wiley-VCH, 2007.

[40] J.-B. Biot, "Mémoire sur les rotations que certaines substances impriment aux axes de polarisation des rayons lumineux," *Mémoires de l'Académie des Sciences de l'Institute*, vol. 2, pp. 41–136, 1817.

[41] L. Pasteur, "Sur les relations qui peuvent exister entre la forme cristalline, la composition chimique et le sens de la polarisation rotatoire," *Annales de Chimie et de Physique, 3rd series*, vol. 24, no. 6, pp. 442–459, 1848.

[42] L. D. Barron, *Molecular Light Scattering and Optical Activity*. Cambridge: Cambridge University Press, 2004.

[43] V. Böhmer, D. Kraft, and M. Tabatabai, "Inherently Chiral Calixarenes," *Journal of Inclusion Phenomena and Molecular Recognition in Chemistry*, vol. 19, pp. 17–39, 1994.

[44] A. Dalla Cort, L. Mandolini, C. Pasquini, and L. Schiaffino, ""Inherent chirality" and curvature," *New Journal of Chemistry*, vol. 28, no. 10, p. 1198, 2004.

[45] M. Nič, J. Jirát, B. Košata, A. Jenkins, and A. McNaught, eds., *IUPAC Compendium of Chemical Terminology*. Research Triangle Park: IUPAC, 2009.

[46] R. S. Cahn, C. K. Ingold, and V. Prelog, "The specification of asymmetric configuration in organic chemistry," *Experientia*, vol. 12, no. 3, pp. 81–94, 1956.

[47] R. S. Cahn, C. Ingold, and V. Prelog, "Specification of Molecular Chirality," *Angewandte Chemie (International ed. in English)*, vol. 5, no. 4, pp. 385–415, 1966.

[48] V. Prelog and G. Helmchen, "Basic Principles of the CIP-System and Proposals for a Revision," *Angewandte Chemie (International ed. in English)*, vol. 21, no. 8, pp. 567–583, 1982.

[49] L. D. Barron, "True and false chirality and absolute enantioselection," *Rendiconti Lincei*, vol. 24, no. 3, pp. 179–189, 2013.

[50] V. Kostelecký and R. Lehnert, "Stability, causality, and Lorentz and CPT violation," *Physical Review D*, vol. 63, no. 6, p. 065008, 2001.

[51] H. Greaves and T. Thomas, "On the CPT theorem," *Studies in History and Philosophy of Modern Physics*, vol. 45, no. 1, pp. 46–65, 2014.

[52] P. Cintas and C. Viedma, "On the physical basis of asymmetry and homochirality," *Chirality*, vol. 24, no. 11, pp. 894–908, 2012.

[53] J. Schwinger, "The Theory of Quantized Fields," *Physical Review*, vol. 82, no. 6, pp. 914–927, 1951.

[54] G. Lüders, "On the Equivalence of Invariance under Time Reversal and under Particle-Antiparticle Conjugation for Relativistic Field Theories," *Matematisk-Fysiske Meddelelser Kongelige Danske Videnskabernes Selskab*, vol. 28, no. 5, pp. 1–17, 1954.

[55] A. Landé, "Niels Bohr and the Development of Physics by W. Pauli, L. Rosenfeld, V. Weisskopf," *The British Journal for the Philosophy of Science*, vol. 7, no. 28, pp. pp. 357–359, 1957.

[56] O. Greenberg, "CPT Violation Implies Violation of Lorentz Invariance," *Physical Review Letters*, vol. 89, no. 23, p. 231602, 2002.

[57] T. Lee and C. Yang, "Question of Parity Conservation in Weak Interactions," *Physical Review*, vol. 104, no. 1, pp. 254–258, 1956.

[58] C. S. Wu, "Experimental Test of Parity Conservation in Beta Decay," *Physical Review*, vol. 105, no. 4, pp. 1413–1415, 1957.

[59] G. C. Branco, L. Lavoura, and J. P. Silva, *CP Violation*. International series of monographs on physics, Oxford: Clarendon Press, 1999.

[60] M. R. Islam, J. G. Mahdi, and I. D. Bowen, "Pharmacological importance of stereochemical resolution of enantiomeric drugs," *Drug safety*, vol. 17, no. 3, pp. 149–65, 1997.

[61] H. Caner and I. Agranat, "Chiral Drugs," *Enantiomer: A Journal of Sterochemistry*, vol. 7, no. 6, pp. 405–406, 2002.

[62] H.-U. Blaser, "Chirality and its implications for the pharmaceutical industry," *Rendiconti Lincei*, vol. 24, no. 3, pp. 213–216, 2013.

[63] T. Eriksson, S. Björkman, B. Roth, A. Fyge, and P. Höglund, "Stereospecific determination, chiral inversion in vitro and pharmacokinetics in humans of the enantiomers of thalidomide," *Chirality*, vol. 7, no. 1, pp. 44–52, 1995.

[64] M. Kawai, Y. Sekine-Hayakawa, A. Okiyama, and Y. Ninomiya, "Gustatory sensation of (L)- and (D)-amino acids in humans," *Amino acids*, vol. 43, no. 6, pp. 2349–58, 2012.

[65] M. Ávalos, R. Babiano, P. Cintas, J. L. Jiménez, and J. C. Palacios, "Homochirality and chemical evolution: new vistas and reflections on recent models," *Tetrahedron*, vol. 21, no. 9-10, pp. 1030–1040, 2010.

[66] J. R. Cronin, "Enantiomeric Excesses in Meteoritic Amino Acids," *Science*, vol. 275, no. 5302, pp. 951–955, 1997.

[67] S. Pizzarello and J. R. Cronin, "Alanine enantiomers in the Murchison meteorite," *Nature*, vol. 394, no. 6690, p. 236, 1998.

[68] M. H. Engel and S. A. Macko, "Isotopic evidence for extraterrestrial non-racemic amino acids in the Murchison meteorite," *Nature*, vol. 389, no. 6648, pp. 265–8, 1997.

[69] S. F. Mason, "Extraterrestrial handedness," *Nature*, vol. 389, no. 6653, p. 804, 1997.

[70] C. Cerf and A. Jorissen, "Is amino-acid homochirality due to asymmetric photolysis in space?," *Space Science Reviews*, vol. 92, pp. 603–612, 2000.

[71] B. Norden, "Was photoresolution of amino acids the origin of optical activity in life?," *Nature*, vol. 266, no. 5602, pp. 567–568, 1977.

[72] J. Bailey, "Circular Polarization in Star Formation Regions: Implications for Biomolecular Homochirality," *Science*, vol. 281, no. 5377, pp. 672–674, 1998.

[73] J. J. Flores, W. A. Bonner, and G. A. Massey, "Asymmetric photolysis of (RS)-leucine with circularly polarized ultraviolet light," *Journal of the American Chemical Society*, vol. 99, no. 11, pp. 3622–3625, 1977.

[74] Y. Yamagata, "A Hypothesis for the Asymmetric Appearance of Biomolecules on Earth," *Journal of Theoretical Biology*, vol. 11, pp. 495–498, 1966.

[75] H. Buschmann, R. Thede, and D. Heller, "New Developments in the Origins of the Homochirality of Biologically Relevant Molecules," *Angewandte Chemie (International ed. in English)*, vol. 39, no. 22, pp. 4033–4036, 2000.

[76] L. Keszthelyi, "Parity-violating energy difference between enantiomers: recent developments," *Mendeleev Communications*, vol. 13, no. 3, pp. 129–130, 2003.

[77] G. Tranter, "The effects of parity violation of molecular structure," *Chemical Physics Letters*, vol. 121, no. 4-5, pp. 339–342, 1985.

[78] R. Zanasi, P. Lazzeretti, A. Ligabue, and A. Soncini, "Theoretical results which strengthen the hypothesis of electroweak bioenantioselection," *Physical Review E*, vol. 59, no. 3, pp. 3382–3385, 1999.

[79] M. Ávalos, R. Babiano, P. Cintas, J. L. Jimenez, and J. C. Palacios, "Symmetry Breaking by Spontaneous Crystallization - Is it the Most Plausible Source of Terrestrial Handedness we have Long Been Looking for? - A Reappraisal," *Origins of Life and Evolution of the Biosphere*, vol. 34, no. 4, pp. 391–405, 2004.

[80] C. J. Welch, "Formation of highly enantioenriched microenvironments by stochastic sorting of conglomerate crystals: a plausible mechanism for generation of enantioenrichment on the prebiotic earth," *Chirality*, vol. 13, no. 8, pp. 425–7, 2001.

[81] M. Ávalos, R. Babiano, P. Cintas, J. L. Jiménez, and J. C. Palacios, "Chiral autocatalysis: where stereochemistry meets the origin of life," *Chemical Communications*, no. 11, pp. 887–892, 2000.

[82] C. Girard and H. B. Kagan, "Nonlinear Effects in Asymmetric Synthesis and Stereoselective Reactions: Ten Years of Investigation," *Angewandte Chemie (International ed. in English)*, vol. 37, no. 21, pp. 2923–2959, 1998.

[83] M. Ávalos, R. Babiano, P. Cintas, J. Jiménez, and J. C. Palacios, "Nonlinear stereochemical effects in asymmetric reactions," *Tetrahedron*, vol. 8, no. 18, pp. 2997–3017, 1997.

[84] K. Soai, "Asymmetric autocatalysis - Pathway to the biological homochirality," *Chimica Oggi - Chemistry Today*, vol. 30, no. 5, pp. 10–13, 2012.

[85] R. M. Hazen and D. A. Sverjensky, "Mineral surfaces, geochemical complexities, and the origins of life," *Cold Spring Harbor Perspectives in Biology*, vol. 2, no. 5, p. a002162, 2010.

[86] R. M. Hazen, T. R. Filley, and G. A. Goodfriend, "Selective adsorption of L- and D-amino acids on calcite: Implications for biochemical homochirality," *Proceedings of the National Academy of Sciences of the United States of America*, vol. 98, no. 10, pp. 5487–90, 2001.

[87] C. A. Orme, A. Noy, A. Wierzbicki, M. T. McBride, M. Grantham, H. H. Teng, P. M. Dove, and J. J. DeYoreo, "Formation of chiral morphologies through selective binding of amino acids to calcite surface steps," *Nature*, vol. 411, no. 6839, pp. 775–9, 2001.

[88] Y. Yun, D. Wei, D. S. Sholl, and A. J. Gellman, "Equilibrium adsorption of d - And l -Alanine mixtures on naturally chiral Cu{3,1,17}R&S surfaces," *The Journal of Physical Chemistry C*, vol. 118, pp. 14957–14966, 2014.

[89] A. J. Gellman, "Chiral surfaces: accomplishments and challenges," *ACS Nano*, vol. 4, no. 1, pp. 5–10, 2010.

[90] K. E. Plass, A. L. Grzesiak, and A. J. Matzger, "Molecular packing and symmetry of two-dimensional crystals," *Accounts of Chemical Research*, vol. 40, no. 4, pp. 287–93, 2007.

[91] A. González-Campo and D. B. Amabilino, "Biomolecules at interfaces: chiral, naturally," *Topics in Current Chemistry*, vol. 333, no. March, pp. 109–56, 2013.

[92] L. Pérez-García and D. B. Amabilino, "Spontaneous resolution, whence and whither: from enantiomorphic solids to chiral liquid crystals, monolayers and macro- and supra-molecular polymers and assemblies," *Chemical Society Reviews*, vol. 36, no. 6, pp. 941–67, 2007.

[93] K.-H. Ernst, "Supramolecular Surface Chirality," in *Supramolecular Chirality* (M. Crego-Calama and D. N. Reinhoudt, eds.), no. February, ch. 6, pp. 209–252, Berlin, Heidelberg: Springer, 2006.

[94] M. M. Green, J. W. Park, T. Sato, A. Teramoto, S. Lifson, R. L. Selinger, and J. V. Selinger, "The Macromolecular Route to Chiral Amplification," *Angewandte Chemie (International ed. in English)*, vol. 38, no. 21, pp. 3138–3154, 1999.

[95] M. M. Green, N. C. Peterson, T. Sato, A. Teramoto, R. Cook, and S. Lifson, "A helical polymer with a cooperative response to chiral information," *Science*, vol. 268, no. 5219, pp. 1860–6, 1995.

[96] F. Masini, N. Kalashnyk, M. M. Knudsen, J. R. Cramer, E. Lægsgaard, F. Besenbacher, K. V. Gothelf, and T. R. Linderoth, "Chiral induction by seeding surface assemblies of chiral switches," *Journal of the American Chemical Society*, vol. 133, no. 35, pp. 13910–3, 2011.

[97] K. Tahara, H. Yamaga, E. Ghijsens, K. Inukai, J. Adisoejoso, M. O. Blunt, S. De Feyter, and Y. Tobe, "Control and induction of surface-confined homochiral porous molecular networks," *Nature Chemistry*, vol. 3, no. 9, pp. 714–9, 2011.

[98] M. Parschau, S. Romer, and K.-H. Ernst, "Induction of homochirality in achiral enantiomorphous monolayers," *Journal of the American Chemical Society*, vol. 126, no. 47, pp. 15398–9, 2004.

[99] I. De Cat, Z. Guo, S. J. George, E. W. Meijer, A. P. H. J. Schenning, and S. De Feyter, "Induction of chirality in an achiral monolayer at the liquid/solid interface by a supramolecular chiral auxiliary," *Journal of the American Chemical Society*, vol. 134, no. 6, pp. 3171–7, 2012.

[100] R. Fasel, M. Parschau, and K.-H. Ernst, "Amplification of chirality in two-dimensional enantiomorphous lattices," *Nature*, vol. 439, no. 7075, pp. 449–52, 2006.

[101] M. Ortega Lorenzo, C. Baddeley, C. Muryn, and R. Raval, "Extended surface chirality from supramolecular assemblies of adsorbed chiral molecules," *Nature*, vol. 404, no. 6776, pp. 376–9, 2000.

[102] T. Chen, W.-H. Yang, D. Wang, and L.-J. Wan, "Globally homochiral assembly of two-dimensional molecular networks triggered by co-absorbers," *Nature Communications*, vol. 4, p. 1389, 2013.

[103] K. Ernst, "Amplification of chirality in two-dimensional molecular lattices," *Current Opinion in Colloid & Interface Science*, vol. 13, no. 1-2, pp. 54–59, 2008.

[104] K.-H. Ernst, "Stereochemistry of 2D molecular crystallization," *Chimia*, vol. 68, no. 1-2, pp. 49–53, 2014.

[105] A. Nuermaimaiti, C. Bombis, M. M. Knudsen, J. R. Cramer, E. Lægsgaard, F. Besenbacher, K. V. Gothelf, and T. R. Linderoth, "Chiral induction with chiral conformational switches in the limit of low "sergeants to soldiers" ratio," *ACS Nano*, vol. 8, no. 8, pp. 8074–81, 2014.

[106] S. Haq, N. Liu, V. Humblot, A. P. J. Jansen, and R. Raval, "Drastic symmetry breaking in supramolecular organization of enantiomerically unbalanced monolayers at surfaces," *Nature Chemistry*, vol. 1, no. 5, pp. 409–14, 2009.

[107] X. Zhao, H. Yan, R. G. Zhao, and W. S. Yang, "Self-Assembled Structures of Glycine on Cu(111)," *Langmuir*, vol. 19, no. 3, pp. 809–813, 2003.

[108] V. Humblot, C. Méthivier, and C.-M. Pradier, "Adsorption of L-lysine on Cu(110): a RAIRS study from UHV to the liquid phase," *Langmuir*, vol. 22, no. 7, pp. 3089–96, 2006.

[109] X. Zhao, Z. Gai, R. Zhao, W. Yang, and T. Sakurai, "Adsorption of glycine on Cu(001) and related step faceting and bunching," *Surface Science*, vol. 424, no. 2-3, pp. L347–L351, 1999.

[110] H. Iwai, M. Tobisawa, A. Emori, and C. Egawa, "STM study of D-alanine adsorption on Cu(001)," *Surface Science*, vol. 574, no. 2-3, pp. 214–218, 2005.

[111] T. E. Jones, C. J. Baddeley, A. Gerbi, L. Savio, M. Rocca, and L. Vattuone, "Molecular ordering and adsorbate induced faceting in the Ag{110}-(S)-glutamic acid system," *Langmuir*, vol. 21, no. 21, pp. 9468–75, 2005.

[112] V. Feyer, O. Plekan, T. Skála, V. Cháb, V. Matolín, and K. C. Prince, "The electronic structure and adsorption geometry of L-histidine on Cu(110)," *The Journal of Physical Chemistry B*, vol. 112, no. 43, pp. 13655–60, 2008.

[113] A. Kühnle, T. R. Linderoth, and F. Besenbacher, "Self-assembly of monodispersed, chiral nanoclusters of cysteine on the Au(110)-(1 x 2) surface," *Journal of the American Chemical Society*, vol. 125, no. 48, pp. 14680–1, 2003.

[114] A. Kühnle, T. R. Linderoth, B. Hammer, and F. Besenbacher, "Chiral recognition in dimerization of adsorbed cysteine observed by scanning tunnelling microscopy," *Nature*, vol. 415, no. 6874, pp. 891–3, 2002.

[115] M. Lingenfelder, G. Tomba, G. Costantini, L. Colombi Ciacchi, A. De Vita, and K. Kern, "Tracking the chiral recognition of adsorbed dipeptides at the single-molecule level," *Angewandte Chemie (International ed. in English)*, vol. 46, no. 24, pp. 4492–5, 2007.

[116] S. Barlow and R. Raval, "Complex organic molecules at metal surfaces: bonding, organisation and chirality," *Surface Science Reports*, vol. 50, no. 6-8, pp. 201–341, 2003.

[117] S. M. Barlow and R. Raval, "Nanoscale insights in the creation and transfer of chirality in amino acid monolayers at defined metal surfaces," *Current Opinion in Colloid and Interface Science*, vol. 13, pp. 65–73, 2008.

[118] J. Reichert, A. Schiffrin, W. Auwärter, A. Weber-Bargioni, M. Marschall, M. Dell'Angela, D. Cvetko, G. Bavdek, A. Cossaro, A. Morgante, and J. V. Barth, "L-tyrosine on Ag(111): universality of the amino acid 2D zwitterionic bonding scheme?," *ACS Nano*, vol. 4, no. 2, pp. 1218–26, 2010.

[119] M. Smerieri, L. Vattuone, T. Kravchuk, D. Costa, and L. Savio, "(S)-glutamic acid on Ag(100): self-assembly in the nonzwitterionic form," *Langmuir*, vol. 27, no. 6, pp. 2393–404, 2011.

[120] D. A. Duncan, M. K. Bradley, W. Unterberger, D. Kreikemeyer-Lorenzo, T. J. Lerotholi, J. Robinson, and D. P. Woodruff, "Deprotonated glycine on Cu(111): Quantitative structure determination by energy-scanned photoelectron diffraction," *The Journal of Physical Chemistry C*, vol. 116, no. 18, pp. 9985–9995, 2012.

[121] T. Eralp, A. Cornish, A. Shavorskiy, and G. Held, "The Study of Chiral Adsorption Systems Using Synchrotron-Based Structural and Spectroscopic Techniques: Stereospecific Adsorption of Serine on Au-Modified Chiral Cu{531} Surfaces," *Topics in Catalysis*, vol. 54, no. 19-20, pp. 1414–1428, 2011.

[122] R. T. Seljamäe-Green, G. J. Simpson, F. Grillo, J. Greenwood, S. M. Francis, R. Schaub, P. Lacovig, and C. J. Baddeley, "Assembly of a Chiral Amino Acid on an Unreactive Surface: (S)-Proline on Au(111)," *Langmuir*, no. 111, 2014.

[123] S. Baldanza, A. Cornish, R. E. Nicklin, Z. V. Zheleva, and G. Held, "Surface chemistry of alanine on Cu{111}: Adsorption geometry and temperature dependence," *Surface Science*, vol. 629, pp. 114–122, 2014.

[124] J.-H. Franke and D. S. Kosov, "Chiral selectivity of amino acid adsorption on chiral surfaces - The case of alanine on Pt," *The Journal of Chemical Physics*, vol. 142, no. 5, p. 054708, 2015.

[125] L. Atanasoska, J. Buchholz, and G. Somorjai, "Low-energy electron diffraction study of the surface structures of adsorbed amino acid monolayers and ordered films deposited on copper crystal surfaces," *Surface Science*, vol. 72, no. 1, pp. 189–207, 1978.

[126] L.-P. Xu, Y. Liu, and X. Zhang, "Interfacial self-assembly of amino acids and peptides: scanning tunneling microscopy investigation," *Nanoscale*, vol. 3, no. 12, pp. 4901–15, 2011.

[127] Y. Izumi, "Modified Raney Nickel (MRNi) Catalyst: Heterogeneous Enantio-Differentiating (Asymmetric) Catalyst," *Advances in Catalysis*, vol. 32, p. 215, 1983.

[128] M. Besson, B. Blanc, M. Champelet, P. Gallezot, K. Nasar, and C. Pinel, "Diastereoselective Hydrogenation of Substituted Aromatics on Supported Metal Catalysts," *Journal of Catalysis*, vol. 170, no. 2, pp. 254–264, 1997.

[129] V. S. Ranade, G. Consiglio, and R. Prins, "Catalytic diastereoselective hydrogenation of (S)-proline-modified anthranilic acid," *Catalysis Letters*, vol. 58, pp. 71–74, 1999.

[130] I. Kuzmenko, I. Weissbuch, E. Gurovich, L. Leiserowitz, and M. Lahav, "Aspects of spontaneous separation of enantiomers in two- and three-dimensional crystals," *Chirality*, vol. 10, no. 5, pp. 415–424, 1998.

[131] J. Jacques, A. Collet, and S. H. Wilen, *Enantiomers, Racemates and Resolutions*. Malabar: Kreiger Publishing Company, 1994.

[132] L. Pérez-García and D. B. Amabilino, "Spontaneous resolution under supramolecular control," *Chemical Society Reviews*, vol. 31, no. 6, pp. 342–356, 2002.

Chapter 2

Surface science techniques: theory

Surfaces represent the interface between two diverse environments and typically exhibit chemical and physical properties that differ profoundly from bulk materials and continuous media. From an atomic perspective, a surface is created via the breaking of some chemical bonds, therefore interfacial atoms experience an altered chemical environment with respect to bulk atoms, and, as a result, usually manifest spatial rearrangements and an enhanced chemical reactivity, in order to compensate their reduced coordination number. Due to their peculiar nature, surface-specific characterisation techniques have been developed in the last decades, exploiting, as diagnostic tools, particle beams, electromagnetic waves, electromagnetic fields and other purpose-built probes.

Research in surface science has seen an extensive growth in the 20^{th} century since the discovery of the Haber-Bosch process for the production of ammonia from nitrogen and hydrogen, which included the utilisation of an iron-based catalyst [1, 2]. Other key passages in the development of the surface science field were the development of formal theories on heterogeneous catalysis and kinetics of adsorption [3, 4], the development of Ultra High Vacuum technology (UHV) in the 1950s [5], the discovery of the scanning probe-based microscopy in the 1980s [6, 7] and the award of the Nobel prize to Gerhard Ertl for his work on chemical processes at surfaces in 2007 [8].

The work presented here has made use, principally, of three complementary surface science tools, namely Scanning Tunneling Microscopy (STM), Low Energy Electron Diffraction (LEED) and Reflection Absorption Infra Red Spectroscopy (RAIRS). These techniques, whose main operational principles are outlined in the following sections of this chapter, have been used to investigate samples kept in Ultra High Vacuum (UHV) environment, i.e. with a pressure lower than 10^{-9} mbar.

2.1 Surface Science: the need of Ultra High Vacuum

One of the main challenges in a surface science experiment is represented by the need of keeping the sample free from undesired contaminations, which are caused by the possible presence of gaseous species in the system. This implies the necessity of an evacuated environment. In order to estimate the acceptable pressure values to avoid significant contaminations in a generic surface science experiment, it is useful to introduce the following physical quantities: the Hertz-Knudsen flux (F) of a given gaseous substance in a system and its sticking coefficient (S) towards the surface. The flux, according to the kinetic theory of gases, represents the number of molecules that collide the unit area in the unit time, and is defined as:

$$F = \frac{P}{\sqrt{2\pi mkT}} \tag{2.1}$$

where m is the mass of a single molecule, P is the pressure, T is the temperature and k is the Boltzmann constant. The sticking coefficient S is a measure of the probability of adsorption upon the collision between a single molecule and the surface, it is unitless and can assume values from 0 (adsorption never occurs) to 1 (adsorption always occurs). Macroscopically, it represents the fraction of incoming molecules that would stick on the considered surface. In general, S varies with the surface coverage and the temperature according to the following Arrhenius-type expression:

$$S = f(\theta) \exp\left(\frac{-E_a}{kT}\right) \tag{2.2}$$

where θ is the adsorbate coverage, E_a is the activation energy of the process and $f(\theta)$ is a function of the adsorbate coverage that, in the example of a Langmuir adsorption process, follows the rule:

$$f(\theta) = 1 - \theta \tag{2.3}$$

The Langmuir adsorption model [9] assumes the individuation of binding sites on the surfaces, i.e. only specific surface sites are able to accommodate the adsorbate species, and the non-interaction between molecules upon adsorption. The adsorption rate R_{ads}, which is a measure of the frequency of adsorption events, is thus calculated with the product between S and F:

$$R_{ads} = SF = f(\theta)\frac{P}{\sqrt{2\pi mkT}} \exp\left(\frac{-E_a}{kT}\right) \tag{2.4}$$

It is possible to obtain a minimum estimate of the time required by a gaseous contaminant (e.g. carbon monoxide or nitrogen) to fully cover a metallic surface by assuming $S = 1$. At $T = 300\,\mathrm{K}$ and atmospheric pressure, according to equations 2.1 and 2.4, the adsorption rate is $R_{ads} = 3 \times 10^{27}\,\mathrm{m^{-2}\,s^{-1}}$. Since a representative value for the density of available surface sites is $10^{19}\,\mathrm{m^{-2}}$, the whole surface is covered with a monolayer

of contaminants in 3×10^{-9} s, which is obviously not acceptable for an experiment to be performed. This issue needs to be addressed by decreasing the pressure of the experimental environment. For instance, the same contaminant in a high vacuum (HV) regime ($P \simeq 10^{-6}$ mbar) would reach a monolayer coverage in 2.6 s, while in an UHV environment ($P \simeq 10^{-10}$ mbar) this process would occur in $\sim 10^4$ s, which represents an acceptable timescale for an experiment. Since in this approximate calculation the sticking coefficient of the contaminant is overestimated and since atmospheric vapours include inert gases and molecules that do not show affinity towards averagely reactive metals at room temperature, the time scale to perform an UHV surface science experiment involving metal substrates results to be longer, in the order of several hours or days. Hence, UHV environments prove necessary for carrying out surface science investigations.

2.2 Crystallography of the Cu(110) surface

There are fourteen possible crystalline structures that a solid can possess and are termed *Bravais lattices* [10]. One of the most frequent structures found in a metal bulk is the face-centred cubic lattice (fcc). This, in fact, along with the hexagonal close-packed (hcp) structure, assures the maximum atomic packing factor (APF) and coordination number (CN) that can be achieved mathematically in a one-component system composed of hard spheres (APF = 0.74, CN = 12). In a cubic structure the three lattice axes are orthogonal and assume the same value. In the case of a (fcc) lattice, an additional atom is positioned at the centre of each face of the cubic repeat unit (figure 2.1a).

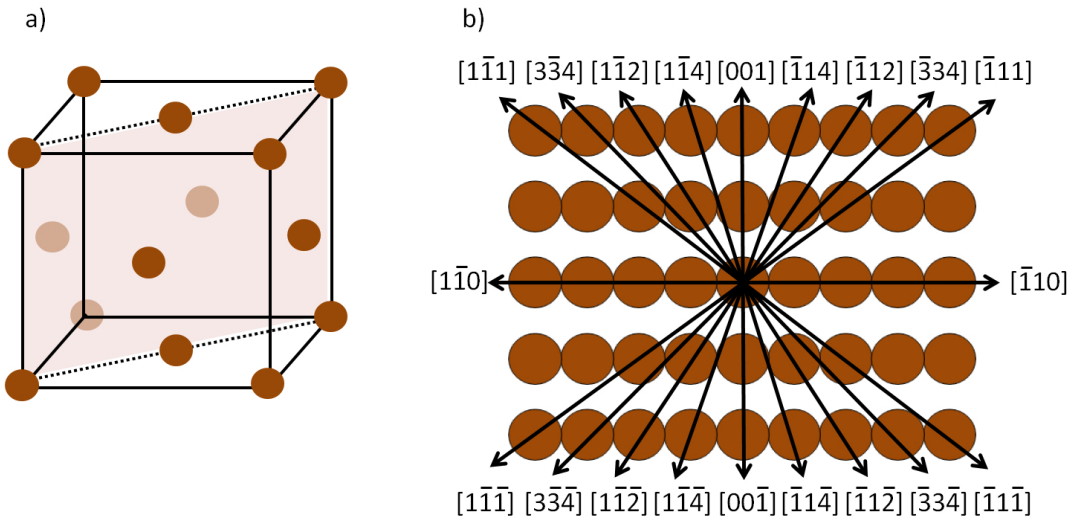

Figure 2.1: a) The (fcc) crystalline structure, showing the cut that leads to the (110) face. b) Indication of the low index surface directions present on a (110) surface.

The fcc-(110) face can be obtained by cutting the unit cell as shown in figure 2.1a, leading to a surface whose 2D representation is given in 2.1b. The unit cell of the surface is rectangular. The (110) face shows a generally higher reactivity in comparison to the other high symmetry cuts, given the low coordination number of its outermost atoms, which is equal to 7. In the case of copper, the surface lattice parameter is equal to 3.615 Å. The Cu(110) face shows a vertical reconstruction, consisting of a vertical displacement respect to the natural bulk termination positions. The distance between the first and the second atomic layer is contracted by 8.5 % in comparison with the bulk spacings, while the second and third layers show an increased separation (+2.3 %) [11, 12]. No lateral reconstruction is however observed, thus the surface lattice parameter assumes the same value as in the bulk.

2.3 Scanning Tunneling Microscopy

Scanning Tunneling Microscopy (STM) is a surface science technique that was developed by Gerd Binnig and Heinrich Rohrer at IBM Zürich [6, 13]. This invention triggered the generation of a novel surface investigation category termed Scanning Probe Microscopy (SPM), that includes techniques that utilise a physical probe to characterise the properties of a surfaces. Depending on the techniques and the probes used, a variety of interactions between the probe and the sample can be measured and different surface physical properties can be studied [14]. A common attribute for scanning probe microscopies is the local nature of the investigation, as opposed to the averaging studies achieved with spectroscopic techniques. While this aspect could be disadvantageous in some circumstances, since the data acquired might not be statistically representative of the entire sample, the high resolution provided by some of the SPM techniques represents a unique benefit when surfaces need to be studied at the molecular or atomic level.

The data acquired through a scanning probe microscope is in the form of an image, i.e. a topography-like two-variable graph that is typically rendered with a false-colour scale. SPM techniques are thus very useful since they provide a real space image of the probed area, in which the physical property of interest is mapped against dimensional coordinates. STM, the principal investigation technique used for the experimental work presented in this thesis, is based on quantum tunneling, a quantum mechanical phenomenon that predicts the penetration of an energetic barrier by a particle possessing a total energy lower than the barrier itself. This process is prohibited for a classical particle, but becomes significant for a quantum particle when the barrier is represented by an atomic scale gap. For instance, in a system constituted by two conductive media separated by a nanometric scale distance, the wavefunctions of the electrons belonging to the two different materials overlap. As a result, if the two conductors were kept at the same potential, electrons would be free to cross the vacuum barrier, but no overall

electrical current would be established (figure 2.3a). If, conversely, a voltage bias were applied to the two materials, an unbalance between the two Fermi levels would arise, determining a steady-state net current through the gap, whose sign depends on the original electrical potential difference applied (figure 2.3b-c).

2.3.1 STM: Basic principles of operation

In STM, whose basic principle of operation is illustrated graphically in figure 2.2, the two materials are represented by the sample of study, that needs to have conductive properties, and the probe, a very sharp metallic tip ideally terminated with a single atom. Semiconductors can also be investigated provided that a suitable bias voltage is applied for the valence band electrons to tunnel out. The sample area of interest is continuously scanned with the probe, and for each positional coordinate (x, y) the tunneling current is recorded. This yields results in the form of two-dimensional graphs that are usually displayed as images with false-colour scale to represent the intensities in the z direction. Typically, dedicated software are used to process and analyse STM images. The data presented in this thesis are analysed with the aid of the softwares Image SXM [15] and WSxM [16].

The nature of the acquired signal depends on the mode of operation of the instrument. STM can be used in two main modalities, namely in the *constant height* and *constant current* modes. In a constant height STM experiment, the tip is scanned along the surface at a distance in z that is kept constant, while the tunneling current intensity is collected for each sampled point. The advantage of this mode lies in not having to adjust the tip position along z, a fact that usually results in a higher scan velocity. On the other hand, this mode of operation is not suitable for characterising areas that possess a high roughness or a non-negligible slope, cases in which the risk of a physical collision between the tip and the sample is considerable. In a constant current STM investigation, conversely, the tunneling current is preset to a value by the experimenter and the z position of the tip is acquired. In order to keep the tunneling current constant, and to adjust the z position accordingly, a feedback system is required. This procedure may result in an increased acquisition time, but renders the system safer and more reliable towards the risk of accidental crashes between the tip and the surface. All the STM images presented in this thesis are collected in a constant current mode, the most used method in the STM science community.

In any STM experiment, an extremely fine tuning of the (x, y, z) positions is required: this is particularly crucial for controlling the z position in a constant current experiment, since a very small displacement in this direction results in a vast change in the total tunneling current (see section 2.3.2 for a quantitative estimation of this effect). The tip movements in the three dimensions are governed by tubular actuators made of piezoelectric materials [17], that show a mechanical response, in the form of expansion

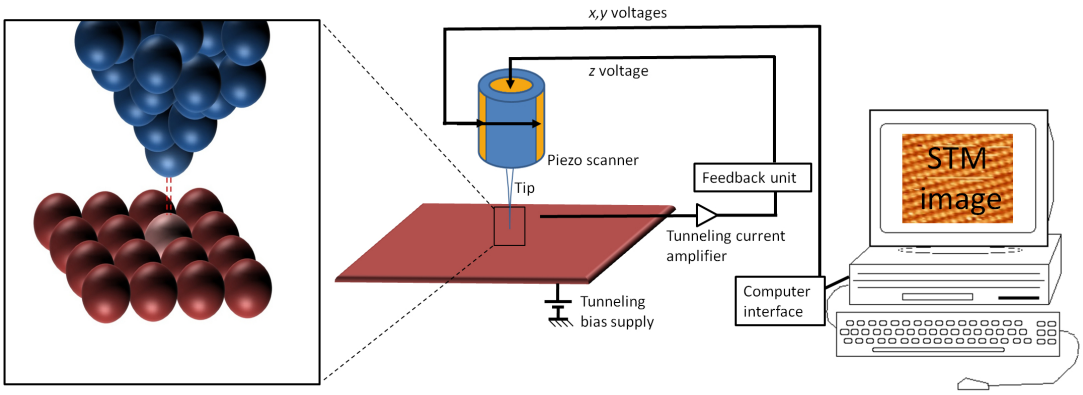

Figure 2.2: STM working principle

or contraction, to electric stimuli. A common material used for the fabrication of a piezoelectric transducer is barium titanate ($BaTiO_3$). Thus, if an electrical potential difference is applied across the piezotubes, these respond with a change in length that is proportional to the applied voltage. Typical values for the voltage sensitivity of piezoelectric actuators are in the order of 10^{-10} $m\mathrm{V}^{-1}$. In the constant current mode, the z voltage is recorded for each acquisition point, and from that the tip-sample distance is deduced by the software. The mechanical response of piezoelectric materials is typically non-linear, and that causes the frequent presence of a drift effect during STM acquisitions. This is mainly due to a creep-like response, with the material undergoing a strain even after the removal of the stress (applied voltage), and needs to be taken into account during STM experiments.

The quality of an STM image is strongly determined by the characteristics of the probe. These are usually unknown, and only approximations can be made on the parts of the tip contributing to the tunneling effect. Ideally only electrons from the very last atom of the tip tunnel towards the surface, and vice versa (see section 2.3.2), but this is not always guaranteed. For this reason, typically the tip can be conditioned via a sputtering treatment with Argon ions (Ar^+), or via in-situ voltage pulses during the scanning, with a trial-and-error approach. Two main tip fabrication materials are commonly used: tungsten (W) and platinum/iridium alloy (PtIr). W tips are formed via electrochemical etching using concentrated aqueous solutions of strong bases (NaOH or KOH). This method proves reliable in obtaining very sharp tip apices. The tungsten oxide layer that tends to be formed on the tip, which is not conductive and thus would prevent electron tunneling, is usually easily removed in vacuum via the usual tip conditioning methods (sputtering and voltage pulsing). The PtIr tips are simply made by a transverse cut of a PtIr wire, which is not prone to oxidation and is thus suitable for STM experiments in air or in rough vacuum.

Another part that is critical in an STM instrument is represented by the electronic controls. High voltage power supplies are required to drive the movement of the piezotubes (x, y, z). Furthermore, a low voltage power supply is used to establish a potential difference between the sample and the tip for a net tunneling current to be established: usually, a bias voltage is applied to the sample, while the tip is earthed. In the constant current mode, the tunneling current passes through an amplifier and is then converted to a voltage. On the basis of this reading, a feedback loop adjusts the high voltage to be sent to the z piezodrive, in order to keep the tunneling current fixed at the value set by the user. The z voltage signal is then recorded by a computer and converted into dimensional units on the basis of the z piezoscanner voltage sensitivity. This signal gives rise to a two-dimensional plot in the (x, y) plane, which is the final output of the STM scan.

Finally, a damping system is always required, in order to remove any noise due to external mechanical sources. For this reason the STM scanner is typically mounted on a suspended stage held with springs, that is placed inside the UHV chamber. Additionally it is advisable to place the instrument on an anti-vibration table, in a room with sound-proof walls and at a low-level floor in a building.

2.3.2 STM: Theory

For a mathematical model of the tunneling of electrons through the gap between tip and sample here the classical Bardeen formalism [18, 19] is used. This is based on a perturbation approach to the two systems, tip and sample, that are initially considered isolated. The time-independent Schrödinger equations for single particles belonging to the sample and to the tip are written in equations 2.5 and 2.6, respectively. $\mathcal{T}$ is the electron kinetic energy, $\mathcal{U}_S$ and $\mathcal{U}_T$ are the potential energies and ψ_μ and χ_ν are the two wavefunctions. Given the isolation of the two systems, $\mathcal{U}_S$ assumes finite values only within the sample, while it is defined null elsewhere. Similarly, $\mathcal{U}_T$ takes non-zero values in the tip only.

$$(\mathcal{T} + \mathcal{U}_S)\,\psi_\mu = E_\mu \psi_\mu \tag{2.5}$$

$$(\mathcal{T} + \mathcal{U}_T)\,\chi_\nu = E_\nu \chi_\nu \tag{2.6}$$

For one electron, the transition probability per time unit $\omega_{\mu\nu}$ from the sample state ψ_μ to the tip state χ_ν is then provided via the Fermi golden rule:

$$\omega_{\mu\nu} = \frac{2\pi}{\hbar} |M_{\mu\nu}|^2 \,\delta\left(E_\nu - E_\mu\right) \tag{2.7}$$

where the matrix element is given by

$$M_{\mu\nu} = \int \chi_\nu^* (x)\, \mathcal{U}_T (x)\, \psi_\mu (x)\, d^3x \tag{2.8}$$

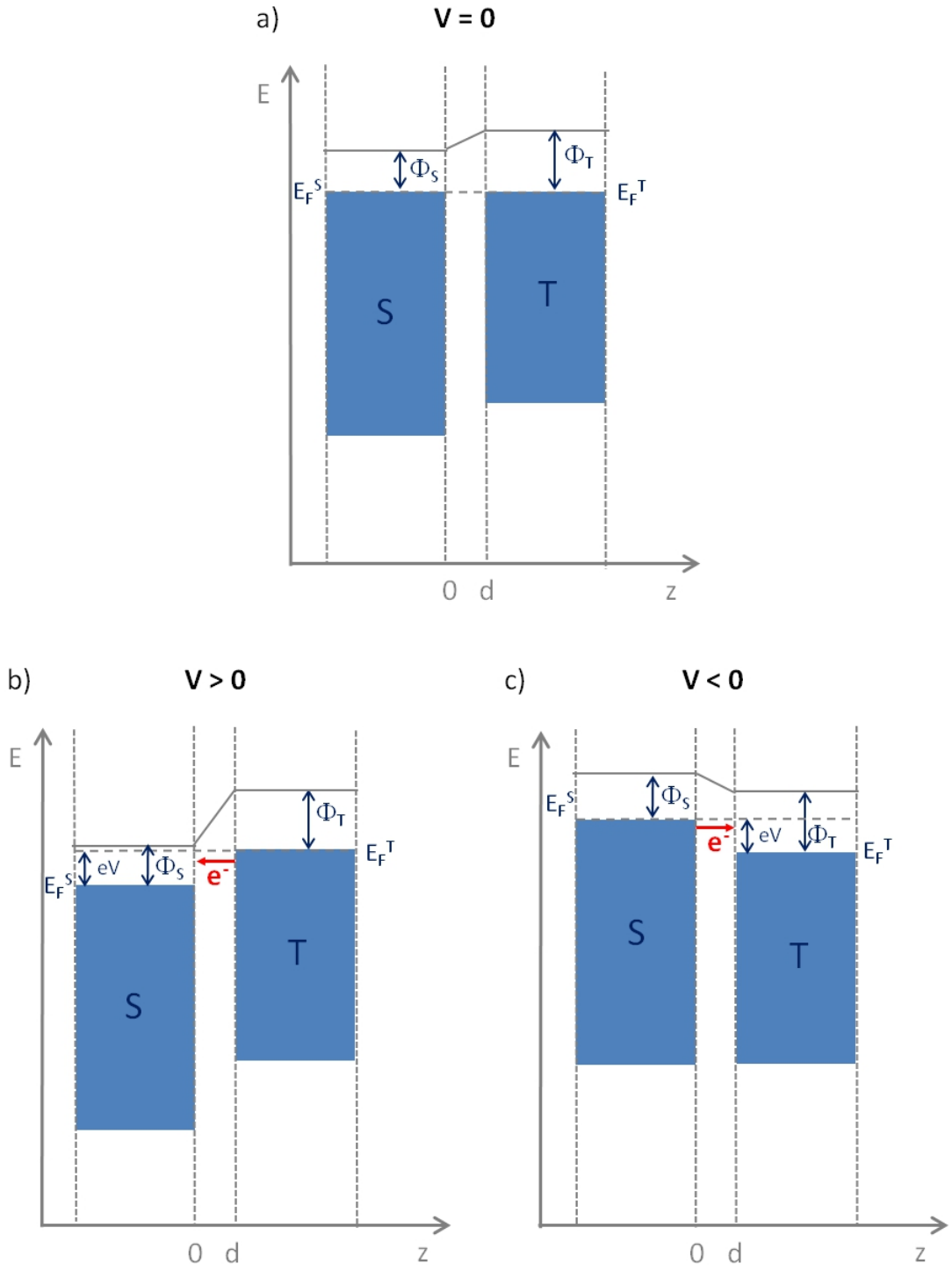

Figure 2.3: Potential energy for a conductor-vacuum-conductor junction. The descriptors used for the two conductive materials, S and T, indicate the *tip* and the *sample*, respectively. a) The two conductors are held at the same potential. b) Conductor S is kept at a positive voltage. c) Conductor S is kept at a negative voltage. Image adapted from [20]

.

It is worth noting that the δ function in equation 2.7 implicitly assumes that the electron tunnels from the tip to the sample between states with equal energy, meaning that it does not account for inelastic tunneling processes. The total current originating from elastic tunneling can then be calculated by multiplying the electron charge e by the summation over all the possible tip and sample states of the transition probability $\omega_{\mu\nu}$. Furthermore, the discrete sum over the states can be alternatively expressed with an integral over all the density of states $\rho(E)$, as follows:

$$\sum_{\mu\nu} |M_{\mu\nu}|^2 \, \delta(E_\nu - E_\mu) = 2 \int f(\epsilon) \, \rho(\epsilon) \tag{2.9}$$

where $f(\epsilon)$ is the Fermi-Dirac function at the energy ϵ and the factor 2 accounts for the spin degeneracy predicted by Pauli's exclusion principle. Hence, approximating the Fermi-Dirac distribution of electron energies to a step function, assumption that is reasonable at low temperatures ($k_B T \ll eV$), it is possible to write the total current in terms of the sample and tip densities of states at the shifted Fermi levels, ρ_S and ρ_T, the bias voltage V and the transition matrix element $M_{\mu\nu}$:

$$I = \frac{4\pi e}{\hbar} \int_0^{eV} \rho_T \left(E_F^T - eV + \epsilon \right) \rho_S \left(E_F^S + \epsilon \right) |M_{\mu\nu}|^2 \, d\epsilon \tag{2.10}$$

The integration interval chosen in 2.10 is valid when positive voltages for the sample are chosen, while for negative voltages one would integrate over the interval $[-e|V|, 0]$. The matrix element $M_{\mu\nu}$ is still unknown, and, in order to simplify 2.10, it is assumed that only the electrons belonging to the extreme atom of the tip contribute to the tunneling process towards the surface atom that lies directly underneath (inset of figure 2.2), which is acceptable for voltage intensities smaller than 2 Volts [21].

In this hypothesis it is possible to proceed with the Wentzel-Kramers-Brillouin (WKB) semiclassical approximation [22], that permits to calculate the tunneling probability, D, of a particle possessing energy ϵ through an unknown energetic barrier U along the coordinate Z, provided that $\epsilon \ll U$. The latter condition is generally true for metallic materials, which possess workfunctions of the order of a few eV.

$$D(\epsilon) = \exp\left\{ -\frac{2}{\hbar} \int_0^d \left[2m \left(U(z) - \epsilon \right) \right]^{\frac{1}{2}} dz \right\} \tag{2.11}$$

Where d is the distance separating the tip and the sample. In the tunneling process, the shape of the barrier $U(z)$ is unknown. Generally, it possesses a trapezoidal shape (figure 2.3), but could be further approximated to a square barrier, defining an effective work function that depends on the applied bias voltage:

$$\phi_{\text{eff}} = \frac{\phi_S + \phi_T + eV}{2} \tag{2.12}$$

where ϕ_S is the work function of the sample and ϕ_T is the work function of the tip. The introduction of an effective work function enables us to reduce equation 2.11 to:

$$D(\epsilon, V, d) = \exp\left[-2d \sqrt{\frac{2m}{\hbar^2} \left(\phi_{\text{eff}} - \epsilon \right)} \right] = \exp(-2kd) \tag{2.13}$$

with the constant k defined as:

$$k = \sqrt{\frac{2m}{\hbar^2}\left(\phi_{\text{eff}} - \epsilon\right)} \tag{2.14}$$

Finally, replacing the tunneling matrix $|M_{\mu\nu}|^2$ in 2.10 with the tunneling probability D, from 2.13, we obtain the following expression for the total tunneling current:

$$I = \frac{4\pi e}{\hbar}\int_0^{eV} \rho_T\left(E_F^T - eV + \epsilon\right)\rho_S\left(E_F^S + \epsilon\right)\exp\left(-2kd\right)d\epsilon \tag{2.15}$$

From 2.15, the total current flowing from the tip to the sample is determined by the applied voltage V, the distance d between the two conductors and the total densities of states ρ_S and ρ_T. Remembering the semiclassical approximation that assumes the involvement of only two atoms in the tunneling phenomenon, one in the sample and one in the tip [21], as in equation 2.11, the densities of states in equation 2.15 pertain to single atoms and for this reason they are termed *local density of states* (LDOS). It is also clear, from equation 2.15, that the total tunneling current decreases exponentially with the distance between sample and tip, with an inverse decay length equal to $2k$. For a quantitative estimation of the STM vertical sensitivity, the constant k is approximated to:

$$k \cong \frac{\sqrt{m\left(\phi_S + \phi_T\right)}}{\hbar} = 0.51\sqrt{\phi_S + \phi_T\,(\text{ eV})}\left(\text{Å}^{-1}\right) \tag{2.16}$$

In the approximation 2.16 the bias voltage is assumed small compared to the two work functions ($eV \ll \phi_S$,ϕ_T). Since typical values for metallic work functions are 4-5 eV, a change of 1 Å in the tip-sample distance provokes an order of magnitude variation in the tunneling probability and, consequently, in the detected tunneling current. This explains the extremely high vertical resolutions achieved in STM experiments , but also the necessity of mechanical isolation systems in a typical STM apparatus, since small vibrations could cause significant oscillations in the flowing tunneling current.

2.4 Low Energy Electron Diffraction

Low Energy Electron Diffraction (LEED) is a technique that exploits the interactions between electrons and solids. The pioneering work performed by Davisson and Germer at Bell Laboratories in 1927 [23], in which they showed a diffraction pattern originated from electrons backscattered from a nickel crystal, confirmed the wave nature of an electron, according to De Broglie's theory [24, 25]. LEED makes use of electrons that possess a kinetic energy between 20 eV and 500 eV, which collide against the sample and are backscattered in specific directions, according to Bragg's law [26]. The information provided by a LEED investigation is linked to the surface crystalline structure and its repeat unit. After an electron beam collides with a crystal, it penetrates into the bulk with an exponential decay. The intensity of the primary electron beam can be

expressed in function of the depth d as:

$$I = I_0 \exp\left(\frac{-d}{\lambda \cos\theta}\right) \tag{2.17}$$

where I_0 is the initial beam intensity, θ in the angle of beam incidence with respect to the surface normal and λ is the inelastic mean free path of electrons in the bulk, defined as the distance one electron can travel before its energy is reduced by the factor $(1/e)$. λ is largely dependent on the electron energy, whereas the material plays a minor role. On the basis of an experimental database for different metals, published by Seah and Dench [27], a universal curve has been proposed for the penetration depth of primary electrons as a function of their energy (figure 2.4).

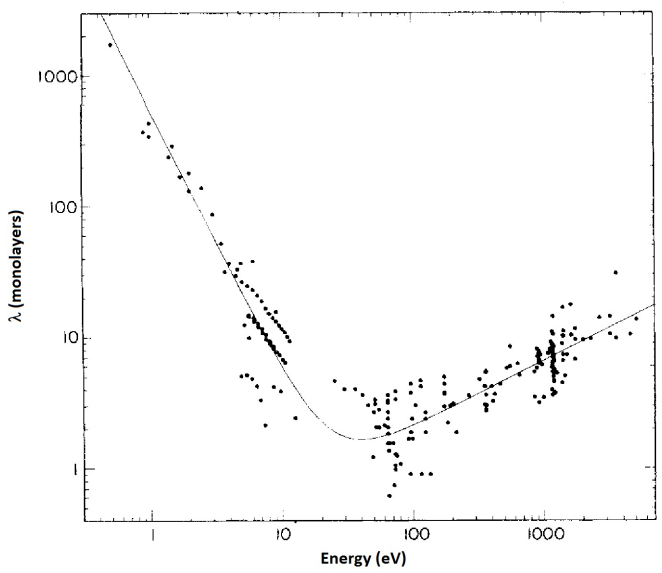

Figure 2.4: The universal curve for inelastic mean free path of electrons in metals. Image adapted from [27].

The minimum of the curve is at an electron energy ~ 50 eV, thus, if electrons with an energy range spanning from 20 to a few hundreds of eV are chosen, they are able to penetrate into the material for few layers only, and the surface sensitivity is intrinsically assured. A fraction of the incoming electrons are elastically backscattered, while the majority undergo processes that imply an energy loss and are scattered inelastically. These inelastic processes include plasmon excitations, phonon excitations and electron-hole pair formations.

2.4.1 LEED: Basic principles of operation

Electrons are emitted from a hot filament and are accelerated through a voltage power supply to the user-defined energy. They are then driven across electrical lenses, which, through the application of certain voltages, focus and direct the electron beam towards the sample. After the collision with the sample, electrons that are backscattered

inelastically are trapped in intermediate negatively biased grids, while elastically backscattered electrons are collected on a screen that is kept at a high positive voltage (3 - 7 kV), while the sample is earthed. The collector screen is made with a fluorescent material, that has the property of emitting a photon in response to a collision with electrons, thus a visible pattern is produced and is typically collected with a standard camera (figure 2.5).

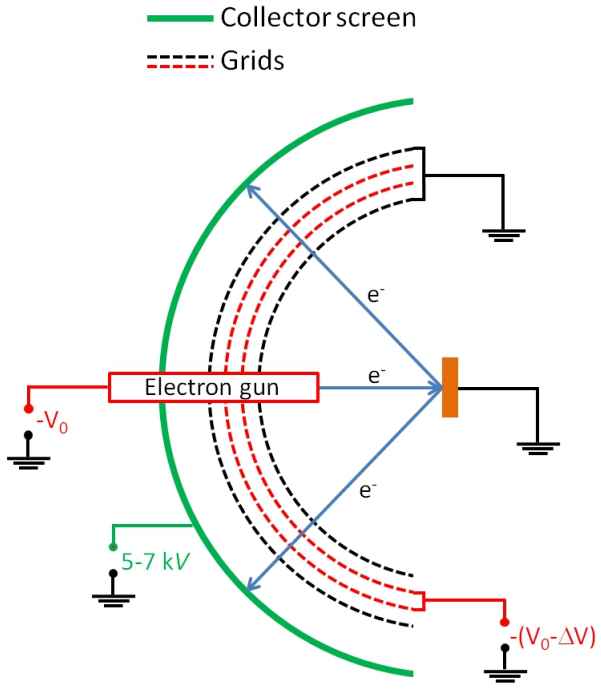

Figure 2.5: The schematics of a rear-view LEED apparatus, in which the observer faces the back of the collector screen that reveals the diffracted electron beams.

2.4.2 LEED: theory

The particle-wave dual nature of electrons permits the De Broglie wavelength for incident electrons (λ_i) to be written as a function of their energy E_k:

$$\lambda_i \left(\text{Å}\right) = \left[\frac{150.6}{E_k \left(\text{eV}\right)}\right]^{\frac{1}{2}} \tag{2.18}$$

In the surface-sensitive energy region (E_k = 20 - 500 eV, see figure 2.4), we obtain De Broglie wavelengths of the electrons spanning from 2.74 to 0.55 Å. These values are comparable with the lattice inter-atomic spacing of crystals, and the diffraction condition [26] is thus satisfied. In the 1-dimensional case, when two electrons are scattered by two consecutive atoms whose lattice spacing is a (figure 2.6), the path difference PD is given by $a \sin\theta_i$, where θ_i is the angle of incidence of the electron beam.

In order to obtain constructive interference from backscattered electrons, the path difference needs to be an integer multiple of the wavelength of the incident electrons, according to Bragg's law:

$$a \sin \theta_i = n\lambda_i \tag{2.19}$$

Where n represents any number belonging to the set of natural numbers ($n \in \mathbb{N}$). Introducing the magnitude of the wavevectors of the incident electrons, $k_i = 2\pi/\lambda_i$, Bragg's law for constructive interference can be rearranged as:

$$k_i \sin \theta_i = n\frac{2\pi}{a} \tag{2.20}$$

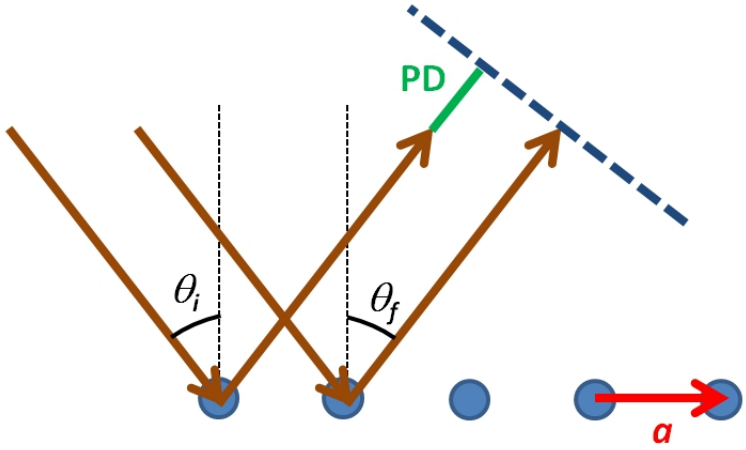

Figure 2.6: The 1D visualisation of the path difference (PD) of two electrons that have been scattered by two consecutive atoms whose distance is equal to a. θ_i and θ_f are the angles of incidence of incoming and backscattered electrons, respectively.

The first member of equation 2.20 represents the momentum of the incident electrons in their component parallel to the plane containing the scattering centres. This is allowed to assume discrete values, namely integer multiples of $2\pi/a$. This value represents the magnitude of the reciprocal lattice spacing in one dimension. Bragg's diffraction condition can, in other words, be expressed in terms of momentum transfer between the electron wave and the surface. Only the component of the momentum parallel to the surface is transferred, in a quantised manner (equation 2.20), while the normal component of the momentum and the energy are conserved during an elastic scattering event. Extending equation 2.20 to a 2D lattice, and thus introducing a new lattice parameter b, we obtain:

$$\Delta k^{\parallel} = k_f^{\parallel} - k_i^{\parallel} = n\frac{2\pi}{a} + m\frac{2\pi}{b} = G'_{nm}, \text{ with } n, m \in \mathbb{N} \tag{2.21}$$

where G'_{nm} is the surface reciprocal lattice matrix. The direct visualisation of the diffraction spots that are obtained upon electron scattering on a 2D lattice can be achieved via the construction of Ewald's circle [28], a geometrical tool aimed at representing the diffraction pattern produced by a crystalline structure, knowing the lattice parameters

and the energy of the probing particles. It is a 2D adaptation of Ewald's sphere, used to visualise the 3D reciprocal space, e.g. in X-ray crystallography. In this reciprocal space representation, lines are drawn, normally to the surface, from the scattering centres. A circle, whose centre coincides with the electron beam centre and whose radius is equal to the intensity of the momentum of incoming electrons (k_i), is then constructed. The circumference of the circle delimits the number of diffraction beams that are produced, given a certain momentum of the primary electron beam (figure 2.7).

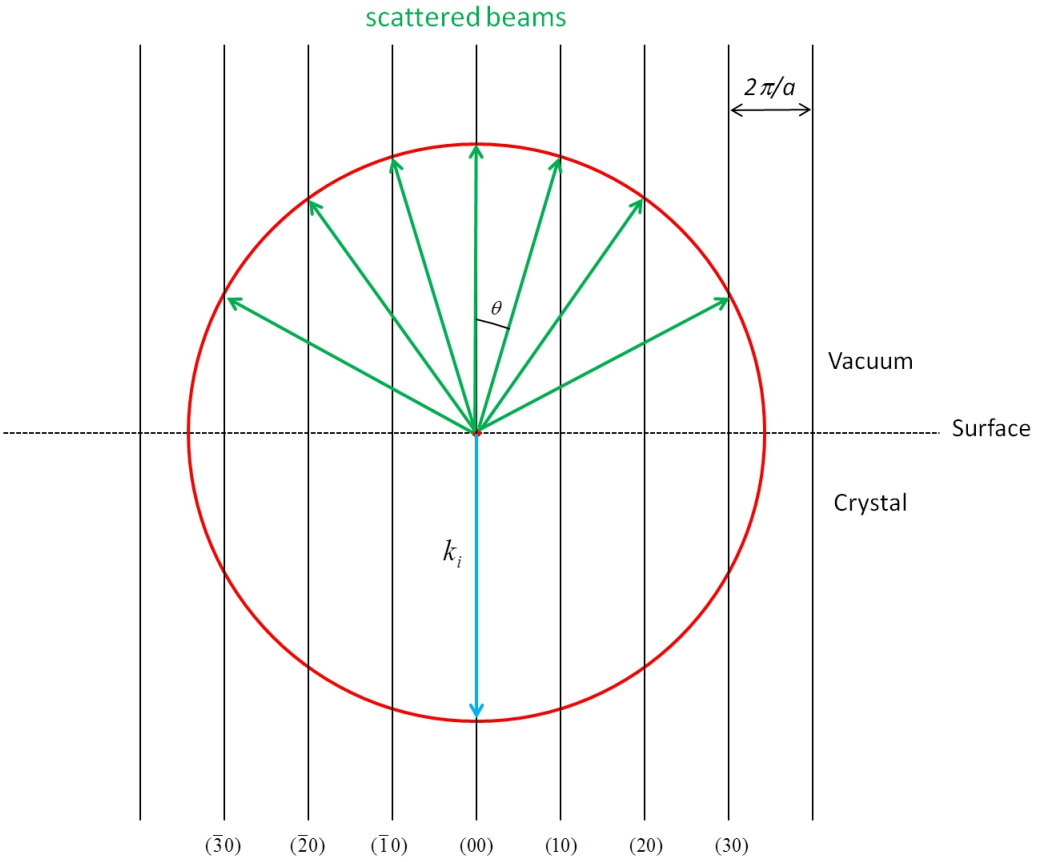

Figure 2.7: The construction of Ewald's circle reciprocal space for determining the diffraction pattern produced by a 1D lattice.

Since Bragg's condition needs to be satisfied simultaneously in both of the surface dimensions, two Ewald's circles can be drawn. The intersection of the series of lines produces a number of spots, which represents the typical diffraction pattern originated from a 2D crystalline structure. Hence, the pattern recorded via a LEED apparatus is a pure projection of the surface lattice in reciprocal space, represented by the matrix G'_{nm}. The deduction of the real space lattice starting from the reciprocal space vectors ($\mathbf{a_1^*}$ and $\mathbf{a_2^*}$) can be thus performed, remembering that the modulus of a vector in reciprocal space is inversely proportional to the modulus of the same vector in real

space:

$$|\mathbf{a_1^*}| = \frac{2\pi}{|\mathbf{a_1}|} \ , \ |\mathbf{a_2^*}| = \frac{2\pi}{|\mathbf{a_2}|} \tag{2.22}$$

Furthermore, the following scalar products holds true:

$$\mathbf{a_1} \cdot \mathbf{a_2^*} = 0 \ , \ \mathbf{a_1^*} \cdot \mathbf{a_2} = 0 \tag{2.23}$$

LEED is also able to detect the periodicity of a given overlayer sitting on top of the crystalline structure described by the vectors $\mathbf{a_1}$ and $\mathbf{a_2}$. Hypothesising that the overlayer structure is represented by the vectors $\mathbf{b_1}$ and $\mathbf{b_2}$, these can be expressed as a function of the substrate vectors:

$$\begin{cases} \mathbf{b_1} = G_{11}\mathbf{a_1} + G_{12}\mathbf{a_2} \\ \mathbf{b_2} = G_{21}\mathbf{a_1} + G_{22}\mathbf{a_2} \end{cases} \tag{2.24}$$

Equations 2.24 can be rearranged in a matricial manner, introducing the matrix $\mathbf{G}$:

$$\begin{pmatrix} \mathbf{b_1} \\ \mathbf{b_2} \end{pmatrix} = \mathbf{G} \begin{pmatrix} \mathbf{a_1} \\ \mathbf{a_2} \end{pmatrix} \text{ , with } \mathbf{G} = \begin{pmatrix} G_{11} & G_{12} \\ G_{21} & G_{22} \end{pmatrix} \tag{2.25}$$

Analogously, a matrix $\mathbf{G^*}$ is defined for the description of the overlayer in terms of the substrate reciprocal space vectors:

$$\begin{pmatrix} \mathbf{b_1^*} \\ \mathbf{b_2^*} \end{pmatrix} = \mathbf{G^*} \begin{pmatrix} \mathbf{a_1^*} \\ \mathbf{a_2^*} \end{pmatrix} \text{ , with } \mathbf{G^*} = \begin{pmatrix} G_{11}^* & G_{12}^* \\ G_{21}^* & G_{22}^* \end{pmatrix} \tag{2.26}$$

Finally, the deduction of the real space matrix $\mathbf{G}$ is performed by taking the inverse transpose of the reciprocal space matrix $\mathbf{G^*}$ [29], which is directly provided by a LEED pattern. This operation is made explicit in equation 2.27, where $(\det \mathbf{G^*})$ represents the determinant of the matrix $\mathbf{G^*}$.

$$\mathbf{G} = \left[(\mathbf{G^*})^{-1} \right]^t = \frac{1}{\det \mathbf{G^*}} \begin{pmatrix} G_{22}^* & -G_{21}^* \\ -G_{12}^* & G_{11}^* \end{pmatrix} \tag{2.27}$$

2.5 Reflection Absorption Infra-Red Spectroscopy

Reflection Absorption Infra-Red Spectroscopy (RAIRS) is a technique that exploits the interaction between electro-magnetic radiation and matter. Molecular vibrational modes are excited upon absorption of light at certain wavelengths in the infra-red (IR) spectral region. In IR spectroscopies, the analysis of the transmitted and/or reflected beam contains information upon the molecular structure of the sample, in particular with regards to the chemical groups present. Infra-red spectroscopy is commonly used to determine the composition and the orientation of molecules adsorbed on a given surface. Since metallic single crystals, such as those studied in this work, are opaque to radiation in the visible and IR region, IR spectroscopy is performed in reflection mode and is termed RAIRS.

2.5.1 RAIRS: Basic principles of operation

The two main components that are essential for RAIR spectroscopy are an IR spectrometer for generating infra-red radiation and a photo-detector, able to convert the intensity of incoming photons into electric signals. The IR beam hits the sample and is consequently reflected towards the detector, that reveals the intensity of light absorption at a certain frequency (figure 2.8). Usually, the Fourier transform (FT) technique is used for IR detection, leading to faster acquisitions. For geometric reasons, the use of mirrors is sometimes necessary. Furthermore, in order to avoid undesired dissipation of light intensity, the sections traversed by the beam need to be purged, since atmospheric gases, such as water vapour and carbon dioxide, are absorbers of IR radiation. When the sample is kept in UHV, the IR beam enters the vacuum chamber and exits it via special windows made with materials that are transparent to IR radiation (typically alkali metal halides). Finally, grazing beam incidence is required in order to maximise the signal intensity. The latter aspect, along with other experimental requirements, will be explained in section 2.5.2.

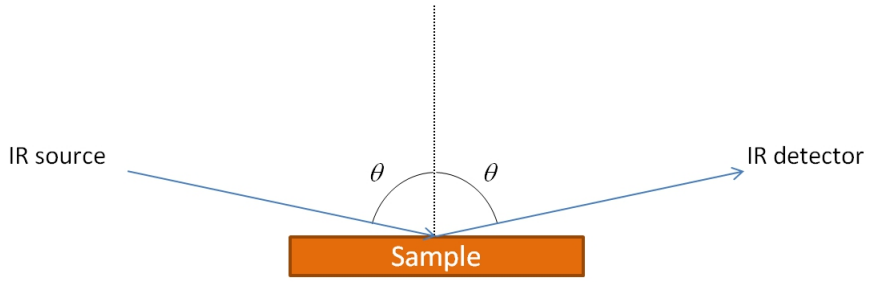

Figure 2.8: The principle of operation of RAIRS. The IR radiation is produced by an IR spectrometer and is reflected by the sample. The angle of incidence and reflection are the same, according to Fresnel's law. The reflected beam is analysed by an IR detector.

2.5.2 RAIRS: Theory

Intra-molecular vibrations occur in all molecules possessing more than one atom. A trivial case is that of a diatomic molecule, whose stretching movement along its axis represents the sole possible vibration. For complex polyatomic molecules composed of N atoms, the vibrational modes are $(3N - 6)$. This number increases by one unit when molecules are linear, which possess $(3N - 5)$ active modes. Since, according to quantum mechanics, vibrational levels are quantised, only photons with a given energy, equalling the energy difference between two vibrational levels of the molecule, are able to induce vibrational transitions. These energy values happen to correspond to electromagnetic radiation in the infra-red region. Additionally, not all the vibrational modes are accessible to IR spectroscopy. The classical selection rule for infra-red spectroscopy requires, in fact, that a vibrational mode induce a variation in the molecular electrical

dipole moment. In the quantum mechanics approach, a vibrational transition between states a and b is infra-red active when its transition moment integral μ_{ba} is non null:

$$\mu_{ba} = \int \psi_b^* \mu \psi_a d\tau \neq 0 \tag{2.28}$$

where τ is the lifetime of the transition. The intensity of an infra-red absorption peak is then proportional to the square of the transition moment integral μ_{ba}:

$$I_{ba} = |\mu_{ba}|^2 \tag{2.29}$$

The properties of reflective IR spectroscopy was thoroughly studied by Greenler in the sixties [30, 31], with an experimental study that laid the foundations of the search for the ideal conditions to perform a RAIRS experiment. Amongst the major findings of this early work, it is worth mentioning the need of an IR source with p-polarised light that is incident on the sample at grazing angles [30].

Before understanding how the chemical form and the molecular orientation of adsorbates are investigated through IR spectroscopy, it is necessary to introduce the properties of the interaction between IR radiation and clean metallic surfaces. Firstly, it is convenient to deconvolute the electric field of the incoming and the reflected electromagnetic waves into two components, one lying in plane with respect to the plane of incidence, E_p, and one perpendicular to it, E_s, as shown in figure 2.9. The refraction index, which is generally a complex number, can be written as:

$$\tilde{n} = n - ik, \text{ with } n^2 + k^2 \gg 1 \tag{2.30}$$

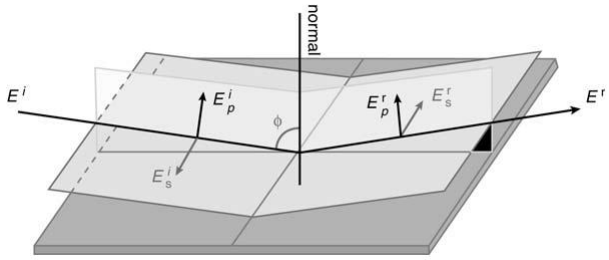

Figure 2.9: The schematic representation of the s- and p- electric field components, in the incident (E^i) and reflected (E^r) IR radiation. Image adapted from [32].

In this condition, according to Fresnel's law [33], the reflectivities for the s- and p-components of infra-red radiation are written as:

$$R_s = \frac{\left(n - \frac{1}{\cos\theta}\right)^2 + k^2}{\left(n + \frac{1}{\cos\theta}\right)^2 + k^2} \tag{2.31}$$

$$R_p = \frac{(n - \cos\theta)^2 + k^2}{(n + \cos\theta)^2 + k^2} \tag{2.32}$$

Moreover, the phase shifts in s- and p- components, δ_s and δ_p, respectively, depend on the refractive index according to the following expression:

$$\tan \Delta = \tan (\delta_s - \delta_p) = \frac{-2k \tan \theta \sin \theta}{\tan^2 \theta - n^2 - k^2} \tag{2.33}$$

Realistic values for the real and imaginary parts of the refractive index of a metal that yields a high reflective intensity are estimated to be $n = 3$ and $k = 30$ [34]. For instance, in the case of copper samples, $n = 2.9$ and $k = 27.5$ [30]. Thus, with metals, the reflectivities and the phase shifts, for s- and p-polarised light, can be plotted against the angle of incidence of the beam, θ (figure 2.10). As visible in figure 2.10, for the

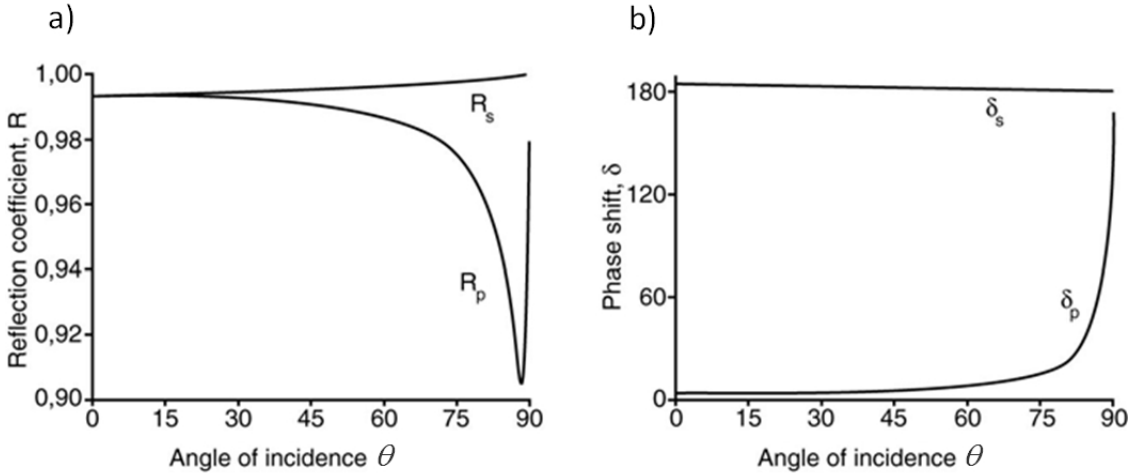

Figure 2.10: a,b) Dependence of the reflection coefficient and phase shift in their s- and p-components against the angle of incidence θ. Adapted after [32].

s-polarised light the reflectivity is close to unity for all the angles of incidence, and, furthermore, the phase shift between the reflected and incident radiation is about 180° for every angle of incidence. This means that, on the surface, the incident and reflected s-polarised beams are in antiphase, and, as a consequence, destructive interference locally occurs. In particular, the electric field E_s is null, thus the transition dipole moments that are parallel to the surface cannot interact with any field in that plane, and no vibrational transitions take place. For the p-polarised radiation, conversely, destructive interference does not take place for most of the possible angles of incidence (figure 2.10b), thus a finite value for E_p, able to interact with the transition dipole moments laying in the plane of incidence, is expected. The necessity of an amount of p-polarised IR radiation is thus the first requirement for performing a RAIRS experiment. E_p can be additionally separated into two different components, $E_{p_\parallel}$ and $E_{p_\perp}$, respectively parallel and perpendicular to the surface. In figure 2.11 the behaviour of $E_{p_\parallel}$ and $E_{p_\perp}$, along with E_s, against the angle of incidence is displayed. The values are normalised to E_0, the magnitude of the electric field of the source radiation. While $E_{p_\parallel}$ manifests a plateau-like dependence, with values close to zero, $E_{p_\perp}$ results larger

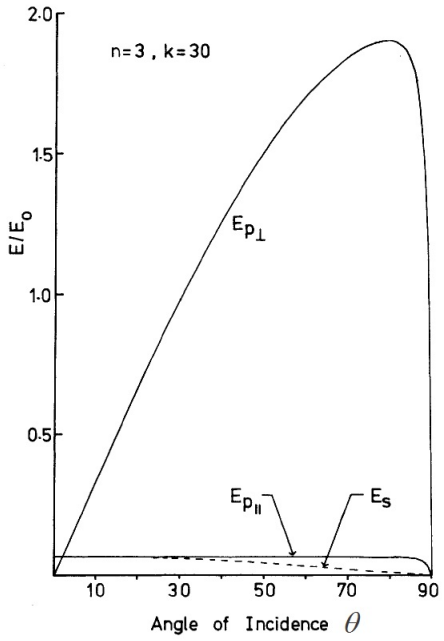

Figure 2.11: Dependence of $E_{p_\parallel}$, $E_{p_\perp}$ and E_s upon angle of incidence, for a material possessing n=3 and k=30. After [32].

than E_i for $\theta \gtrsim 40°$. As a result, at the reflection point the only component of the electric field that possesses a significant non-null value is the p-polarised electric field whose direction is normal to the surface. This intrinsically selects the surface dipoles that are active to RAIRS, i.e. those dipoles whose gradient along the surface normal is non null upon vibration. The dipoles lying parallel to the surface are not active to RAIRS. This rule is termed the *surface selection rule* and is of fundamental importance when studying the conformation of molecules adsorbed on a surface through RAIRS. Additionally, figure 2.11 shows that $E_{p_\perp}$ reaches higher intensities for very high values of θ. This means that glancing incidence is needed for RAIRS experiments. Greenler calculated the optimum angle of incidence (θ_m) for different metallic reflective surfaces, finding that $80° < \theta_m < 88°$ [30].

An alternative way of visualising the surface selection rule consists of making use of the image charge theory. According to this, in a system composed of a charged particle and a conductive material, whose linear dimensions are large compared to the size of the particle, the electric field in the vacuum can be reproduced by adding an imaginary charge into the metal bulk, with opposite charge, at a distance from the interface equalling the distance between the interface and the particle in vacuum. This method is based on the fact that in a conductive material electrons are free to move, and would rearrange themselves in order to compensate the presence of local charges in their proximity. In the case of a dipole in-plane with the surface (figure 2.12a), the imaginary charges are placed in such a way that the imaginary dipole vector has

the same magnitude and opposite direction with respect to the original dipole, thus the local electric field of the electromagnetic wave would experience a net null dipole. Conversely, a dipole whose direction is perpendicular to the surface would induce an imaginary dipole with the same magnitude and direction, yielding an effective dipole whose intensity is enhanced (figure 2.12b). This is an intuitive and qualitative method to explain the surface selection rule for RAIRS active vibrational modes.

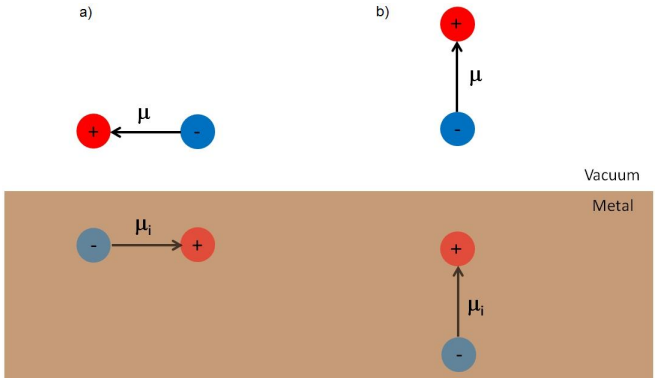

Figure 2.12: The representation of the surface selection rule for RAIRS through the use of image charges. a) Dipole parallel to the surface. b) Dipole perpendicular to the surface. The vectors μ and μ_i represent the adsorbate dipole moment and its image moment within the metal bulk, respectively.

The RAIR spectra presented in this thesis display the behaviour of the difference in reflectivity $(R_0 - R)$ induced by the molecular adsorption, normalised to the reflectivity of the bare metal R_0, as a function of the radiation wavenumber. In other words, the intensity A of a peak is calculated as follows:

$$A = \frac{R_0 - R}{R_0} \tag{2.34}$$

References for chapter 2

[1] F. Haber and R. Le Rossignol, "Production of ammonia," *United States Patent Office - US Patent 1,202,995*, 1916.

[2] T. Kandemir, M. E. Schuster, A. Senyshyn, M. Behrens, and R. Schlögl, "The Haber-Bosch process revisited: on the real structure and stability of "ammonia iron" under working conditions," *Angewandte Chemie (International ed. in English)*, vol. 52, no. 48, pp. 12723–6, 2013.

[3] I. Langmuir, "Chemical Reactions at Low Pressures," *Journal of the American Chemical Society*, vol. 37, no. 5, pp. 1139–1167, 1915.

[4] G. Gaines and G. Wise, "Insiders, Outsiders, and Surfaces: Irving Langmuir's Contribution to Catalysis," in *Heterogeneous Catalysis* (B. H. Davis and W. P. Hettinger, eds.), vol. 222 of *ACS Symposium Series*, ch. 2, pp. 13–22, Washington, D.C.: American Chemical Society, 1983.

[5] D. Alpert, "Ultrahigh Vacuum: a Survey," *Physics Today*, vol. 16, no. 8, p. 22, 1963.

[6] G. Binnig, H. Rohrer, C. Gerber, and E. Weibel, "Surface Studies by Scanning Tunneling Microscopy," *Physical Review Letters*, vol. 49, no. 1, pp. 57–61, 1982.

[7] G. Binnig and C. F. Quate, "Atomic Force Microscope," *Physical Review Letters*, vol. 56, no. 9, pp. 930–933, 1986.

[8] G. Ertl, "Reactions at surfaces: from atoms to complexity (Nobel Lecture)," *Angewandte Chemie (International ed. in English)*, vol. 47, no. 19, pp. 3524–35, 2008.

[9] I. Langmuir, "The adsorption of gases on plane surfaces of glass, mica and platinum," *Journal of the American Chemical Society*, vol. 40, no. 9, pp. 1361–1403, 1918.

[10] A. Bravais, "Mémoire sur les systèmes formés par les points distribués régulièrement sur un plan ou dans l'espace," *Journal de l'École polytechnique*, vol. 19, pp. 1–128, 1850.

[11] J. Woll, G. Meister, U. Barjenbruch, and A. Goldmann, "Oxygen chemisorption on Cu(110): A combined study by second-harmonic spectroscopy and photoemission," *Applied Physics A*, vol. 60, no. 2, pp. 173–178, 1995.

[12] F. Besenbacher and J. K. Nørskov, "Oxygen chemisorption on metal surfaces: General trends for Cu, Ni and Ag," *Progress in Surface Science*, vol. 44, no. 1, pp. 5–66, 1993.

[13] G. Binnig and H. Rohrer, "Scanning tunneling microscope," *United States Patent Office - US Patent 4,343,493*, 1982.

[14] B. Bhushan, *Scanning probe microscopy in nanoscience and nanotechnology*. Berlin, London: Springer, 2010.

[15] S. D. Barrett, "Image SXM - http://www.ImageSXM.org.uk," 2014.

[16] I. Horcas, R. Fernández, J. M. Gómez-Rodríguez, J. Colchero, J. Gómez-Herrero, and A. M. Baro, "WSXM: A software for scanning probe microscopy and a tool for nanotechnology," *Review of Scientific Instruments*, vol. 78, no. 1, p. 013705, 2007.

[17] G. Binnig and D. P. E. Smith, "Single-tube three-dimensional scanner for scanning tunneling microscopy," *Review of Scientific Instruments*, vol. 57, no. 8, p. 1688, 1986.

[18] J. Bardeen, "Tunnelling from a Many-Particle Point of View," *Physical Review Letters*, vol. 6, no. 2, pp. 57–59, 1961.

[19] A. D. Gottlieb and L. Wesoloski, "Bardeens tunnelling theory as applied to scanning tunnelling microscopy: a technical guide to the traditional interpretation," *Nanotechnology*, vol. 17, no. 8, pp. R57–R65, 2006.

[20] A. Della Pia and G. Costantini, "Scanning Tunneling Microscopy," in *Surface Science Techniques* (G. Bracco and B. Holst, eds.), vol. 51 of *Springer Series in Surface Sciences*, ch. 19, pp. 565–597, Berlin, Heidelberg: Springer Berlin Heidelberg, 2013.

[21] N. Lang, "Spectroscopy of single atoms in the scanning tunneling microscope," *Physical Review B*, vol. 34, no. 8, pp. 5947–5950, 1986.

[22] M. Razavy, "Semi-Classical Approximations," in *Quantum theory of tunneling*, ch. 3, pp. 23–40, River Edge: World Scientific, 2003.

[23] C. Davisson and L. Germer, "Diffraction of Electrons by a Crystal of Nickel," *Physical Review*, vol. 30, no. 6, pp. 705–740, 1927.

[24] L. De Broglie, "The wave nature of the electron," *Nobel lecture*, vol. 12, pp. 244–256, 1929.

[25] L. De Broglie, "The reinterpretation of wave mechanics," *Foundations of Physics*, vol. 1, pp. 5–15, 1970.

[26] W. L. Bragg, "The Diffraction of Short Electromagnetic Waves by a Crystal," *Proceedings of the Cambridge Philosophical Society*, vol. 17, pp. 43–57, 1914.

[27] M. P. Seah and W. A. Dench, "Quantitative electron spectroscopy of surfaces: A standard data base for electron inelastic mean free paths in solids," *Surface and Interface Analysis*, vol. 1, no. 1, pp. 2–11, 1979.

[28] P. P. Ewald, "Introduction to the dynamical theory of X-ray diffraction," *Acta Crystallographica A*, vol. 25, no. 1, pp. 103–108, 1969.

[29] G. Attard and C. Barnes, *Surfaces*. No. 59 in Oxford science publications, Oxford, New York: Oxford University Press, 1998.

[30] R. G. Greenler, "Infrared Study of Adsorbed Molecules on Metal Surfaces by Reflection Techniques," *The Journal of Chemical Physics*, vol. 44, no. 1, p. 310, 1966.

[31] R. G. Greenler, "Reflection Method for Obtaining the Infrared Spectrum of a Thin Layer on a Metal Surface," *The Journal of Chemical Physics*, vol. 50, no. 5, p. 1963, 1969.

[32] V. Humblot and C.-M. Pradier, "RAIRS under ultrahigh vacuum conditions on metal surfaces," in *Biointerface characterization by advanced IR spectroscopy* (C.-M. Pradier and Y. J. Chabal, eds.), ch. 1, pp. 1–26, Amsterdam: Elsevier B.V., 1st ed., 2011.

[33] S. A. Francis and A. H. Ellison, "Infrared Spectra of Monolayers on Metal Mirrors," *Journal of the Optical Society of America*, vol. 49, no. 2, p. 131, 1959.

[34] D. P. Woodruff and T. A. Delchar, *Vibrational spectroscopies*. Cambridge, New York: Cambridge University Press, 1994.

Chapter 3

Experimental details

In this chapter the principal pieces of equipment utilised for the completion of the work described in the present thesis are described, along with the basic methods for achieving UHV, cleaning a copper single crystal in UHV and depositing organic molecules via sublimation in vacuum. For UHV studies, three different stainless steel chambers, incorporating various surface science tools, have been used.

3.1 The UHV environment

The UHV environment is necessary when performing surface science investigations, especially when substrates with a high reactivity towards atmospheric gaseous species are used (see section 2.1). Copper, in particular, manifests a high chemical affinity with oxygen, and, moreover, the (110) cut shows the highest reactivity amongst the high symmetry faces, due to the low coordination number of its outermost atoms (see section 2.2). The UHV environment, that is a pressure lower than 10^{-9} mbar, is obtained via different pumping systems, depending on the chamber, whose functions are usually complementary. The pumps used can be divided in two main categories: *roughing* (or *backing*) *pumps* and *UHV pumps*. The former are used to reach rough vacuum ($10^{-3} - 10^{-2}$ mbar) from atmospheric pressure, while the latter start to function at a later time, when a rough vacuum has already been reached. The reason for needing these two complementary pumping methods lies in the diverse characteristics of the flow encountered at different pressures. In fact, at high pressures, when the mean free path λ of the molecules is very small compared to a significant geometrical dimension, e.g. the diameter d of the pipes, ($\lambda/d << 1$), a viscous flow is established. The aforementioned empirical quantity (λ/d) is termed *Knudsen number* and is indicated with Kn [1]. In this flow regime, molecules are densely distributed and experience more collisions with themselves than with the pipe wall, and is possible to introduce a *group velocity*, distinct from the thermal velocity possessed by each molecule. In this case the

flow depends on pressure. On the other hand, at low pressures ($\lambda/d >> 1$) molecules undergo collisions mostly with the walls. A molecular flow is established, in which molecules can freely move in any direction, resulting in no net collective movement. In this situation the flow does not depend on the total pressure [2, 3].

The most commonly used roughing pumps in vacuum technology are the rotary and the sorption pumps. In the UHV pumps category there are several pump types: these are the turbomolecular, the diffusion, the ion and the cryo pumps. As an additional system, the titanium sublimation pump is largely used together with the standard pumping units. However, any combination of these different pumps is insufficient to evacuate an experimental chamber from atmospheric pressure to UHV. In fact, gaseous species trapped on the walls of a chamber that have been exposed to atmospheric pressure would be released at slow rate, resulting in a base pressure in the order of 10^{-8} mbar. In order to avoid this inconvenience, the release of trapped gases is accelerated with a thermal treatment, during which the entire chamber is baked with dedicated resistive heaters and temperature-control devices. For a UHV chamber with typical dimensions, a *bakeout* process is performed at a temperature of 400 K, approximately, for a minimum time of 12 hours. During this process, a UHV-grade pump needs to be in operation. The main principles of operation of the pumps used will be briefly described in the following subsections.

3.1.1 The roughing pumps

3.1.1.1 The rotary vane pump

The rotary vane pump, also called rotary pump, is largely used for backing UHV pumps such as turbomolecular or diffusion pumps. Its principal components are a stator and an eccentric rotor. Vanes, held together by springs, are pressed towards the wall of the stator. During the rotor movement, the vanes mechanically push the molecules coming from the inlet (vacuum system) towards the outlet, which ends up in the exhaust. The accumulation of molecules, due to the rotor compression, in proximity of the outlet causes a pressure rise, that is released through the opening of a specific valve (figure 3.1). In optimum conditions, the rotary vane pump is able to reach 10^{-3} mbar. The production of mechanical vibrations is unavoidable due to the rotor movement, and this could be a drawback when used with techniques that are sensitive to vibrations (e.g. STM). This pumping system has been used as a backing unit for all the UHV chambers used for the experiments presented herein.

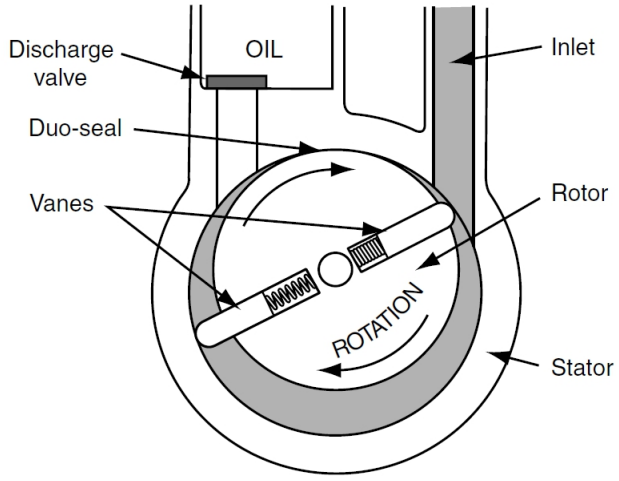

Figure 3.1: Scheme of a rotary pump. After [4].

3.1.2 The UHV pumps

3.1.2.1 The turbomolecular pump

The turbomolecular pump, usually abbreviated to turbo pump, is one of the most prevalent UHV-grade pumping systems. It mainly consists of a series of stator/rotor couples equipped with inclinated blades. The rotors transfer their momentum to the pumped molecules, which are driven towards the subjacent stator. The slope of the blades of the stator then directs the molecules to the following rotor, and the procedure is repeated, until the molecules are finally pumped through the backing unit. The spinning of the rotors can reach 30 krpm, and this can cause significant vibrational problems. Turbomolecular pumps have been used in both the UHV chambers equipped with STM (see sections 3.4.2 and 3.4.3).

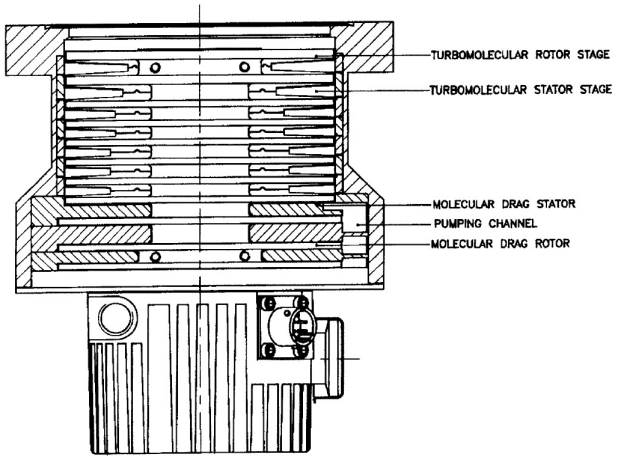

Figure 3.2: Section of a turbomolecular pump. After [5].

3.1.2.2 The diffusion pump

The diffusion pump is based on the heating of oil molecules. These, due to the thermal energy, evaporate and are directed upwards, in a central column, and are then ejected downwards at high speed. After colliding with the molecules, the oil vapour hits the internal surface of the pump, which is held at low temperature with the use of a water-cooling system. The condensed oil is then recovered by the reservoir at the base, while the pumped molecules reach the outlet, to the backing pump (figure 3.3). The absence of moving pieces makes the diffusion pump useful when the system is sensitive to acoustic noise and vibrations. Its major demerit is the possibility of having a backflow of oil to the vacuum chamber. For this reason, low temperature traps, typically a liquid nitrogen container, are continuously used. A diffusion pump has been used for evacuating the chamber utilised in performing RAIRS and LEED experiment, described in subsection 3.4.1.

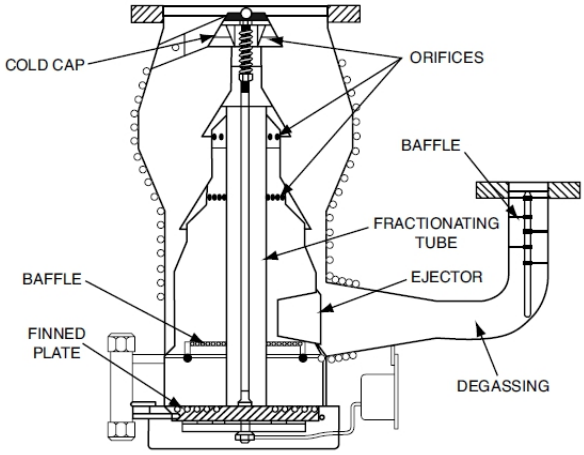

Figure 3.3: Section of a diffusion pump. After [6].

3.1.2.3 The sputter ion pump

The sputter ion pump, commonly abbreviated in ion pump (figure 3.4), is a UHV pump that starts to work at pressures lower than 10^{-4} mbar. The latter requirement implies the preliminary activation of a better than roughing pump, usually a turbo pump. The principle of operation of an ion pump consists in creating an electric discharge between two electrodes, kept at a few kV potential. The gas molecules present in the cell are consequently ionised, accelerated towards the cathode and adsorbed on its surface, usually made of titanium. A magnetic field can also be added, in order to induce a higher collision rate between molecules and discharging electrons, thanks to the helical

path of the latter. Like the diffusion pump, an ion pump possesses no mechanical movements, a feature that makes it desirable for systems equipped with techniques that are sensitive to vibrations. Ion pumps are installed on both the UHV chambers used for STM experiments, described in sections 3.4.2 and 3.4.3.

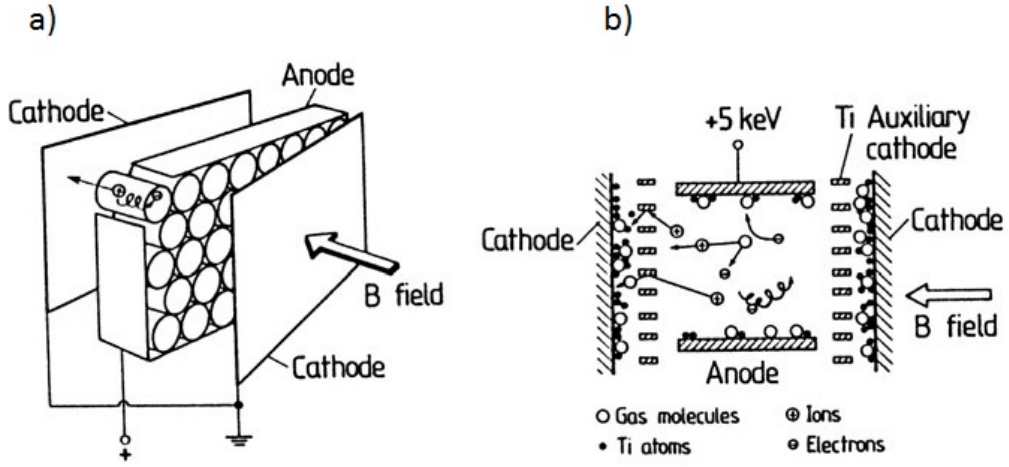

Figure 3.4: a) Schematic drawing of a sputter ion pump composed of multiple cells and equipped with magnets. b) The principle of operation of a single cell. Image reproduced from [7].

3.1.2.4 The titanium sublimation pump

The titanium sublimation pump (TSP) is a discontinuous sorption system that is frequently used as an add-on to the standard pumps. It exploits the affinity between titanium films and atmospheric gases. Its main part consists of a titanium filament, through which a high electric current is passed. As a consequence, titanium is evaporated and is deposited on a large surface, which can be a special stainless steel collector or the interior walls of the vacuum chamber. Once the Ti film is formed, gaseous molecules are chemisorbed on it, with variable sticking coefficients depending on the gas considered [8]. At low temperatures, titanium films manifest an increased chemisorption activity, due to their porous nature [9]. At room temperature, typically the titanium sublimation needs to be activated for one minute every 8 hours.

The continuous use of these pumping techniques coupled with the initial *bakeout* procedure creates a clean and controlled environment. In the following sections the techniques and methods necessary to prepare the samples of interest will be described.

3.2 Substrate preparation

Monocrystalline copper samples are cleaned with several cycles of sputtering and annealing. The sputtering consists of a bombardment of the surface with noble gas ions (typically Ar^+), in order to physically remove organic contaminants from the metallic surface. Firstly the chamber is filled with argon up to a pressure of $10^{-6} - 10^{-5}$ mbar, depending on the system, then a sputter gun ionises the argon molecules via impact with electrons. Those electrons are generated by a discharge between two electrodes kept at ~ 0.5 kV voltage. Once the Ar^+ cations are produced, they are accelerated with a voltage of 1-2 kV towards the surface, which is kept in front of the gun for more efficient results. In order to check the effectiveness of the sputtering, the drain current on the sample surface is measured. In the case of copper crystals, a typically successful sputter process produces a surface current of $5\,\mu A\,cm^{-2}$ and is applied for 30 minutes [7]. During the sputtering it is important to verify the absence of gaseous contaminants (e.g. oxygen) in the chamber, since crystals sputtered with reactive species can remain contaminated with them for longer times. The sputtering of a monocrystalline metal surface is known to remove the first atomic layers along with the adsorbates [10], thus inducing a change in the surface crystallography. Furthermore, noble gas atoms may remain embedded in the crystal upon sputtering. These two inconveniences are addressed with a subsequent sample annealing, usually performed with resistive heating and electron bombardment. The conditions for annealing the sample can vary largely, but a requisite consists in reaching a temperature, lower than the metal melting point, that allows the rearrangement of the interfacial atoms. For copper crystals, a temperature of 770-820 K is required. After a successful annealing process, the surface crystallography is recovered and the argon molecules that have potentially remained trapped in the surface are liberated. However, additional impurities present in the bulk of the crystal may migrate to the surface upon annealing, and this is the reason for the necessity of multiple cycles of sputtering/annealing before achieving an acceptable level of surface cleanliness. The latter condition is checked, depending on the experiment, via LEED or STM.

3.3 Molecular deposition from the vapour phase

The deposition of organic molecules in UHV environment occurs via a gas-phase deposition method. The solid powder, which represents the molecular source, is kept in an open glass crucible, wrapped with tantalum wire ($\varnothing = 0.25\,mm$). The tantalum wire is connected to two metallic arms and physically holds the crucible in place. An electrical connection, made via spot welding of the wire, is then established between the arms and the wire. The arms extend through a UHV flange, that assures that the molecular source is kept in vacuum while an electrical potential difference can be externally ap-

plied to the two pins. A power supply is used to apply a voltage to the two pins, and electrical current is allowed to travel through the circuit that includes the two arms and the wrapping wire. Given the small diameter of the tantalum wire, this provides the highest contribution to the total electrical resistance of the circuit. Thanks to the Joule effect (ohmic heating), energy is released via dissipation in a quantity proportional to the total resistance and to the square of the electric current:

$$Q = RI^2 \tag{3.1}$$

In practice, the application of a current to this circuit induces a temperature rise, until a steady state is achieved. In this situation, when the energy given to the system is compensated by the energy dissipated, a correspondence between the current applied and the temperature achieved can be established. The actual temperature of the crucible can be measured with a thermocouple. However, the reproducibility of the fabrication of the dosers allows the temperature of the molecular source at a given current to be estimated. In order to achieve more reproducibility in the dosing conditions, the crucible is enveloped in seven coils of the tantalum wire. Furthermore, the calibration of the doser can be made with a trial-and-error approach, checking the sample coverage following a deposition (e.g. via STM) and adjusting the dosing conditions accordingly.

3.4 The UHV chambers

The experiments presented herein have been carried out in three distinct UHV chambers, two of which are mainly dedicated to STM characterizations and one to RAIR spectra acquisition. All the chambers are equipped with LEED optics and additional complementary tools. This section contains a brief description of the components present in the three vacuum chambers, along with their schematic representations.

3.4.1 RAIRS chamber

A specific UHV chamber is dedicated to RAIRS studies (figure 3.5). A LEED system and a quadrupole mass spectrometer are also installed, as complementary techniques. The sample is held on a manipulator, that can be moved in (x, y, z, θ) directions, attached via two tungsten wires. These are also used to resistively heat the sample when needed. A thermocouple is also connected to the rear side of the sample. The manipulator is equipped with a liquid nitrogen well, used for cooling the sample and performing RAIRS at low temperatures. The UHV chamber is pumped via a diffusion pump, backed with a rotary pump, and is also equipped with a titanium sublimation pump and a ion gauge pressure reader. A sputter gun and a leak valve used to admit gases into the chamber are also present. A separate turbo/rotary system is used to pump the doser section for molecular deposition. The IR radiation is produced by a

Nicolet Magna-IR 860 Fourier Transform Infra-Red (FTIR) spectrometer and enters the UHV chamber via a KBr window, a material that is transparent to IR wavelengths, after having been reflected by two mirrors, one of which has focussing properties. The beam is then reflected off the sample and exits the chamber through another KBr window, then reaches a focussing mirror and the mercury-cadmium-telluride (MCT) detector, that needs to be cooled via liquid nitrogen during operation. The detector is able to detect IR radiation in the wavenumber region 400 cm^{-1} to 4000 cm^{-1}. Outside the UHV chamber, the beam crosses regions that are sealed, purged and desiccated, in order to avoid or minimise IR absorption by atmospheric gases, such as carbon dioxide and water vapour. The alignment between all the components is crucial in a RAIRS experiment, since, given the grazing incidence of the beam, non-negligible intensity losses can be caused by small displacements. IR spectra are collected via the software Omnic, that permits the performance of some data processing, including background corrections and the removal of signals determined by the presence of undesired gases along the beam path. The spectral resolution is 4 cm^{-1}, and the final spectra are achieved with the addition of 256 scans. These conditions are usually sufficient for RAIRS studies of molecular monolayers on a surface in an UHV environment.

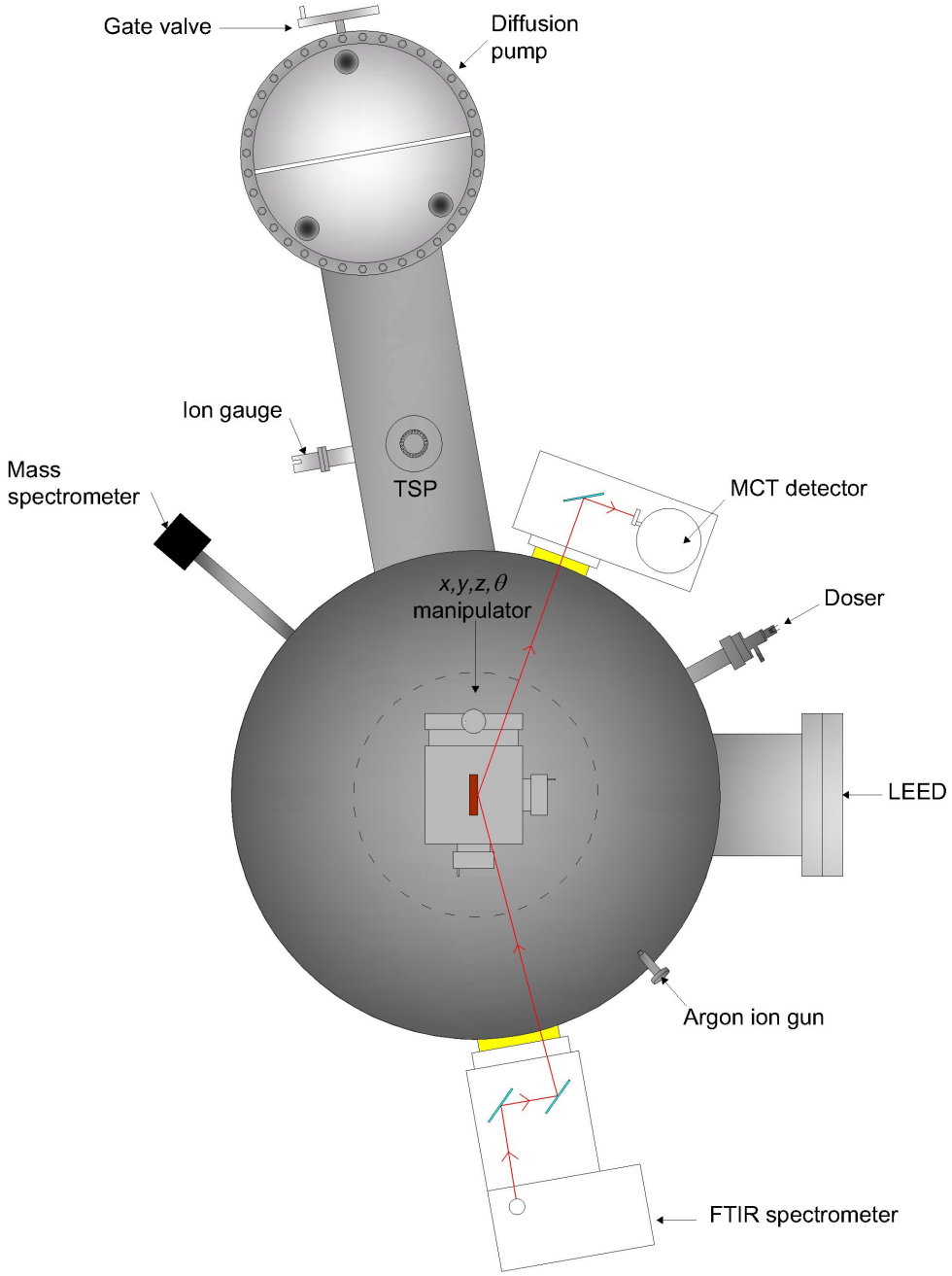

Figure 3.5: Schematic representation of the RAIRS chamber. Diagram inspired by reference [11].

3.4.2 Specs STM LT chamber

The Specs STM LT (Low Temperature) UHV chamber houses an STM (Specs GmbH Aarhus 150 STM) and LEED optics (see figure 3.6 for a scheme of the chamber). The machine consists of one single chamber, equipped with a turbo/rotary pump system, an ion pump and a titanium sublimation pump, along with an ion gauge for pressure measurements. A gate valve can separate the turbo pump from the chamber: this is mainly to switch the turbo pump off during STM acquisition, while the pumping is assured by the non-mechanical ion pump. The base pressure normally reached during operation is 10^{-10} mbar. The dosing section, used for introducing the source for the molecular sublimation in vacuum, is pumped with another turbo/rotary set and is separated from the main chamber with a manual gate valve. The instrument is endowed with a sample manipulator, used for the crystal cleaning procedure and for the storage of up to five different samples, and two transfer arms, one long, used for the dosing process and to perform LEED experiments, and one short, used to move the samples between the long arm, the manipulator and the STM. The manipulator can be heated resistively and, if necessary, with the aid of electron beams, in order to induce sample annealing. A thermocouple is attached to the manipulator. The chamber is provided with a sputter gun, used for sputtering the crystal with Ar^+. In the proximity of the sputter gun, there is a leak valve, connected to a gas line that brings argon into the chamber. An additional leak valve is used for letting other gases (e.g. oxygen) into the chamber at the desired pressure.

The STM is positioned on a stage that is held with springs, in order to provide a damping system against vibrations during STM operation. However, the stage can be locked to a fixed position for some operations, for instance during sample transfers, with a specific horizontal linear drive. The STM operations are driven with the built-in Specs GmbH software. The complex STM electronic controls are in connection with the chamber and are interfaced with the computer. The software shows the formation of a STM image in real time, and allows some tip-conditioning activities to be performed, basically applying a user-defined voltage to the tip for a short time, in order to improve the tip resolution.

The extremity of an STM apparatus, consisting in the unit that allows the scanning and the electron tunneling to take place, is termed *STM head*.

Figure 3.7a, taken from reference [12], represents a picture of the UHV flange onto which the STM stage is mounted. The stage is held with springs, that function as an anti-vibrational system, during normal operation. When the STM is unused, the STM stage can be locked with a horizontal linear drive: this fixes the position of the STM stage and allows operations such as the transfer of the sample. In the drawing of figure 3.7c, also taken from reference [12], the sectioned STM head is shown. It is visible that the rod that sustains the STM tip has a cylindrical shape, with its vertical movement

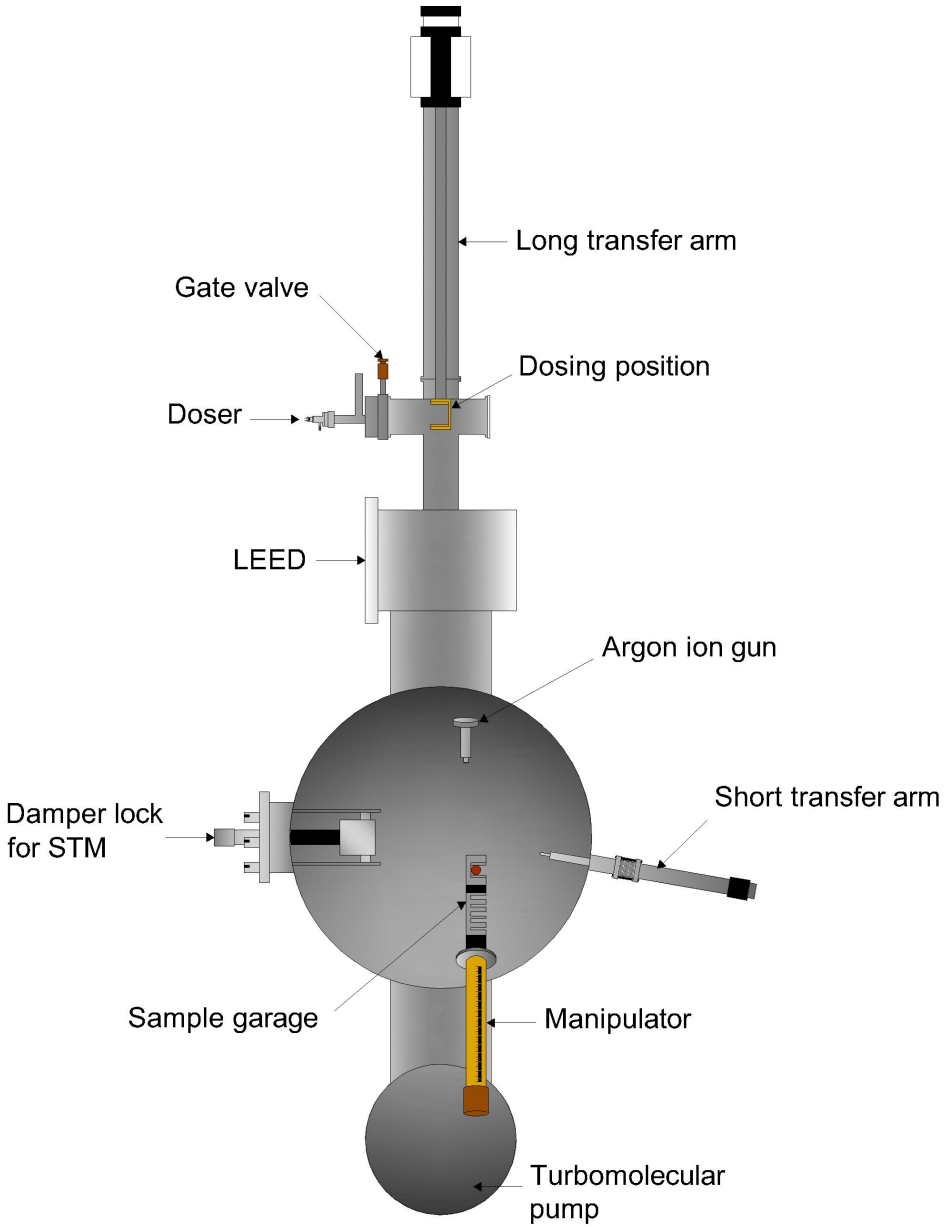

Figure 3.6: Schematic representation of the Specs STM chamber. Diagram inspired by reference [11].

controlled by a dedicated motor. In this system, the sample faces downwards, and is kept tight on the sample-holder with the aid of specific copper clips. When the clips become loose due to the continuous use, a significant noise is detected in STM investigations, and they thus need replacing.

Regarding the vertical upwards movement of the motor rod towards the sample, this is regulated by a specific mechanism called *inchworm*. This mechanism was designed at the University of Aarhus [13, 14] and was scaled up commercially by Specs GmbH. The motor used for the coarse approach consists in a hollow cylinder made of piezoelectric material that envelops the rod. Three specific electrodes compose the inchworm motor: two, placed at the top and and the bottom, are designed to hold accurately the motor rod and serve as clamps. The central tube can also be expanded and contracted. Applying a defined software-controlled sequence of voltages the rod can be moved upwards. In particular, the sequence "upper clamping, lower unclamping, central contraction, lower clamping, upper unclamping, center expansion" induces the rod to proceed upwards [15]. The opposite sequence drives the rod in the opposite direction. Also the speed of this coarse movement is controlled by the software. A typical rate for a coarse tip approach towards the sample is 1 mm/min. The fine (x,y,z) movement of the tip, used during the STM scanning, is controlled by a different piezotube, which is placed on top of the motor road and below the tip (see diagram in figure 3.7b).

The complex electronic controls required for the functioning of this STM are guaranteed via feedthroughs that are placed at the external side of the UHV flange. The electrical connections are then established with wires that run in vacuum to the STM head. Three separate feedthroughs are connected to the STM UHV flange. A preamplifier is used to amplify the tunneling current and to transform it into a voltage. Additional pieces of equipment, though unused for the production of the results presented in this thesis, include a Variable Temperature Controller (VTC20), that allows STM investigations to be performed in the range 90-400 K, and Monitor-Digipot controller, that permits to manually control the position of the head in the x,y directions.

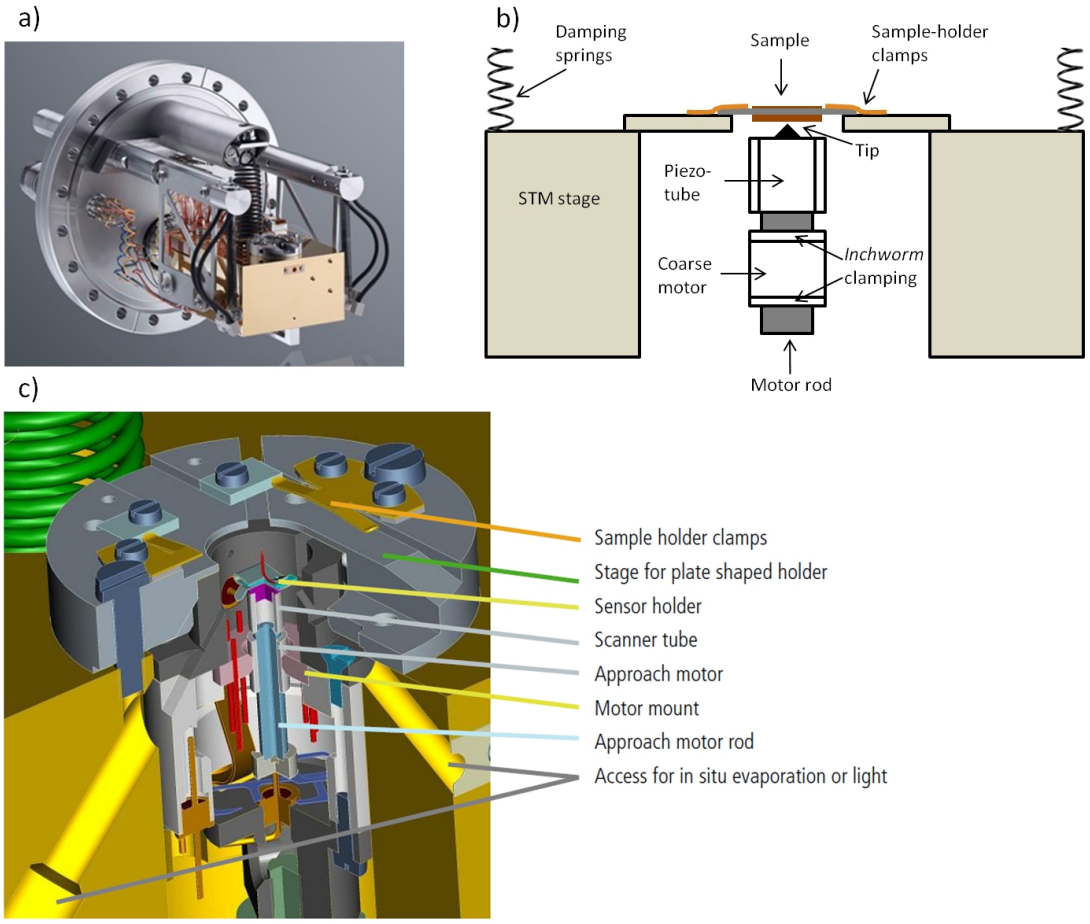

Figure 3.7: a) Picture of an Aarhus type Specs 150 STM, showing the STM stage and the UHV flange onto which it is mounted. Picture taken from reference [12]. b) Schematic representation of the Specs STM head, with a focus on the piezotubes that drive the movement of the probe. The scheme is adapted from reference [15]. c) Scheme, reproduced from reference [12], representing the sectional view of a Specs STM head.

3.4.3 VT STM chamber

The VT (variable temperature) Omicron STM machine (figure 3.8) consists of two linked UHV chambers, separated by a manual valve. One of these chambers is dedicated to the sample analysis (analysis chamber) via STM and LEED, while the other one is mainly used to clean the substrate and to deposit molecules (preparation chamber). The latter is pumped with a turbo/rotary system, which can be valved off via a pneumatic valve. Both chambers are provided with dedicated ion pumps, titanium sublimation pumps, ion gauges and leak valves. A load-lock system, contiguous with the preparation chamber, allows the fast introduction of samples in vacuum. The sputter gun is located in the preparation chamber, where a quadrupole mass spectrometer is also available. In ideal conditions, the analysis chamber is held at a lower pressure ($\sim 5 \times 10^{-11}$ mbar). Two manipulators with (x, y, z, θ) movement freedom are available, one for each chamber, both provided with resistive heating, electron beam heating and a thermocouple. The movement of the samples from one chamber to the other is performed via a long magnetic transfer arm. In the analysis chamber, a wobble stick is used to transfer samples from the manipulator to the STM stage. A sample carousel, containing twelve slots, is also accessible with the wobble stick. The STM system, called VT-STM and produced by Omicron Vacuum Physik GmbH, is held on a damped stage. The electronic feedthroughs for the STM controllers are situated below the STM. The controller is connected to a computer and the STM tip movement, tip conditioning and data acquisition and saving are managed through the Omicron Scala Pro software. Finally, a magnifying camera, pointed towards the STM tip, helps in visualising the coarse tip approach towards the sample.

In figure 3.9a an Omicron VT STM stage out of vacuum is pictured [16]. The STM stage and the vertical linear drive, or push-pull motion drive, are visible. The latter is used to lock/unlock the STM stage. When the stage is unlocked, it is held by four spring that are contained in tubes. The springs are used to minimise the effects of mechanical vibrations. As an additional anti-vibration system, en eddy current is exploited. As visible in the diagram of figure 3.9b [11], the stage is encircled by a series of permanent magnets and copper fins: the resulting eddy current in the fins, due to the Lorentz force, provides the system with additional stability. In figure 3.9c, finally, the proper STM sample holder is pictured in a top-view fashion. The tip is visible, while the sample clips, used to clamp the sample to its holder in a manner similar to the one described in figure 3.7b, are not present in this picture.

With regards to the motor for the (x,y,z) coarse positioning of the tip, a tripodal piezodrive is utilised in this system. The scanner is enveloped in sliders which are magnetically coupled with three shear-piezos, to which voltages are applied. The mechanism of function relies on the slip/stick effect that takes place when a sawtooth voltage is applied to the shear piezos. During the fast movement of the piezos, the sliders slip

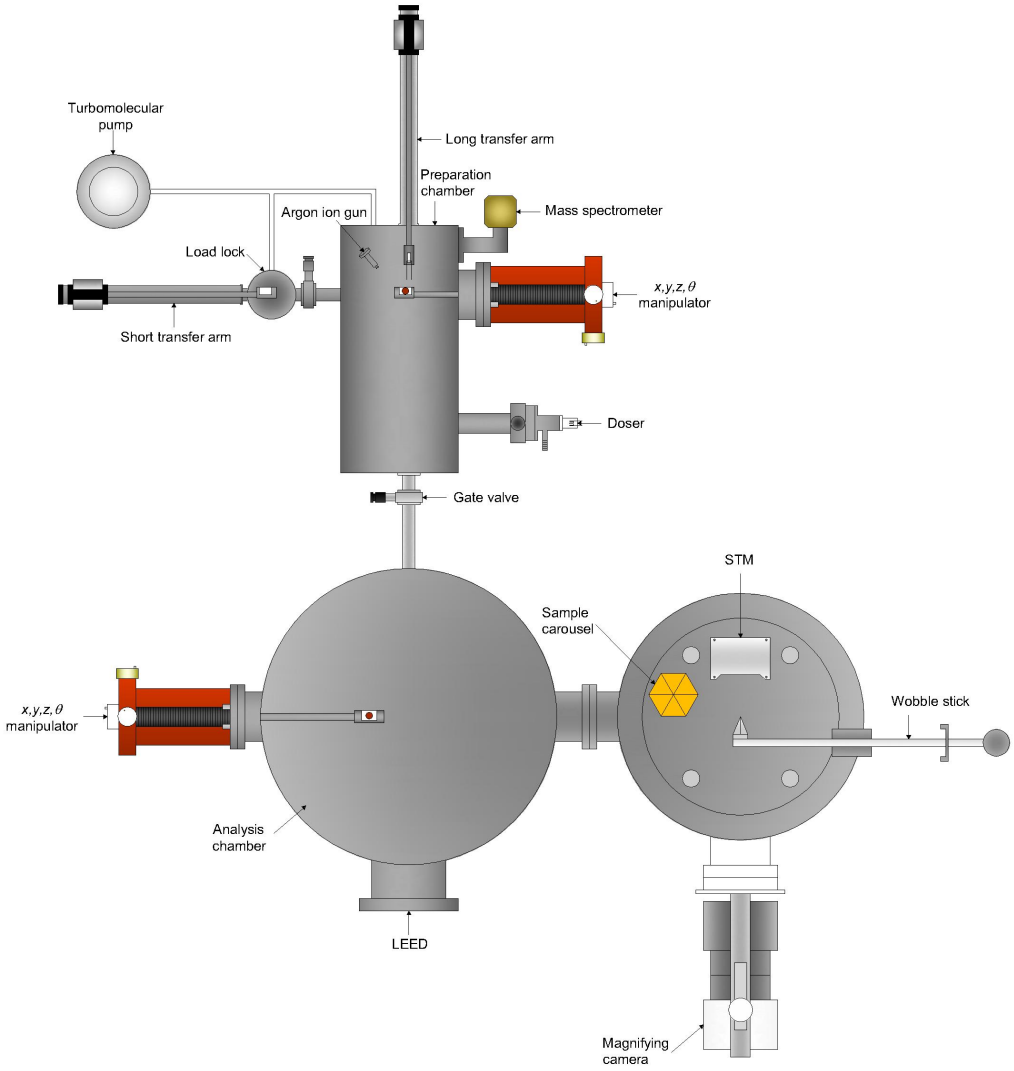

Figure 3.8: Schematic representation of the Omicron VT STM chamber. Diagram inspired by reference [11].

towards the desired direction, while during the slow movement of the piezos, the sliders move thanks to their inert mass, assuring a steady step-wise moving of the whole scanner [17]. These movements can be performed manually or automatically, through the use of a dedicated remote control. A fine-movement z piezo is positioned on top of the scanner. It is kept fully retracted during the coarse approach and is used to maintain the tunneling conditions, by means of retraction or expansion, once these is achieved. The control on the fine piezo is ensured by the Scala PRO software and the remote control, in order to avoid tip crashes during data acquisition. This STM has been designed to operate in the temperature range spanning from 25 to 1500 K.

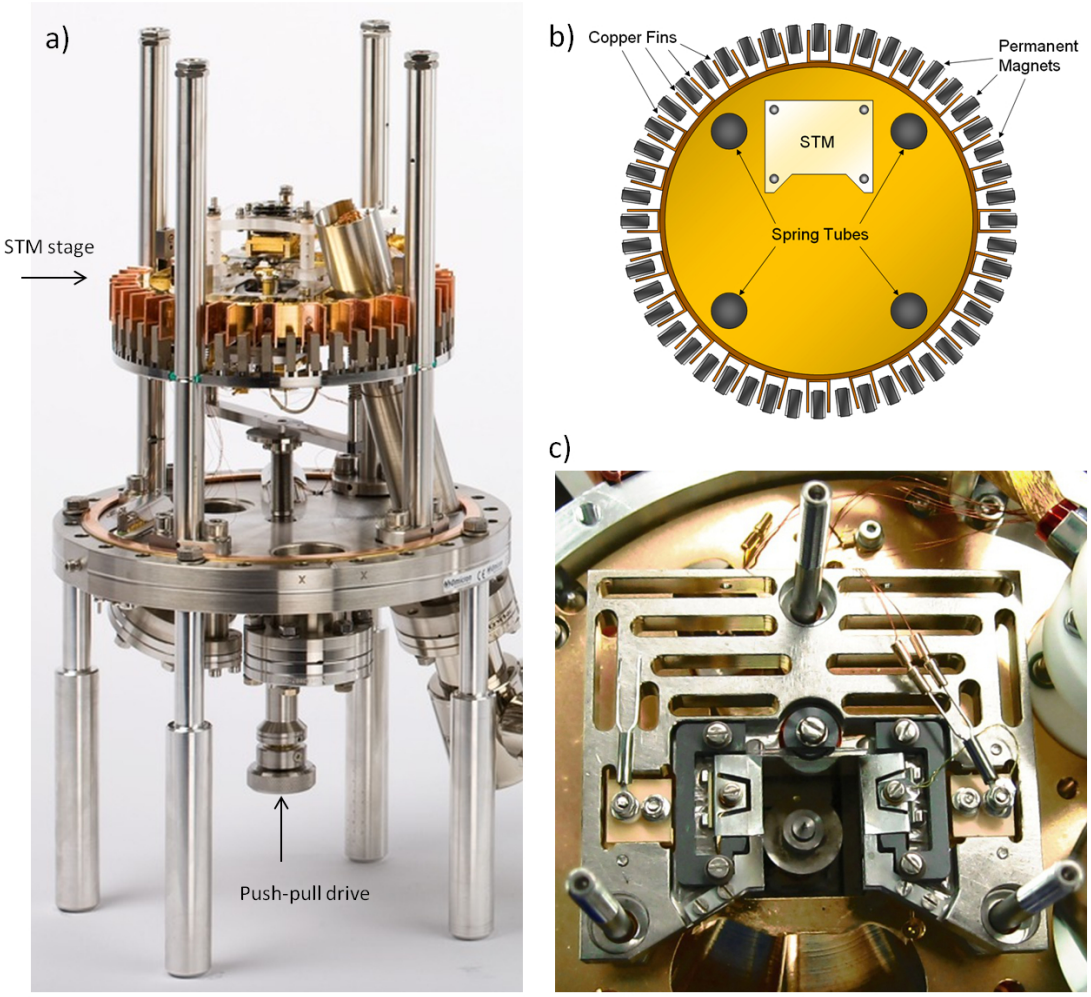

Figure 3.9: a) Picture of the Omicron VT STM, as display on the Omicron website [16]. b) Diagram that schematically represents the STM stage, with two mechanisms for depleting vibrations, that are the suspending springs and the eddy current system. Diagram reproduced from reference [11]. c) Picture showing the sample holder and the tip of the system used for this study. In this case, the sample-holding clips, necessary during the STM operation, are not present.

References for chapter 3

[1] "Knudsen Number," in *Encyclopedia of Microfluidics and Nanofluidics* (D. Li, ed.), pp. 906–907, Springer US, 2008.

[2] G. M. Fryer, "A Theory of Gas Flow Through Capillary Tubes," *Proceedings of the Royal Society A*, vol. 293, no. 1434, pp. 329–341, 1966.

[3] V. M. Zhdanov, "Flow and diffusion of gases in capillaries and porous media," *Advances in Colloid and Interface Science*, vol. 66, pp. 1–21, 1996.

[4] N. Yoshimura, "Vacuum pumps," in *Vacuum technology: practice for scientific instruments*, ch. 2, pp. 35–84, Berlin, Heidelberg: Springer, 2008.

[5] G. Levi, "Combination of turbomolecular pumping stages and molecular drag stages," *Journal of Vacuum Science & Technology A*, vol. 10, no. 4, p. 2619, 1992.

[6] M. H. Hablanian, "Advances in Diffusion Pump Technology," *Journal of Vacuum Science and Technology*, vol. 10, no. 1, p. 58, 1973.

[7] H. Lüth, "Surface and Interface Physics: Its Definition and Importance," in *Solid surfaces, interfaces and thin films*, ch. 1, pp. 1–28, Heidelberg, Dordrecht, London, New York: Springer, 5th ed., 2010.

[8] D. J. Harra, "Review of sticking coefficients and sorption capacities of gases on titanium films," *Journal of Vacuum Science and Technology*, vol. 13, no. 1, p. 471, 1976.

[9] D. J. Hucknall and A. Morris, "Pumps and Pumping Systems," in *Vacuum technology: calculations in chemistry*, ch. 3, pp. 56–113, Cambridge: RSC, 2003.

[10] M. Koedam and A. Hoogendoorn, "Sputtering of copper single crystals bombarded with A+, Kr+ and Ne+ ions with energies ranging from 300-2000 eV," *Physica*, vol. 26, no. 5, pp. 351–352, 1960.

[11] P. J. Donovan, *Adsorption and Self-assembly of Cobalt(II)-Tetraphenylporphyrin on Cu(110)*. Phd thesis, University of Liverpool, 2009.

[12] "STM Aarhus 150 - http://www.specs.de/cms/front_content.php?idcat=242."

[13] E. Lægsgaard, F. Besenbacher, K. Mortensen, and I. Stensgaard, "A fully automated, 'thimble-size' scanning tunnelling microscope," *Journal of Microscopy*, vol. 152, no. 3, pp. 663–669, 1988.

[14] F. Besenbacher, E. Lægsgaard, K. Mortensen, U. Nielsen, and I. Stensgaard, "Compact, high-stability, "thimble-size" scanning tunneling microscope," *Review of Scientific Instruments*, vol. 59, no. 7, pp. 1035–1038, 1988.

[15] M. Schunack, *Scanning Tunneling Microscopy Studies of Organic Molecules on Metal Surfaces*. PhD thesis, University of Aarhus (Denmark), 2002.

[16] "Omicron VT SPM - http://www.omicron.de/en/products/variable-temperature-spm/instrument-concept."

[17] T. Berghaus and P. Klaede, "Adjusting device for microscopic movements," *United States Patent Office - US Patent 5,237,238*, 1993.

Chapter 4

R-serine on Cu(110): an experimental study combined with theory

4.1 Introduction

One of the peculiar traits of biochemistry is the strict homochirality of the key molecules that govern life. Amongst these, the most evident are the right-handed sugars that are involved in the formation of nucleic acids and the left-handed proteinogenic amino acids. Living organisms provide, thus, a distinctive chiral environment in which enantiomers manifest different behaviours and reactivities, and this has a direct effect, for example, on the configuration of molecules that need to be used as medical drugs [1, 2]. Chirality has been extensively studied since its discovery in 1848 by L. Pasteur [3], and is usually, but not exclusively [4], determined by the presence stereogenic atomic centres in an organic chemical structure (see also section 1.3).

When a two-dimensional environment is considered, novel manifestations of chirality appear, created by the inherent symmetry-breaking nature that a surface possesses [5, 6]. For instance, an achiral surface may be rendered *handed*, at a global or local scale, through the adsorption of chiral molecules [6, 7]. Furthermore, in some specific cases, the constrictive nature of two-dimensional confinement forces the adsorbed molecules to assume a chiral adsorption geometry, termed *footedness*: this has to be distinguished and is in general independent from the intrinsic molecular chirality, i.e. *handedness* [8]. Inorganic surfaces functionalised with organic molecules have been widely studied recently, due to their possible application in diverse fields, like enantioselective heterogeneous catalysis [9–11], biomineralisation [12] and biosensing [13], and also for their possible role in having triggered an enantiomeric imbalance in the prebiotic era that could have determined the homochirality of life [14, 15].

Particularly, the interaction between amino acids and high-symmetry single-crystal metal surfaces is a topic that has been thoroughly investigated [8, 16–53], since amino acids are ubiquitous in biochemistry and have been shown to introduce stereoselectivity in catalysis [10, 54, 55]. The complete understanding of the local interaction between amino acids and a given metallic surface is generally challenging, due to the relatively small dimensions of the adsorbed molecules and to the several possibilities in which the interaction may occur. In particular, the difficulty consists in the need of providing the chemical form, the geometry of adsorption and the type of footprint for every molecule adsorbed on the surface. The stabilisation of an amino acid overlayer on a metal substrate is usually the result of a balance that takes into account the interactions between the amino acid and surface atoms, but also the inter-molecular and intra-molecular forces. The latter, consisting principally of hydrogen bonds, are especially important for amino acids, and are often responsible for the self-organisation and the ordering of those overlayers. The choice of a copper surface guarantees a good compromise in terms of reactivity with organic molecules, while the selection of the (110) face symmetry assures an enhanced affinity with two-dimension chirality, usually triggering the chiral organisation of achiral and prochiral molecules (see for example ref [56]), as a result of the two-fold symmetry that the surface possesses.

On the Cu(110) surface several amino acids have been studied through diverse surface science tools. The most frequent adsorption geometry is found to be established via a tridentate bonding contact, through the amino and carboxylic moieties of the amino acids and the interfacial copper atoms (μ_3 species [28]). The most common arrangement that is found for these systems is the achiral (nx2) organisation (see chapter 1). The recurrent tripodal geometry of amino acids on Cu(110) has been demonstrated to represent a distinctive symmetry breaking factor, since the molecular atoms coordinated to the metal surface can be arranged spatially in two different ways. In this manner the footednesses lambda (λ) and delta (δ) are introduced (figure 4.1). The two conformers are chiral in the sense that they are mirror-image objects in two dimensions, non-superimposable via simple rotational in-plane symmetry operations. This type of chirality refers solely to the stereodistribution of atoms in contact with the surface and is autonomous from the molecular chirality of the considered molecule. Namely, the left-footed geometry (λ) is found when the amino group lies at the bottom left of the carboxylic scaffold, vice versa a right-footed geometry (δ) is defined when, looking at the carboxylic moiety, the amino group is positioned at its bottom right [42].

Those systems whose behaviour on the Cu(110) surface is best understood are glycine [17, 30–32, 34, 35, 41, 50, 57], alanine [27, 33, 36–40] and proline [8, 16, 42, 43, 45, 47, 49], thanks to the complementary use of experimental techniques and theoretical calculations. These amino acids lose a proton from the carboxylic group upon adsorption on the Cu(110) surface, assuming an anionic form. The enantiopure systems give

rise, when adsorbed in the μ_3 geometry, to achiral (nx2) organisations with n=3,4, that are made stable by networks of intra-molecular and inter-molecular hydrogen bonds. It is noteworthy that these enantiopure systems are all organised in structures with a minimum asymmetric unit constituted by two molecules that have opposite footednesses. In other words, while these systems possess, intrinsically, a uniform molecular handedness, they also show a systematic alternation in the terms of the chirality at the footprint level.

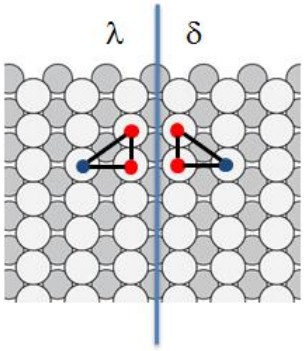

Figure 4.1: The footednesses λ and δ that a generic amino acid can assume on the Cu(110) surface when it is adsorbed as a μ_3 species through its carboxylate and amino moieties. The amino acid is sketched with a triangle, in order to visualise its tridentate geometry upon adsorption. The red and blue circles at the vertices represent the oxygen atoms of the carboxylic group and the nitrogen atoms of the amino group, respectively.

4.2 The amino acid serine

The amino acid serine is a polar proteinogenic amino acid, possessing a hydroxymethyl (CH_2OH) residual group. In the majority of cases, it is a non-essential amino acids for living organisms, since it can be synthesised in-vivo from other metabolites [58, 59]. Naturally the most biologically relevant enantiomer is S-serine, however its mirror image, R-serine, has been demonstrated to be involved in signalling processes within the human brain [60]. The chemical constitutions of serine in both its enantiomers are depicted in figure 4.2.

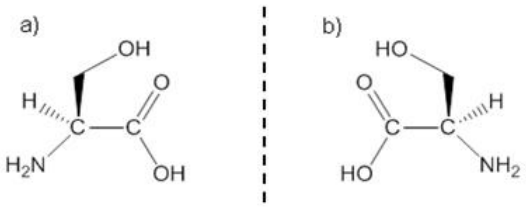

Figure 4.2: a,b) The amino acid serine in a neutral chemical state in its S- and R- configurations, respectively.

The amino acid studied in this work, serine, has been the object of different experimental works aiming at studying its possible role in the origin of the chiral homogeneity of life, due to its inclination to form clusters, made of eight homochiral units, in the gas phase [61, 62]. Racemic serine crystals have also been shown to possess enantiospecific recognition properties towards the occlusion of threonine molecules [63–65].

In the surface science context, serine has been studied on copper substrates with different symmetries and modifications [28, 46, 51, 66, 67]. S-serine has been shown to adopt a dehydrogenated chemical form on the Cu(001) surface and to prefer self-assembled organisation in dimers, stabilised by hydrogen bonds which see the involvement of the hydroxyl moiety [66]. The deprotonated form of serine has been proved to be present also on the intrinsically chiral Cu(531) [67] and Au-modified Cu(531) [51] surfaces, as well as on the Cu(110) surface [46], the same surface symmetry used in the present study. The latter work, carried out by Eralp and collaborators [46], consists of a multitechnique investigation on the properties of enantiopure and racemic serine adsorbed on Cu(110), performed by means of Scanning Tunneling Microscopy (STM), Low Energy Electron Diffraction (LEED), X-ray Photoelectron Spectroscopy (XPS), Near-Edge X-ray Absorption Fine Structure Spectroscopy (NEXAFS) and Temperature-Programmed Desorption (TPD). This paper has shown that serine molecules adsorb in their anionic dehydrogenated form. The adsorption geometry is characterised by a three-point interaction, with the amino group, via its nitrogen atom, and the deprotonated carboxylic group (carboxylate), via its two oxygen atoms, in direct contact with the interface. The side group β-OH moiety is not in contact with copper atoms, as confirmed by the XPS results, which allow to exclude the possibility of a four-point interaction with the surface. Furthermore, the NEXAFS data presented localise the orientation of the carboxylate group along the short-bridge site of the Cu(110) surface lattice, i.e. with the carboxylate (COO) plane roughly parallel to the [1-10] direction. The STM data presented [46] (figure 4.3a,b) clearly show that enantiopure serine molecules, when deposited on the Cu(110) surface, self-assemble into dimers, i.e. two molecules in close proximity, which represent the minimum repetitive motifs of a homochiral serine adlayer. The characteristic chiral expressions of this system, strictly dictated by the molecular handedness considered, are manifested in several aspects, namely in the orientation of the dimers, in the unit mesh of the overlayer (see LEED patterns in figure 4.3c,d) and in the shape of the molecular islands formed. A preferred structural model, characterised by the homochirality in footedness (figure 4.3e), has been proposed in view of the experimental results [46].

In the present work the problem of a rigorous determination of the most favoured structural models that represent the geometry adopted by enantiopure serine on Cu(110), is addressed. The behaviour of R-serine is studied in detail as a model system, being an exact mirror-image of the S-serine assembly. The possible positions of the R-serine

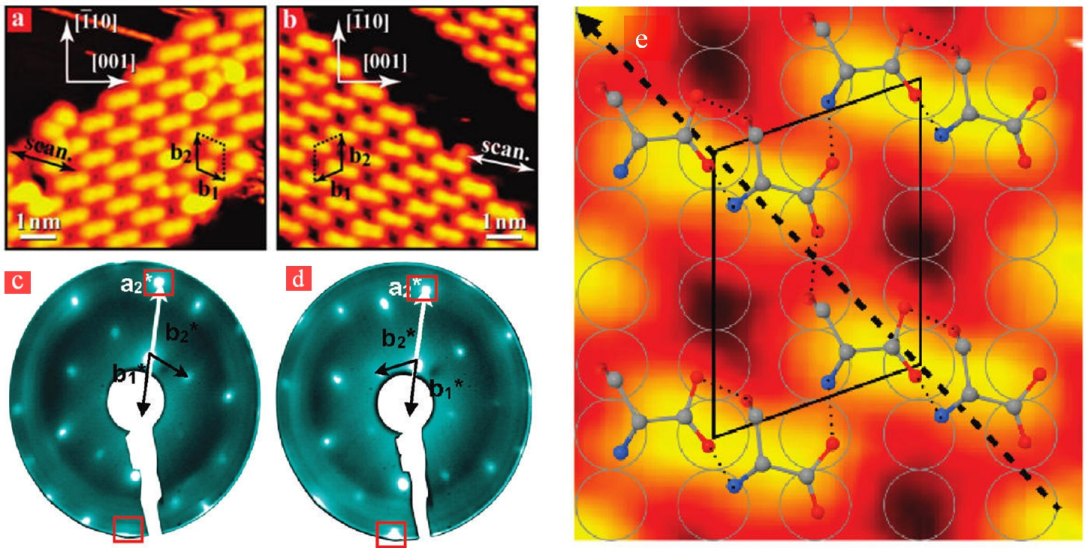

Figure 4.3: a,b) STM images of islands of S- and R-serine on Cu(110), respectively, after annealing to 370 K. Each single feature is attributed to a serine dimer. The mirror-image island elongations and unit cells are clearly visible. c,d) LEED patterns of saturated chemisorbed layers (0.25 ML) of S- and R-serine, respectively, annealed to 420 K. The substrate and overlayer vectors in reciprocal space are indicated. e) Structural model proposed for the adsorption of R-serine on Cu(110). The model is superimposed to an STM image. Possible H-bonds, unit cell and direction of elongation of molecular islands are indicated. All the images are adapted after reference [46].

molecules within the unit cell are discussed in terms of their footedness, taking into account the *carboxylate rule* [68], an interpretative key that allows some molecular positioning to be excluded on the basis of analogous systems previously studied. As a result of experimental characterisations via RAIRS and single-molecule resolution STM, supported with computational results, consisting of DFT calculations and STM simulations, two possible geometrical models are suggested, with a special focus on their possible distributions in footprint chirality. Finally, the inter-molecular hydrogen bonds that confer stability to these two possible structures are discussed.

4.3 Experimental results

4.3.1 RAIRS

The nature of the organic overlayer created as a result of the adsorption of single-handedness serine on Cu(110) is investigated through Reflection Absorption Infra-Red Spectroscopy (RAIRS). Figure 4.4 shows the time lapse spectra acquisition during the dosing of R-serine on top of a Cu(110) crystal. The increasing trend of peak intensities with time is clear during the deposition process. The spectrum in figure 4.4e is related to a saturated coverage.

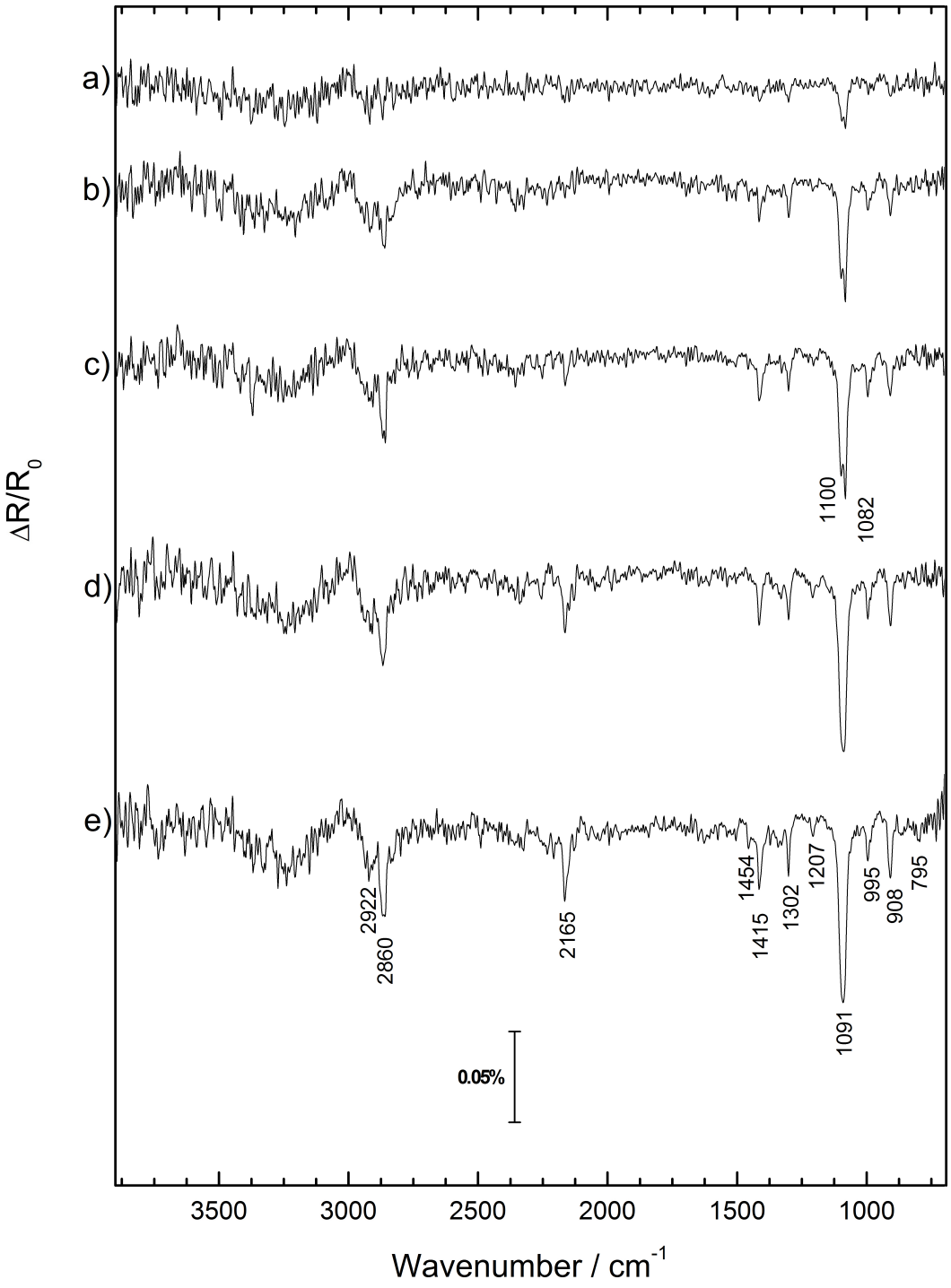

Figure 4.4: a-e)RAIRS spectra recorded upon adsorption of R-serine on Cu(110). The series of spectra (a-e) shows the increase of the relevant vibrational bands (see text and table 4.1 for details) until a monolayer coverage is reached (e).

The major observable peaks and their assignments with respect to specific molecular vibrations from which they originate are listed in table 4.1. One of the most significant vibrations is located at 1415 cm^{-1} and is caused by a symmetric stretching of the carboxylate group $\nu_s(OCO^-)$. This has previously been shown to be associated with the loss of hydrogen from the carboxylic group after the adsorption on the copper substrate [40]. In addition, the loss of a proton induces delocalisation of the double bond in the carbonyl (CO) group between the carbon and the two oxygen atoms of the carboxylate, therefore the carbonyl stretching mode (ν(CO) ~1700 cm^{-1}) does not appear in the spectra. The anionic form of the serine molecules (serinate) is confirmed by the presence of a peak at 1100 cm^{-1}, attributed to the amino $\omega(NH_2)$ wagging mode, with the simultaneous absence of a peak at $\sim$ 1660 cm^{-1}, that would be produced by a zwitterionic ammonium group (NH_3^+). The band present at 1207 cm^{-1} could be tentatively associated to a scissoring mode involving the COH group, since Jarmelo and co-workers have attributed an IR peak at 1209 cm^{-1} obtained from crystals of S-serine to this mode [69]. It is worth noting, finally, that the peaks associated with the ν_{as}(CCN) stretch (1082 cm^{-1}) and with the $\omega(NH_2)$ wag (1100 cm^{-1}) appear separated at low coverages (figure 4.4a-c), but become convoluted in one larger peak (1091 cm^{-1}) at coverages close to a monolayer (figure 4.4d-e). The origin of the band present at 2165 cm^{-1} is unknown and might be tentatively attributed to a cyanogen bond bearing contaminant or to adsorbed carbon monoxide. Alternatively, it could represent an overtone of the band at 1082 cm^{-1}. In conclusion, no coverage-dependent phase transitions are observed for R-serine on the Cu(110) surface. Instead, it has been suggested previously that a μ_3-μ_2 transition in the molecule-surface coordination takes place with increasing coverage, namely with one of the two oxygen atoms of the carboxylate group moving away from the substrate [28]. This geometry would have produced an IR absorption peak at $\sim$ 1625 cm^{-1}, corresponding to the $\nu_{as}(OCO^-)$ asymmetric stretch. This transition has been shown to occur with alanine [40] and glycine [30] on Cu(110).

Wavenumber (cm^{-1}) of observed band	**Molecular vibration**
2922	$\nu_{as}(CH_2)$ [30]
2860	$\nu_s(CH_2)$ [30]
2165	possibly ν(C≡O) or ν(C≡N) (contaminants)
1415	$\nu_s(OCO^-)$ [30, 40, 42]
1302	$\omega(CH_2)$ [30] or δ(CH)+$\nu_s(OCO^-)$ [40]
1207	δ(COH) [69]
1100	$\omega(NH_2)$ [30]
1082	ν_{as}(CCN) [40]
995	ν(COH) [70]
908	ν(CN) + $\delta_s(OCO^-)$ [40]
795	ν(CC) [30, 40]

Table 4.1: Assignments of the RAIRS observable peaks (figure 4.4) to the molecular vibrations from which they arise. These are based on previous literature of amino acid adsorption studies on Cu(110) [28, 30, 40, 42], on IR investigations of serine-copper chelates [70] and enantiopure serine crystals [69]. Keys for molecular vibrations: ν = stretch, δ = bend, ω = wag. The symmetric or asymmetric nature of the molecular vibration is denoted respectively with the subscripts $_s$ or $_{as}$.

4.3.2 LEED

The ordering of molecules at surfaces can be revealed by Low Energy Electron Diffraction (LEED), a technique that is sensitive to repetitive unit meshes on a surface. Figure 4.5 contains the diffraction patterns generated by a Cu(110) surface covered with serine in both its enantiopure forms. The LEED patterns for both R- and S-serine clearly give evidence of a long range chiral organisation. R-serine, when deposited on a Cu(110) surface, gives rise to the LEED pattern shown in figure 4.5a. In the reciprocal space, the R-serine overlayer vectors, $\mathbf{a_0^*}$ and $\mathbf{b_0^*}$, can be described in terms of the metal surface vectors, $\mathbf{a_S^*}$ and $\mathbf{b_S^*}$, in the following manner:

$$\mathbf{a_0^*} = \frac{1}{4}\mathbf{a_S^*} + \frac{1}{8}\mathbf{b_S^*} \ , \ \mathbf{b_0^*} = 0\mathbf{a_S^*} + \frac{1}{2}\mathbf{b_S^*} \tag{4.1}$$

In the matrix notation for reciprocal space, equations 4.1 can be summarised with the expression:

$$\begin{pmatrix}\mathbf{a_0^*}\\ \mathbf{b_0^*}\end{pmatrix} = \mathbf{G}^*\begin{pmatrix}\mathbf{a_S^*}\\ \mathbf{b_S^*}\end{pmatrix} \text{ , with } \mathbf{G}^* = \begin{pmatrix}\frac{1}{4} & \frac{1}{8}\\ 0 & \frac{1}{2}\end{pmatrix} \tag{4.2}$$

In order to adapt the expression 4.2 to the real space arrangement and determine the real space overlayer vectors, $\mathbf{a_0}$ and $\mathbf{b_0}$, in terms of the surface unit vectors, $\mathbf{a_S}$ and $\mathbf{b_S}$, it is necessary to calculate the inverse transposition of the matrix $\mathbf{G}^*$, since:

$$\begin{pmatrix}\mathbf{a_0}\\ \mathbf{b_0}\end{pmatrix} = \mathbf{G}\begin{pmatrix}\mathbf{a_S}\\ \mathbf{b_S}\end{pmatrix} \text{ , with } \mathbf{G} = \left[(\mathbf{G}^*)^{-1}\right]^t \tag{4.3}$$

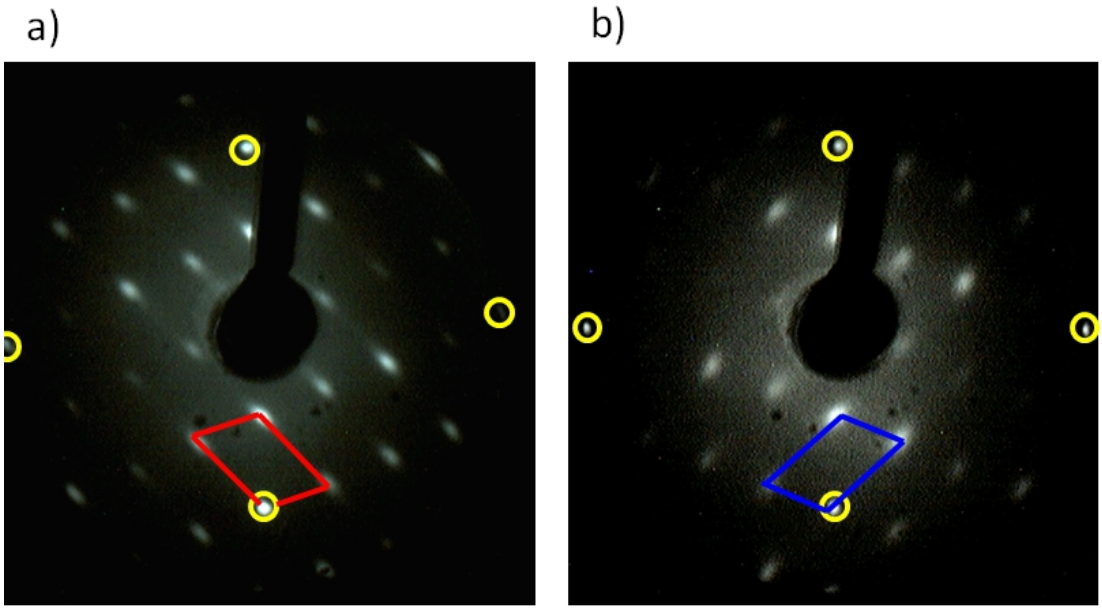

Figure 4.5: a) LEED pattern for R-serine on Cu(110). Energy = 41 eV. b) LEED pattern for S-serine on Cu(110). Energy = 42 eV. Both samples are annealed to 373 K. The unit cells in the reciprocal space are indicated with parallelograms. The visible Cu(110) primary spots are circled in yellow.

Therefore, the real space matrix that expresses the R-serine vectors in terms of the Cu(110) substrate vectors is found to be the following (see figure 4.6 for a schematic representation of the vectors in real and reciprocal spaces):

$$\mathbf{G} = \begin{pmatrix} 4 & 0 \\ -1 & 2 \end{pmatrix}, \text{ i.e. } \mathbf{a_0} = 4\mathbf{a_S} + 0\mathbf{b_S} \ , \ \mathbf{b_0} = -1\mathbf{a_S} + 2\mathbf{b_S} \tag{4.4}$$

Regarding the diffraction pattern generated by S-serine on Cu(110) (figure 4.5b), analogous calculations can be made, resulting in the following matrices, $\mathbf{G}^*$ and $\mathbf{G}$, that relate the unit vectors belonging to the adsorbate structure with the ones pertaining to the surface in the reciprocal and in the real space, respectively.

$$\mathbf{G}^* = \begin{pmatrix} 0 & -\frac{1}{2} \\ \frac{1}{4} & \frac{1}{8} \end{pmatrix} \tag{4.5}$$

$$\mathbf{G} = \begin{pmatrix} 1 & 2 \\ -4 & 0 \end{pmatrix} \tag{4.6}$$

These results are consistent with previous findings [28, 46] (see figure 4.3c-d) and highlight the chiral nature of the two dimensional arrangements that arise upon the adsorption of either of the enantiomers of the amino acid serine on the Cu(110) surface. In particular, the [1-10] direction represents the axis by which the two unit cells can be superimposed by a simple out-of-plane reflection. To make this more evident to the reader, the unit cells of R- and S-serine in the real space are sketched in figure 4.7.

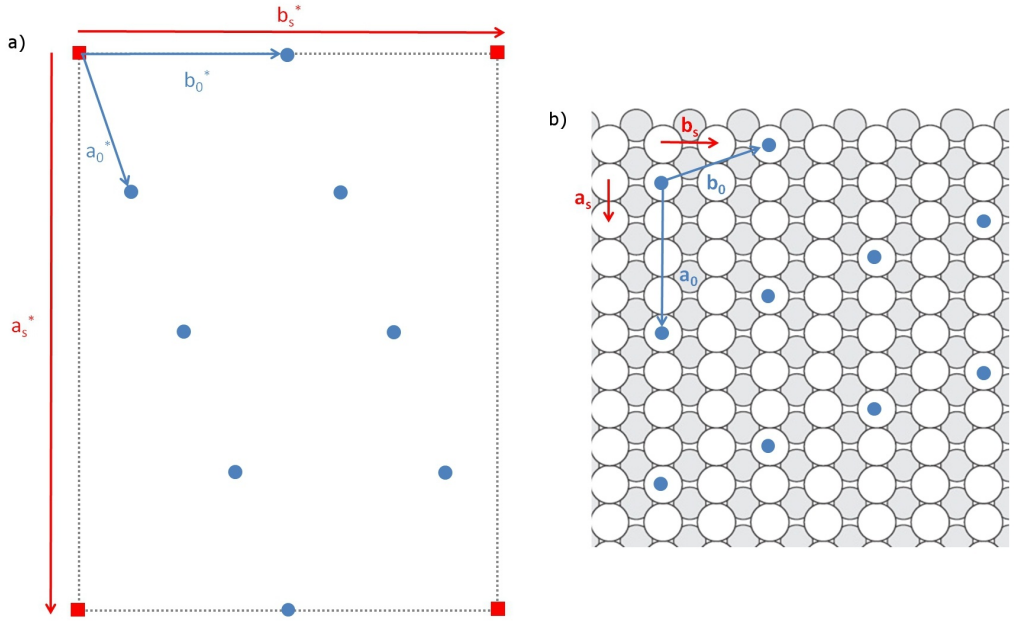

Figure 4.6: Schematic depiction of the LEED pattern for R-serine on Cu(110), from figure 4.5a. The substrate spots are represented with red squares and the overlayer spots with blue circles. b) The substrate and overlayer real space vectors with the same colour code. The choice of the vector for the matricial expression of the overlayer in terms of the Cu(110) surface parameters (expression 4.4) has been made in accordance with the International Tables for Crystallography Conventions [28, 71].

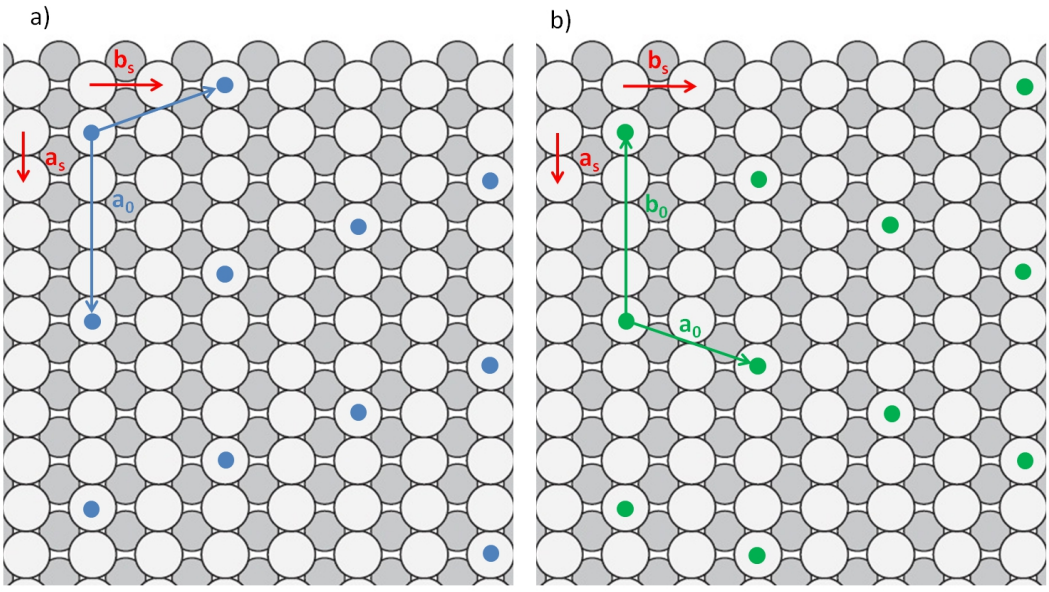

Figure 4.7: a) Unit cell of R-serine (4 0,-1 2) on Cu(110). b) Unit cell (1 2,-4 0) of S-serine on Cu(110). The direction and the magnitude of the vectors are deduced from LEED. The substrate ($\mathbf{a_S}$ and $\mathbf{b_S}$) and the adsorbate ($\mathbf{a_0}$ and $\mathbf{b_0}$) vectors are named according to the standard rules for the matrix notation of surface crystallography [28, 71].

4.3.3 STM

New insights into the chiral manifestations of the serine/Cu(110) system are provided by the direct visualisation of its real space arrangement by means of STM. In figures 4.8a,b typical STM images representing R-serine and S-serine islands on Cu(110), respectively, are shown. The islands possess a preferred direction of elongation, indicated by the vectors W_R and W_S, the unit cells of R- and S-serine are described by the matrices (4 0,-1 2) and (1 2,-4 0), respectively, while the smallest observable features possess an oval shape with their main axis forming an angle of $\sim \pm 20°$ with respect to the [001] surface direction. The elongation of the molecular islands, the unit cells and the orientation of the oval features in the STM images are aligned along non-symmetric surface directions and possess chiral characteristics in two dimensions, which depend strictly on the molecular chirality of the adsorbed serine molecules. These results are in agreement with the work published by Eralp and co-workers (see figure 4.3a,c) [46]. In this chapter the details of the self-assembly of R-serine on Cu(110) are investigated. The properties of S-serine on the same surface can be thus inferred by reflecting the structure of R-serine, since the two enantiomers give rise to mirroring molecular organisations.

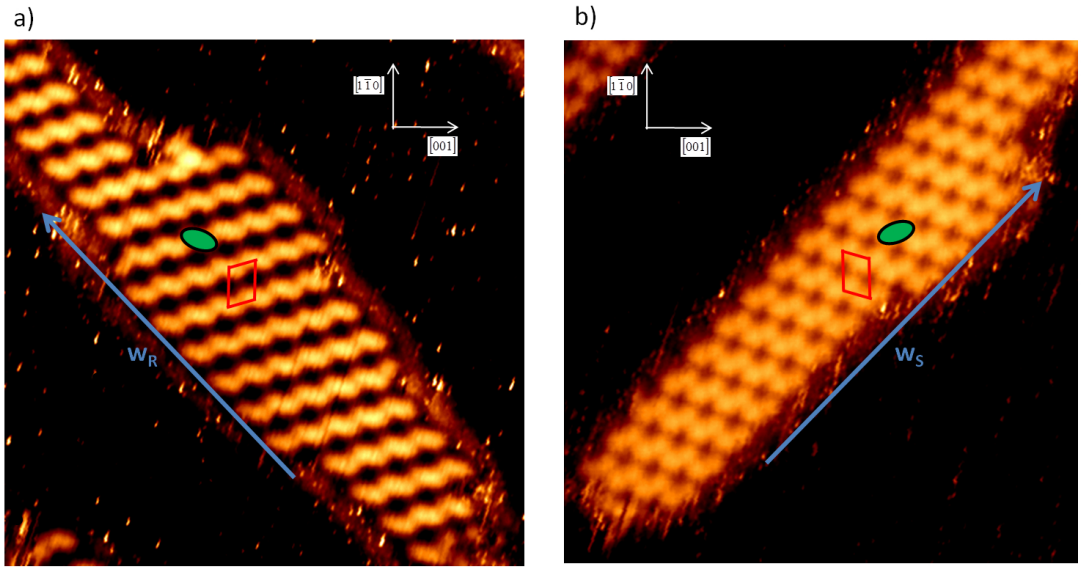

Figure 4.8: a) R-serine island on Cu(110). 14.24x14.41 nm^2,V=-831.0 mV, I=-0.100 nA. b) S-serine island on Cu(110). 14.09x14.33 nm^2, V=-670.5 mV, I=-0.110 nA. In each image, a serine dimer is highlighted with a green oval and the unit cell with a red parallelogram. The directions of elongation of the islands are represented with the vectors W_R and W_S for R- and S-serine, respectively.

The most common type of imaging that is obtained with STM is the one reproduced in figures 4.9a,b, with features possessing elliptical shapes. In figure 4.9a the growth of R-serine islands on Cu(110) is depicted, with the island elongation vector indicated with W_R, which points along the (-3,-2) surface direction. Figure 4.9b shows a close-up image of an R-serine island, with the indication of the unit cell and the STM appearance of a

R-serine dimer. It is worth noting that the term dimer used here does not involve any implications in terms of chemical reactions that may have taken place between different adsorbed molecules, but refers solely to the geometrical closeness of two molecules that give rise to the formation of apparent single features in typical STM images. This phenomenon is possibly caused by the distribution of electron densities in this specific system. Thus, every unit cell is filled with two R-serine molecules that are, in general terms, non-equivalent and represent the asymmetric unit to which it is possible to apply the overlayer vectors in order to describe the entire surface. In general, the study of the geometry of molecules adsorbed at a given surface by means of STM is extremely challenging, due to the intrinsically low sensitivity that STM possesses towards the chemical information of a given sample. This is especially true when molecules have small dimensions, as in the case of amino acids. In this respect, the level of resolution visible in the images of figures 4.8 and 4.9 does not provide sufficient information to establish the structure of a serine dimer, its intra-dimer and inter-dimer interactions.

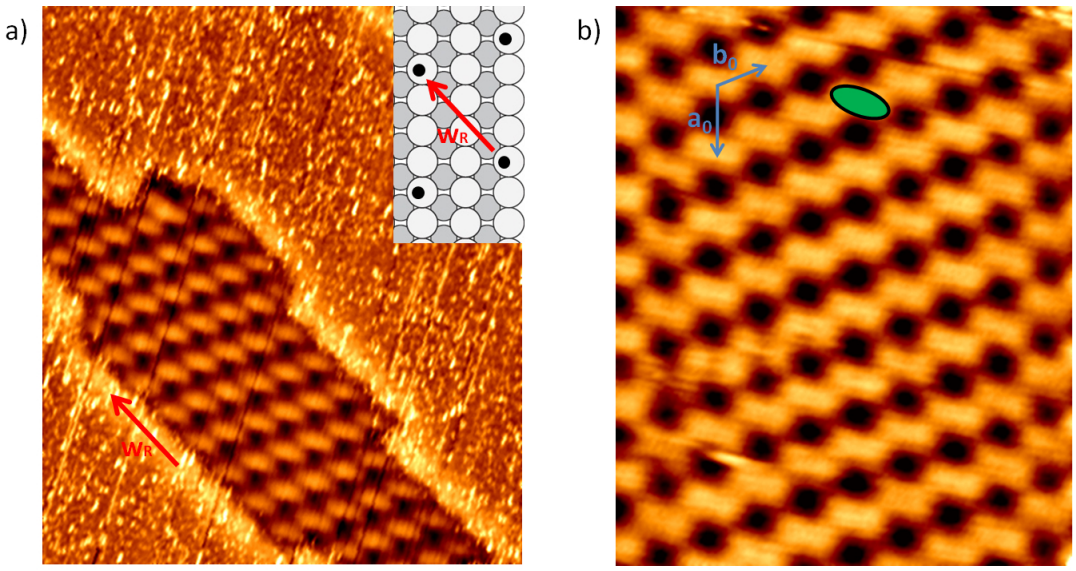

Figure 4.9: a) As deposited R-serine island on Cu(110). 12.04x14.00 nm^2,V=-781.5 mV, I=-0.160 nA. The main direction of elongation of the island, W_R, is indicated. Insight: direction of W_R respect to the Cu(110) surface. b) Internal part of an R-serine island on Cu(110). 6.90x8.50 nm^2,V=-700.0 mV, I=-0.100 nA, with indication of the unit cell and a dimer.

Nevertheless, further steps towards understanding the positions of individual R-serine dimers in the unit cell can be made by exploiting particular experimental conditions that allow the resolution of single molecules. The crucial parameters in this step are represented by the lateral resolution of the scanning probe, which is usually difficult to control, and the tunnelling conditions (i.e. bias voltage and tunneling current) that can be set for a certain experiment. Moreover, additional events affecting the imaging may occur occasionally. In the STM image of figure 4.10, for instance, although the

tunneling parameters are kept at constant values during the scanning of the area, an evident alteration in the type of imaging takes place: this is due to a local modification of the electronic states of the tip, possibly associated with a physical change in the tip termination, such as a different shape or functionalisation with a different atom or molecule. In this case the *tip change* happens to favour a better lateral resolution that permits the visualisation of blunt shapes of single R-serine molecules in place of the usual unresolved dimers. In figure 4.10 the appearance of two serine dimers, one prior and one subsequent to the tip change, are highlighted. The different orientations with the respect to the surface of the features associated to a serine dimer in the two different imaging modes are appreciated.

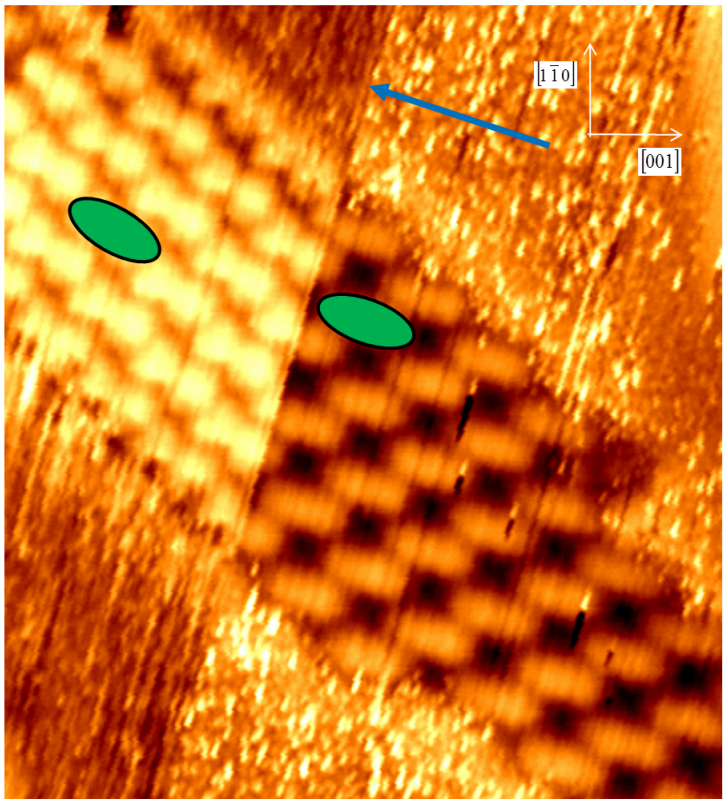

Figure 4.10: a) R-serine island on Cu(110). 8.40x9.30 nm^2, V=-860.0 mV, I=-0.120 nA. The image features a spontaneous tip change during an STM scan. The blue arrow represents the vector normal to the scan direction. After the tip modification, some details of the individual R-serine molecules composing a dimer are observable. The two green ovals indicate the different imaging modes of a serine dimer, with different apparent orientations. Also, a different imaging of the Cu(110) substrate is evident after the tip modification.

A further change in the tunneling settings provides us with diverse kinds of imaging modes, in which some additional details can be appreciated. The area represented in figure 4.11 has been scanned repeatedly varying the applied bias voltage and the tunneling current. All the images displayed in figure 4.11 present a resolution that allows the apparent visualisation of single R-serine molecules instead of the standard R-serine

dimers. In each image, green ovals highlight the STM appearance of a R-serine dimer. A common characteristic belonging to the images portrayed in figure 4.11 consists in the internal symmetry within an R-serine dimer. In fact, the intensities originating from the two R-serine molecules seem to possess an internal rotational symmetry, i.e. they seem to be superimposable with an in-plane rotation of 180°. This aspect is particularly evident in the images of figure 4.11c,d, is less clear in the image in figure 4.11e, but is loosely present in all the STM images displayed. This phenomenon might provide hints and suggestions about the actual molecular geometry of the single molecules composing a dimer, however it is stressed that this procedure is not valid generally, especially in the case of small adsorbed molecules, since it is not typically known which part of the molecule produces the highest intensity in STM images collected with given tunneling conditions. For this reason, theoretical calculations are essential (see section 4.5).

Additional STM images presenting a clear single molecule resolution are depicted in figure 4.12. These are obtained with a sample that has undergone a post-deposition annealing process up to a temperature of 383 K. It has been shown that such a procedure does not induce any phase change in the enantiopure serine structure, as long as the thermal treatment does not exceed 420 K [46]. Although in these images the single serine molecules hardly show any internal structure, there is a clear distinction between the intensities generated by the two inequivalent molecules in a dimer (labelled with 1 and 2 in figure 4.12). A dimer for each STM image is highlighted with a green oval. In other words, the two R-serine molecules appear clearly separated, thus adding information on the positions of the single molecules in the unit cell. With regards to the STM intensities originated from the two molecules positioned in the non-equivalent sites 1 and 2, no appreciable asymmetries are detected (see the line profiles in figure 4.12c,d). Establishing the distribution of STM intensities within the R-serine unit cell represents the starting point towards the comprehension of the molecular and atomic positioning.

In summary, with the variation of the tunneling conditions, R-serine molecules manifest themselves in many different imaging modes, which are not a trivial representation of the actual geometry, and thus are not conclusive in terms of a thorough understanding of the adsorption geometry. For this objective supporting theoretical calculations are required. These, based on Density Functional Theory (DFT), are commonly able to identify which part of molecule gives the highest signal, once the tunneling conditions are known. The selection criteria of adsorption geometries that have been the subject of the theoretical calculations are outlined in the following section.

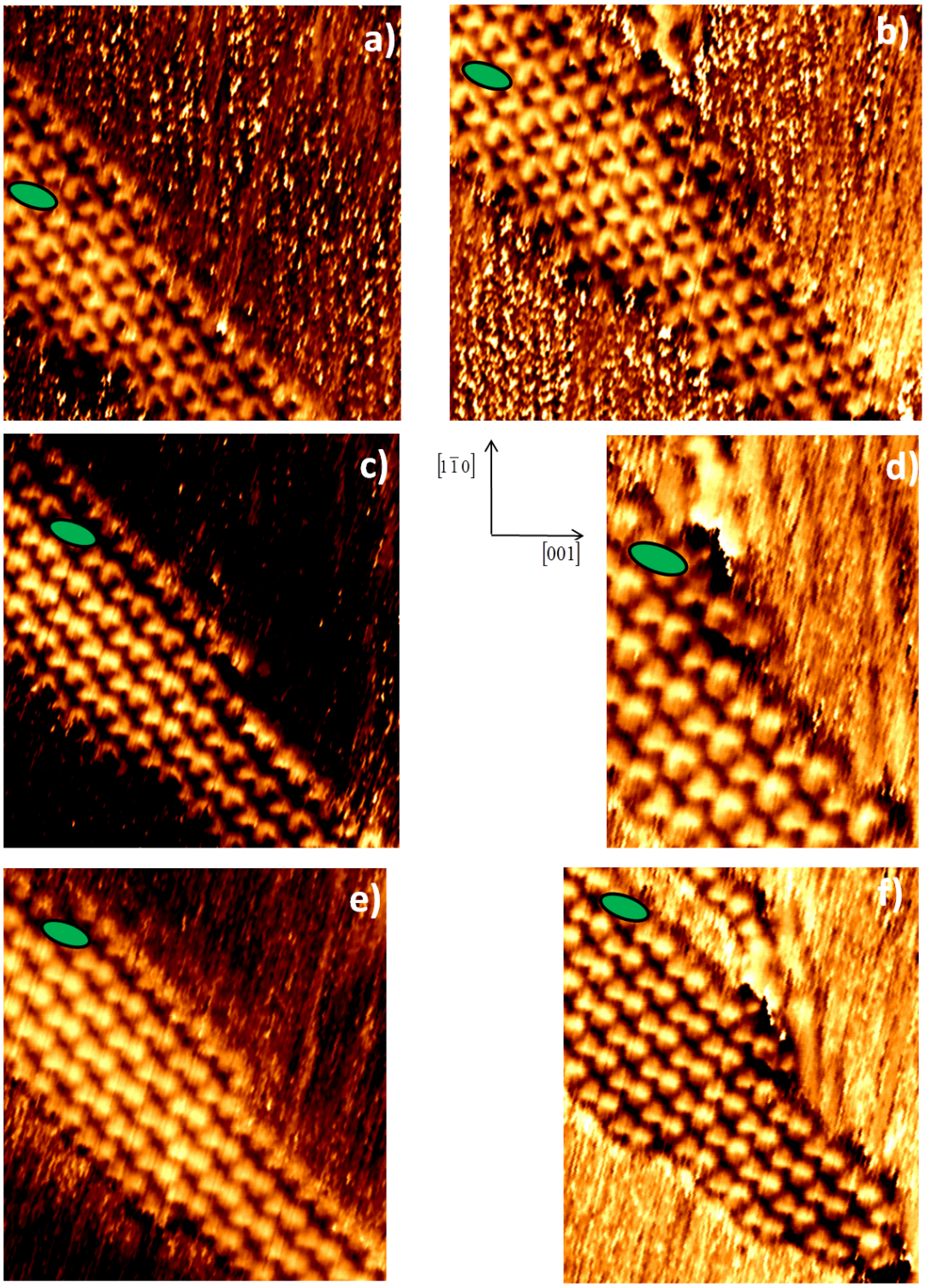

Figure 4.11: a-f) As-deposited R-serine island scanned with different tunneling conditions. Green ovals are placed in correspondence of a R-serine dimer in each image. a) 8.81x9.20 nm^2, V=-691.2 mV, I=-0.330 nA. b) 9.92x8.75 nm^2, V=-557.5 mV, I=-0.180 nA. c) 9.02x9.43 nm^2, V=-860.0 mV, I=-0.150 nA. d) 5.03x6.66 nm^2, V=-196.2 mV, I=-0.140 nA. e) 8.83x9.53 nm^2, V=-806.0 mV, I=-0.120 nA. f) 8.09x9.47 nm^2, V=-275.3 mV, I=-0.110 nA.

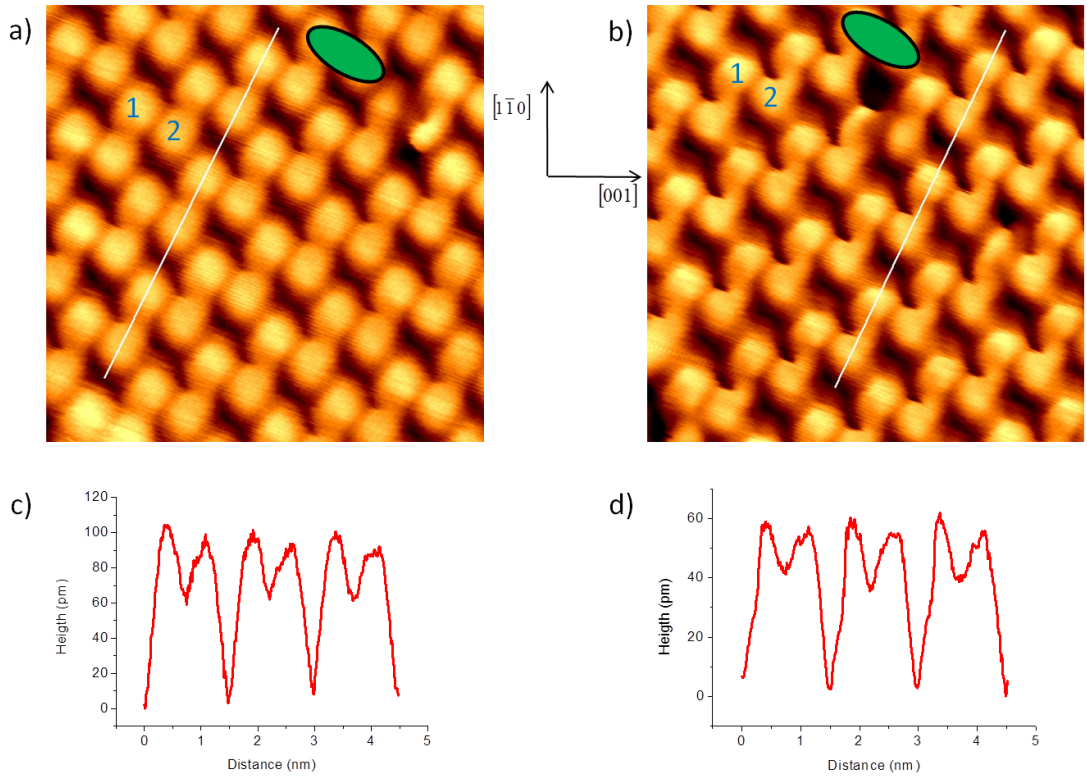

Figure 4.12: a-b) Insights of an R-serine monolayer obtained using two different tunneling settings. The sample has been prepared via deposition in vacuum (multilayer) and subsequent annealing process up to 383 K, which has induced the desorption of the outermost molecular layers. The STM intensities arising from each R-serine molecule are clearly distinguishable. In both images two R-serine dimers are indicated with green ovals. a) 5.0x5.0 nm^2, V=+1250.0 mV, I=+0.440 nA. b) 5.0x5.0 nm^2, V=+1030.3 mV, I=+0.420 nA. c-d) Profiles measured along the lines indicated in a) and b), respectively.

4.4 Structural models

Since there are numerous possibilities to locate two R-serine molecules in a unit cell, it is necessary to identify those geometrical models that are compatible with the results of this work and previous works on analogous systems. In particular, those models that manifest an obviously unfavourable atomic distribution, e.g. two repulsive moieties in close proximity, are discarded, while the remaining are kept as the basis for calculations with DFT. The adsorption of amino acids on Cu(110) is a well-studied area, and comprehensive models have been proposed, for example, for proline [8, 16, 42, 43, 45, 47, 49], alanine [27, 33, 36–40] and glycine [17, 30–32, 34, 35, 41, 50, 57]. The following discussion is mainly based on the finding that the carboxylate group in contact with the copper surface (figure 4.1) lies along the short-bridge Cu(110) site, with the two oxygen atoms bonded to two consecutive copper atoms along the [1-10] direction. This type of adsorption geometry has been shown, for extended 2D structures [47, 68], to induce a significant surface stress, caused by the copper atom relaxations away from the bulk positions in response to the carboxylate bonding. For this reason adsorbed carboxylate groups occupying adjacent positions in both of the high symmetry surface directions are unfavoured, and therefore such structures are not taken into account (figure 4.13a). This assumption is termed the *carboxylate rule* [68].

For simplicity, in figure 4.13 the carboxylate double contact with the Cu(110) surface is represented through two red circles, representing the oxygen atoms involved in adsorption, connected with black lines . Taking into account the unit cell that R-serine forms on Cu(110), it is possible to find only two ways in which the carboxylate backbones can be placed (figure 4.13b,c). However, given that a (110) surface possesses a two-fold symmetry, it is clear that the two structures in figure 4.13b and 4.13c are superimposable via a simple rotation of 180° and thus are totally equivalent. Thus, in the carboxylate rule assumption, there is only one manner in which the carboxylate scaffolds can be placed in an R-serine/Cu(110) unit cell (figure 4.13b), since a different positioning of the central carboxylate (position 2) would either not satisfy this hypothesis or would represent a redundancy. For this reason the sole carboxylate scaffold of figure 4.13b is taken into account and represents the starting point for building all the geometric models compatible with the R-serine unit cell. This restriction limits the number of plausible geometries to be considered. In order to proceed towards finding all the potential structures, a further consideration has been made. Particularly, any situation where a surface atom is simultaneously bonded to two different serine molecules has been excluded.

As it is suggested from STM results (figure 4.12), the unit cell is filled with two inequivalent R-serine molecules, i.e. the molecules whose carboxylate scaffold is indicated with the number 1 in figure 4.13b will be totally equivalent in terms of adsorption geometry and footedness, while molecule 2 possesses characteristics that are independ-

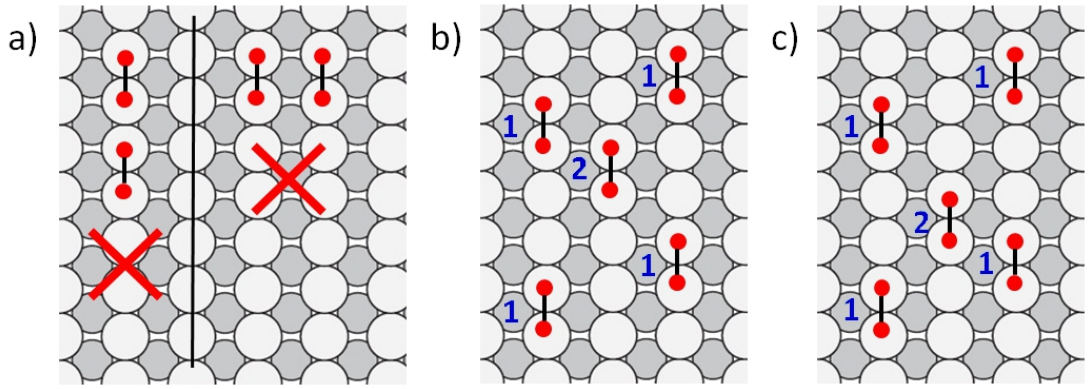

Figure 4.13: a) Representation of the disallowed positions for the carboxylate scaffolds along the Cu(110) high symmetry directions (carboxylate rule [68], see text for details). b-c) The two carboxylate backbones that can be formed in an R-serine unit cell in the carboxylate rule hypothesis. Equal numbers indicate equivalent molecules. The two scaffolds are rotamers.

ent from the adsorption geometry of molecule 1. The different models are constructed placing all the possible combinations of footprints, including the two possible rotamers for each footprint chirality, in the positions 1 and 2. This essentially consists in placing the nitrogen atom next to each carboxylate scaffold of figure 4.13b, in order to reproduce all the possible footednesses for the two inequivalent molecules forming a dimer. In position 1 it is possible to have two lambda rotamers (figures 4.14A and 4.14B), but just one rotamer with a delta footprint (figure 4.14C), since the other delta conformer would have its nitrogen atom coordinated with a substrate copper atom that is already participating in binding with an oxygen atom. In figure 4.14, a different colour code is used to represent the molecules in position 1: in order to highlight the footprint chirality, lambda and delta molecules are represented with red and blue triangles, respectively.

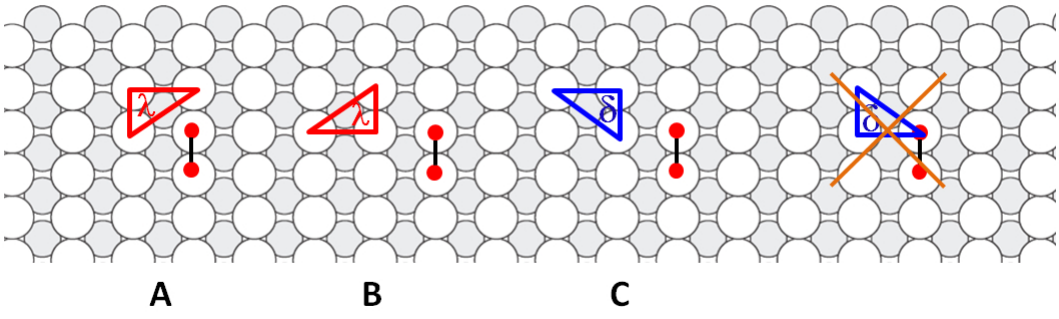

Figure 4.14: The possible footprints that an R-serine molecule in position 1 can adopt. The footprint chirality is rendered with the following colour code: red triangles for λ and blue triangles for δ. The carboxylate backbone in position 2 is still represented by two circles connected with a line, as in figure 4.13. Each of the possible conformers is denoted with the letters A,B and C.

In order to produce a dimer, these three possibilities for position 1 (figure 4.14) have to be combined with all the possibilities in which an R-serine molecule can sit in position 2: these are shown in figure 4.15. Once again, it is noticeable that one combination where molecule 2 possesses a right-footed adsorption geometry (figure 4.15) is forbidden, while the other three options are all theoretically possible.

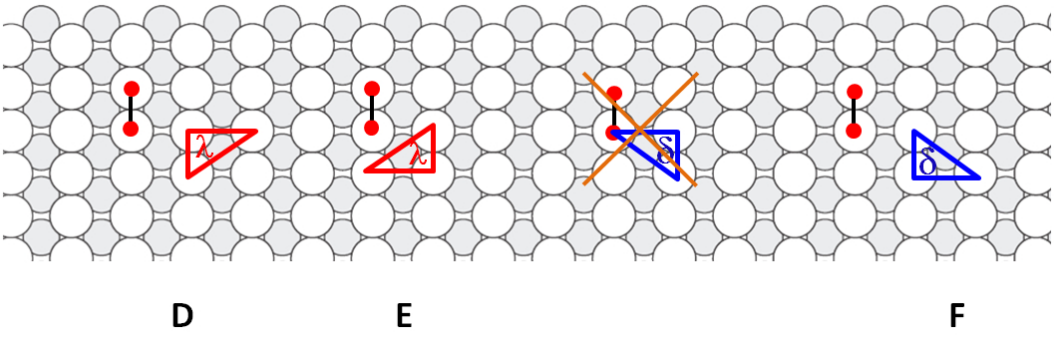

Figure 4.15: a-d) The possible adsorption footprints that an R-serine molecule in position 2 can take up. The footprint chirality is rendered with the following colour code: red triangles for λ and blue triangles for δ. The carboxylate backbone in position 1 is schematically represented by two circles connected with a line, as in figures 4.13 and 4.14. Each of the possible conformers is denoted with the letters D, E and F.

The multiplication of the three conformations of position 1 by the three conformations of position 2 gives rise to nine different potential structures that are displayed in figure 4.16. The resulting nine geometries (figure 4.16) are not all inequivalent, and this becomes clear when the entire structures are drawn. In figure 4.17 each structure is visualised with eight R-serine molecules, with the relevant dimers positioned at each vertex of the unit cell: from this we can deduce the structures with equivalent unit cells. Particularly it is noticeable that some unit cells are simply rotational conformers of each other. Namely, the structures in figure 4.17a and 4.17e are totally superimposable through a 180° rotation, as are the structures in figure 4.17c and 4.17h, as well as those in figure 4.17f and 4.17g. Only one of the geometries of these pairs of rotamers is thus taken into account.

After having considered the geometrical possibilities in terms of the footprint combinations, we are left with six different structures, which are depicted in figure 4.18 with the usual triangles representing the molecular atoms in contact with the surface. Note that all geometries are renamed with Roman numerals from 1(I) to 6(VI), and will be referred to in this manner in the following discussion. In figure 4.18 the molecular footedness is denoted by the letters λ and δ that are located next to each molecule composing a dimer. Evidently, each model features unique characteristics in terms of chirality of the footprint and of the intra-dimer molecular positioning. Footprint-wise, there are three non equivalent homochiral λ-λ structures (figures 4.18a,b,d), one δ-

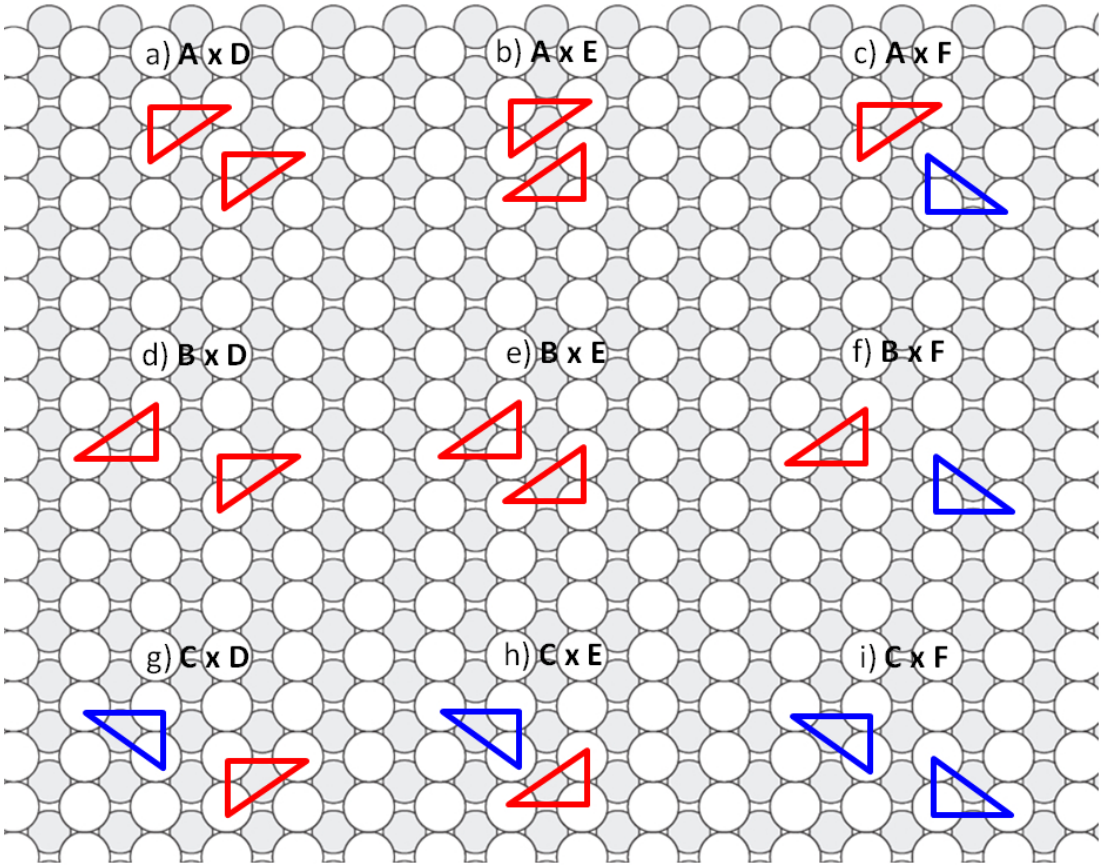

Figure 4.16: a-i) The nine dimeric structures that are obtainable by multiplying the three operations describing the molecule in position 1 by the three related to the molecule in position 2. Each resulting dimer is labelled with the operations applied (see figures 4.14 and 4.15).

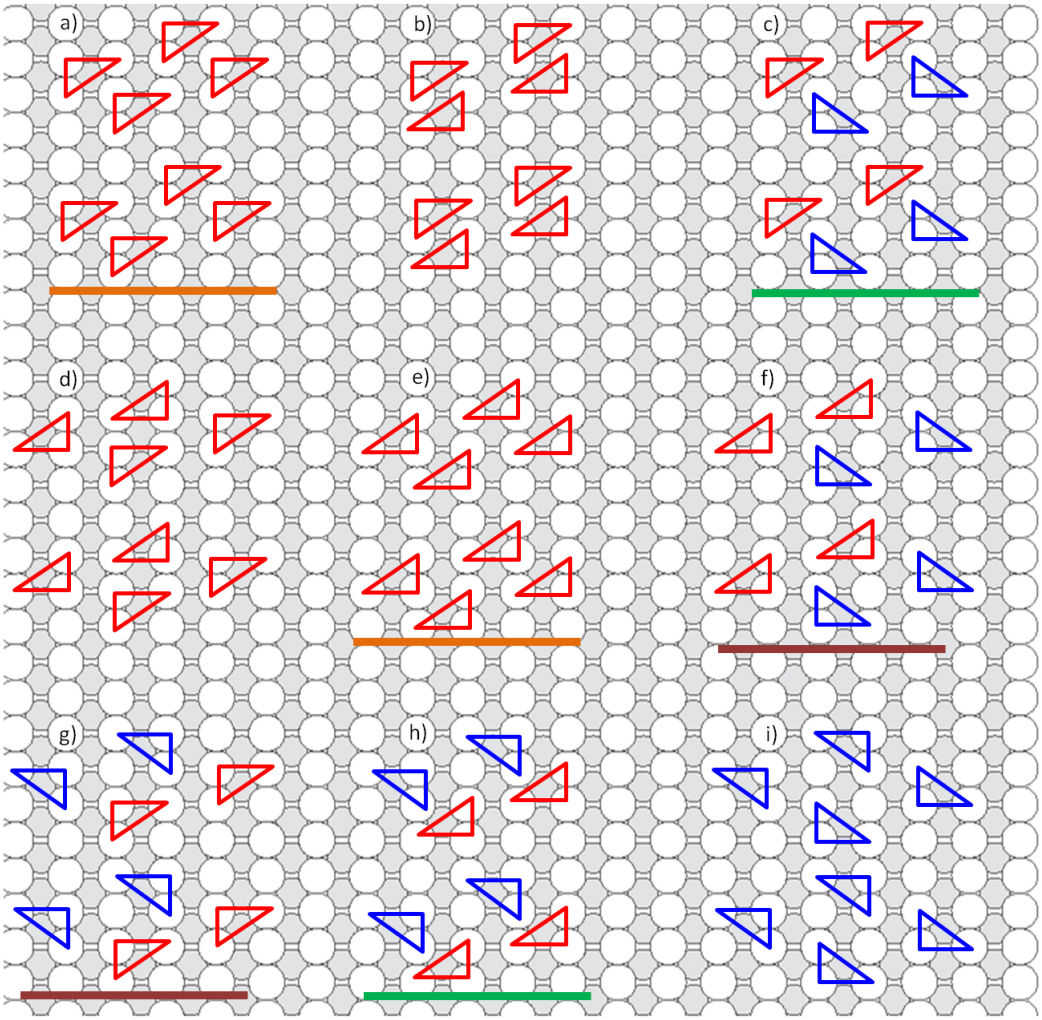

Figure 4.17: a-i) The nine structures of figure 4.16 placed in a R-serine/Cu(110) unit cell. In this manner repetitions are visible. In particular, a,e) represent the same geometry since they are rotamers. The same consideration applies for the couples c,h) and f,g). The rotameric structures are underlined with lines of the same colour. For these reasons, only six of the nine structures are unique. These are displayed in figure 4.18.

δ structure (figure 4.18f) and two heterochiral λ-δ structures (figures 4.18c,e). This asymmetry in the number of homochiral models can be explained in terms of the chirality that the unit cell possesses, which intrinsically forbids some specific geometries, especially when both molecules assume a right-footed conformation. The six structural models portrayed in figure 4.18 are in theory all possible, and have been the object of theoretical calculations via relaxation through DFT, aiming at determining which of them are the most energetically favoured. Furthermore, for each structure, STM simulations have been performed, in order to establish which parts of an R-serine molecule is responsible for a higher intensity in an STM experiment at certain tunneling conditions, and, more importantly, which structure better reproduces the experimental STM results. The combination of these tools is able to provide us with a restricted number of models, which, ideally, will help to illuminate the molecular geometry on the Cu(110) surface.

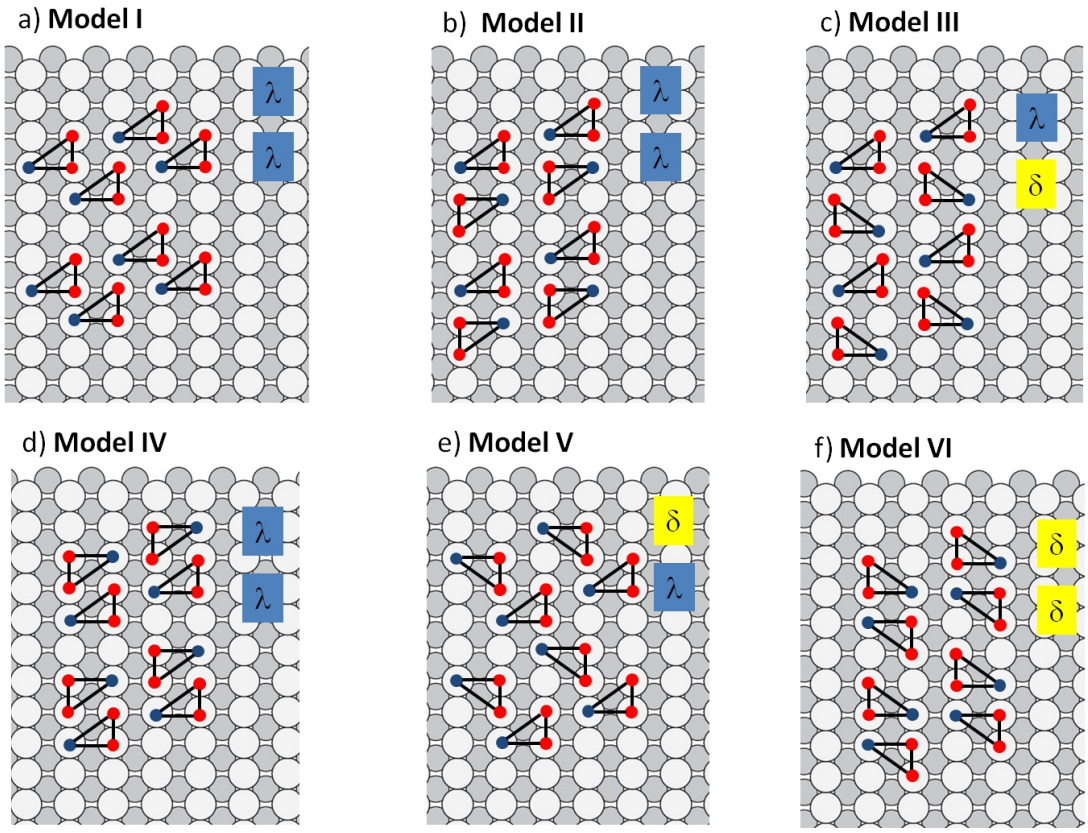

Figure 4.18: a-f) The final six models for the adsorption geometry of R-serine on Cu(110). The red and blue spots represent the molecular atoms in contact with the surface, i.e. the carboxylate oxygen atoms and the amino nitrogen atoms, respectively. The footedness of the two inequivalent molecules in each model is also indicated with the symbols λ and δ.

4.5 DFT calculations

The six different models proposed in figure 4.18 have been the subjects of theoretical calculations aimed at determining their minimum energy in their relaxed state. The calculations have been carried out by our collaborators at the Fritz-Haber-Institut der Max-Planck-Gesellschaf in Berlin, Germany. These calculations have been carried out using density functional theory (DFT) with corrections for Van der Waals interactions and Coulomb screening effects in the bulk. For the details of the theoretical calculations see section 4.7.

4.5.1 Single conformers

First of all, the energy pertaining to an adsorbed R-serine molecule, in its two footprint geometries, is calculated. The final energies after DFT relaxation are equal to -19.3956 eV and -19.3960 eV for the λ and δ conformers, respectively (figure 4.19). The difference between these two values, less than 1 meV, is minuscule and not significant, thus a preference towards either of the two footprint chiralities cannot be deduced from the calculation of a single adsorption event of an enantiopure serine molecule on Cu(110). The final molecular geometries, depicted in figure 4.19, show that in the δ conformer the OH moiety represents the highest point of the molecule, while in the mirror-image footprint the molecule appears more planar, with the hydroxyl group placed at 4Å away from the outermost copper layer. In any case, a four-point coordination (μ_4) involving the hydroxy-terminated residual group seems to be energetically unfavoured.

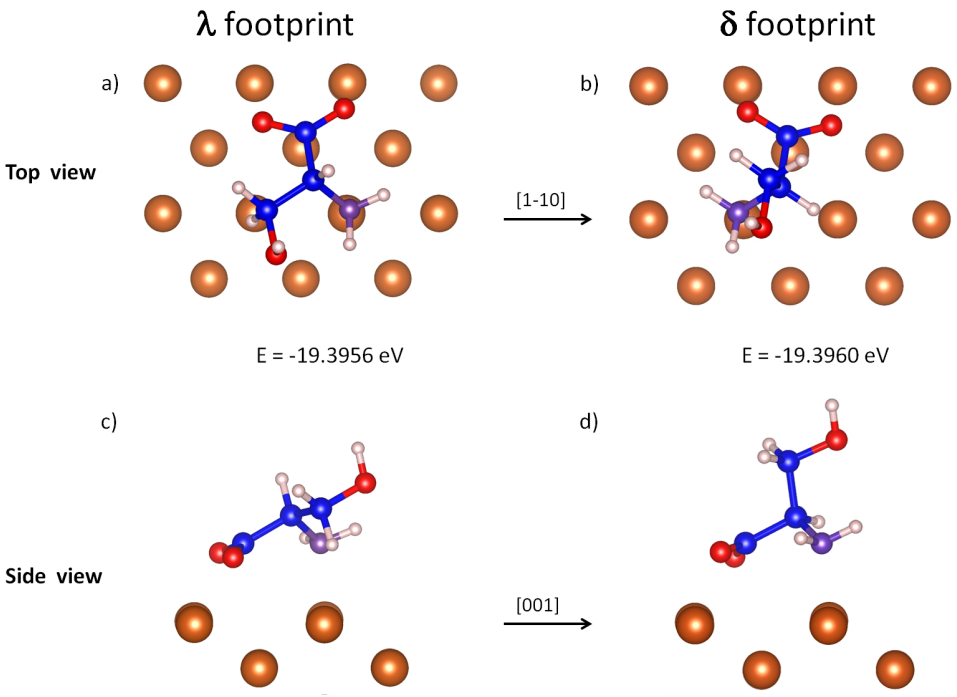

Figure 4.19: a-d) Molecular geometries after DFT relaxation of λ and δ conformers of R-serine on Cu(110). Top- and side-views geometries are placed as labelled in the figure. The calculated energies for each conformer are indicated. Colour code: brown = copper, red = oxygen, blue = carbon, purple = nitrogen, white = hydrogen.

4.5.2 Extended structures

Subsequently, DFT calculations have been performed on extended structures of R-serine adlayers composed of 8 dimers. The starting models that have been the objects of the DFT studies are those displayed in figure 4.18. The resulting minimum adsorption energies are displayed in table 4.2. The energetic values refer to a serine dimer after the DFT relaxation of the structures. It is noteworthy that structure IV shows a spatial rearrangement. This behaviour leads to a final structure that looks equivalent to structure III in terms of its footprint (not shown). As a consequence, we can disregard the starting geometry IV, since it does not show stability over the time of a DFT relaxation. All the other five geometries converge to a stable configuration. The structures possessing a lower energy are structure II and structure III. Their difference in energy, equal to 58 meV per dimer, is comparable with the thermal energy at room temperature, and, in addition, the accuracy of DFT calculations has to be taken into account. For these reasons, a discrimination between structure II and structure III cannot be proposed solely on the basis of DFT energies, while the remaining structures (I,V and VI) can be excluded on the basis of their final energies.

Model	**Energy (eV)**
I	-3.534
II	-4.030
III	-4.088
IV	unstable[1]
V	-3.500
VI	-3.860

Table 4.2: The minimum energies per R-serine dimer of the six structures displayed in figure 4.18. The energy values refer to an R-serine dimer.

Models II and III feature different properties in terms of footedness. In the former, two λ conformers, superimposable on each other via a 180° in-plane rotation, are present in the unit cell, whereas in model III the R-serine dimers are heterochiral in footprint (figures 4.18b,c). The DFT-relaxed structures II and III are displayed in figures 4.20a and 4.20b, respectively. In structure II, intra-dimer hydrogen bonds take place between the hydroxyl moieties (OH–O) of the molecules (letter A in figure 4.20a), placed at a distance of 1.710 Å. Inter-dimer hydrogen bonds appear to be established between the double mutual interactions of carboxylate oxygens and amine hydrogens (letters B and C in figure 4.20a) at distances of 1.765 Å and 1.780 Å, respectively. This double interaction is facilitated by the fact that the two molecules are rotamers in terms of footprint. Additional possible double inter-dimer interactions might be established

[1]The structure IV moves during the DFT relaxation and is converted into a geometry similar to that of structure III. This change in geometry is lead by the steric hindrance due to the starting closeness of two serine molecules in a dimer (figure 4.18d). As a consequence, this structure is disregarded.

between a carboxylate oxygen and a methyl hydrogen (letters D and E in figure 4.20a). In the latter cases, however, the distances between the involved atoms, equal to 3.313 Å and 3.278 Å, respectively, are high, and it is unlikely that these interactions contribute significantly to the stabilisation of the molecular adlayer. It is reminded that intermolecular hydrogen bonds are discussed because they are thought to be responsible for the overall stabilisation of amino acid overlayers [42]. In this case, a directionality of the hydrogen bond-mediated interactions might represent the cause of the direction of growth and elongation of R-serine islands on Cu(110), which is indicated with the arrow (W_R) in figure 4.20. It has been observed previously that the formation of strong hydrogen bonds, i.e. bonds established between two atoms placed less that 2.2 Å apart [72], governs the direction of elongation of the molecular islands formed. This is the case of the adsorption of enantiopure proline on Cu(110), which shows a slight preference for the formation of islands along the [1-10] surface direction. In the case of model II for the adsorption of R-serine on Cu(110) (figure 4.20a), it is noted that the strong hydrogen bonds denoted with the letters A, B and C show a compatibility, in their directionality, with the direction of growth of the molecular islands along the (-3,-2) direction, indicated by the vector W_R in figure 4.20.

In structure III (figure 4.20b), an intra-dimer (OH–O) bond is clearly visible (letter D, 1.944 Å), along with a hydrogen bond between an oxygen atom of the hydroxyl group and an amine hydrogen atom (letter E, 2.110 Å). Additionally, inter-dimer interactions take place between amino hydrogen atoms and one carboxylate oxygen (letters A and B, 1.815 Å and 1.923 Å, respectively). A weaker interaction is finally established between a methyl hydrogen and a carboxylate oxygen (letter C), placed at a distance of 2.780 Å. In summary, in the molecular structure of model III there are four hydrogen bonds that can be classified as strong, i.e. those indicated with the letters A,B,D,E in figure 4.20b. These show a less clear directionality, with respect to model II, in explaining the direction of elongation of molecular islands that take place along the W_R direction.

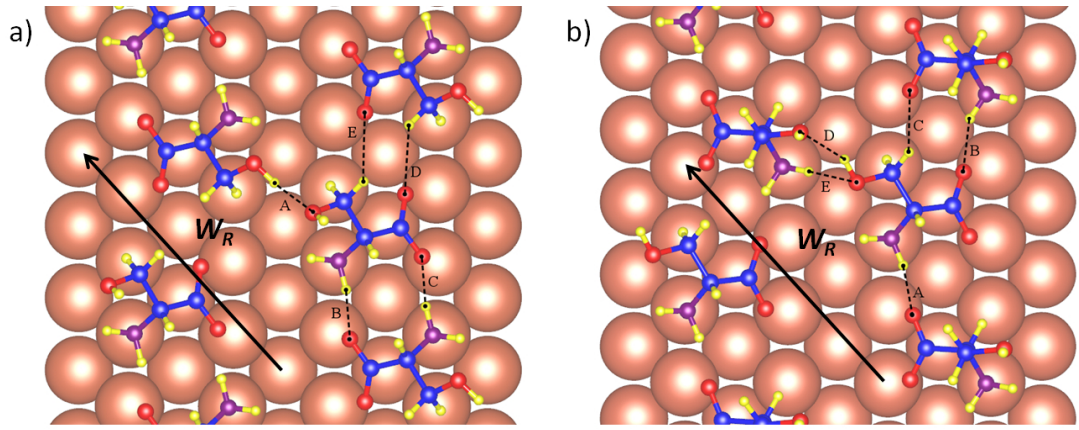

Figure 4.20: a-b) Final DFT-relaxed structures for model II and model III, respectively. Inter-dimer and intra-dimer hydrogen bonds are denoted with dotted lines and letters. The direction of elongation of R-serine molecular islands W_R is indicated with a vector arrow in both figures. The distances between atoms involved in the formation of hydrogen bonds are as follows. a) A: 1.710 Å, B: 1.765 Å, C: 1.789 Å, D: 3.313 Å, E: 3.278 Å. b) A:1.815 Å, B: 1.923 Å, C: 2.780 Å, D: 1.944 Å, E: 2.110 Å. Colour code: brown = copper, red = oxygen, blue = carbon, purple = nitrogen, yellow = hydrogen.

4.5.3 Single dimers

In addition to the investigation on the extended structure, DFT calculations have been performed on single serine dimers placed isolated on the surface, for structure II and III (figure 4.21). These have been carried out with the purpose of highlighting energetic differences in the final states of serine molecules in the whole overlayer and in the single building unit of the molecular organisation. The calculations have produced final energies per dimer of -3.805 eV for structure II and -3.858 eV for structure III, with a difference of 53 meV in favour of structure III. This value is consistent with the energies calculated for the extended overlayer (table 4.2) and thus does not add significant additional information in terms of the thermodynamically favoured model. In addition, the molecular geometries are very similar to those in figure 4.20.

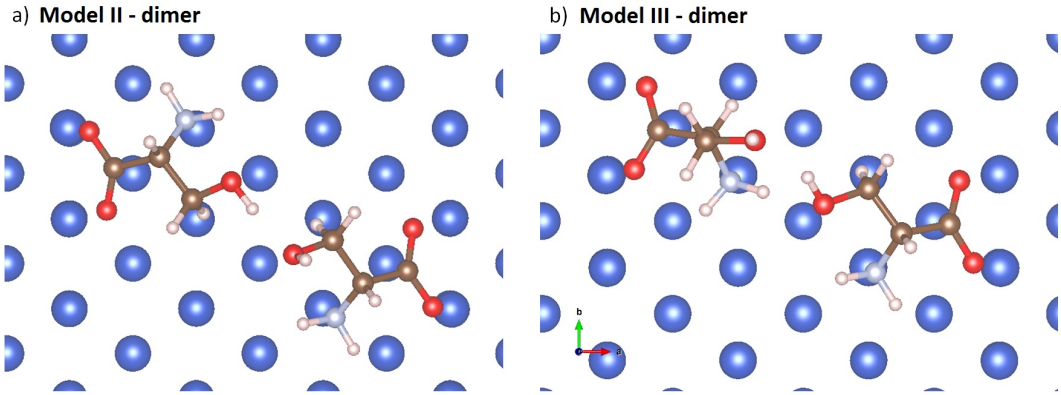

Figure 4.21: a-b) Final DFT-relaxed structures of an R-serine dimer in the cases of model II and model III, respectively. a) Energy = -3.805 eV. b) Energy = -3.858 eV. The values are reported for a dimer. Colour code: blue = copper, red = oxygen, brown = carbon, light blue = nitrogen, white = hydrogen.

4.5.4 STM simulations

Since DFT calculations prove unable to conclusively propose a unique geometrical model, further calculations are essential. For this purpose, STM simulations have been performed on the remaining five structures, yielding the simulated STM images of figure 4.22, which are also obtained via the *FHI-aims* package [73]. Those have been calculated assuming a sample bias voltage of 1 V. In figure 4.22, R-serine molecules in their final geometries are superimposed to the simulated images. It is noticeable that, in any case, the highest contribution to the STM intensity is given by the lateral hydroxyl group and the amino group of R-serine molecules, while the carboxylate moieties are located in correspondence of low-intensity regions. This finding is consistent with previous STM simulations performed on amino acid overlayers on Cu(110) [42].

Interestingly the most stable structures according to DFT calculations, which are model II and model III (table 4.2), show very distinct appearances in the simulated images. In particular, in the simulation of structure II the R-serine dimers have symmetric properties, with the intensities originating from the two molecules having a comparable magnitude. Conversely, the simulation of structure III leads to a clear and strong asymmetry in the signals produced by the two inequivalent molecules. This becomes clearer in figure 4.23, where the STM simulations for structure II and III are placed next to each other. Note the different false colour scale, more similar to the one used for representing experimental STM images in this work. The molecular footprints for both models are also represented in figure 4.23.

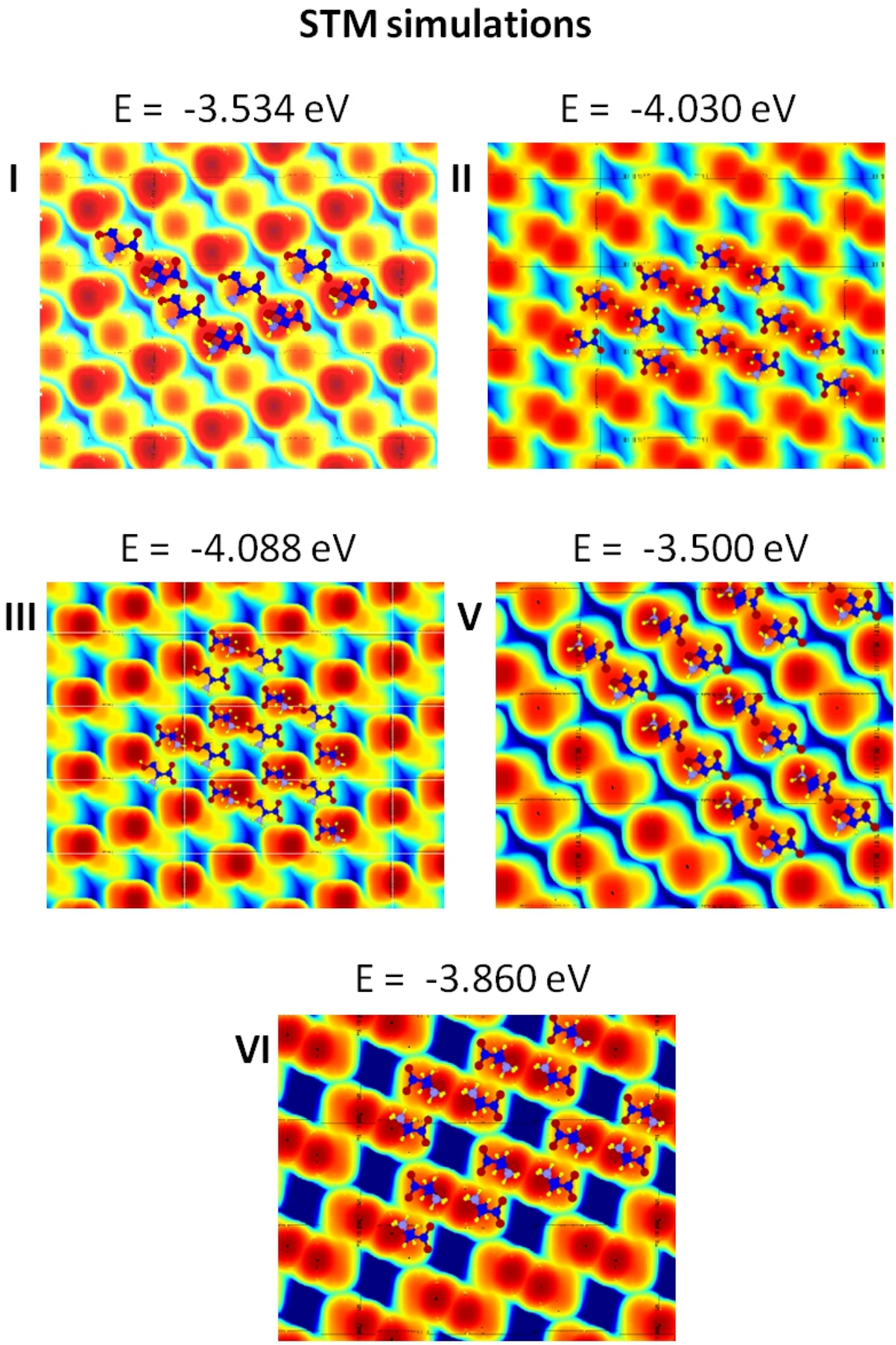

Figure 4.22: STM simulations of the remaining five structures (I,II,III,V,VI). The bias voltage for each of the simulated images is equal to 1 V. In this case, the false colour scale is represented by the colours blue-yellow-red, with increasing intensities. The molecular adlayer is partially superimposed to the relevant simulation. The final energy for the corresponding model is also indicated on top of each image.

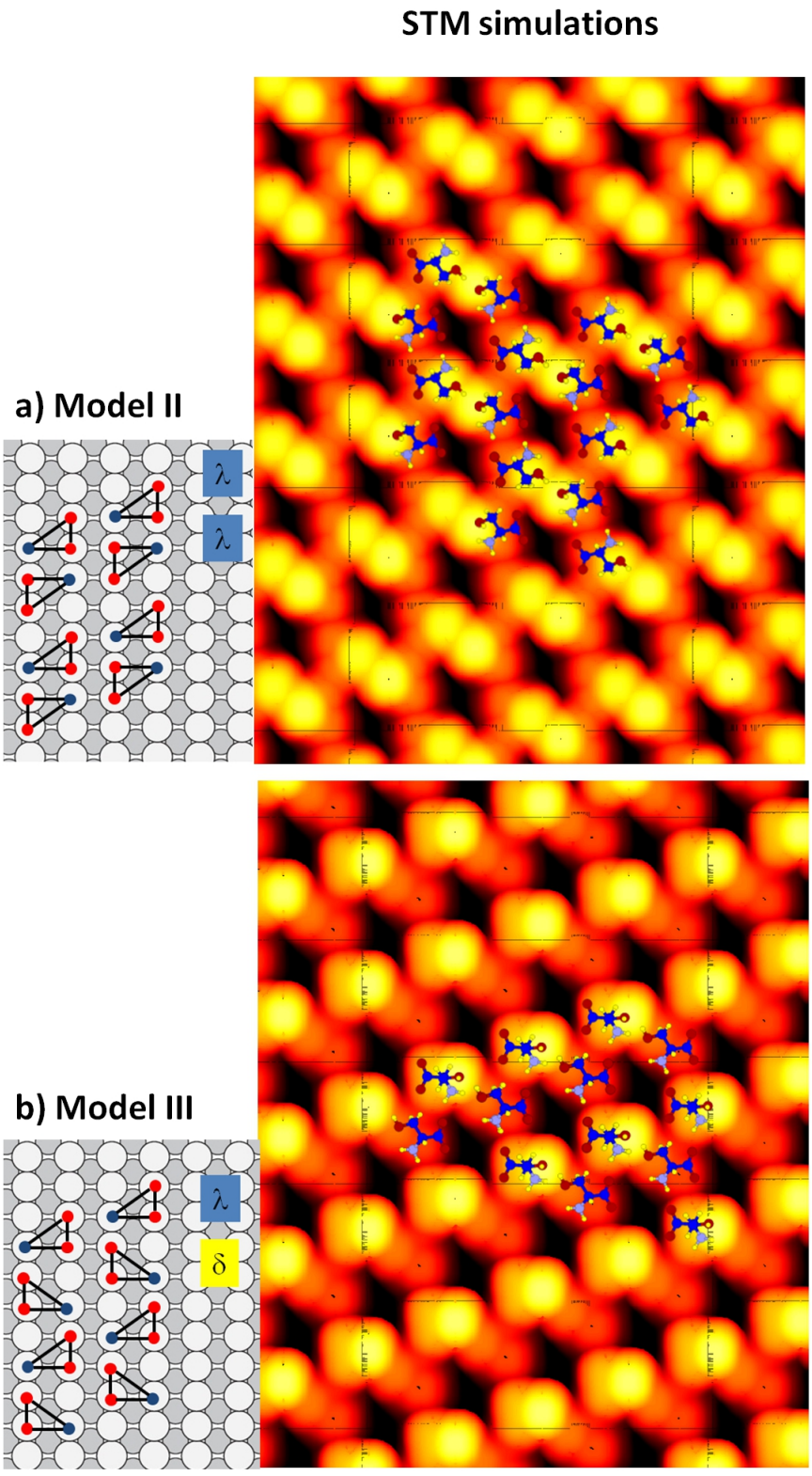

Figure 4.23: a-b)STM simulations of structures II and III, respectively, performed with a bias voltage of +1 V. DFT-relaxed molecular structures are superimposed to each simulated image. In the insets, the footedness of the conformers constituting model II and III are presented again.

In experimental STM images, asymmetries in the STM intensities arisen from inequivalent R-serine molecules composing a dimer are not detected to a significant extent. For this reason, albeit model III cannot be totally excluded as a possible geometry on the basis of the energetics, structure II is proposed as the best representation of the conformational geometry assumed by R-serine on the Cu(110) surface. In figure 4.24 a direct comparison between a simulated STM image of structure II and an experimental image is displayed, in order to show this agreement.

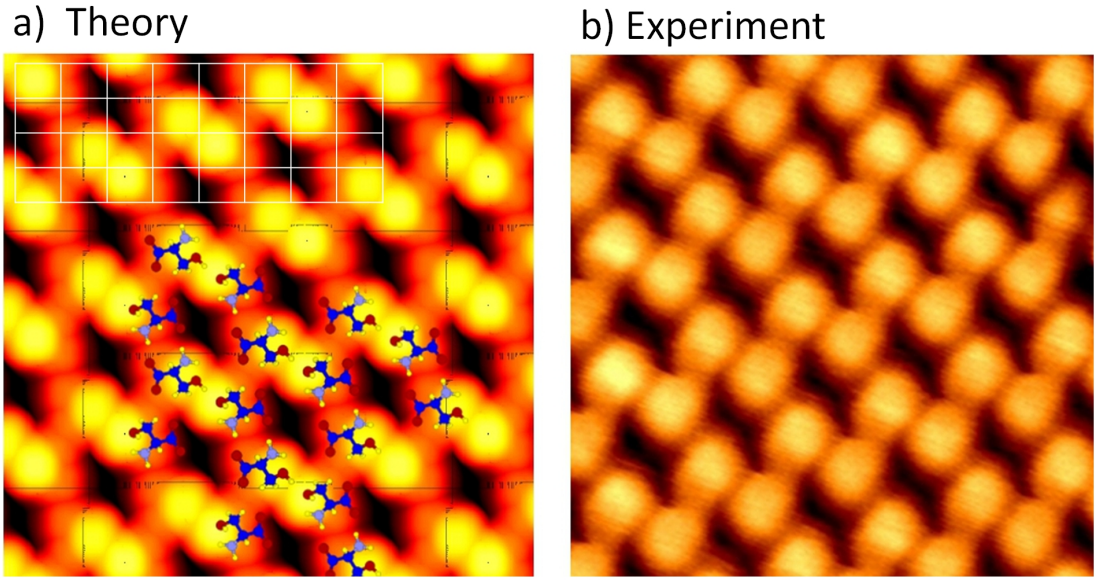

Figure 4.24: a) Calculated STM image arisen from the simulation of structure II. V=1V. The Cu(110) lattice is indicated with a white net. b) Experimental STM image. V=+1.250 V, I=+0.440 nA. The two images are to scale.

Finally, the side-views of the final conformations of R-serine dimers according to structural models II and III are depicted in figure 4.25. In these geometries, the more symmetrical characteristics of model II are evident. As an example, the difference in height between the two hydroxyl oxygen atoms is equal to 0.07 Å in model II. This value increases to 1.06 Å in model III. This difference is due to the two diverse conformations that R-serine can adopt upon adsorption on the basis of its footedness. In fact, in model II the two molecules are both left-footed, while in model III molecules with heterochiral footprints coexist in a dimer. The heights of the hydroxyl moieties in the two models are highlighted here because this part of the molecule is found to be responsible for the highest contribution in STM intensities, as shown in figure 4.23.

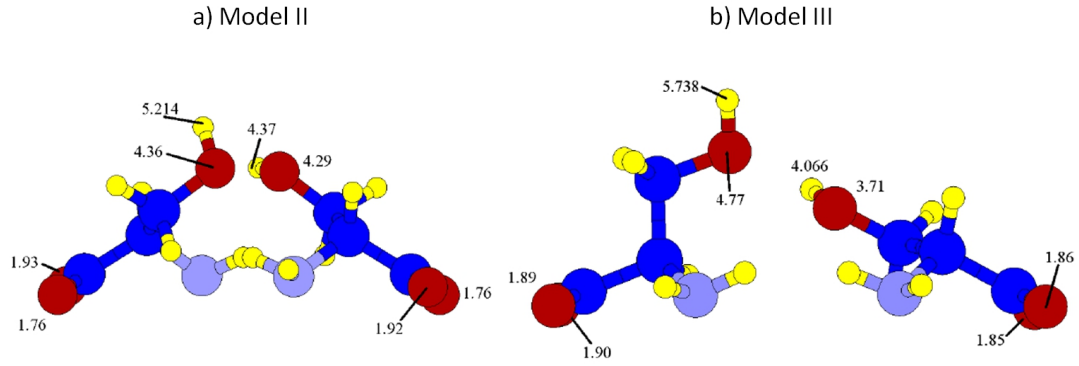

Figure 4.25: a,b) Side-views of an R-serine dimer within the extended adlayer, according to the DFT results performed on model II and model III, respectively. For each atom, the vertical distance with the outermost copper layer is indicated. Colour code: red = oxygen, blue = carbon, purple = nitrogen, yellow = hydrogen.

4.6 Conclusion

The properties of the self assembly of the amino acid serine in its enantiopure R-form on the Cu(110) surface are described in this chapter. With RAIRS, the deprotonated anionic chemical form of R-serine is confirmed. By means of STM and LEED, it is verified that the chiral long-range and local organisations are in agreement with previous studies [28, 46]. Single-molecule resolution STM images shown herein represent a first basis towards the understanding of the molecular positioning within the chiral unit cell. Furthermore, a discussion over the allowed chiral footprints that molecules can adopt is presented. The resulting six models are studied by means of theoretical methods, which include DFT-relaxation and STM simulations. The former are used to restrict the research to two potential models, one homochiral (model II) and one heterochiral (model III) in terms of the molecular footedness of the molecules populating them. STM simulations, used in a direct comparison with experimental images, point towards a higher compatibility of the homochirally footed model. However, a similar energy is computed in the case of model III. The small energetic difference between the two calculated structures, which equals 58 meV per R-serine dimer, is, on the other hand, too small to represent the basis for a discrimination in terms of energy. For these reasons, model II, characterised by homochiral λ-λ footednesses with C_2 rotational property within a dimer, is proposed as a model for R-serine adlayers on Cu(110). However, model III, heterochiral in footprint, cannot be excluded definitively. Furthermore, the possible hydrogen bonds that can be established within a dimer and between different dimers are discussed and interpreted as possible factors for the characteristic symmetry-breaking direction of elongation of R-serine islands on the Cu(110) surfaces. In this respect, the distribution of strong hydrogen bonds in the

molecular model II is more compatible with the strong directionality that the R-serine islands adopt. The homochirally footed geometry (model II) proposed for R-serine would bring forward a hypothesis on the link between the distribution of footprints and the long-range organisation of amino acids on Cu(110). In fact, the amino acids glycine [57], S-alanine [74] and S-proline [42] have been shown to adopt a strict alternating distribution in footedness while they are assembled in an achiral (nx2) cell. In the case of R-serine, the suggested homogeneity in footedness is accompanied by a chiral unit cell and a chiral long-range organisation. The observation of these contrasting behaviours, manifested in the connection between heterochiral and homochiral footprints with achiral and chiral organisations, respectively, might represent the basis for a "rule" describing the μ_3 adsorption of amino acids on Cu(110). This hypothesis needs to be investigated further with a more extended range of systems.

4.7 Methods section

The LEED and RAIRS experiments have been carried out in the RAIRS chamber (section 3.4.1), whereas the Specs STM chamber (section 3.4.2) has been used for the STM experiments. R-serine is bought from Sigma-Aldrich (purity > 98%) and used as received. The molecular source is held in a glass crucible, wrapped in a tantalum wire with a diameter of 0.25 mm, with which the crucible is resistively heated. A current of 0.80 A, corresponding to an approximate temperature of 373 K, is required to induce the sublimation of R-serine molecules.

The theoretical calculations, carried out at the Fritz-Haber-Institut der Max-Planck-Gesellschaf in Berlin, have been performed using density functional theory (DFT) with the Perdew-Burke-Ernzerhof (PBE) functional [75] to include standard exchange-correlation (XC) contributions. The missing long-range correlation interactions, i.e. van der Waals (VdW) interactions, are obtained via the VdW^{surf} functional [76], an extension of the density-dependent pairwise interatomic Tkatchenko-Scheffler (TS) functional [77]. All the systems used in this work are composed with a surface of five metal layers. Two different unit cells are used. The first is a (8x4) Cu(110) supercell that contains a monolayer made with 8 serine molecules: this has been used to test the various possible conformations of the R-serine monolayer. The second is a (8x8) supercell with only one isolated R-serine dimer. Following the DFT geometrical relaxations of each model, the minimum adsorption energy E_{ads} is calculated according to the formula:

$$E_{ads} = E_{tot} - E_{Cu(110)} - NE_{mol} + N\left(H/Cu(110) - E_{Cu(110)}\right) \tag{4.7}$$

where the first term is the total energy of the system, the second is the surface energy and the third corresponds to the energy of N isolated R-serine molecules. The term in parentheses takes into account the dehydrogenation of the N R-serine molecules: we subtract the energy of the bare Cu(110) surface to the energy of the surface with an hydrogen atom on it. All the structures tested are composed with 8 serine molecule, thus E_{ads} is divided by four to obtain the cohesive energy of a single dimer. The STM images are calculated using the Tersoff-Hamann approximation [78]: in this regard the STM intensity is obtained via a calculation of the partial electron density at a position $\mathbf{r}$ due to the Kohn-Sham eigenstates that fall in the energy window between the Fermi energy, E_F, and E_{F+V}, where V is the applied voltage.

References for chapter 4

[1] H. Caner and I. Agranat, "Chiral Drugs," *Enantiomer: A Journal of Sterochemistry*, vol. 7, no. 6, pp. 405–406, 2002.

[2] M. R. Islam, J. G. Mahdi, and I. D. Bowen, "Pharmacological importance of stereochemical resolution of enantiomeric drugs," *Drug safety*, vol. 17, no. 3, pp. 149–65, 1997.

[3] L. Pasteur, "Sur les relations qui peuvent exister entre la forme cristalline, la composition chimique et le sens de la polarisation rotatoire," *Annales de Chimie et de Physique, 3rd series*, vol. 24, no. 6, pp. 442–459, 1848.

[4] K. Mislow and J. Siegel, "Stereoisomerism and local chirality," *Journal of the American Chemical Society*, vol. 106, no. 11, pp. 3319–3328, 1984.

[5] K.-H. Ernst, "Molecular chirality in surface science," *Surface Science*, vol. 613, pp. 1–5, 2013.

[6] R. Raval, "Chiral expression from molecular assemblies at metal surfaces: insights from surface science techniques," *Chemical Society Reviews*, vol. 38, no. 3, pp. 707–21, 2009.

[7] J. Elemans, I. De Cat, H. Xu, and S. De Feyter, "Two-dimensional chirality at liquid-solid interfaces," *Chemical Society Reviews*, vol. 38, no. 3, pp. 722–36, 2009.

[8] M. Forster, M. S. Dyer, M. Persson, and R. Raval, "Tailoring homochirality at surfaces: going beyond molecular handedness," *Journal of the American Chemical Society*, vol. 133, no. 40, pp. 15992–16000, 2011.

[9] Y. Izumi, "Modified Raney Nickel (MRNi) Catalyst: Heterogeneous Enantio-Differentiating (Asymmetric) Catalyst," *Advances in Catalysis*, vol. 32, p. 215, 1983.

[10] C. J. Baddeley, "Fundamental investigations of enantioselective heterogeneous catalysis," *Topics in Catalysis*, vol. 25, no. November, pp. 17–28, 2003.

[11] Z. Ma and F. Zaera, "Competitive chemisorption between pairs of cinchona alkaloids and related compounds from solution onto platinum surfaces," *Journal of the American Chemical Society*, vol. 128, no. 51, pp. 16414–16415, 2006.

[12] S. Mann, D. D. Archibald, J. M. Didymus, T. Douglas, B. R. Heywood, F. C. Meldrum, and N. J. Reeves, "Crystallization at Inorganic-organic Interfaces: Biominerals and Biomimetic Synthesis," *Science*, vol. 261, no. 5126, pp. 1286–1292, 1993.

[13] M. Tirrell, E. Kokkoli, and M. Biesalski, "The role of surface science in bioengineered materials," *Surface Science*, vol. 500, no. 1-3, pp. 61–83, 2002.

[14] R. M. Hazen and D. A. Sverjensky, "Mineral surfaces, geochemical complexities, and the origins of life," *Cold Spring Harbor Perspectives in Biology*, vol. 2, no. 5, p. a002162, 2010.

[15] J.-F. Lambert, "Adsorption and polymerization of amino acids on mineral surfaces: a review," *Origins of Life and Evolution of the Biosphere*, vol. 38, no. 3, pp. 211–42, 2008.

[16] E. Mateo Marti, S. Barlow, S. Haq, and R. Raval, "Bonding and assembly of the chiral amino acid S-proline on Cu(110): the influence of structural rigidity," *Surface Science*, vol. 501, no. 3, pp. 191–202, 2002.

[17] Q. Chen, D. Frankel, and N. Richardson, "Chemisorption induced chirality: glycine on Cu{110}," *Surface Science*, vol. 497, no. 1-3, pp. 37–46, 2002.

[18] X. Zhao, H. Yan, R. G. Zhao, and W. S. Yang, "Self-Assembled Structures of Glycine on Cu(111)," *Langmuir*, vol. 19, no. 3, pp. 809–813, 2003.

[19] V. Humblot, C. Méthivier, and C.-M. Pradier, "Adsorption of L-lysine on Cu(110): a RAIRS study from UHV to the liquid phase," *Langmuir*, vol. 22, no. 7, pp. 3089–96, 2006.

[20] X. Zhao, Z. Gai, R. Zhao, W. Yang, and T. Sakurai, "Adsorption of glycine on Cu(001) and related step faceting and bunching," *Surface Science*, vol. 424, no. 2-3, pp. L347–L351, 1999.

[21] H. Iwai, M. Tobisawa, A. Emori, and C. Egawa, "STM study of D-alanine adsorption on Cu(001)," *Surface Science*, vol. 574, no. 2-3, pp. 214–218, 2005.

[22] T. E. Jones, C. J. Baddeley, A. Gerbi, L. Savio, M. Rocca, and L. Vattuone, "Molecular ordering and adsorbate induced faceting in the Ag{110}-(S)-glutamic acid system," *Langmuir*, vol. 21, no. 21, pp. 9468–75, 2005.

[23] V. Feyer, O. Plekan, T. Skála, V. Cháb, V. Matolín, and K. C. Prince, "The electronic structure and adsorption geometry of L-histidine on Cu(110)," *The Journal of Physical Chemistry B*, vol. 112, no. 43, pp. 13655–60, 2008.

[24] A. Kühnle, T. R. Linderoth, and F. Besenbacher, "Self-assembly of monodispersed, chiral nanoclusters of cysteine on the Au(110)-(1 x 2) surface," *Journal of the American Chemical Society*, vol. 125, no. 48, pp. 14680–1, 2003.

[25] A. Kühnle, T. R. Linderoth, B. Hammer, and F. Besenbacher, "Chiral recognition in dimerization of adsorbed cysteine observed by scanning tunnelling microscopy," *Nature*, vol. 415, no. 6874, pp. 891–3, 2002.

[26] M. Lingenfelder, G. Tomba, G. Costantini, L. Colombi Ciacchi, A. De Vita, and K. Kern, "Tracking the chiral recognition of adsorbed dipeptides at the single-molecule level," *Angewandte Chemie (International ed. in English)*, vol. 46, no. 24, pp. 4492–5, 2007.

[27] S. M. Barlow, S. Louafi, D. Le Roux, J. Williams, C. Muryn, S. Haq, and R. Raval, "Supramolecular assembly of strongly chemisorbed size- and shape-defined chiral clusters: S- and R-alanine on Cu(110)," *Langmuir*, vol. 20, no. 17, pp. 7171–6, 2004.

[28] S. Barlow and R. Raval, "Complex organic molecules at metal surfaces: bonding, organisation and chirality," *Surface Science Reports*, vol. 50, no. 6-8, pp. 201–341, 2003.

[29] S. M. Barlow and R. Raval, "Nanoscale insights in the creation and transfer of chirality in amino acid monolayers at defined metal surfaces," *Current Opinion in Colloid and Interface Science*, vol. 13, pp. 65–73, 2008.

[30] S. Barlow, K. Kitching, S. Haq, and N. Richardson, "A study of glycine adsorption on a Cu{110} surface using reflection absorption infrared spectroscopy," *Surface Science*, vol. 401, no. 3, pp. 322–335, 1998.

[31] N. Booth, D. Woodruff, O. Schaff, T. Gießel, R. Lindsay, P. Baumgärtel, and A. Bradshaw, "Determination of the local structure of glycine adsorbed on Cu(110)," *Surface Science*, vol. 397, no. 1-3, pp. 258–269, 1998.

[32] J.-H. Kang, R. L. Toomes, M. Polcik, M. Kittel, J.-T. Hoeft, V. Efstathiou, D. P. Woodruff, and A. M. Bradshaw, "Structural investigation of glycine on Cu(100) and comparison to glycine on Cu(110)," *The Journal of Chemical Physics*, vol. 118, no. 13, p. 6059, 2003.

[33] R. B. Rankin and D. S. Sholl, "Structures of glycine, enantiopure alanine, and racemic alanine adlayers on Cu(110) and Cu(100) surfaces," *The Journal of Physical Chemistry B*, vol. 109, no. 35, pp. 16764–73, 2005.

[34] M. Nyberg, M. Odelius, A. Nilsson, and L. G. M. Pettersson, "Hydrogen bonding between adsorbed deprotonated glycine molecules on Cu(110)," *The Journal of Chemical Physics*, vol. 119, no. 23, p. 12577, 2003.

[35] S. Blankenburg and W. G. Schmidt, "Steric effects and chirality in the adsorption of glycine and phenylglycine on Cu(110)," *Nanotechnology*, vol. 18, no. 42, p. 424030, 2007.

[36] S. Barlow, S. Louafi, D. Le Roux, J. Williams, C. Muryn, S. Haq, and R. Raval, "Polymorphism in supramolecular chiral structures of R- and S-alanine on Cu(110)," *Surface Science*, vol. 590, no. 2-3, pp. 243–263, 2005.

[37] G. Jones, L. Jones, F. Thibault-Starzyk, E. Seddon, R. Raval, S. Jenkins, and G. Held, "The local adsorption geometry and electronic structure of alanine on Cu{110}," *Surface Science*, vol. 600, no. 9, pp. 1924–1935, 2006.

[38] D. Sayago, M. Polcik, G. Nisbet, C. Lamont, and D. Woodruff, "Local structure determination of a chiral adsorbate: Alanine on Cu(110)," *Surface Science*, vol. 590, no. 1, pp. 76–87, 2005.

[39] S. Haq, A. Massey, N. Moslemzadeh, A. Robin, S. M. Barlow, and R. Raval, "Racemic versus enantiopure alanine on Cu(110): an experimental study," *Langmuir*, vol. 23, no. 21, pp. 10694–700, 2007.

[40] J. Williams, S. Haq, and R. Raval, "The bonding and orientation of the amino acid l-alanine on Cu{110} determined by RAIRS," *Surface Science*, vol. 368, no. 1-3, pp. 303–309, 1996.

[41] R. B. Rankin and D. S. Sholl, "Assessment of heterochiral and homochiral glycine adlayers on Cu(110) using density functional theory," *Surface Science*, vol. 548, no. 1-3, pp. 301–308, 2004.

[42] M. Forster, M. S. Dyer, M. Persson, and R. Raval, "Probing conformers and adsorption footprints at the single-molecule level in a highly organized amino acid assembly of (S)-proline on Cu(110)," *Journal of the American Chemical Society*, vol. 131, no. 29, pp. 10173–81, 2009.

[43] M. Forster, M. S. Dyer, M. Persson, and R. Raval, "2D random organization of racemic amino acid monolayers driven by nanoscale adsorption footprints: proline on Cu(110)," *Angewandte Chemie (International ed. in English)*, vol. 49, pp. 2344–2348, 2010.

[44] J. Reichert, A. Schiffrin, W. Auwärter, A. Weber-Bargioni, M. Marschall, M. Dell'Angela, D. Cvetko, G. Bavdek, A. Cossaro, A. Morgante, and J. V. Barth, "L-tyrosine on Ag(111): universality of the amino acid 2D zwitterionic bonding scheme?," *ACS Nano*, vol. 4, no. 2, pp. 1218–26, 2010.

[45] A. G. Mark, M. Forster, and R. Raval, "Direct visualization of chirality in two dimensions," *Tetrahedron*, vol. 21, no. 9-10, pp. 1125–1134, 2010.

[46] T. Eralp, A. Shavorskiy, Z. V. Zheleva, G. Held, N. Kalashnyk, Y. Ning, and T. R. Linderoth, "Global and local expression of chirality in serine on the Cu{110} surface," *Langmuir*, vol. 26, no. 24, pp. 18841–51, 2010.

[47] M. Forster, M. S. Dyer, M. Persson, and R. Raval, "Assembly of Chiral Amino-Acids at Surfaces from a Single Molecule Perspective: Proline on Cu(110)," *Topics in Catalysis*, vol. 54, no. 1-4, pp. 13–19, 2011.

[48] M. Smerieri, L. Vattuone, T. Kravchuk, D. Costa, and L. Savio, "(S)-glutamic acid on Ag(100): self-assembly in the nonzwitterionic form," *Langmuir*, vol. 27, no. 6, pp. 2393–404, 2011.

[49] A. G. Mark, M. Forster, and R. Raval, "Recognition and ordering at surfaces: the importance of handedness and footedness," *Chemphyschem*, vol. 12, no. 8, pp. 1474–80, 2011.

[50] M. L. Clegg, L. Morales de la Garza, S. Karakatsani, D. A. King, and S. M. Driver, "Chirality in Amino Acid Overlayers on Cu Surfaces," *Topics in Catalysis*, vol. 54, no. 19-20, pp. 1429–1444, 2011.

[51] T. Eralp, A. Cornish, A. Shavorskiy, and G. Held, "The Study of Chiral Adsorption Systems Using Synchrotron-Based Structural and Spectroscopic Techniques: Stereospecific Adsorption of Serine on Au-Modified Chiral Cu{531} Surfaces," *Topics in Catalysis*, vol. 54, no. 19-20, pp. 1414–1428, 2011.

[52] R. T. Seljamäe-Green, G. J. Simpson, F. Grillo, J. Greenwood, S. M. Francis, R. Schaub, P. Lacovig, and C. J. Baddeley, "Assembly of a Chiral Amino Acid on an Unreactive Surface: (S)-Proline on Au(111)," *Langmuir*, no. 111, 2014.

[53] S. Baldanza, A. Cornish, R. E. Nicklin, Z. V. Zheleva, and G. Held, "Surface chemistry of alanine on Cu{111}: Adsorption geometry and temperature dependence," *Surface Science*, vol. 629, pp. 114–122, 2014.

[54] K. Sakthivel, W. Notz, T. Bui, and C. F. Barbas, "Amino acid catalyzed direct asymmetric aldol reactions: a bioorganic approach to catalytic asymmetric carbon-carbon bond-forming reactions," *Journal of the American Chemical Society*, vol. 123, no. 22, pp. 5260–7, 2001.

[55] T. Kawasaki, T. Sasagawa, K. Shiozawa, M. Uchida, K. Suzuki, and K. Soai, "Enantioselective synthesis induced by chiral crystal composed of DL-serine in conjunction with asymmetric autocatalysis," *Organic Letters*, vol. 13, no. 9, pp. 2361–3, 2011.

[56] P. Donovan, A. Robin, M. S. Dyer, M. Persson, and R. Raval, "Unexpected Deformations Induced by Surface Interaction and Chiral Self-Assembly of Co(II)-Tetraphenylporphyrin (Co-TPP) Adsorbed on Cu(110): A Combined STM and Periodic DFT Study," *Chemistry - A European Journal*, vol. 96, no. 110, pp. 11641–11652, 2010.

[57] Z. V. Zheleva, T. Eralp, and G. Held, "Complete Experimental Structure Determination of the p(3 x2)pg Phase of Glycine on Cu{110}," *The Journal of Physical Chemistry C*, vol. 116, pp. 618–625, 2012.

[58] P. J. Reeds, "Dispensable and indispensable amino acids for humans," *The Journal of Nutrition*, vol. 130, no. 7, pp. 1835S–40S, 2000.

[59] P. Fürst and P. Stehle, "What are the essential elements needed for the determination of amino acid requirements in humans?," *The Journal of Nutrition*, vol. 134, no. 6 Suppl, pp. 1558S–1565S, 2004.

[60] J. P. Mothet, A. T. Parent, H. Wolosker, R. O. Brady, D. J. Linden, C. D. Ferris, M. A. Rogawski, and S. H. Snyder, "D-serine is an endogenous ligand for the glycine site of the N-methyl-D-aspartate receptor," *Proceedings of the National Academy of Sciences of the United States of America*, vol. 97, no. 9, pp. 4926–31, 2000.

[61] R. G. Cooks, D. Zhang, K. J. Koch, F. C. Gozzo, and M. N. Eberlin, "Chiroselective self-directed octamerization of serine: implications for homochirogenesis," *Analytical Chemistry*, vol. 73, no. 15, pp. 3646–55, 2001.

[62] S. C. Nanita and R. G. Cooks, "Serine octamers: cluster formation, reactions, and implications for biomolecule homochirality," *Angewandte Chemie (International ed. in English)*, vol. 45, no. 4, pp. 554–69, 2006.

[63] L. Addadi, Z. Berkovitch-Yellin, I. Weissbuch, M. Lahav, L. Leiserowitz, and S. Weinstein, "Use of "enantiopolar" directions in centrosymmetric crystals for direct assignment of absolute configuration of chiral molecules: application to the system serine/threonine," *Journal of the American Chemical Society*, vol. 104, no. 7, pp. 2075–2077, 1982.

[64] I. Weissbuch, L. Shimon, L. Addadi, Z. Berkovitch-Yellin, S. Weinstein, M. Lahav, and L. Leiserowitz, "Stereochemical Discrimination at Organic Crystal Surfaces 1: The Systems Serine/Threonine and Serine/Allothreonine," *Israel Journal of Chemistry*, vol. 25, no. 3-4, pp. 353–361, 1985.

[65] I. Weissbuch and M. Lahav, "Crystalline architectures as templates of relevance to the origins of homochirality," *Chemical Reviews*, vol. 111, no. 5, pp. 3236–67, 2011.

[66] H. Iwai, A. Emori, and C. Egawa, "STM study of L-serine adsorption on Cu(001)," *Surface Science*, vol. 600, no. 8, pp. 1670–1673, 2006.

[67] T. Eralp, A. Ievins, A. Shavorskiy, S. J. Jenkins, and G. Held, "The importance of attractive three-point interaction in enantioselective surface chemistry: stereospecific adsorption of serine on the intrinsically chiral Cu{531} surface," *Journal of the American Chemical Society*, vol. 134, no. 23, pp. 9615–21, 2012.

[68] M. Forster and R. Raval, "Simple Rules Steer Complex Chiral Organisations on Surfaces : Amino-acids on Cu(110)," *in preparation*.

[69] S. Jarmelo, I. Reva, P. Carey, and R. Fausto, "Infrared and Raman spectroscopic characterization of the hydrogen-bonding network in L-serine crystal," *Vibrational Spectroscopy*, vol. 43, no. 2, pp. 395–404, 2007.

[70] Y. Inomata, T. Inomata, and T. Moriwaki, "Infrared Absorption Spectra and Normal Coordinate Analysis of Metal-DL-α-Serine Chelates," *Bulletin of the Chemical Society of Japan*, vol. 44, no. 2, pp. 365–372, 1971.

[71] W. N. Unertl, "Surface crystallography," in *Physical structure* (W. N. Unertl, ed.), no. v. 1 in Handbook of surface science, ch. 1, pp. 3–49, Amsterdam, New York: Elsevier, 1996.

[72] G. Desiraju and T. Steiner, *The Weak Hydrogen Bond*. Oxford University Press, 2001.

[73] M. Bockstedte, A. Kley, J. Neugebauer, and M. Scheffler, "Density-functional theory calculations for poly-atomic systems: electronic structure, static and elastic properties and ab initio molecular dynamics," *Computer Physics Communications*, vol. 107, no. 1-3, pp. 187–222, 1997.

[74] R. B. Rankin and D. S. Sholl, "Structure of enantiopure and racemic alanine adlayers on Cu(110)," *Surface Science*, vol. 574, no. 1, pp. L1–L8, 2005.

[75] J. P. Perdew, K. Burke, and M. Ernzerhof, "Generalized Gradient Approximation Made Simple," *Physical Review Letters*, vol. 77, no. 18, pp. 3865–3868, 1996.

[76] V. Ruiz, W. Liu, E. Zojer, M. Scheffler, and A. Tkatchenko, "Density-Functional Theory with Screened van der Waals Interactions for the Modeling of Hybrid Inorganic-Organic Systems," *Physical Review Letters*, vol. 108, no. 14, pp. 2–6, 2012.

[77] A. Tkatchenko and M. Scheffler, "Accurate Molecular Van Der Waals Interactions from Ground-State Electron Density and Free-Atom Reference Data," *Physical Review Letters*, vol. 102, no. 7, p. 073005, 2009.

[78] J. Tersoff and D. R. Hamann, "Theory and Application for the Scanning Tunneling Microscope," *Physical Review Letters*, vol. 50, no. 25, pp. 1998–2001, 1983.

Chapter 5

Racemic serine on Cu(110): thermodynamic versus kinetic effects in chiral recognition

5.1 Introduction

The resolution of racemic mixtures has represented a prevalent ambition in the scientific community in recent years, due to the increased necessity for single-handed compounds in various sectors. For instance, the higher effectiveness that optically active drugs manifest in chiral environments, such as the biochemical environment of living organisms, has triggered the development of a wide area of pharmaceutical research aiming at producing single-enantiomer products [1–4]. Another important area of application of this research consists in the synthesis of tactic polymers, whose mechanical properties are determined by the stereo distribution of the substituents of the monomeric units [5–8]. For these reasons research on stereoselective synthesis has been on the increase, with the development of asymmetric catalytic methods that lead to the formation of a given preferred enantiomer over its mirror-image product [9]. Amongst these, crystallisation methods have proved to be successful in a small percentage of cases, in which racemic compounds have been shown to undergo natural local segregation in enantiopure domains, termed conglomerates [10]. Chiral resolution via crystallisation can possess a spontaneous nature or, alternatively, can be induced artificially via enantiospecific seeding processes with the objective of promoting the crystallisation of a specific enantiomer [11].

In regard to chiral resolution processes confined in two dimensions, intrinsically chiral surfaces have been the subject of much interest, due to their ability to selectively adsorb one enantiomer from a racemic mixture [12]. In some of the first studies of this type, small differences in the desorption energies have been measured for the two enantiomers of propylene oxide and 3-methyl-cyclohexanone on the intrinsically chiral Cu(643) surface [13, 14]. An interesting work in this field has been published recently

by Yun and Gellman, with a study on the adsorption equilibrium of the racemic amino acid aspartic acid on the intrinsically chiral Cu(3 1 17) surface. The enantioselective adsorption of R-aspartic acid on Cu(3,1,17)^S has been found to occur with an enantiomeric excess of 39% and with an energetic difference of 3.15 kJ/mol with respect to the mirror-image S-aspartic acid [15].

Chiral resolution of racemic mixtures in the absence of a chiral substrate have also been studied. Weissbuch and co-workers have demonstrated the possibility of obtaining homochiral crystallites of amino acids at the air-water interface, tailoring the intermolecular interactions via the molecular design of the side chains of the amino acids [16]. The characterisation of chiral resolution phenomena at surfaces with scanning probe microscopy was achieved for the first time in 1993 by Eckhardt and collaborators, who observed, with an atomic force microscope, mirror-image domains of amphiphilic monolayers deposited on mica [17]. In 1996, Stevens and co-workers proved, with scanning tunneling microscopy, that chiral resolution occurs in racemic overlayers of biphenylbenzoates deposited on highly oriented pyrolytic graphite [18]. With regards to the chiral resolution of biomolecules at metal surfaces, a seminal paper was published in 1978: it demonstrated the possibility of adsorption of chiral biomolecules on metallic surfaces in an ultra high vacuum environment for the first time. In particular, the objects of study were layers of amino acids on copper surfaces with (111) and (100) symmetries. By means of low energy electron diffraction, the authors showed that R- and S-tryptophan self-assemble intact on the two copper surfaces with mirroring unit cells, demonstrating the possibility of creating interfaces with chiral properties starting from the interaction between an achiral metal surface and organic chiral molecules [19]. This field has experienced rapid expansion since the 1990s, with the appearance of multiple studies of chiral phenomena at hybrid inorganic-organic surfaces. This coincided with the increase of availability of scanning probe techniques, in particular STM, that allows chiral behaviour and mechanisms for chiral recognition in two dimensions to be tracked at the mesoscale [20], nanoscale [21] and even at the molecular level [22]. Comprehensive reviews on chiral recognition phenomena at surfaces have been published since then [10, 23–28].

Amino acids nanoconfined in two dimensions have received attention thanks to their role in controlled biominerilisation [29], to their enantiospecific catalytic activity [30–33] and to the biocompatible characteristics that they might bear when they are used to functionalise metal nanoparticles [34]. For these reasons, over the last few decades an extensive body of work has been produced with the goal of understanding the interaction at the molecular level between amino acids and selected metallic crystalline surfaces [35]. Racemic mixtures deposited on metal surfaces have been studied, and different molecular organisations and chiral recognition phenomena have been observed. In particular, homochiral recognition phenomena that trigger the resolution of

racemates into enantiomerically pure domains have been observed for a diverse range of systems. As an example, the amino acid cysteine, in its racemic form, has been shown to arrange in the form of homochiral dimers on the reconstructed Au(110) surface, manifesting a clear preference for homochiral recognition and spontaneous chiral resolution [36]. Homochiral recognition phenomena have also been proven in the stereoselective molecular recognition between diphenylalanine [37] and phenylglycine [38] molecules on Cu(110). Heterochiral recognition events at surfaces have been studied to a lesser extent so far. As an example, it is worth mentioning the property of the racemic assembly of succinic acid on Cu(110), which shows a strict enantioselectivity towards the incorporation of individual guest molecules of tartaric acid in the molecular organisation [39].

The molecular system which is the subject of the present work, the racemic amino acid serine, has been shown to adsorb with a stereospecific preference on the intrinsically chiral Cu(531) surface [40] and on the same surface covered with gold [41]. On the Cu(110) surface, the interface used in the study presented herein, racemic serine has been revealed to undergo spontaneous chiral resolution in small enantiopure domains following an annealing process of the sample up to 370 K [42]. The authors of this publication highlight, with the use of STM and LEED, a tendency shown by racemic serine to self-organise in homochiral dimers, as seen for the enantiopure deposition on the same surface (figure 5.1). However, the more complex as-deposited structure, deprived of the annealing step, is not analysed. In the present work we characterise the stereospecific recognition events of racemic serine on Cu(110) by means of STM. LEED and RAIRS are used as complementary tools to reveal long-range organisational properties and the chemical form of the adsorbates, respectively. In view of the obtained results, while the propensity for chiral resolution at the thermodynamic equilibrium is confirmed, novel manifestations of chiral recognition phenomena, with heterochiral nature, are discovered in kinetically stable states, i.e. before the thermodynamic equilibrium is reached.

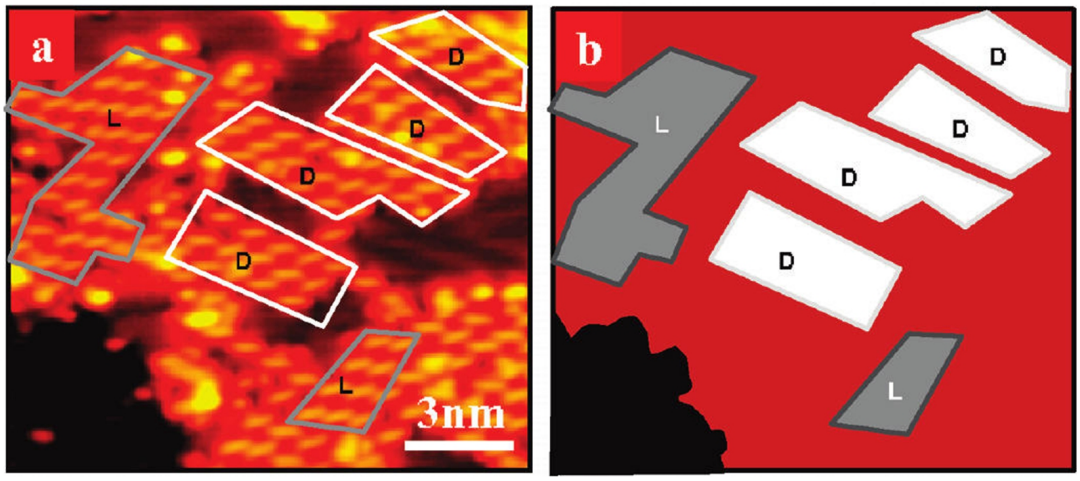

Figure 5.1: a) STM image of homochiral domains formed by racemic serine on the Cu(110) surface. V=-1250.0 mV, I=-0.390 nA. b) Sketch representing the shapes of the domains with a given chirality shown in a). Images adapted from [42].

5.2 Experimental results

5.2.1 RAIRS

The adsorption of racemic serine on the Cu(110) surface is studied firstly by means of RAIRS, with the aim of establishing the presence of possible differences in the molecular orientation with respect to the enantiopure serine adlayer, presented in the chapter 4. Figure 5.2a-d shows the spectra recorded whilst racemic serine is dosed upon the surface, until a monolayer coverage is achieved (figure 5.2d). Within the spectral resolution, the observed vibrational intensities are the same as those produced by the enantiopure R-serine on Cu(110). For a direct comparison, see figure 4.4 and table 4.1 in chapter 4. As a consequence, the presence of serine molecules with different chiralities on the surface is assumed not to have any influence on the adsorption geometry of serine molecules, which are in their anionic form. The amino acid binds via a three-point contact with the surface via the carboxylate and the amino moieties, with the oxygen atoms of the carboxylate positioned across two consecutive copper atoms. Further annealing of the racemic serine adlayer up to a temperature of 393 K does not cause any significant structural change to the adlayer (figure 5.2e-f), except the appearance of a weak band at 1034 cm^{-1}. The assignment of this peak to any of the molecular vibrations is not clear. For the adsorption of alanine on Cu(110), a band at 1036 cm^{-1} was assigned to the combined ν(CN) + ν_s(OCO) [43]. The appearance of a peak at this wavenumber might signify a partial rearrangement of the backbone of the amino acid, without involving the modes of coordination to the surface. However, this interpretation is not conclusive. A decrease in the intensities of the peaks is observed when the sample is brought to 393 K which might indicate a partial desorption of the overlayer without any decomposition processes in the molecules that have remained in contact with the

surface. Once the annealing process reaches the temperature of 418 K (figure 5.2g), the disappearance of all the main peaks testifies the complete desorption of the amino acid overlayer. The simultaneous increase in intensity of the broad absorption band at wavenumbers greater than 3000 cm^{-1} indicates that the latter is produced by the presence of condensed water in the MCT infra-red detector, that practically renders that spectral region inaccessible for characterisations of samples, as hypothesised in chapter 4.

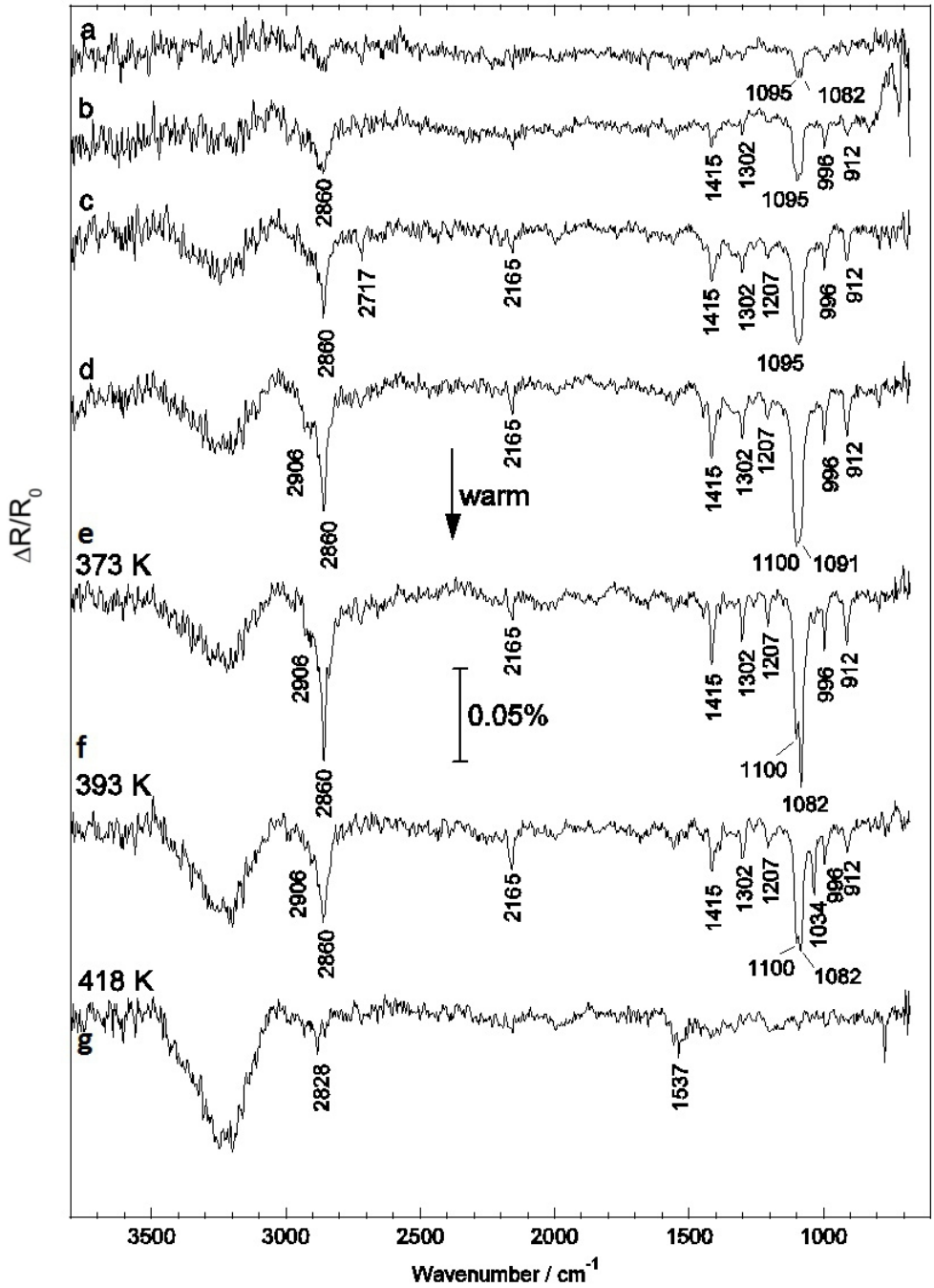

Figure 5.2: a-d) Time lapse RAIR spectra acquired during the deposition at room temperature of racemic serine on Cu(110). e-g) Room temperature RAIR spectra originated by the same sample after subsequent annealing processes up to the temperatures indicated in figure.

5.2.2 LEED

LEED is a useful tool to understand the long range organisation of molecular organic layers at surfaces. Once the racemic serine is deposited on the Cu(110) surface, a LEED pattern is acquired (figure 5.3b). A comparison between this reciprocal space representation and those acquired on the enantiopure serine systems (see figure 4.5 in chapter 4) provides us with some additional information on the order of the adlayer. Although some of the spots visible in the homochiral samples are found in the racemic deposition, the latter does not represent the exact superimposition of the two enantiomerically pure samples (figure 5.3a). This analysis suggests that, while segregation into enantiopure domains, with their stereospecific unit cells, occurs to a certain extent, this process is not complete. Thus, we have an indication of some more complex ordering taking place. In fact, the diffraction spots in figure 5.3b that are not superimposable to any of those of the enantiopure serine patterns imply a different kind of ordered structure, rather than a disordered overlayer, that would not produce single spots but diffuse diffraction intensities. On the other hand, the background intensity of the LEED pattern is not negligible, thus a shorter range structural order can be hypothesised for the racemic system with respect to the single-handedness one. Furthermore, as indicated by the yellow arrows in figure 5.3b, a spot splitting effect is detected. In place of a spot produced by both the enantiomers, as visible in the sketch of figure 5.3a, there are two separated spots. This effect is commonly observed when the periodicity of the adlayer is interrupted in a systematic manner, i.e. when a change in the periodicity regularly occurs on the surface. It will be shown in the next section that this phenomenon occurs on the as-deposited samples of RS-serine on Cu(110) by means of STM, able to track the real-space positioning of individual molecules.

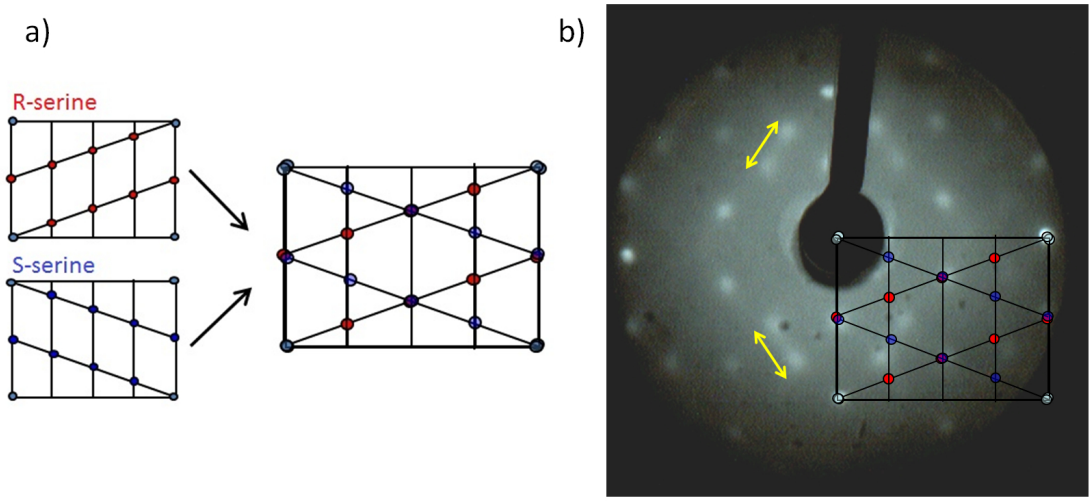

Figure 5.3: a) The schematically represented diffraction pattern expected via the simple superimposition of the spots produced by R- and S-serine on Cu(110) individually. b) LEED pattern acquired on as-deposited racemic serine on Cu(110). Energy = 63 eV. The scheme in a) is superimposed to the experimental pattern. The yellow arrows indicate some spot-splitting effects with respect to the superimposition of the patterns produced by the two enantiomers singularly.

5.2.3 STM

The use of STM allows a clearer understanding of the behaviour of racemic serine on Cu(110) to be obtained, due its ability to image the organisation of molecules in real space and to track, ideally, chirality at a single-molecule level. A typical STM image of a racemic serine mixture adsorbed on Cu(110) at room temperature is represented in figure 5.4. The oval-shape single features (dimers) visible in the STM images of the enantiopure adlayers, with their enantiospecific orientations, are also observed here. This is direct evidence of the formation of homochiral dimers. Furthermore, the characteristic directions of growth of the molecular islands, W_R and W_S, which are also specific to R-serine and S-serine, respectively, are partially retained in the racemic depositions, as indicated with the blue arrows in figure 5.4. However, it is not possible to distinguish a clear and total segregation into homochiral domains. Instead, more complex local structures seem to arise in the internal zones of the islands, some of which are indicated with green circles in figure 5.4.

The lateral STM resolution as seen in figure 5.4, however, does not allow any additional information to be gained about the molecular recognition events taking place in the inner parts of a racemic serine island, neither about the mechanisms that drive the partial chiral resolution of the two enantiomers. Additionally, the racemic serine overlayer (figure 5.4) does not possess a strict island growth mode, but rather gives rise to a network-like structure. This effect might be interpreted as a result of a kind of heterochiral interaction, which accompanies the dominant homochiral recognition effect.

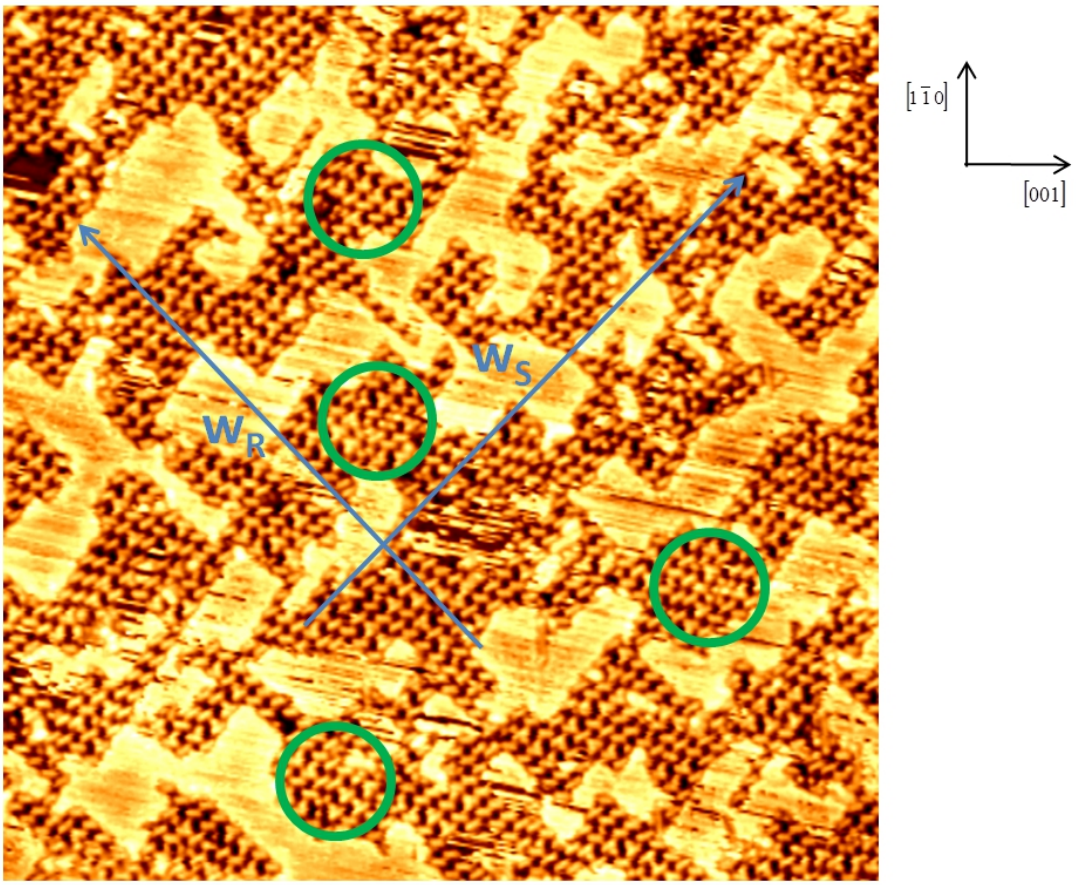

Figure 5.4: RS-serine on Cu(110), as-deposited structure. 50.0x50.0 nm^2,V=-1095.6 mV, I=-0.680 nA. The vectors W_R and W_S indicate the prevalent directions of elongation of the islands. The green circles highlight some internal island zones that reveal complex inter-molecular interactions.

5.2.3.1 The heterochiral interaction

The possible heterochiral interaction is explored through STM analysis of differently prepared samples. In the images shown in figure 5.5, the overlayer is prepared through two successive depositions of enantiopure serine molecules. Specifically, R-serine is dosed first, then S-serine is subsequently deposited. The resulting sample shows that molecules are separated in enantiopure elongated domains, with no signs of mixing of the two chiralities (*cf.* figure 5.4). Nevertheless, islands of S-serine, the molecules deposited last, seem to develop from regions in proximity of R-serine islands, as an indication of heterochiral interactions between domains possessing different chiralities (see red circles in figure 5.5a). In addition, the creation of trimers can be speculated, as shown in the green circle in figure 5.5b. However, this hypothesis cannot be confirmed on the basis of the images in figure 5.5, being the chiral resolution into enantiopure domains the major effect observed in this sample. In fact, once islands with a homogeneous chirality are formed, these are not disrupted by the interaction of the opposite enantiomer that is introduced on the surface in a second time.

The STM images in figure 5.6 correspond to a sample that is prepared via deposition of R-serine first, then racemic serine is added to the surface, yielding a sample that is enantioenriched. The resulting STM images show islands with an overall direction of elongation along W_R, due to the higher presence of the R enantiomer on the surface, but also small islands along W_S, formed by S-serine from the racemic mixture. The green circles in figure 5.6a highlight regions where trimers are formed. These are originated from the deposition of the racemic mixture. In figure 5.6b, that features an STM image of the same sample that has undergone a final annealing up to 373 K, the number of trimers is reduced, indicating that an annealing process tends to render the trimers unstable, while favouring the molecular organisation in enantiopure islands. In the inset of figure 5.6b a zone with a trimer is shown. Once again, homochiral regions with different chirality seem to share boundaries (see red circles in figure 5.6b). Importantly, the STM images portrayed in figures 5.5 and 5.6 confirm that heterochiral interactions take place to a certain extent.

Hence, the heterochiral interaction between R-serine and S-serine on the Cu(110) surface, even though less favourable compared to the interaction occurring between molecules possessing the same chirality, seems to play a significant role. The interplay and the competition between homochiral and heterochiral recognition in adlayers of racemic serine deposited on Cu(110) are studied in the remaining part of this chapter. A systematic STM study of this kind requires the preparation of a diverse range of samples with varying coverage levels, and subsequent annealing in order to gauge the effect of thermal energy on the stereospecific recognition events taking place. In particular, the kinetic versus thermodynamic nature of the enantiospecific interactions are investigated.

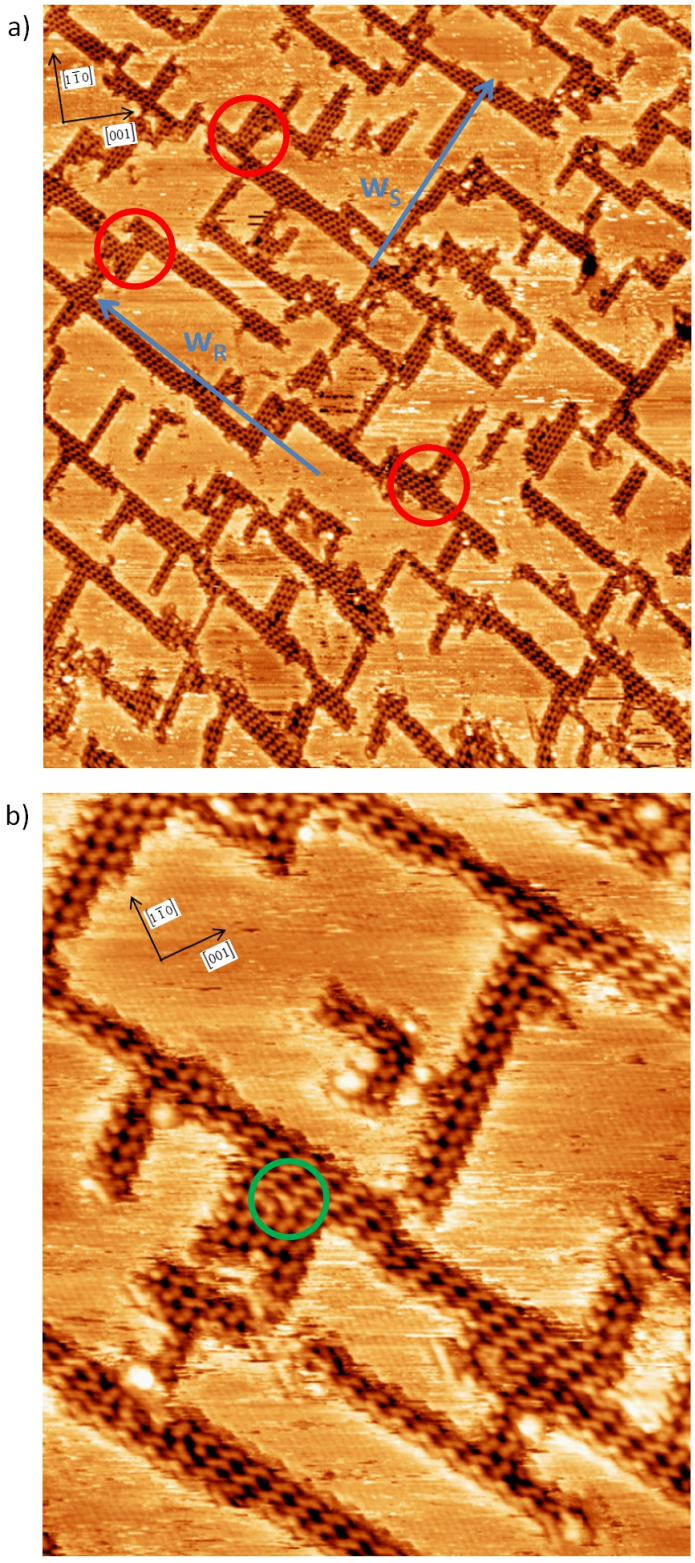

Figure 5.5: a,b) STM images of a Cu(110) sample covered with both serine enantiomers, which are dosed on the surface via two successive enantiopure depositions. a) 107.1x126.5 nm^2, V=-1500 mV, I=-0.900 nA. The enantiospecific directions of elongation of the islands, W_R and W_S, are indicated. The red circles highlight some zones in which enantiopure domains share boundaries. b) 32.1x38.0 nm^2, V=-1300 mV, I=-0.900 nA. The green circle indicates, possibly, the formation of a trimer.

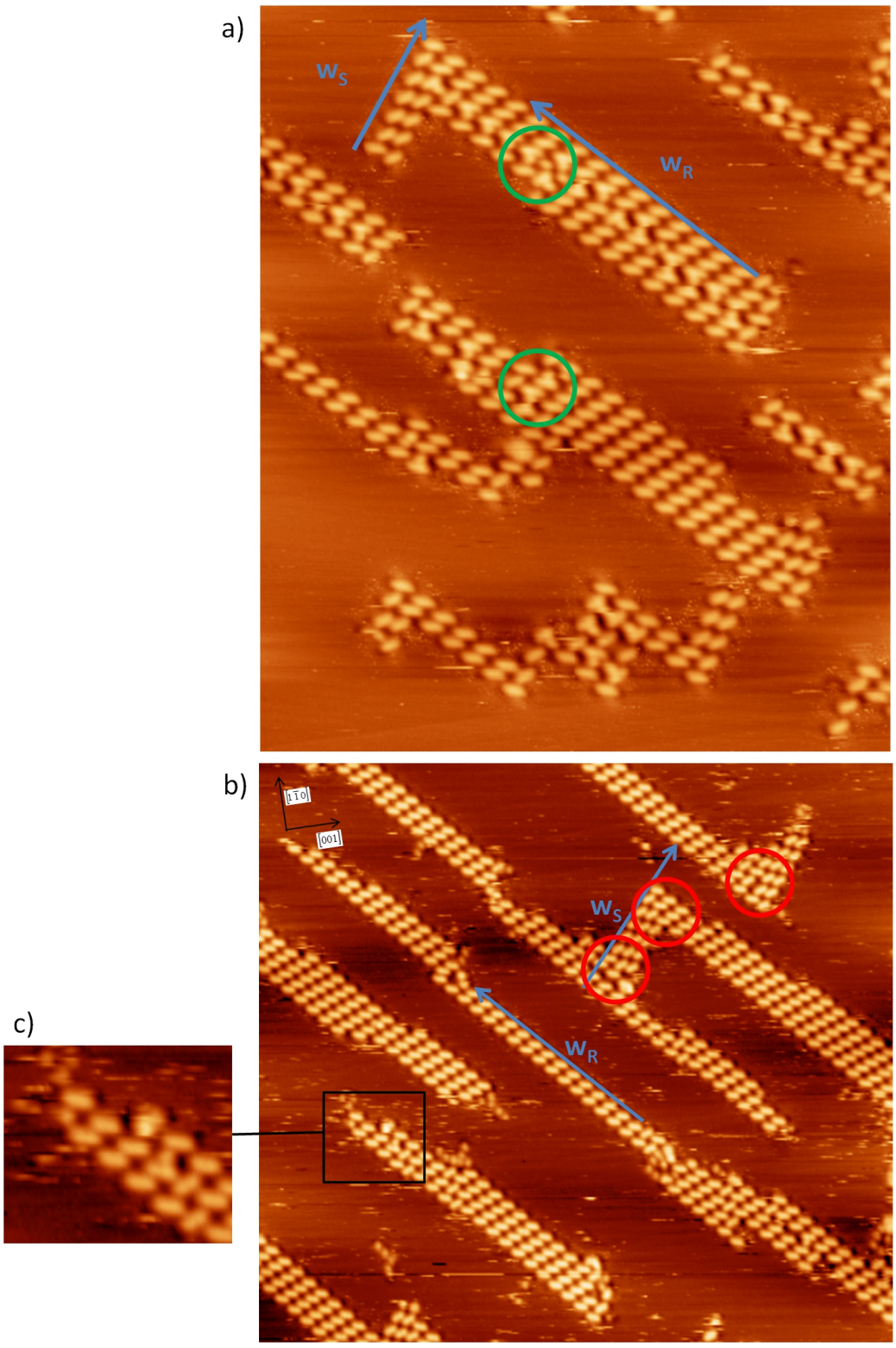

Figure 5.6: a,b) STM image of a Cu(110) sample covered with enantioenriched serine. The deposition of R-serine precedes the deposition of racemic serine. a) 35.2x41.6 nm^2, V=-1300 mV, I=-0.900 nA. The green circles denote a region in which trimers, originated from the racemic deposition, are created. b) 53.5x48.9 nm^2, V=-1500 mV, I=-0.200 nA. The sample has been annealed to 373 K. The red circles highlights areas in which domains with opposite chiralities share boundaries. c) Magnification of the area indicated by the black rectangle in b), featuring a serine trimer.

5.2.3.2 Low-coverage racemic depositions

Firstly, it is noticeable that a serine racemic mixture manifests an appreciable mobility on Cu(110). In figure 5.7, the time-lapse STM acquisition on a given area of a low-coverage racemic deposition is reported. The spatial evolution occurring in one small island of a racemic mixture of serine is followed over a 30 minute-time interval, approximately. Clearly, serine molecules within an island rearrange themselves with time. Although it is not possible to identify, on the basis of the available STM images, the nature and the enantiospecificity of the interactions occurring during the molecular motion, the presence of a significant degree of molecular mobility is unquestionable. This effect, not seen to any significant extent in the enantiopure overlayers, is observed especially when the adlayer coverage is low (approximately < 0.4 ML), whereas at higher coverages this phenomenon is more limited.

In figure 5.8 some representative STM images of samples of racemic serine deposited on Cu(110) at low coverage ($\sim$0.1 ML) are displayed. It is visible that under these conditions molecules tend to separate in homochiral dimers spontaneously. In figure 5.8a islands with a single chirality are detected, whereas in figures 5.8b,c enantiopure domains are in contact, giving rise to domain boundaries between areas with opposite chiralities. In this case, the high mobility that molecules experience on the surface allows them to self-assemble mainly in homochiral dimers that then are distributed in islands with enantiospecific elongations and unit cells, as for the enantiopure serine depositions. Hence the chiral resolution of the enantiomers is in this case truly spontaneous, with the intermolecular interactions being predominantly homochiral in nature.

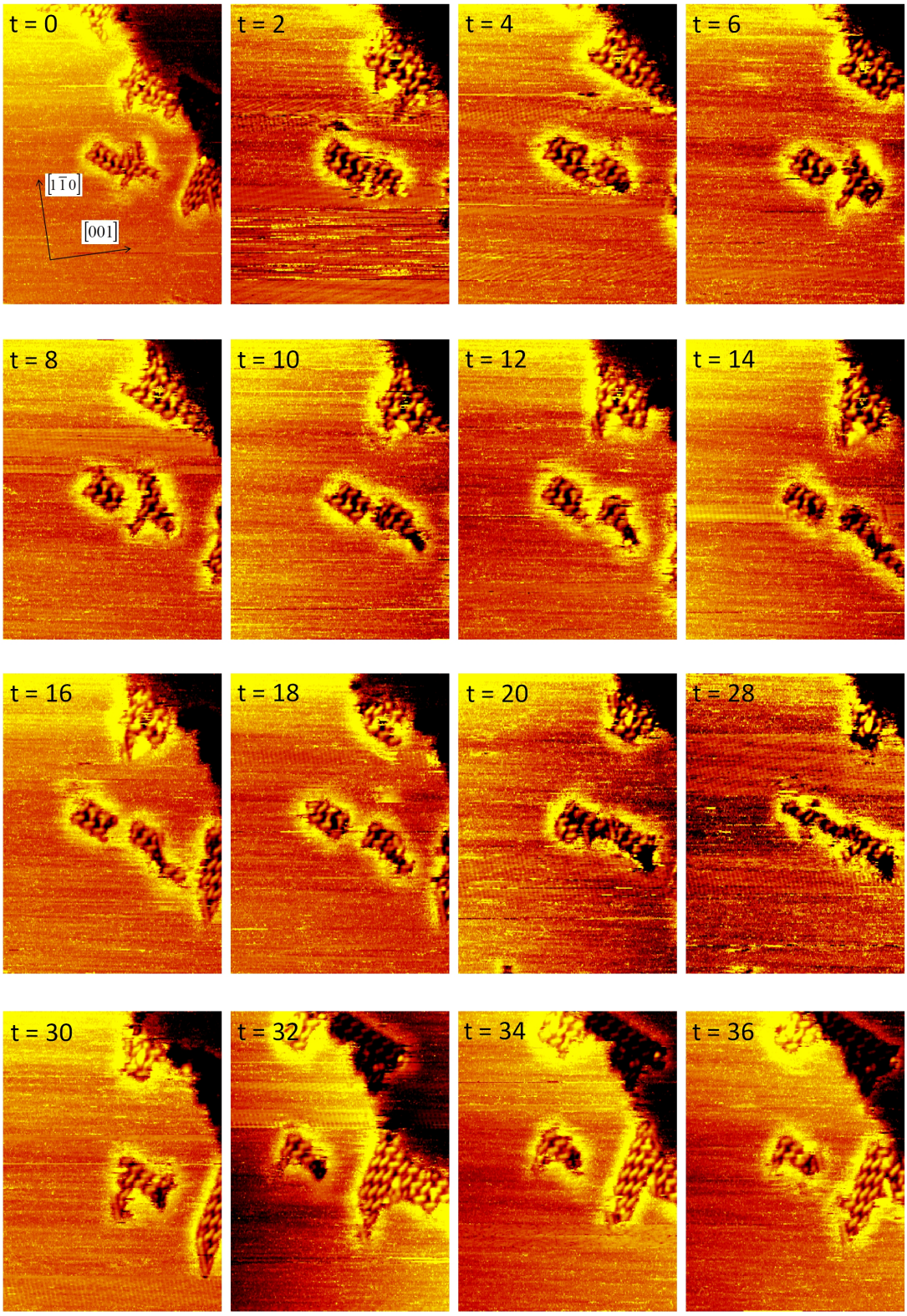

Figure 5.7: Evolution with time of a small racemic serine island. Dimensions of each frame: 22.8x31.3 nm^2. V=-1277.1 mV, I=-0.570 nA. At the top-left of each image the time, starting from t=0, is indicated in minutes. The indication of the time is approximate.

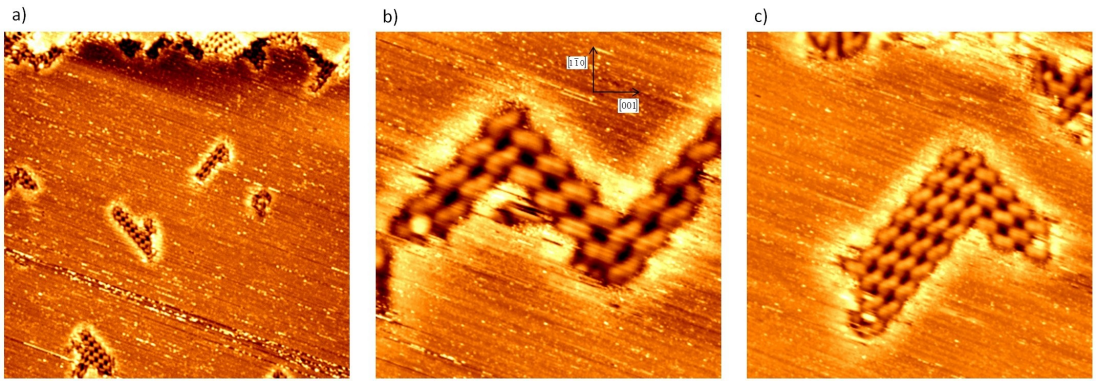

Figure 5.8: STM images of as-deposited racemic serine on Cu(110). Coverage 0.1 ML. a) 50.0x50.0 nm^2, V=-1250.0 mV, I=-0.850 nA. b) 10.0x10.0 nm^2, V=-1250.0 mV, I=-0.650 nA. c) 15.0x15.0 nm^2, V=-1250.0 mV, I=-0.710 nA.

5.2.3.3 Effect of annealing on chiral resolution

The mobility of molecules on a surface may be increased by the addition of energy to the system. Thermal energy is particularly easy to convey to the sample, via the resistive heating filaments available in the sample holder manipulators of the UHV chamber used. These annealing processes have been performed on the prepared sample up to the desired temperature, afterwards the sample is left to cool down to room temperature, at which point STM characterisations are performed. As the molecular coverage is increased, the as-deposited samples show less evident manifestations of spontaneous chiral resolution (see figure 5.4). The STM images displayed in figure 5.9 refer to the same sample, whose coverage is estimated to be $\sim$ 0.7 monolayers. The varying parameter of these images is the temperature to which the sample is annealed prior to the STM characterisation, spanning from 353 K to 383 K.

The step-wise annealing process of the sample shows a progressive enhancement of the chiral resolution of the enantiomers in homochiral dimers, rows or small domains. When the sample is annealed up to 353 K (figure 5.9a,b) this process is almost complete, however some trimers are still present (circled area in figure 5.9b). In figures 5.9c,d, which refers to a sample annealed up to 373 K, the enantiomers are basically separated. Enantiopure domains of R- and S-serine molecules are denoted with red and blue parallelograms, respectively, in figure 5.9d. It is noteworthy that the chiral segregation does not always take place at the 2D domain level, but it can also occur in rows along the [1-10] surface direction, as denoted with the green arrows in figure5.9d, or even at the single dimer level. Further annealing up to 383 K of the highly covered samples leads to the partial dissociation of adsorbed molecules, with fragments left on the surface. The sparsely dispersed islands that are left on the surface are characterized by a strict homochiral arrangement (figure 5.9e,f). The temperature of dissociation for racemic serine on Cu(110) is lower than the one found in the work performed by Eralp and co-workers via temperature programmed desorption, 438 K [42]. This might be

due to an underestimation of the sample temperature in the experiments presented herein and a different ramping rate of the temperature in the annealing procedures. Additionally, it is noted that in this case an on-surface decomposition seems to occur, a process that does not imply an evolution of gaseous species. In any case, racemic serine is proven to be more sensitive to higher temperatures with respect to the homochiral overlayers, on account of the greater stability that the latter organisations achieve by means of a stronger network of hydrogen bonds [42]. In short, one of the outcomes of the set of STM experiments is the tendency of racemic serine to segregate in small homochiral regions on the Cu(110) surface, as long as the system is provided with sufficient energy, depending on the molecular coverage. This aspect is in agreement with the findings presented in reference [42]. Thus, it is assumed that the chiral resolution of the enantiomers manifests itself as a thermodynamic equilibrium state, which is achieved only if molecules possess enough mobility. The latter property can be given to the molecules by the abundance of binding sites on the surface, as in the case of low-coverage samples, or with an external source of energy, as it has been shown for the high-coverage samples.

Once the enantiomers are resolved into 2D homochiral areas, a further analysis can be performed at the boundaries between two adjacent enantiopure domains, as the one depicted in figure 5.10a. A model with triangular features that indicate single serine molecules with their molecular chirality (handedness) and adsorption-induced chirality (footedness) is drawn on the basis of the two most favoured structural models that have been proposed for the enantiopure systems. These are called model II and model III, and feature homochiral and heterochiral footprint arrangements, respectively (see chapter 4). In the schematic representation, the empty triangles indicate R-serine molecules, while the filled triangles represent S-serine molecules. The footprint chirality of the molecules is indicated by the colours red and blue for λ and δ footprints, respectively. The yellow ovals represent serine dimers, orientated as they appear on a STM image (figure 5.10b). From this simple analysis it is noticeable that at the boundaries between homochiral regions the carboxylate adsorption sites (smaller sides of the triangles) of the molecules are always staggered. This holds true for both the favoured structures of the homochiral overlayers (figure 5.10c,d). This suggests that the carboxylate rule [44] for the adsorption of simple amino acids on Cu(110), which has been proposed for long-range 2D structures, also remains valid locally at the regions of interaction between domains having opposite chiralities. Furthermore, the requirement of accommodating carboxylate moieties in a staggered manner might represent one of the driving forces for the chiral resolution of the two enantiomers on Cu(110). This aspect, though, needs further investigation.

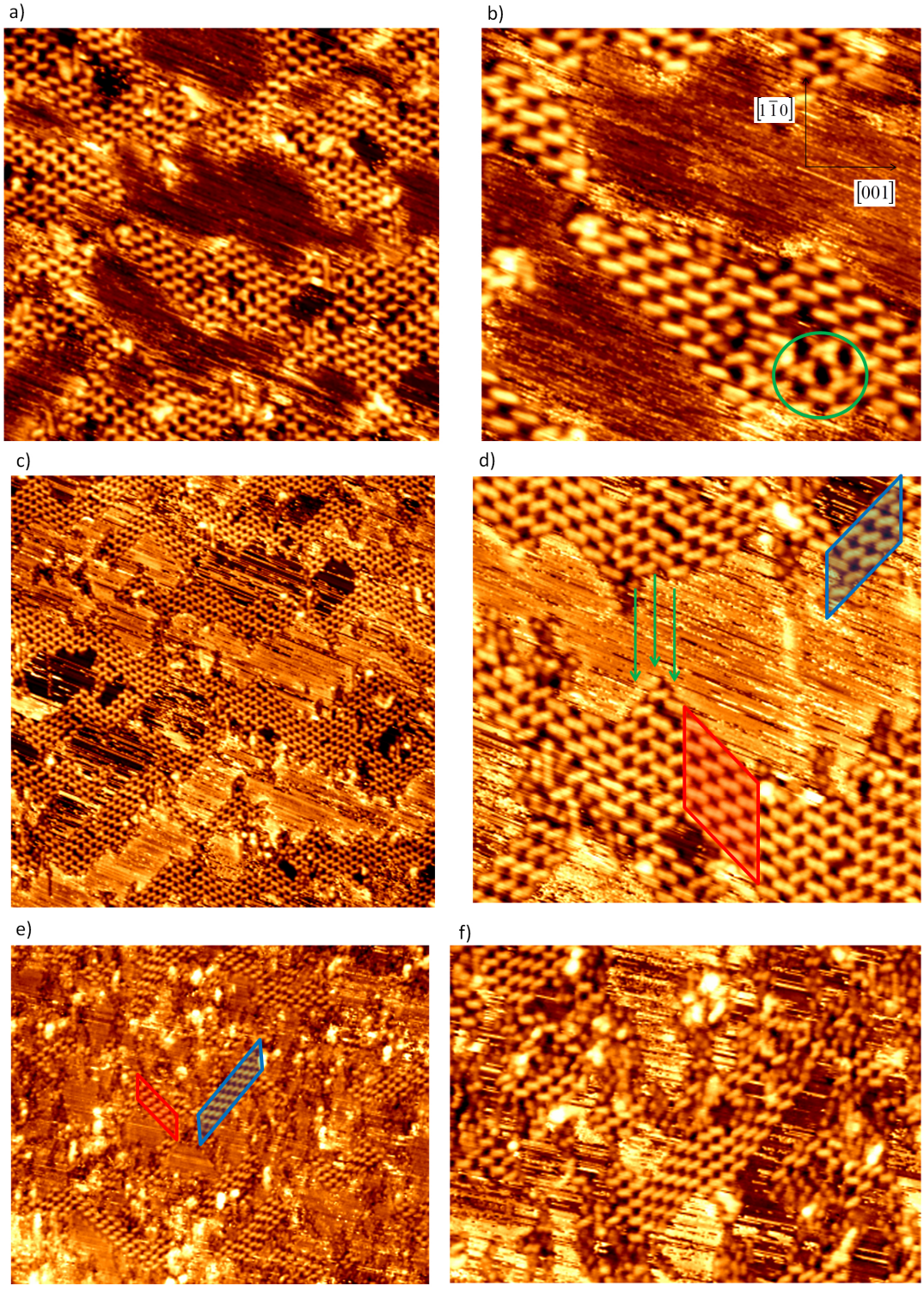

Figure 5.9: a-f) STM of racemic serine adlayers on Cu(110). Coverage $\sim$ 0.7 ML. a,b) Sample annealed up to 353 K. a) 29.5x28.0 nm^2, V=-1250.0 mV, I=-0.550 nA. b) 14.8x13.9 nm^2, V=-1250.0 mV, I=-0.480 nA. c,d) Sample annealed up to 373 K. c) 47.0x47.9 nm^2, V=-1250.0 mV, I=-0.740 nA. d) 18.5x17.6 nm^2, V=-1250.0 mV, I=-0.660 nA. e,f) Sample annealed up to 383 K. e) 48.4x37.3 nm^2, V=-1250.0 mV, I=-1.140 nA. f) 29.2x20.9 nm^2, V=-1250.0 mV, I=-0.670 nA.

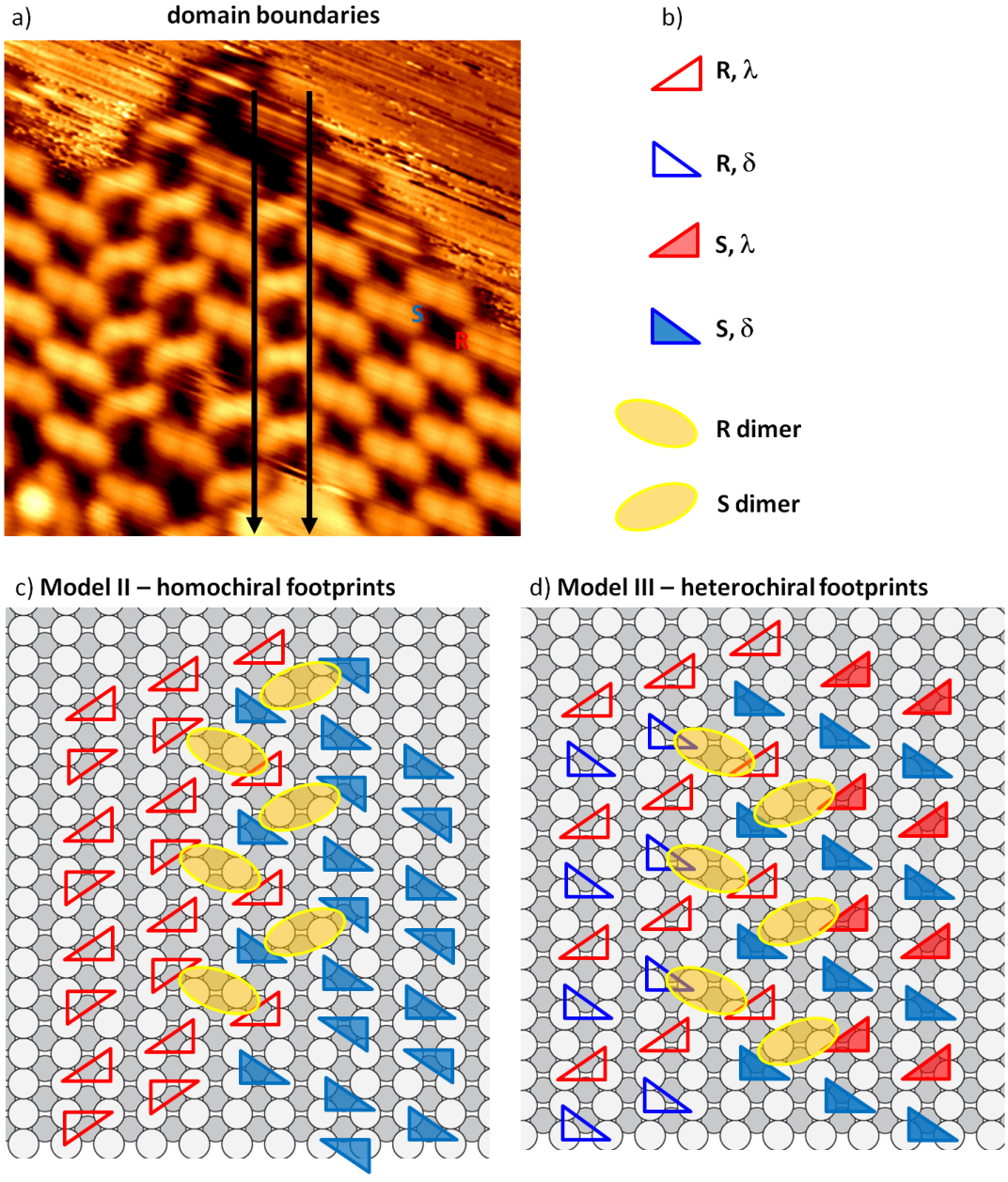

Figure 5.10: a) Insight of an STM image of a chirally resolved racemic serine adlayer on Cu(110), with an indication of some of the boundary zones between enantiopure domains. 6.9x6.6 nm^2, V=-1250.0 mV, I=-0.590 nA. b) Key for the schematic representation of serine dimers and molecules, in terms of their molecular chirality and footprint chirality. c) Structural model that represents the positioning of the molecules at the boundaries between homochiral domains according to model II (see chapter 4). d) Same structure according to model III (see chapter 4). It is noted that the models in c,d) do not aim to reproduce the image shown in a), but the molecular arrangement at a generic boundary between islands with different chirality.

5.2.3.4 The kinetically stable trimers

In the second part of this chapter the kinetically stable states, characterised by a non-complete chiral resolution of racemic serine on Cu(110), is investigated, in order to verify the possible presence of inter-molecular interactions with specific and defined selectivities. In figure 5.11a, a typical STM image of a Cu(110) surface highly covered (~ 0.8 ML) with racemic serine is depicted. It is clearly visible that there are many areas in which chiral resolution is not observed and trimers are present (see for example the area circled in green). In order to visualise the degree of segregation of the enantiomers, in the sketch of figure 5.11b, ovals and triangles are drawn on top of serine dimers and trimers, respectively. According to this approximate calculation, in the area represented in figure 5.11a, about 40% of the molecules are included within a trimer, while the remaining 60% form homochiral dimers.

The chiral nature of the three-lobe features visible in as-dosed racemic serine overlayers (see circle in figure 5.11a) is the object of the remaining part of this study. In figure 5.12, highly detailed STM images are able to provide an insight into the enantioselectivity of the interactions taking place within those features. STM images in figure 5.12 allows the characteristics of each molecule composing a trimer to be interrogated. In fact, in the same images homochiral serine dimers are present, imaged with single-molecule resolution. Furthermore, each molecule images with a distinct shape and orientation with respect to the main surface directions. This allows a direct comparison between the STM appearance of each serine molecule within a trimer with those belonging to a homochiral dimer. On the basis of this visual evaluation, it is possible to assign the molecular chirality to each serine molecule in a metastable trimer. The STM images portrayed in figure 5.12a-d represent an example of this situation. It is found that a trimer is formed by two serine molecules with the same chirality (RR or SS dimer) and a single molecule with opposite chirality (S or R molecule), as denoted in figure 5.12b,c,d. Thus the latter effect consists in an additional chiral recognition property, possessing heterochiral nature. In particular, four kinds of trimers are detected, given by the combination of interactions between an RR-dimer with an S molecule and vice versa (see figure 5.12e). Namely, it is found that a serine molecule with a given chirality is able to interact with a serine dimer with opposite handedness from both sides of it. The absence of selectivity in this interaction suggests a symmetric geometry (e.g. a C_2 rotational property) for a serine dimer, since the presence of a break of this internal symmetry may have established a preferential side for the interaction. The multiple observation of the serine trimers, especially in as-deposited samples, indicate that these states are made stable kinetically by an energetic barrier that prevents the system achieving its thermodynamic equilibrium, i.e. the chiral resolution of the en-

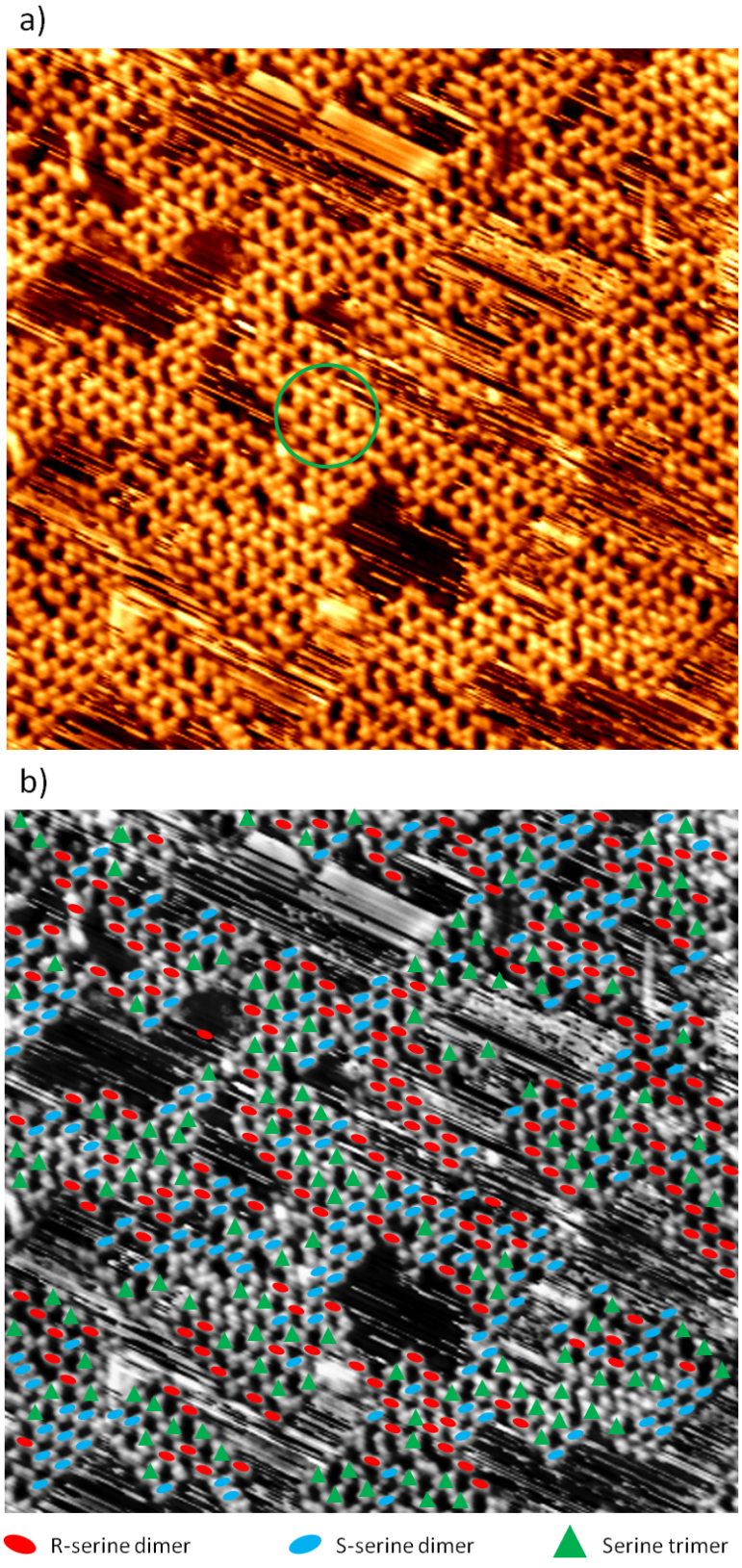

Figure 5.11: a) As deposited racemic serine. Coverage $\sim$ 0.8 ML. 28.8x27.7 nm^2, V=-493.2 mV It=-0.570 nA. The green circle highlights an area containing trimers. b) Sketch superimposed onto the STM image of a), which is displayed in gray scale. Red and blue ovals represent R-serine and S-serine dimers, respectively, green triangles stand for serine trimers.

antiomers. These local minima, away from equilibrium, are interpreted as metastable states, and can be seen as situations in which the mobility of serine molecules is not sufficient to allow them to couple with a homochiral molecule, the thermodynamically favoured recognition event.

In some circumstances, the on-surface molecular mobility allows the interconversion between different kinds of serine trimers. For instance, in figures 5.13a-d, which show the STM characterisation of the same area performed in a time interval of few minutes, the movement of two S-serine molecules is observed. In particular, an S-serine molecule is initially part of a trimer with two R-serine molecules (figure 5.13a). In the following scan, it is seen that the S-molecule has changed position, having moved towards an adjacent R-serine molecules (curved blue arrow in figure 5.13b). This displacement is also observed for an additional S-molecule (figures 5.13c,d). The time scale of this movement seems to be small compared to the time required by STM investigations, since no intermediate positioning is observed. Furthermore, net lines, parallel to the scan direction, are produced in correspondence of the molecular movements, as indicated by the green arrows in figures 5.13b-d. In this manner the STM is somehow able to catch the molecular movement, which, on this basis, could also be induced by the tip. Interestingly, in figure 5.13d the interaction of a S-serine molecule with two different RR-serine dimers appears in the same STM image. Moreover, the shape of the STM intensities produced by S-serine molecules in their initial and final states suggests that this movement consists of a rotation of 180°. This molecular movement, summarised in the schematic of figure 5.13e, corroborates the hypothesis that homochiral dimers do not show selectivity in terms of which side is prone to establish an interaction with a single molecule having opposite chirality.

The formation of the four types of trimers sees the interaction between either an RR dimer and an S molecule, or between an SS dimer and an R molecule. The STM image in figure 5.14a, which shows both situations, is taken as a model to infer the positioning of serine molecules with a given chirality in a trimer. In figure 5.14b,c molecules are represented by triangles using the same representational code as in figure 5.10b-d. The heterochiral molecule within a trimer is represented with a yellow circle. With the formation of the trimers, there are two adjacent carboxylate scaffolds along the close-packed row of the Cu(110) surface. This holds true for both the favoured models (model II in figure 5.14b and model III in figure 5.14c). The nature of these interactions, which take place locally, does not invalidate the general reasoning and interpretation of the carboxylate rule [44], which applies to long-range ordered structures. Furthermore, this might be a further explanation of the relative instability of the heterochiral serine trimers, which have been shown herein to possess a metastable nature.

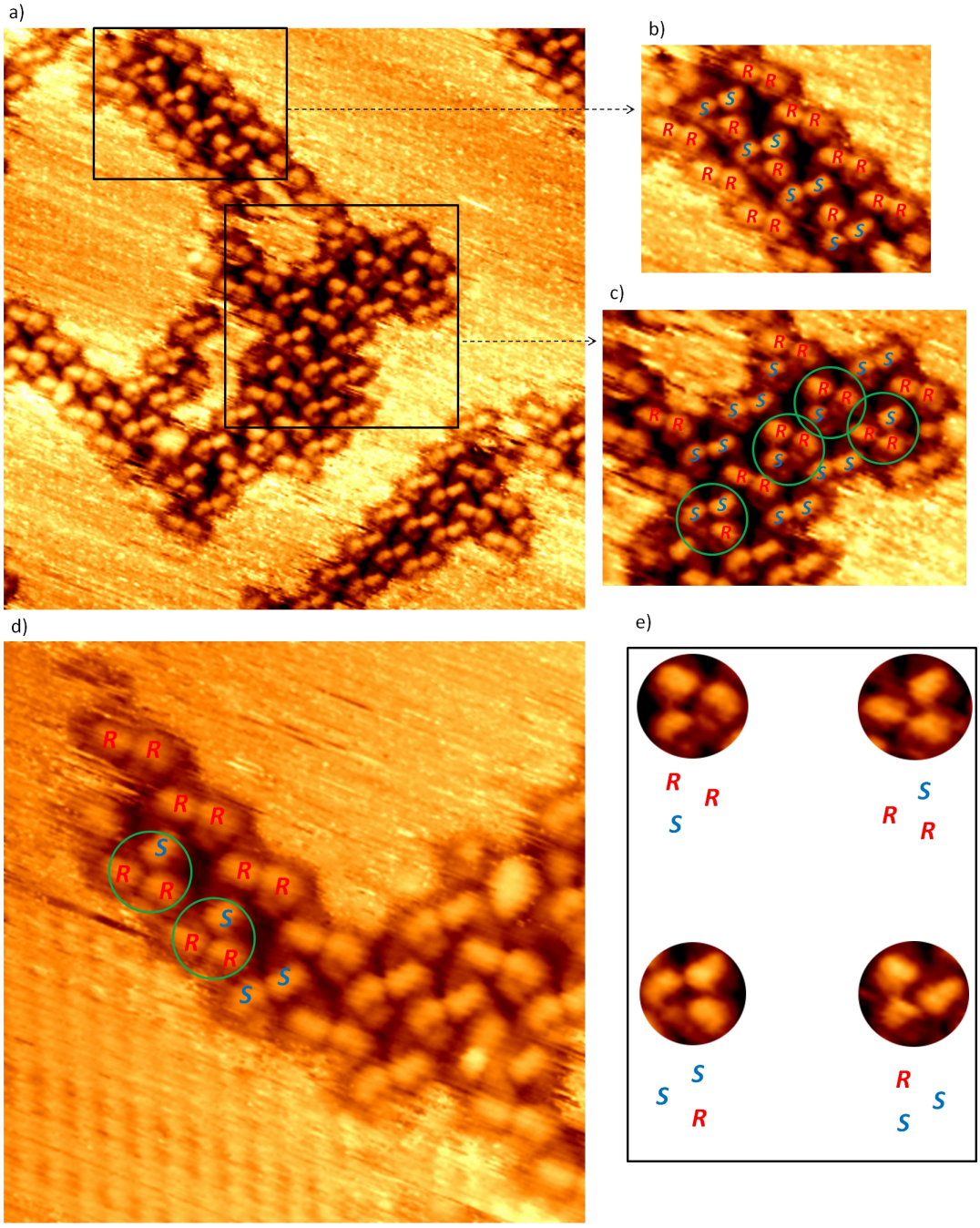

Figure 5.12: a) As-deposited racemic serine on Cu(110). 15.0x15.0 nm^2, V=+691.2 mV, I=+0.850 nA. b-c) Insights showing magnified areas of image in a). The chirality of each molecule composing a trimer is attributed on the basis of their orientation, as a result of the comparison with homochiral dimers present in the same area. Some trimers are circled in green. d) As-deposited racemic serine on Cu(110). 7.0x7.0 nm^2, V=+691.2 mV, I=+0.910 nA. e) The STM appearances of the four types of serine trimers that are formed on the Cu(110) surface

.

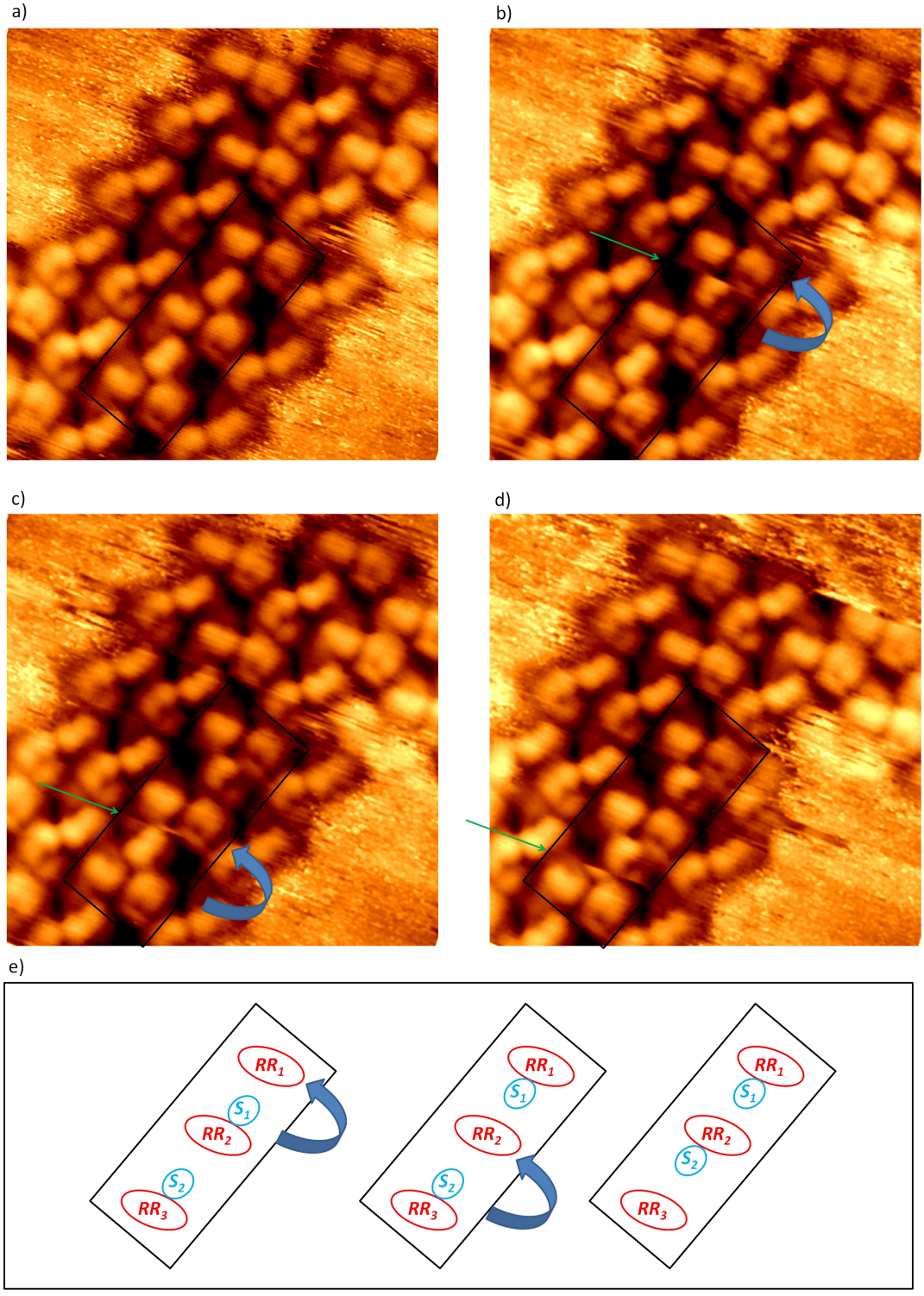

Figure 5.13: a-d) Time-lapse STM characterisation of a molecular island composed of racemic serine on Cu(110), spanning a total interval of approximately five minutes. The curved blue arrows indicate the movement of S-serine molecules as they establish interactions with diverse RR-serine dimers. All images 5.0x5.0 nm^2, V=+691.2 mV, I=+0.870 nA. e) Scheme that summarises the movement of two S-serine molecules (S_1 and S_2) as they interact with RR-dimers (RR_1, RR_3 and RR_3), as observed in a-d).

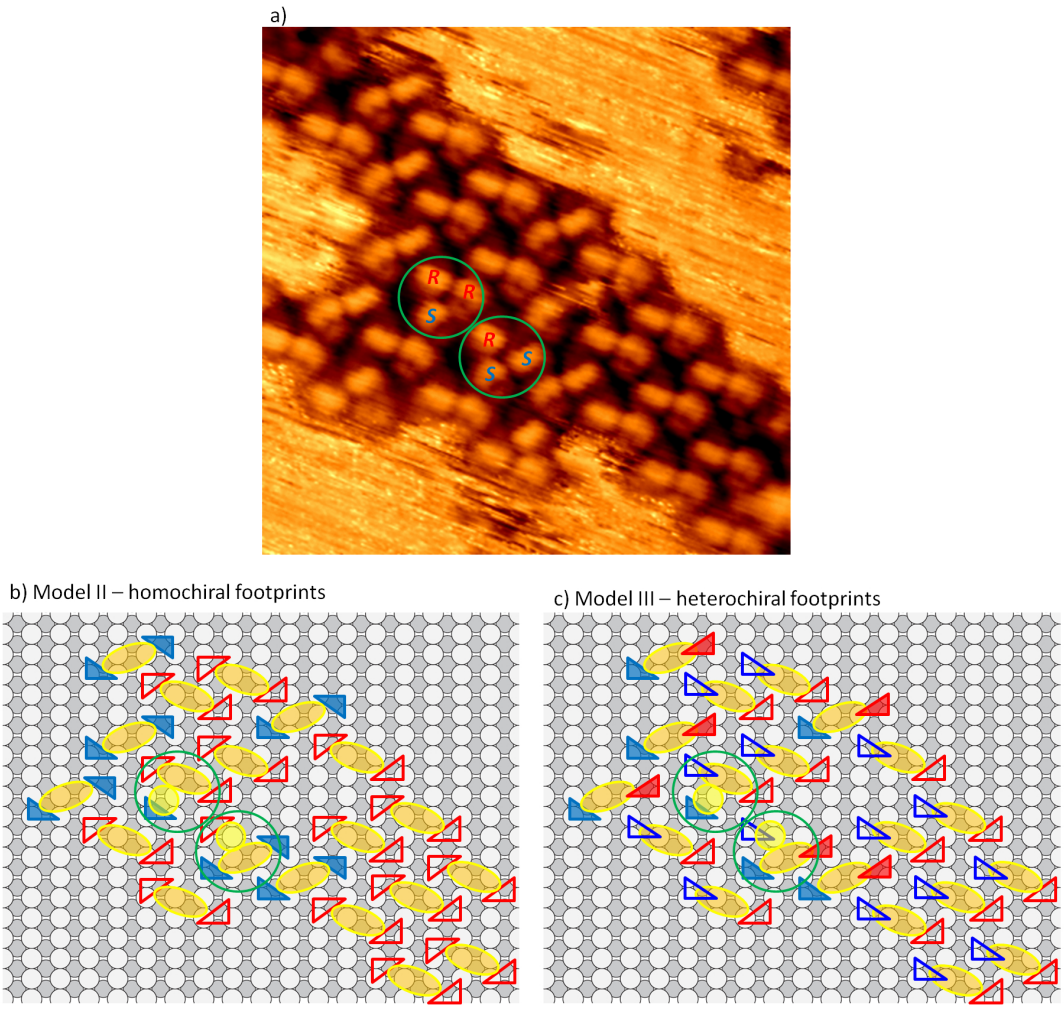

Figure 5.14: a) STM image of a racemic serine island containing the two kinds of trimers, circled in green. The chirality of the molecules composing the two trimers is indicated b-c) Model of the structure according to the image in a). Model II and model III for enantiopure serine (see chapter 4) are used, respectively. The key for the representation of molecules with a given handedness/footedness is the same as in figure 5.10. A yellow circle is used herein to indicate the heterochiral molecule contained in a trimer.

In an attempt of individuating the relevant inter-molecular forces that occur within a serine trimer, two models are presented in figure 5.15. They are based on the DFT structures that have been calculated for enantiopure serine (chapter 4). In figure 5.15a the model of a trimer consisting of an R-serine dimer and an S-serine molecule is represented, along with its sketch as in figure 5.14, according to model II. In figure 5.15b the same structure is represented in the same manner, according to model III. Note that the geometrical models presented are not the outcomes of any theoretical calculations, but are the result of a simple positioning of the serine molecules according to the models proposed in chapter 4. Hence, a quantitative interpretation of the intermolecular forces is not attempted. A characteristic that these two models share is the position of the hydroxyl group. In the three molecules, this group faces the internal part of a trimer. This positioning thus may facilitate the creation of mutual hydrogen bonds of the (OH–O). This hypothesis fits better with model II than with model III (figure 5.15a). According to these geometries, the hydrogen atoms of the amine groups are also possible candidates for the formation of hydrogen bonds with oxygen atoms of hydroxyl groups belonging to neighbouring molecules. On the other hand, steric hindrance due to the possible interaction between hydrogen atoms belonging to the CH_2 and the NH_2 groups might be significant. This, however, is compatible with the non-thermodynamic stability of the trimers. It is finally stressed that this reasoning is purely qualitative, not having taken into account any possible molecular rearrangement in the heterochiral interaction.

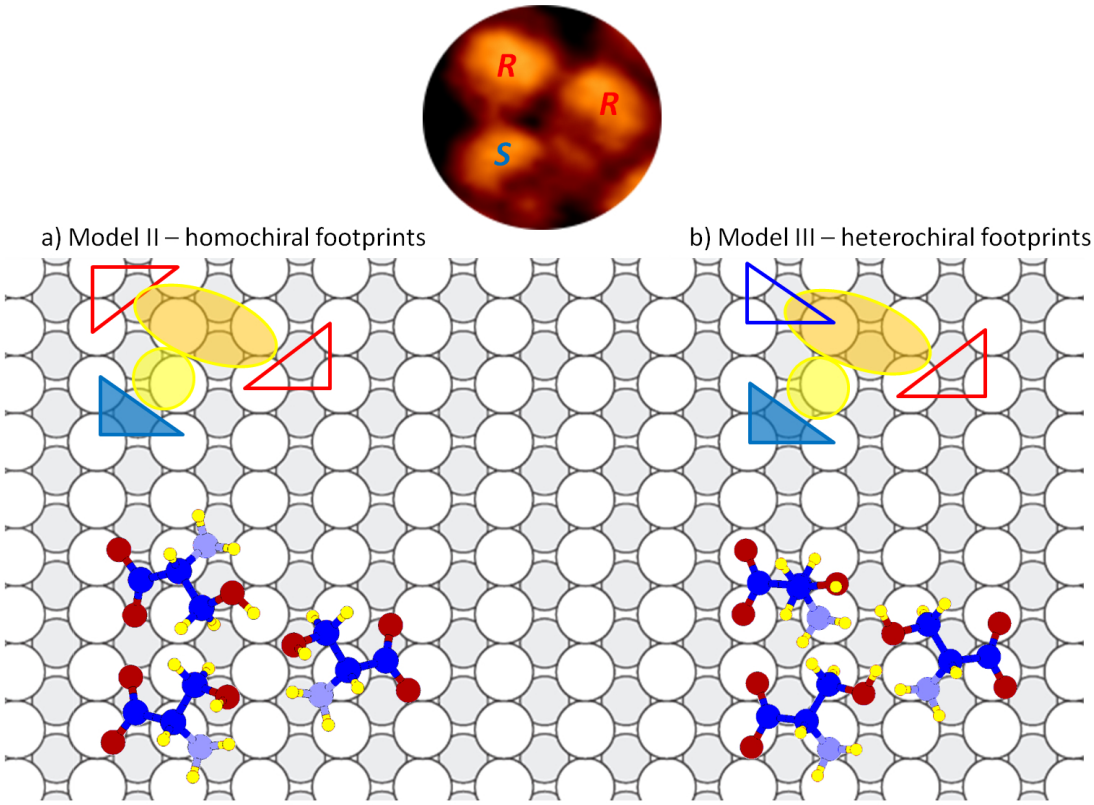

Figure 5.15: a,b) Possible molecular models of a serine trimer (RR dimer + S molecule), drawn according to the structures II and III presented in chapter 4, respectively. The sketches of the trimer according to the key in figure 5.14 are reminded.

5.2.3.5 Chiral probe

In summary, it has been shown that in order to track the types of intermolecular stereospecific interactions that occur in the racemic serine adlayers, with STM, it is necessary to have a sufficiently high lateral resolution of the probe. In particular, the ability to identify the chirality of single molecules has proven to be a fundamental attribute. In the STM images shown so far, chirality at the single molecule level has been identified by the stereospecific orientations of the STM appearances of a molecule with a given chirality. Typically serine molecules and homochiral dimers emerge with mirror-image protrusions in STM, whose orientations are dictated by the intrinsic handedness of the molecules (see for example STM images in figure 5.12). In some circumstances, however, more complex molecule-tip interactions are established. In figure 5.16, for instance, clear asymmetries can be noticed in the appearance of the two enantiomers in STM images. Particularly, single S-serine molecules appear as single protrusions with a drop-like shape and give rise to a higher STM intensity, whereas R-serine molecules originate double-lobe features with less intensity (see the two magnifications in figure 5.16). Thus, the two enantiomers produce images that are not superimposable via an out-of-plane reflection. These outcomes represent an example of how the STM tip is able, in some occasions, not only to track the chirality of single molecules on the basis of their geometrical positioning, but also to interact in a distinct manner with them, depending on the chirality of the probed molecule. The mechanisms that underpin this chiral interaction are not understood, since the state of the probe is not known. It can be speculated that the probe has been functionalised, during the sample characterisation, with a serine molecule, which possess a given chirality, and this casual functionalisation could have rendered the tip *handed* in the sense of establishing non-symmetrical interactions with adsorbed molecules possessing diverse chiralities.

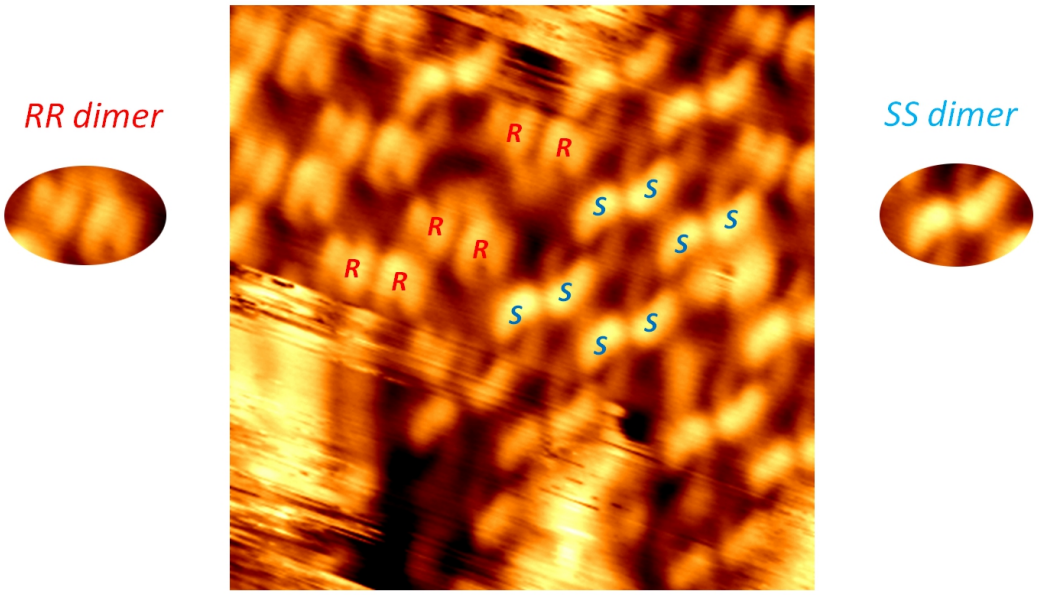

Figure 5.16: a) Insight of an island of as-deposited racemic serine on Cu(110) 5.0x5.0 nm^2, -781.5 mV, -0.410 nA. The chirality of some molecules are indicated, in order to highlight chiral sensitivity of the tips towards molecular chirality.

5.3 Conclusion

In this chapter it is shown that several manifestations of chirality occur when racemic serine is adsorbed on a Cu(110) surface. Through RAIRS no significant differences in the chemical state and in the adsorption geometry of serine in its racemic form with respect to the enantiopure systems, studied in chapter 4 of this thesis, are found. The LEED pattern at room temperature reveals incomplete chiral resolution of the enantiomers, as well as reduced long-range ordering of the self-assembled molecules. These aspects are confirmed with real-space investigations performed with STM. A tendency towards separation into enantiopure dimers, rows and small domains is observed. Chiral resolution occurs when molecules possess a high mobility, i.e. at low coverages, or as a consequence of a thermal treatment of the sample. Hence it is assumed that chiral resolution represents the thermodynamically favoured state. In addition, kinetically stable states, protected by an energy barrier into a local minimum, are identified, especially in as-deposited adlayers. In these metastable states, specific heterochiral recognition events take place between homochiral dimers and single molecules with differing handedness. Four kinds of trimers are observed. A tentative molecular positioning is proposed for the boundaries between mirror-image domains and for the metastable trimers, whose relative stability might be caused by possible hydrogen bonds involving

hydroxyl and amino groups. Furthermore, it is illustrated that it is possible to map the chirality on a molecule-by-molecule basis via STM. Finally, it is shown that the tip-molecule interactions can occur in a very enantiospecific manner, with distinctive and non-mirroring STM intensities arising from molecules with opposite chiralities.

5.4 Methods section

The RAIRS and LEED experiment have been performed in the chamber dedicated to RAIRS (section 3.4.1), while the STM images have been collected via both the Specs and Omicron STMs (sections 3.4.2 and 3.4.3, respectively). RS-serine (purity > 98%) is supplied Sigma Aldrich and used as received. The molecular source is held in a glass crucible, wrapped in a tantalum wire with a diameter of 0.25 mm, with which the crucible is resistively heated. A current of 0.85 A is required to induce the sublimation of racemic serine molecules. This corresponds to a sublimation temperature of 383 K. When necessary, the sample is annealed resistively, and the sample temperature is controlled via a thermocouple attached to the UHV manipulators holding the crystal. This device is thus not able to provide the exact temperature of the surface. However, good temperature estimations are possible thanks to previous calibrations of the thermocouple. In summary, the annealing temperatures given herein can be accepted with an error of ± 10 K.

References for chapter 5

[1] H. Caner and I. Agranat, "Chiral Drugs," *Enantiomer: A Journal of Sterochemistry*, vol. 7, no. 6, pp. 405–406, 2002.

[2] I. Agranat, H. Caner, and J. Caldwell, "Putting chirality to work: the strategy of chiral switches," *Nature Reviews. Drug discovery*, vol. 1, no. 10, pp. 753–68, 2002.

[3] M. R. Islam, J. G. Mahdi, and I. D. Bowen, "Pharmacological importance of stereochemical resolution of enantiomeric drugs," *Drug safety*, vol. 17, no. 3, pp. 149–65, 1997.

[4] W. H. Porter, "Resolution of chiral drugs," *Pure and Applied Chemistry*, vol. 63, no. 8, 1991.

[5] G. Natta, P. Pino, P. Corradini, F. Danusso, E. Mantica, G. Mazzanti, and G. Moraglio, "Crystalline High Polymers of α-Olefins," *Journal of the American Chemical Society*, vol. 77, no. 6, pp. 1708–1710, 1955.

[6] P. Pino and R. Mülhaupt, "Stereospecific Polymerization of Propylene: An Outlook 25 Years after Its Discovery," *Angewandte Chemie (International ed. in English)*, vol. 19, no. 11, pp. 857–875, 1980.

[7] M. M. Green, N. C. Peterson, T. Sato, A. Teramoto, R. Cook, and S. Lifson, "A helical polymer with a cooperative response to chiral information," *Science*, vol. 268, no. 5219, pp. 1860–6, 1995.

[8] H. H. Brintzinger, D. Fischer, R. Mülhaupt, B. Rieger, and R. M. Waymouth, "Stereospecific Olefin Polymerization with Chiral Metallocene Catalysts," *Angewandte Chemie (International ed. in English)*, vol. 34, no. 11, pp. 1143–1170, 1995.

[9] B. M. Trost, "Asymmetric catalysis: an enabling science," *Proceedings of the National Academy of Sciences of the United States of America*, vol. 101, no. 15, pp. 5348–55, 2004.

[10] L. Pérez-García and D. B. Amabilino, "Spontaneous resolution, whence and whither: from enantiomorphic solids to chiral liquid crystals, monolayers and macro- and supra-molecular polymers and assemblies," *Chemical Society Reviews*, vol. 36, no. 6, pp. 941–67, 2007.

[11] D. K. Kondepudi and K. E. Crook, "Theory of Conglomerate Crystallization in the Presence of Chiral Impurities," *Crystal Growth & Design*, vol. 5, no. 6, pp. 2173–2179, 2005.

[12] R. M. Hazen and D. S. Sholl, "Chiral selection on inorganic crystalline surfaces," *Nature Materials*, vol. 2, no. 6, pp. 367–74, 2003.

[13] J. D. Horvath and A. J. Gellman, "Enantiospecific Desorption of R- and S-Propylene Oxide from a Chiral Cu(643) Surface," *Journal of the American Chemical Society*, vol. 123, no. 32, pp. 7953–7954, 2001.

[14] J. D. Horvath and A. J. Gellman, "Enantiospecific Desorption of Chiral Compounds from Chiral Cu(643) and Achiral Cu(111) Surfaces," *Journal of the American Chemical Society*, vol. 124, no. 10, pp. 2384–2392, 2002.

[15] Y. Yun and A. J. Gellman, "Enantioselective separation on naturally chiral metal surfaces: D,L-aspartic acid on Cu(3,1,17)(R&S) surfaces," *Angewandte Chemie (International ed. in English)*, vol. 52, no. 12, pp. 3394–7, 2013.

[16] I. Weissbuch, M. Berfeld, W. Bouwman, K. Kjaer, J. Als-Nielsen, M. Lahav, and L. Leiserowitz, "Separation of Enantiomers and Racemate Formation in Two-Dimensional Crystals at the Water Surface from Racemic α-Amino Acid Amphiphiles: Design and Structure," *Journal of the American Chemical Society*, vol. 119, no. 5, pp. 933–942, 1997.

[17] C. J. Eckhardt, N. M. Peachey, D. R. Swanson, J. M. Takacs, M. A. Khan, X. Gong, J.-H. Kim, J. Wang, and R. A. Uphaus, "Separation of chiral phases in monolayer crystals of racemic amphiphiles," *Nature*, vol. 362, no. 6421, pp. 614–616, 1993.

[18] F. Stevens, D. J. Dyer, and D. M. Walba, "Direct Observation of Enantiomorphous Monolayer Crystals from Enantiomers by Scanning Tunneling Microscopy," *Angewandte Chemie (International ed. in English)*, vol. 35, no. 8, pp. 900–901, 1996.

[19] L. Atanasoska, J. Buchholz, and G. Somorjai, "Low-energy electron diffraction study of the surface structures of adsorbed amino acid monolayers and ordered films deposited on copper crystal surfaces," *Surface Science*, vol. 72, no. 1, pp. 189–207, 1978.

[20] R. Fasel, M. Parschau, and K.-H. Ernst, "Amplification of chirality in two-dimensional enantiomorphous lattices," *Nature*, vol. 439, no. 7075, pp. 449–52, 2006.

[21] M. Ortega Lorenzo, C. Baddeley, C. Muryn, and R. Raval, "Extended surface chirality from supramolecular assemblies of adsorbed chiral molecules," *Nature*, vol. 404, no. 6776, pp. 376–9, 2000.

[22] M. Forster, M. S. Dyer, M. Persson, and R. Raval, "Probing conformers and adsorption footprints at the single-molecule level in a highly organized amino acid assembly of (S)-proline on Cu(110)," *Journal of the American Chemical Society*, vol. 131, no. 29, pp. 10173–81, 2009.

[23] K.-H. Ernst, "Supramolecular Surface Chirality," in *Supramolecular Chirality* (M. Crego-Calama and D. N. Reinhoudt, eds.), no. February, ch. 6, pp. 209–252, Berlin, Heidelberg: Springer, 2006.

[24] J. Elemans, I. De Cat, H. Xu, and S. De Feyter, "Two-dimensional chirality at liquid-solid interfaces," *Chemical Society Reviews*, vol. 38, no. 3, pp. 722–36, 2009.

[25] I. Weissbuch and M. Lahav, "Crystalline architectures as templates of relevance to the origins of homochirality," *Chemical Reviews*, vol. 111, no. 5, pp. 3236–67, 2011.

[26] N. V. Richardson, "Adsorption-induced chirality in highly symmetric hydrocarbon molecules: lattice matching to substrates of lower symmetry," *New Journal of Physics*, vol. 9, no. 10, p. 395, 2007.

[27] R. Raval, "Chiral expression from molecular assemblies at metal surfaces: insights from surface science techniques," *Chemical Society Reviews*, vol. 38, no. 3, pp. 707–21, 2009.

[28] A. González-Campo and D. B. Amabilino, "Biomolecules at interfaces: chiral, naturally," *Topics in Current Chemistry*, vol. 333, no. March, pp. 109–56, 2013.

[29] S. Mann, D. D. Archibald, J. M. Didymus, T. Douglas, B. R. Heywood, F. C. Meldrum, and N. J. Reeves, "Crystallization at Inorganic-organic Interfaces: Biominerals and Biomimetic Synthesis," *Science*, vol. 261, no. 5126, pp. 1286–1292, 1993.

[30] Y. Izumi, "Modified Raney Nickel (MRNi) Catalyst: Heterogeneous Enantio-Differentiating (Asymmetric) Catalyst," *Advances in Catalysis*, vol. 32, p. 215, 1983.

[31] C. J. Baddeley, "Fundamental investigations of enantioselective heterogeneous catalysis," *Topics in Catalysis*, vol. 25, no. November, pp. 17–28, 2003.

[32] Z. Ma and F. Zaera, "Competitive chemisorption between pairs of cinchona alkaloids and related compounds from solution onto platinum surfaces," *Journal of the American Chemical Society*, vol. 128, no. 51, pp. 16414–16415, 2006.

[33] E. R. Jarvo and S. J. Miller, "Amino acids and peptides as asymmetric organocatalysts," *Tetrahedron*, vol. 58, no. 13, pp. 2481–2495, 2002.

[34] R. Lévy, "Peptide-capped gold nanoparticles: towards artificial proteins," *Chembiochem*, vol. 7, no. 8, pp. 1141–5, 2006.

[35] L.-P. Xu, Y. Liu, and X. Zhang, "Interfacial self-assembly of amino acids and peptides: scanning tunneling microscopy investigation," *Nanoscale*, vol. 3, no. 12, pp. 4901–15, 2011.

[36] A. Kühnle, T. R. Linderoth, B. Hammer, and F. Besenbacher, "Chiral recognition in dimerization of adsorbed cysteine observed by scanning tunnelling microscopy," *Nature*, vol. 415, no. 6874, pp. 891–3, 2002.

[37] M. Lingenfelder, G. Tomba, G. Costantini, L. Colombi Ciacchi, A. De Vita, and K. Kern, "Tracking the chiral recognition of adsorbed dipeptides at the single-molecule level," *Angewandte Chemie (International ed. in English)*, vol. 46, no. 24, pp. 4492–5, 2007.

[38] Q. Chen, C. W. Lee, D. J. Frankel, and N. V. Richardson, "The formation of enantiospecific phases on a Cu{110} surface," *PhysChemComm*, vol. 2, no. 9, p. 41, 1999.

[39] N. Liu, S. Haq, G. R. Darling, and R. Raval, "Direct Visualization of Enantiospecific Substitution of Chiral Guest Molecules into Heterochiral Molecular Assemblies at Surfaces," *Angewandte Chemie (International ed. in English)*, vol. 119, no. 40, pp. 7757–7760, 2007.

[40] T. Eralp, A. Ievins, A. Shavorskiy, S. J. Jenkins, and G. Held, "The importance of attractive three-point interaction in enantioselective surface chemistry: stereospecific adsorption of serine on the intrinsically chiral Cu{531} surface," *Journal of the American Chemical Society*, vol. 134, no. 23, pp. 9615–21, 2012.

[41] T. Eralp, A. Cornish, A. Shavorskiy, and G. Held, "The Study of Chiral Adsorption Systems Using Synchrotron-Based Structural and Spectroscopic Techniques: Stereospecific Adsorption of Serine on Au-Modified Chiral Cu{531} Surfaces," *Topics in Catalysis*, vol. 54, no. 19-20, pp. 1414–1428, 2011.

[42] T. Eralp, A. Shavorskiy, Z. V. Zheleva, G. Held, N. Kalashnyk, Y. Ning, and T. R. Linderoth, "Global and local expression of chirality in serine on the Cu{110} surface," *Langmuir*, vol. 26, no. 24, pp. 18841–51, 2010.

[43] J. Williams, S. Haq, and R. Raval, "The bonding and orientation of the amino acid l-alanine on Cu{110} determined by RAIRS," *Surface Science*, vol. 368, no. 1-3, pp. 303–309, 1996.

[44] M. Forster and R. Raval, "Simple Rules Steer Complex Chiral Organisations on Surfaces : Amino-acids on Cu(110)," *in preparation*.

Chapter 6

The 2D achiral organisation of chiral molecules: S-valine on Cu(110)

6.1 Introduction

The conferring of single handedness to a defined surface originally deprived of chirality presents interesting implications in terms of the chiral recognition phenomena that are specific to environments confined in two dimensions. One of the ways used to imprint chirality upon an achiral surface consists of using adsorbers with a known handedness. As it has been reviewed in section 1.7, only the utilisation of chiral modifiers guarantees the formation of *global chirality* on the whole surface, while achiral and prochiral adsorbers would produce, even though possibly chiral domains at a local scale, an overall racemic system [1]. The use of organic adsorbers with a given chirality represents thus the simplest method by which chirality is bestowed upon a surface.

The field of enantioselective heterogeneous catalysis [2] embodies the main area of application of this branch of research. Examples worth noting include the asymmetric hydrogenation of α-ketoesters by means of platinum functionalised with chiral cinchona alkaloids [3, 4] and the enantioselective hydrogenation of β-ketoesters and 2-alkanones on nickel chirally modified with tartaric acid [5–7]. With regard to the latter example, the adsorption of (R,R)-tartaric acid on the Ni(110) surface has been shown to take place with a profound preference (6 kJ/mol) for one of the two possible mirror footprints, a mechanism that might underpin the origin of the enantioselective catalytic activity of the adsorbate [8]. Furthermore, in some cases the functionalisation through chiral ligands has been calculated to distort the underlying metal structure in a chiral manner. This is the case of gold clusters capped with chiral thiols [9], in which the metal-based electronic transitions (MBET), whose intensities are detected via chiroptical spectroscopic techniques [10], are allegedly influenced by the chirality of the adsorbed ligands [11].

For the above-mentioned reasons the studies upon the adsorption of chirally pure biomolecules, such as amino acids, on defined high-symmetry metal surfaces have produced a wealthy area of research that has allowed manifold expressions of chirality to be observed and classified. For instance, the competitive molecule-molecule and substrate-molecule interactions may induce diverse chemical forms of the adsorbers, coverage and temperature specific adsorption footprints and numerous possibilities for long-range organisation [12]. Furthermore, the observation of adsorbate-induced metal surface reconstructions testifies a true transfer of chirality from the molecular system to the underlying surface. As an example, the adsorption of simple enantiopure amino acids like glycine, alanine and lysine on copper surfaces that originally expose the (001) face has been shown to cause a displacement of the outermost metallic atoms to give rise to a faceting with (3 1 17) symmetry. This surface symmetry is intrinsically chiral and possesses a given chirality depending on the handedness of the adsorbates [13–16].

On the Cu(110) surface, the substrate utilised in the present study, the μ_3 adsorption, mediated by the carboxylate and amino moieties, is the molecular geometry most commonly adopted by amino acids and has been shown to intrinsically define the footprint chirality, or *footedness*. This kind of chirality bears characteristics that are in principle autonomous from the molecular chirality of the amino acid considered, with the possibility of defining chiral recognition phenomena at the footprint level even with systems that are homogeneously chiral [17] (see section 1.7.1).

6.1.1 The amino acid valine

Valine is a branched-chain, nonpolar amino acid, possessing an isopropyl moiety as its residual group (figure 6.1). Its S-form is an essential amino acid for humans, since it cannot be synthesised in vivo via precursors [18]. Its derivative S-valinol, which possesses a hydroxyl group in place of the carboxylic moiety of the parent amino acid, is a precursor of chiral ligands that are used in asymmetric catalysis [19]. The importance of the amino acid valine in the biochirogenesis research field is linked, to a certain extent, to the retrieval of α-methyl amino acids in *ee* on the famous Murchison meteorite [20]. It has been demonstrated, in fact, that L-α-methylisoleucine, one of the compounds found on the meteorite, can react with 3-methyl-2-oxobutanoate, in presence of copper-based catalysts, to yield small *ee*s of S-valine. These *ee*s can be amplified further on the basis of the different solubility properties that enantiopure and racemic crystals possess [21, 22]. Furthermore, racemic valine derivatives, namely (R,S)-valine-*N*-carboxyanhydrides (Val-NCA), have been proven to polymerise stereospecifically into isotactic oligopeptides via the intermediate formation of racemic β-sheet secondary structures [23]. NCAs of α-amino acids, albeit unstable compounds,

are in fact thought to be precursors for the formation of early biologically relevant peptides [24, 25]. Interestingly, enantioselective adsorption of valine has also been demonstrated to occur on oxide thin films (TiO_2) that are rendered chiral via their deposition on top of gold-supported self-assembled monolayers of chiral molecules [26, 27].

Figure 6.1: a,b) The molecular representation of the amino acid valine in its S- and R- forms, respectively.

On the Cu(110) surface, the amino acid S-norvaline, a constitutional isomer of S-valine that possesses a non-branched propyl chain as residual group, has been shown to undergo deprotonation at the carboxylic site upon adsorption, and to adopt a coverage-dependent adsorption geometry consisting of a μ_3-μ_2 evolution as the coverage increases, signalled by the emergence of non-equivalent interactions between the two carboxylate oxygen atoms and the surface atoms, as revealed by RAIRS. The latter geometry is also associated with a molecular self-organisation with a (3x2) periodicity [28].

The adsorption of valine in its enantiopure form on the Cu(110) surface has been previously investigated in the group [29]. RAIRS experiments demonstrate that valine molecules undergo dehydrogenation at the carboxylic moiety, thus assuming an anionic chemical form on the surface. No coverage or temperature-dependent polymorphism is observed, up to a temperature of 373 K. Outcomes of STM experiments reveal the formation of symmetry-breaking unidirectional assemblies, whose chirality is dictated by the enantiomers considered (figure 6.2a,b). The unit cells formed by as-deposited S- and R-valine on Cu(110) are described by the matrices (0 7, -2 -1) and (0 7, -2 1), respectively, as confirmed via LEED (figure 6.2c,d). Each unit cell is populated with four valine molecules, which typically give rise to four distinguishable signals with varying intensities. Namely, as visible in STM images of figures 6.2a,b, in each unit cell two bright rounded features are present, along with two additional signals that possess a weaker intensity and a more elongated shape. The connection between the STM appearance of the enantiopure valine adlayer and the molecular geometry of the single molecules filling the unit cell is not understood. According to preliminary theoretical calculations that have been performed on this system, the weakest intensities might originate from valine molecules that are bound via a μ_3 geometry, but with the carboxylate oxygen atoms placed across the long-bridge surface direction, i.e. roughly parallel to the [001] direction [29].

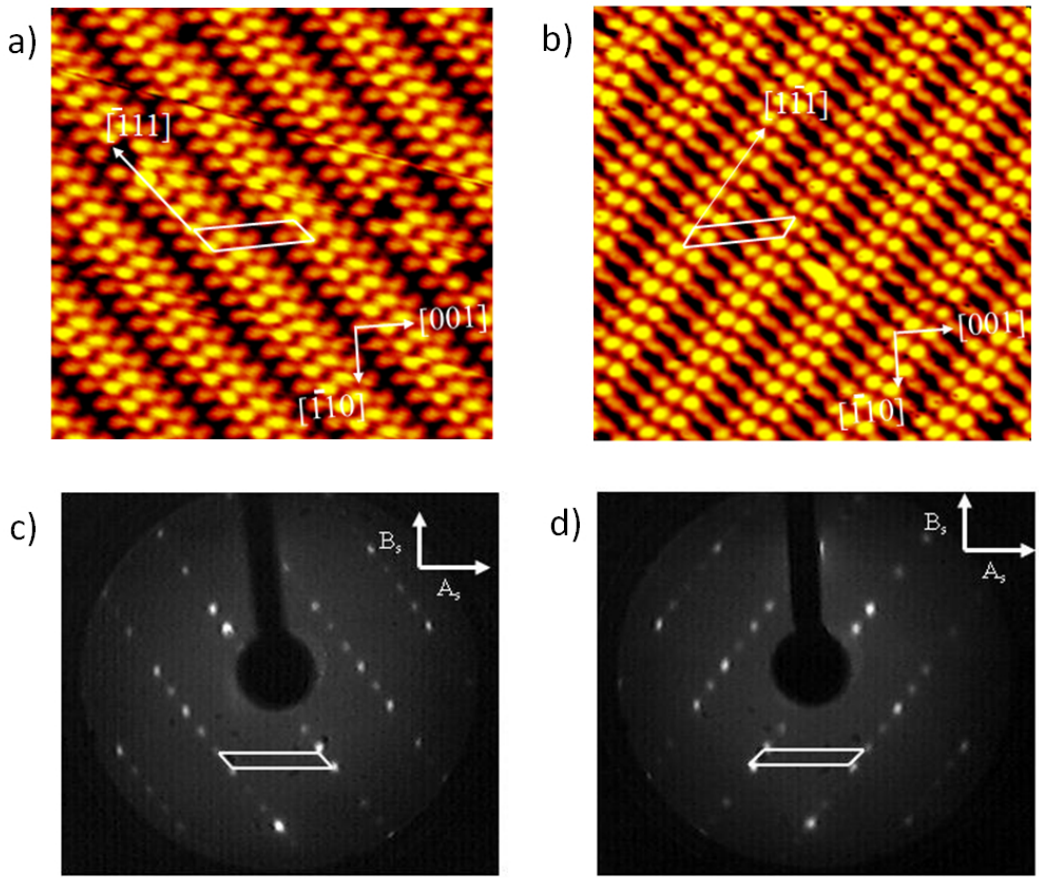

Figure 6.2: a,b) STM images of as-dosed S and R-valine on Cu(110), respectively. 13.6x13.6 nm^2, V=-880.0 mV, I=-0.370 nA. In both images, the surface high-symmetry axes, the unit cell and the direction of the unidimensional chains are indicated. c,d) LEED patterns acquired on as-dosed S and R-valine on Cu(110), respectively. Energy = 44 eV. The molecular unit cell in reciprocal space is indicated. A_S and B_S denote the substrate vectors in reciprocal space. Figure adapted from [29].

When an enantiopure valine adlayer is annealed up to 473 K a new phase is clearly observed. It possesses achiral characteristics at the organisational level, namely a (nx2) repeat unit is detected [29]. However, on the basis of the available STM and LEED data, it is not possible to ascertain the exact repeat unit along the [1-10] direction. This phase, in fact, proves sensitive to electron beam damage, a characteristic that renders LEED characterisations challenging. In addition, the STM experiments are prone to significant dimensional error along the *(x,y)* directions, arising from the scanner calibration procedure. This is particularly true for systems possessing features at the sub-nanometric scale. Specifically, (3x2) and (4x2) unit cells, whose sides placed along the close-packed surface direction would differ by only 2.56 Å and would be extremely difficult to distinguish in an STM investigation.

In this chapter the achiral high-temperature phase displayed by enantiopure S-valine on Cu(110) is systematically studied. The integrity of the molecular adlayer after thermal treatments is checked with RAIRS. Furthermore, by means of LEED and STM, the repeat unit cell is determined. On the basis of these experimental results combined with theoretical calculations performed on the single adsorbed S-valine molecule and extended molecular adlayers, a favoured geometrical model is proposed and discussed.

6.2 Experimental results

6.2.1 RAIRS

The achiral organisation of S-valine on Cu(110) is achieved progressively as a result of a thermal treatment of as-deposited samples. Specifically, a complete conversion from the chiral to the achiral phase is obtained after the sample is annealed up to 473 K. In order to verify the chemical state of the ad-molecules after each stage of annealing, RAIR spectra are acquired continuously after the molecular deposition and while the crystal is annealed in a step-wise manner. Each spectrum in figure 6.3 is collected at room temperature, meaning that after an annealing process is carried out the crystal is allowed to cool down to room temperature before the acquisition of the relevant spectrum. This procedure, while assuring an improved signal processing, since the background IR spectrum is always collected on the clean sample at ambient temperature, guarantees a better comparison with the STM investigations, that are also carried out at room temperature.

In table 6.1 the detected vibrational bands are assigned to specific molecular motions, on the basis of precedent RAIRS studies performed on amino acid overlayers on Cu(110) [30–32], as well as on IR investigations carried out upon metal-$(Val)_2$ complexes [33] and upon matrix-isolated neutral valine conformers [34].

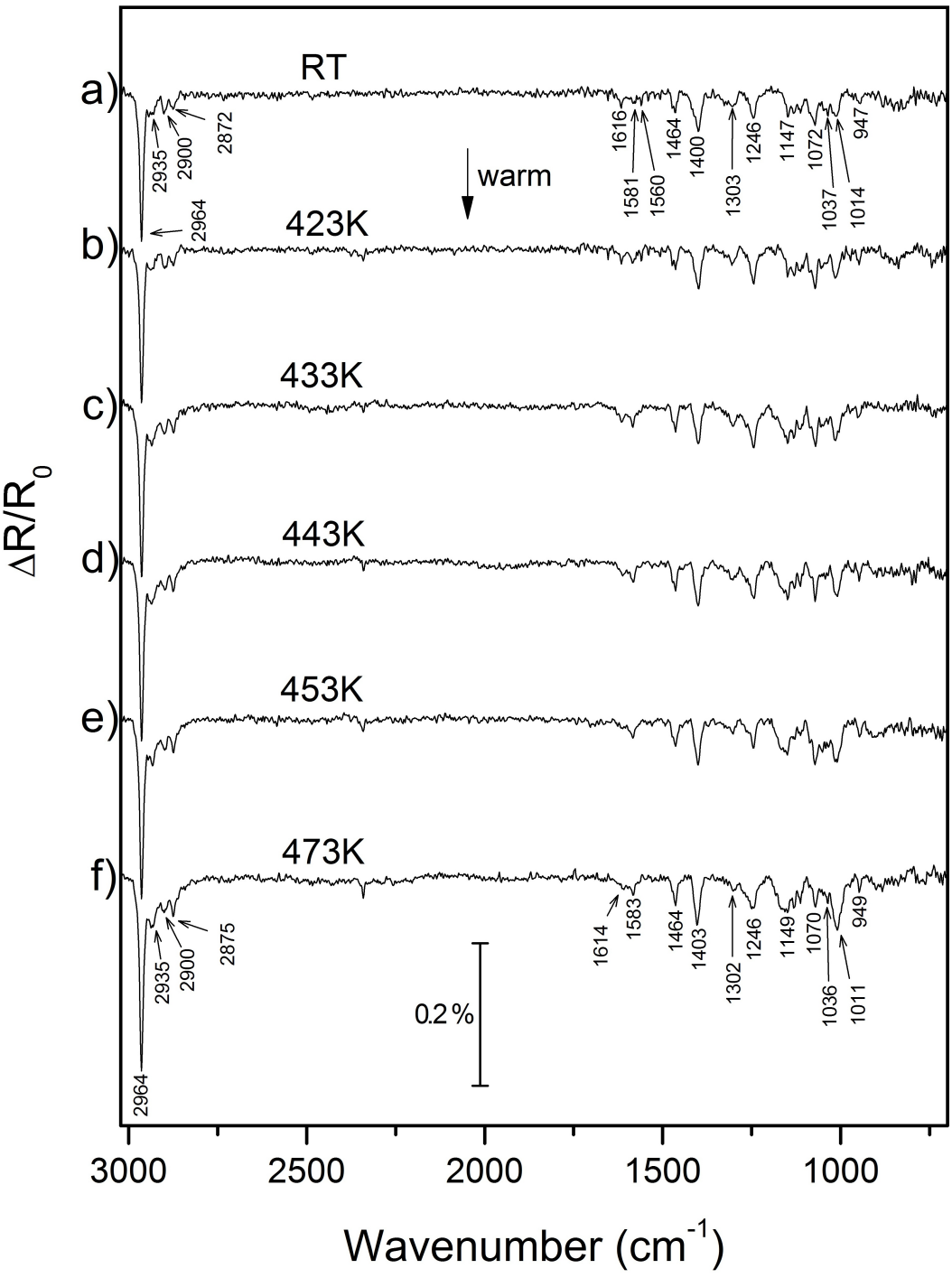

Figure 6.3: a) RAIR spectrum acquired after the deposition of S-valine monolayer on Cu(110). b-f) RAIR spectra acquired after the monolayer is annealed up to the temperatures of 423 K, 433 K, 443 K, 453 K and 473 K, respectively. All the spectra are collected at room temperature.

The as-deposited S-valine layer reveals a strong adsorption peak at 2964 cm^{-1}, with an intensity over 0.2% (figure 6.3a). This is associated to the $\nu_{as}(CH_3)$ asymmetric stretch produced in the methyl moieties present in the residual group of valine, and indicates that the dipole moments involved in these vibrations have a significant component in the direction normal to the surface. Another important band is located at 1400 cm^{-1}, which is attributed to the $\nu_s(OCO^-)$ symmetric stretch. This spectral feature, along with the absence of the $\nu(CO)$ carbonyl stretch ($\sim$1700 cm^{-1}), demonstrates that S-valine molecules undergo deprotonation at the carboxylic site upon adsorption. The anionic chemical form of S-valine molecules is further confirmed by the simultaneous absence of a signal at $\sim$1660 cm^{-1}, expected from a $\nu_{as}(NH_3^+)$ stretching mode of a potential ammonium group present in the zwitterionic form of amino acids. A weak signal at 1616 cm^{-1} is also present and is attributed to the $\nu_{as}(OCO^-)$ asymmetric stretch. This peak was observed in the same spectral region for the amino acids alanine [30] and glycine [31] in specific circumstances: in those cases, the appearance of this band was attributed to a μ_3-μ_2 evolution of the molecular geometry, in which one of the carboxylate oxygen atom moves away from the surface. In the present case, however, this interpretation cannot be brought forward, given the weakness of the associated peak. Only a slight asymmetry in the surface coordination of the oxygen atoms can be hypothesised.

Following step-wise annealing treatments of the S-valine adlayer, no significant changes are detected up to the annealing temperature of 453 K (figure 6.3b-e). Finally, after the sample has undergone an annealing process up to 473 K, which, as will be shown in sections 6.2.2 and 6.2.3 via LEED and STM investigations, induces a complete phase transition at the organisational level, a slight change is visible in the resulting spectrum in figure 6.3f. The vibrational peaks that show a difference in comparison with the as-deposited sample are found in the spectral region 1000-1200 cm^{-1}, which is linked to the skeletal part of amino acids. Namely, the peaks at 1011 and 1070 cm^{-1}, which show an increase and a decrease, respectively, upon annealing at 473 K, are mainly related to vibrations of the CCN amino acidic backbone, coupled with additional molecular vibrations. None of the bands indicative of the surface-molecule coordination and of the chemical form of the adsorbed molecules show detectable modifications upon annealing. Furthermore, the intensities of the major peaks, in particular the $\nu_{as}(CH_3)$ at 2964 cm^{-1}, do not show reductions upon any of the annealing steps, thus any chemical changes of the adlayer, e.g. a thermal decomposition of the molecules, can be ruled out on this basis. For a detailed attribution of the relevant peaks to the molecular vibrations from which they originate in each phase the reader is directed to table 6.1.

Wavenumber (cm^{-1}), LT phase[1]	**Wavenumber (cm^{-1}), HT phase[2]**	**Molecular vibration**
2964	2964	$\nu_{as}(CH_3)$ [33, 34]
2935	2935	$\nu(CH)$ [33]
2872	2875	$\nu_s(CH_3)$ [33]
1616	1614	$\nu_{as}(OCO^-)$ [30, 31]
1581	1583	$\delta_s(NH_2)$ [30, 31]
1464	1464	$\delta_{as}(CH_3)$ [30]
1400	1403	$\nu_s(OCO^-)$ [30–32]
1303	1302	$\delta(CH) + \nu_s(OCO^-)$ [30, 34]
1147	1149	$\omega(NH_2)$ [30]
1072	1070	$\nu_{as}(CCN)$ [30]
1037	1036	$\nu(CN) + \nu_s(OCO^-)$ [30]
1014	1011	$\rho(CH_3) + \nu(CC) + \omega(NH_2)$ [33]
947	949	$\nu(CC)$ [34]

[1] As-deposited. [2] Following post-deposition annealing at 473 K.

Table 6.1: Assignments of the RAIRS bands (figure 6.3) to the molecular vibrations from which they are originated. The numerical values of the relevant wavenumbers refer to the spectra acquired on the as-dosed sample (LT phase, figure 6.3a) and on the sample after annealing at 473 K (HT phase, figure 6.3f). The assignments are based on previous literature of amino acid adsorption studies on Cu(110) [30–32] and on IR investigations of metal-$(Val)_2$ complexes [33] and matrix-isolated valine in neutral state [34]. Key for molecular vibrations: ν = stretch, δ = bend, ω = wag, ρ = rock. The symmetric or asymmetric nature of the molecular vibration is indicated respectively with the subscripts $_s$ or $_{as}$.

6.2.2 LEED

The long-range organisational properties of S-valine on the Cu(110) surface as a function of the annealing temperature is investigated via LEED. Figure 6.4 features the evolution of the LEED pattern produced by an S-valine adlayer upon deposition on Cu(110) (figure 6.4a) and after annealing to increasing temperatures, up to 473 K (figure 6.4b-d).

The as-deposited sample structure manifests a chiral on-surface organisation, confirming previous results [29], with a unit cell (0 7, -2 -1) in real space (figure 6.4a, *cf* figure 6.2c). This phase is found to be stable when the sample is annealed at 373 K (figure 6.4b). The emergence of a new phase, however, becomes clear when the annealing temperature is increased to 463 K, as shown in figure 6.4c. The novel diffraction spots, circled in red, reveal that an additional molecular phase emerges on the surface. Finally, when the sample is annealed to 473 K (figure 6.4d), the original chiral phase disappears, with the high-temperature phase remaining the only phase able to produce a diffraction pattern. The latter molecular organisation represents the main subject of the research presented in this chapter, and is analysed further in this and in the following sections.

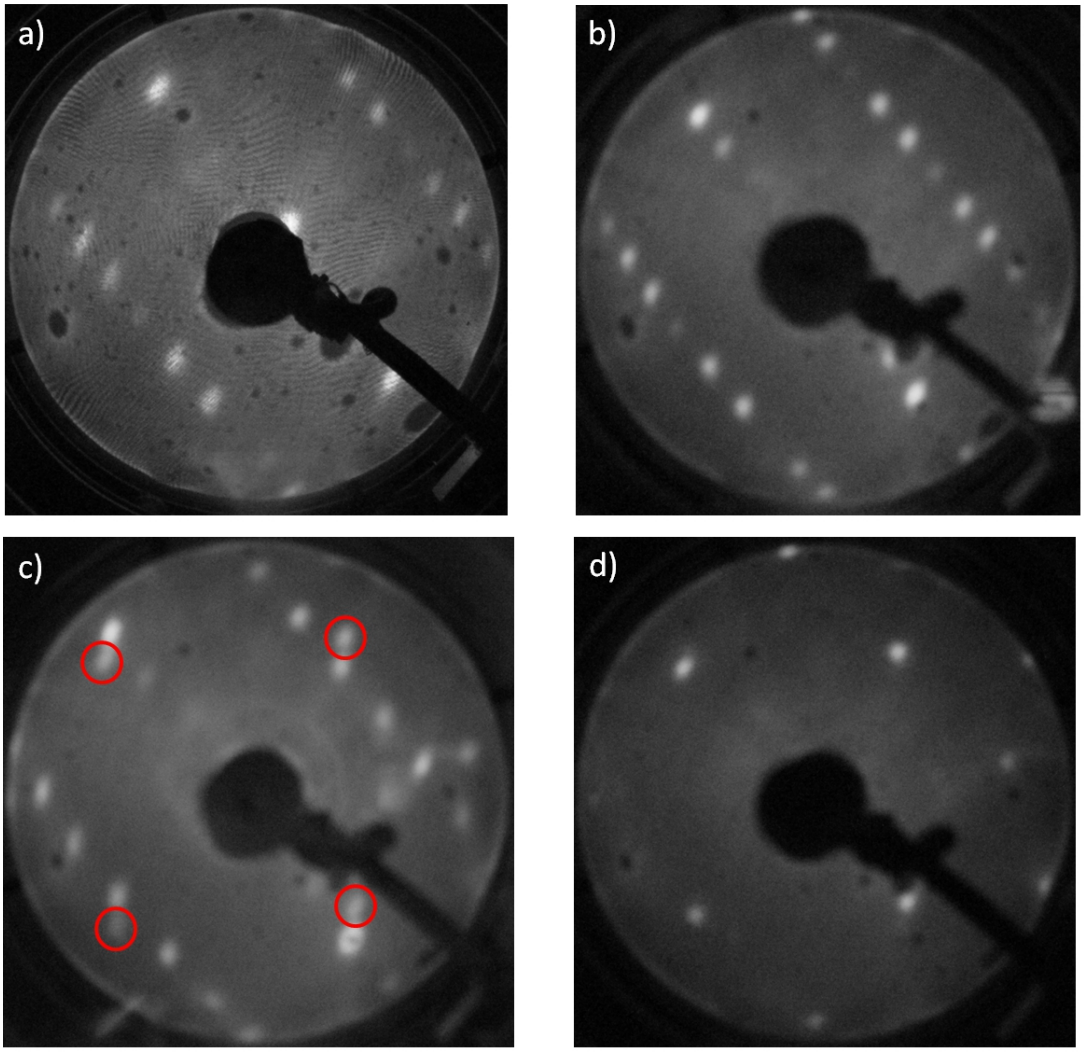

Figure 6.4: LEED patterns produced by S-valine adsorbed on the Cu(110) surface. All patterns are collected at room temperature. a) As-deposited S-valine, energy = 20 eV. b) Sample annealed at 373 K, energy = 23 eV. c) Sample annealed at 463 K, energy = 20 eV. The diffraction spots belonging to the high-temperature phase are circled in red. d) Sample annealed at 473 K, energy = 23 eV.

One of the main intrinsic difficulties that has been encountered during the LEED study of S-valine on Cu(110) consists in the damage that the beam of electrons causes to the molecular adlayer. This effect has been observed previously in the LEED study of weakly interacting molecular adlayers, and namely in amino acid monolayers on metal surfaces (see for example references [35, 36]). In particular, in this investigation it has been observed that long exposure times of the sample to the electron source causes the fading or the disappearance of the diffraction spots on the collecting screen: this is especially true for studies when relatively high energy electrons are used (> 25 eV). The resolution of the camera that is used to collect the LEED diffraction patterns is thus crucial, along with the promptness of the experimenter in collecting the data while the sample is exposed to the beam.

Figure 6.5 reproduces the LEED patterns originating from an S-valine/Cu(110) sample in its high-temperature achiral phase. The sample has been analysed following a post-deposition annealing up to 473 K, in a manner equivalent to the sample whose diffraction pattern is shown in figure 6.4d. Diffraction patterns resulting as outcomes of electron bombardment with increasing energies are displayed in figure 6.5a-e. In figure 6.5e the substrate unit cell in reciprocal space is indicated with a white rectangle. A (nx2) achiral long-range organisation is confirmed. In particular, a (3x2) organisation, with "zigzag distortion" is attributed to this phase.

The latter hypothesis is corroborated by the direct comparison between the pattern in figure 6.5 with the "distorted" (3x2) LEED pattern produced by enantiopure and racemic alanine on Cu(110) [12, 37] (see figure 6.6). The positional displacement shown by some diffraction spots along the [001] direction in reciprocal space testifies an imperfect molecular organisation in a (3x2) arrangement, with a partial loss of registry with the substrate unit cell. This phenomenon, widely observed in racemic and enantiopure alanine adlayers on the same surface, remains unclear [37]. Further insight on the long-range organisation of S-valine are given in the following section (6.2.3), in which the real-space molecular positioning is observed via STM. Moreover, interpretations on the origin of the loss of periodicity will be given in the following sections of this chapter, on the basis of DFT calculations and recently published experimental studies performed on the alanine/Cu(110) system [39, 40].

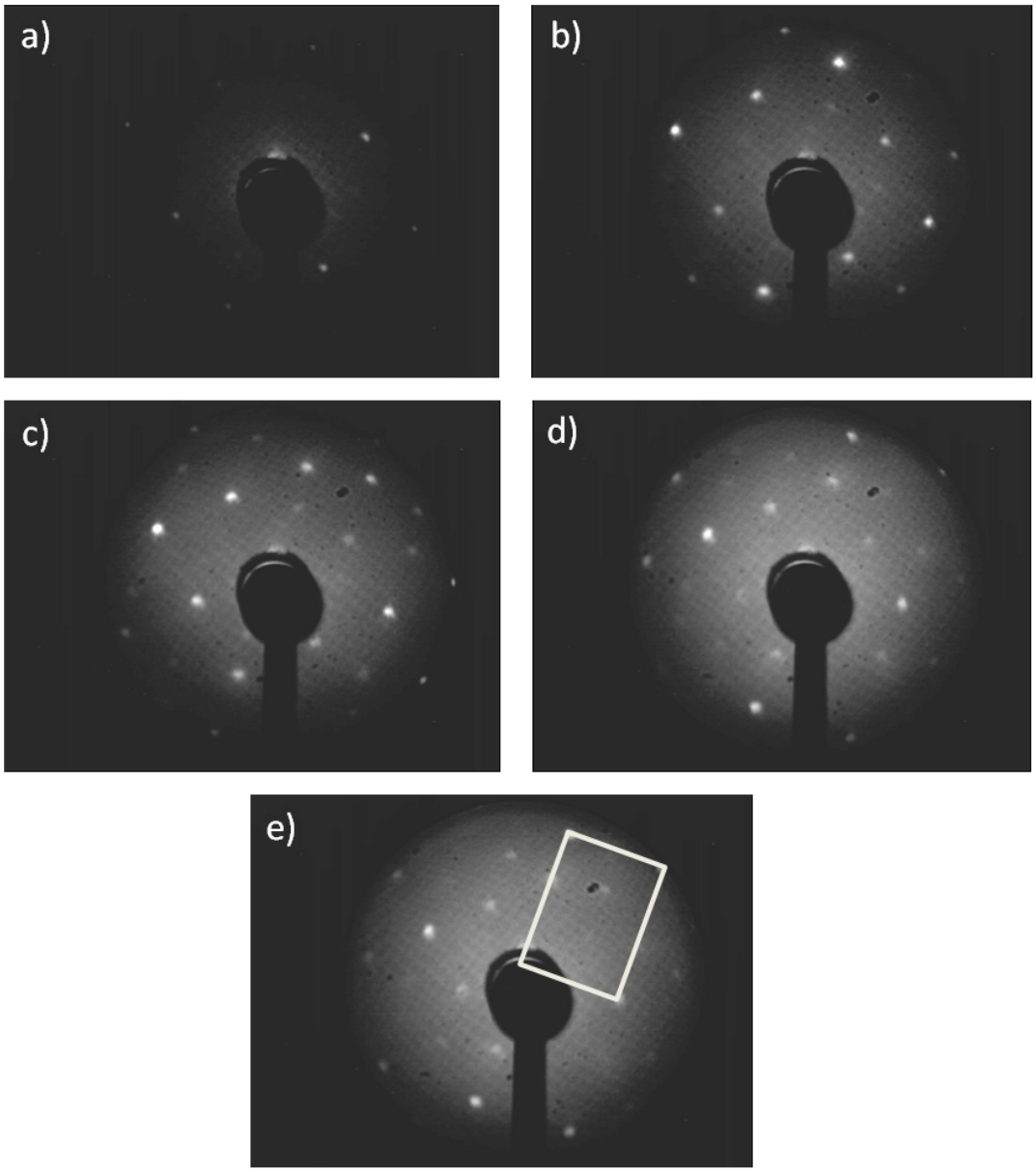

Figure 6.5: LEED patterns originated by S-valine adsorbed on the Cu(110) surface in its high-temperature phase, once the sample has been annealed to 473 K. All patterns are collected at room temperature. The beam energy varies as follows. a) Energy = 35 eV. b) Energy = 40 eV. c) Energy = 45 eV. d) Energy = 48 eV. e) Energy = 53 eV.

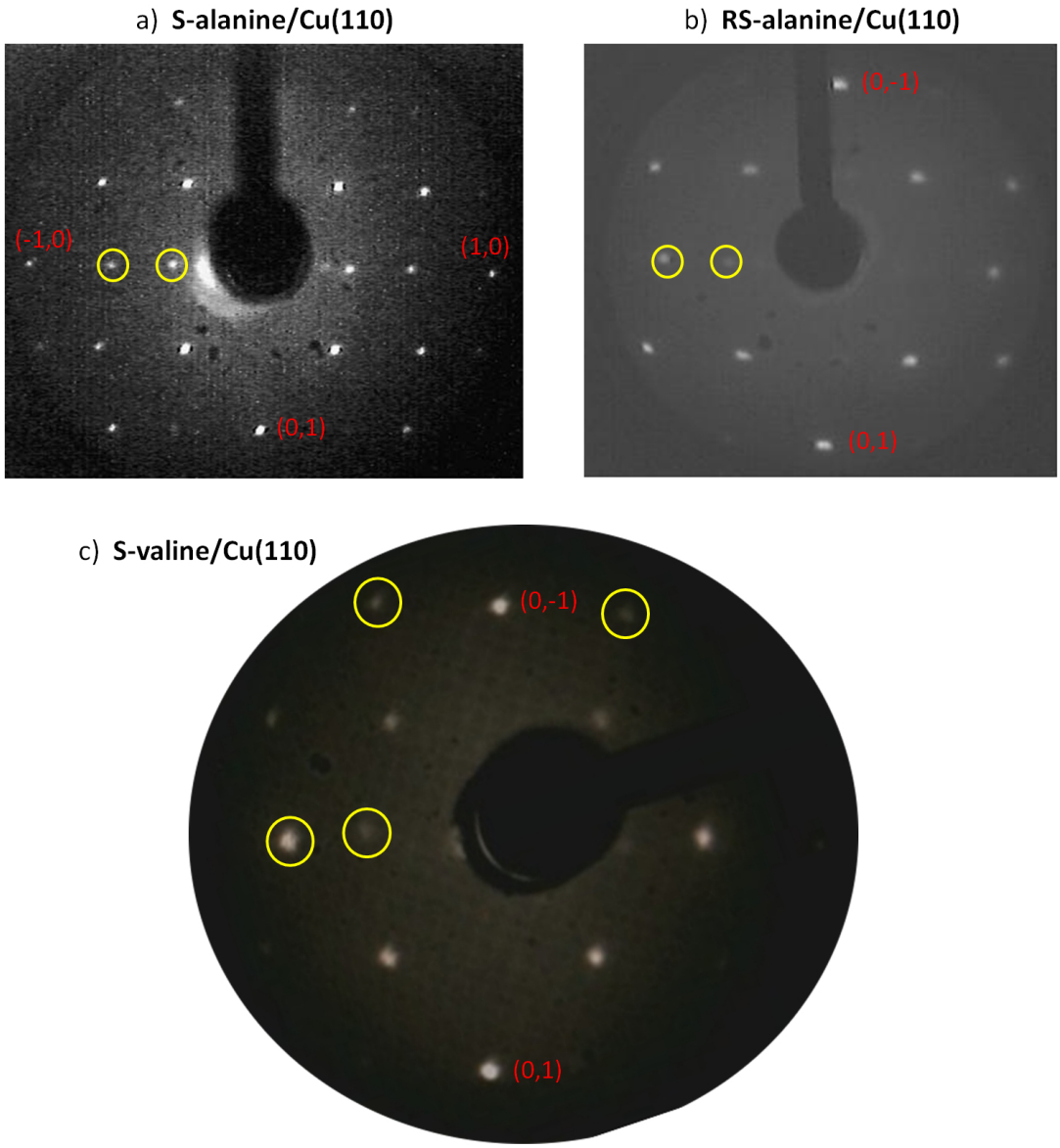

Figure 6.6: LEED patterns showing the "distorted" (3x2) periodicity of several amino acids adsorbed on Cu(110). a) Phase IV of S-alanine on Cu(110), annealed at 483 K, energy = 75 eV. Reproduced from [38]. b) RS-alanine on Cu(110) at submonolayer coverage, annealed at 423 K, energy = 29 eV. Reproduced from [37]. c) Achiral phase of S-valine on Cu(110), annealed at 473 K, energy = 45 eV (this work). Some "distorted" spots are circled in yellow in each pattern.

6.2.3 STM

The on-surface conversion from a chiral to an achiral organisation manifested by S-valine on Cu(110), as shown by the LEED characterisation (figure 6.4) can also be followed by means of STM. In the STM images of figure 6.7a,b it is shown that the molecular organisation evolves from a chiral organisation with unit cell (0 7, -2 -1) to an achiral arrangement. These images, which refer to a sample annealed to 453 K, interestingly show a partial chiral-achiral phase change, with the coexistence of both phases in the same image. This state of the sample is equivalent to the LEED pattern displayed in figure 6.4c. Interestingly, in the proximity of the phase boundaries, indicated by red dashed lines in the images of figure 6.7, some low-intensity regions are observed. These "holes" might be the indication of a local molecular rearrangement that might take place as a result of accommodating molecules belonging to different organisational phases. It is also noted that a possible reconstruction of the underlying surface might take place in areas where a local stress may play a role, as at the boundary between two different molecular phases. Finally, defects in the chiral phase, as indicated for example by the arrow in figure 6.7a, are visible. For a comparison, see the STM representation of the chiral phase in figure 6.2a. The origin of these defects is unknown, however a boundary effect on the chiral phase cannot be excluded.

The real-space characterisation of the achiral phase displayed by S-valine on the Cu(110) surface confirms the experimental findings resulting from the LEED investigation (see section 6.2.2). In figure 6.8a-c the outcomes of STM characterisation of three different areas are displayed. The sample has undergone an annealing process following molecular deposition up to 473 K. Each feature in STM images, on the basis of their dimensions, is attributed to a single adsorbed S-valine molecule.

The overall molecular organisation of S-valine in its high-temperature phase is confirmed to possess an ordered nature, as predicted by the production of diffraction patterns with defined spots (see figure 6.5). However, further analysis reveals the presence of a more complex arrangement, with irregularities within the molecular organisation and a certain degree of mismatch with the Cu(110) registry. As an example, the line profile presented in figure 6.8d, measured as indicated by the light blue line in figure 6.8c along the [1-10] surface direction, reveals discrepancies in the spacing between consecutive molecules placed along the close-packed surface direction. The numerical values placed on top of the line profile curve denote the distance between two consecutive peaks along the profile. These numbers are expressed in multiples of the close-packed periodicity of the surface, which equals 2.56 Å. As an example to clarify this point, the first number in figure 6.8d, 3.55, signifies that the distance between the first two peaks in the line profile is equal to 3.55 x 2.56 = 9.09 Å. It is observed that some of the distances, underlined with black double ended arrows, are equivalent to three lattice spacings along [1-10]. However, there are situations in which the distance between two

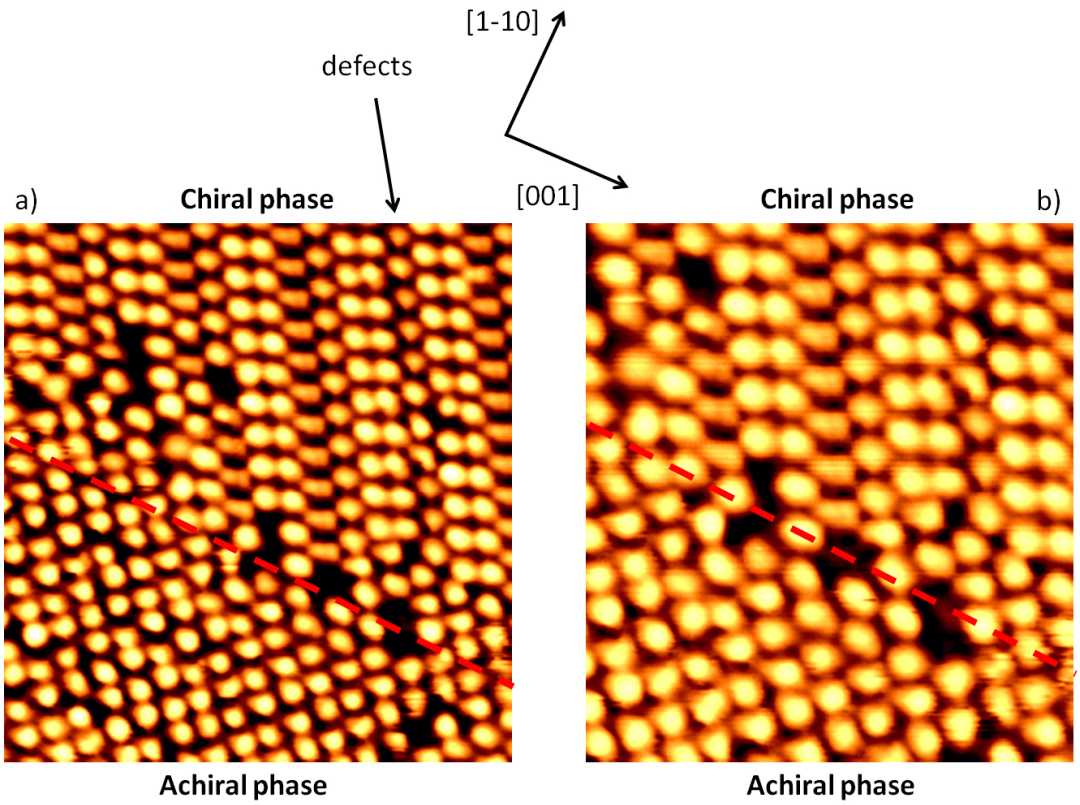

Figure 6.7: a,b) STM images showing boundaries between chiral (top) and achiral (bottom) phases of S-valine on Cu(110). The sample is annealed to 453 K. The dashed red lines are placed to indicate the phase boundaries, which run along the [001] surface direction. Defects in the chiral arrangement are visible, as indicated by the black arrow (*cf* figure 6.2a). a) 9.3x9.8 nm^2, V=+758.0 mV, I=+0.540 nA. b) 6.5x7.2 nm^2, V=+758.0 mV, I=+0.570 nA.

adjacent peaks differs significantly from that value. These occurrences are underlined with red double ended arrows in figure 6.8d. This rough measurement on an STM image, albeit not strictly accurate in determining the molecular positioning, given that it is generally unknown which part of the molecule produces the highest STM signal (i.e. the peak in a line profile), provides us with a confirmation of the imperfections with which the (3x2) structure is formed.

The latter aspect is verified further when a net with (3x2) periodicity is superimposed on an STM image collected on the S-valine/Cu(110) high temperature phase (figure 6.9). More precisely, the net is created through the repeat of the original vectors, indicated in blue and red at the centre of figure 6.9, which are equal, respectively, to 3 short-bridge lattice spacings (7.68 Å) and 2 long-bridge lattice spacings (7.23 Å). It is noted that the full (3x2) periodicity is not adhered to in areas of few nm^2 containing tens of molecules, such as the one shown in figure 6.9. This is in agreement with similar findings in the cases of enantiopure and racemic alanine on Cu(110) [37], and might be the origin of the "zigzag distortion" observed in the LEED patterns (figure 6.5). In the remaining part of this section a more detailed study of this non-canonical (3x2) arrangement will be attempted by means of the available STM images of this phase.

A more in-depth analysis of the STM images allows further insights to be gained into the nature of the (3x2) structure adopted by S-valine on the Cu(110) surface. As highlighted in figure 6.8, clearly there are points in which the three-fold periodicity along the [1-10] surface direction is not respected. These are highlighted with red double-ended arrows in figure 6.8d. At other points the adlayer is in close registry with the underlying surface: this is indicated by a black double-ended arrow in figure 6.8d. Additionally, in the STM images shown in figure 6.10 it is evident that some molecular rows, spanning along the [001] direction, exhibit a larger than average spacing with the adjacent ones. Some of these situations, which are indicated for clarity with blue dashed lines in figure 6.10, are consistent with occasional larger inter-molecular spacings along the [1-10] direction. The presence of these interruptions in the molecular organisation can be considered as defects in the (3x2) arrangement of S-valine on Cu(110). This aspect will be discussed further in section 6.5, in which the possible molecular arrangements and their compatibility with a long-range (3x2) organisation, though partially defective, will be analysed.

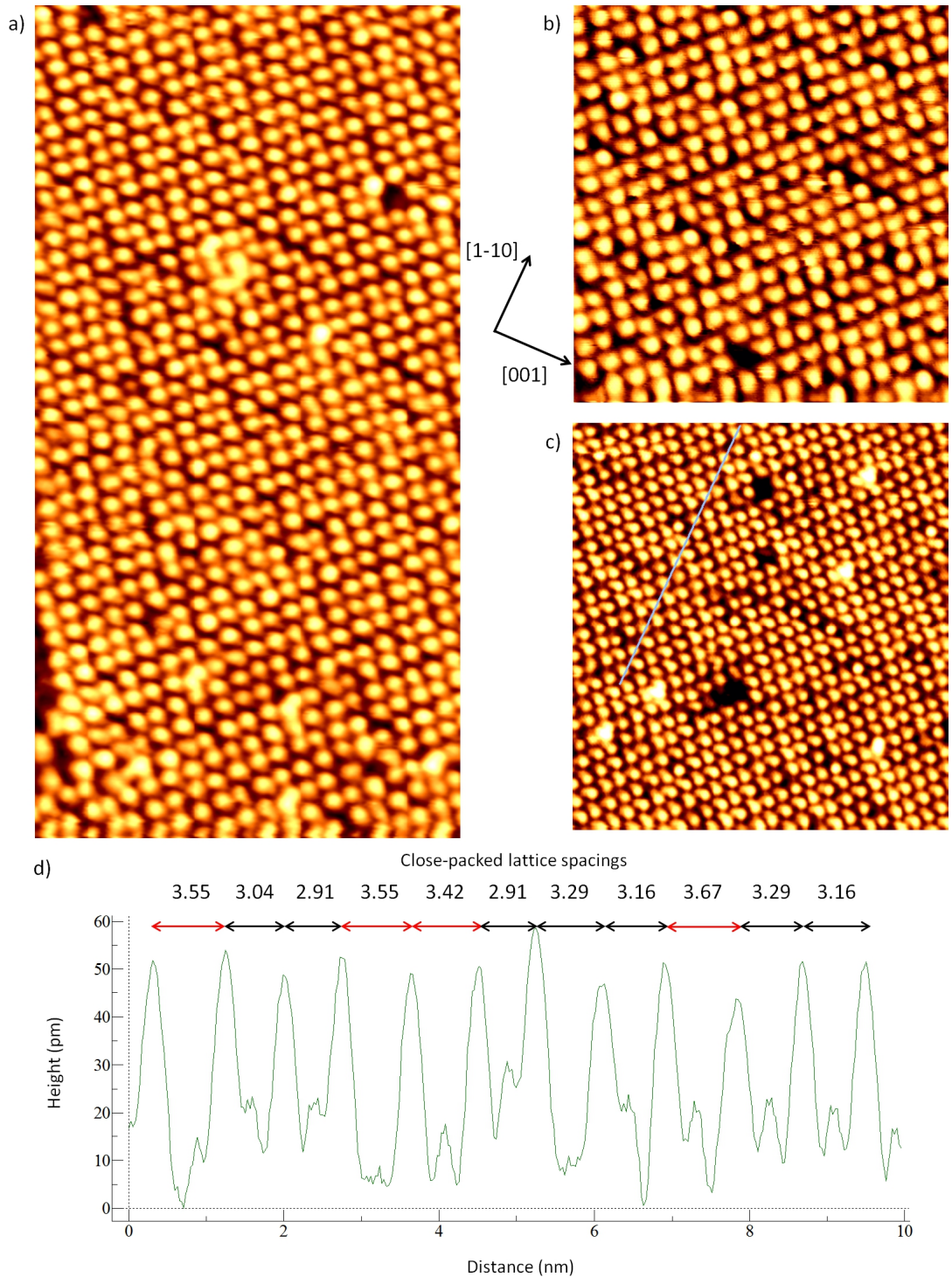

Figure 6.8: a-c) STM images collected on sample of S-valine on Cu(110) that has undergone an annealing process to 473 K. a) 11.0x21.4 nm^2, V=+611.3 mV, I=+0.420 nA. b) 9.3x9.8 nm^2, V=+758.0 mV, I=+0.560 nA. c) 13.2x14.2 nm^2, V=+1095.6 mV, I=+0.720 nA. d) Z profile collected along the light-blue line shown in c). The distances between the peaks are indicated in multiples of units of lattice spacings along the [1-10] surface direction. 1 unit = 2.56 Å. Double-ended black lines underline distances compatible with a 3-fold lattice spacing (7.68 Å), whereas double-ended red lines underline distances that are higher than this value.

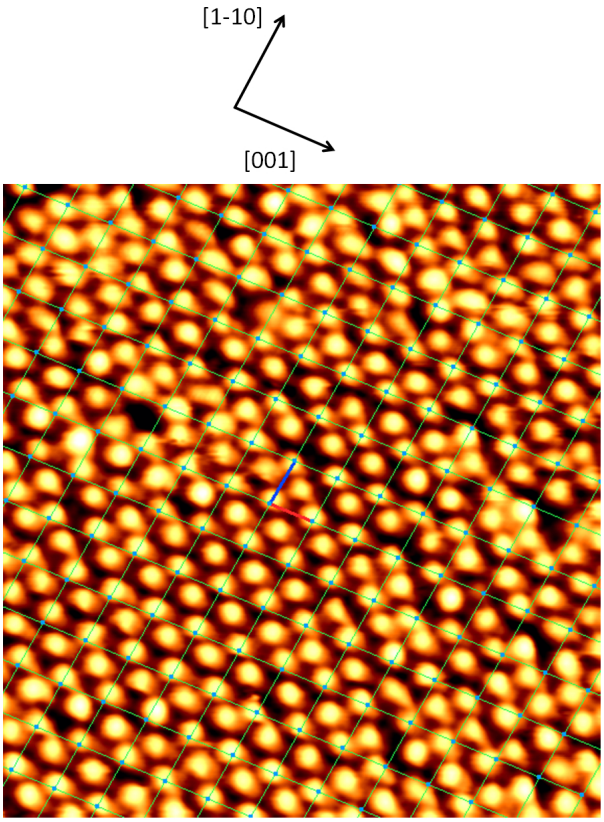

Figure 6.9: STM image acquired on S-valine on Cu(110), following annealing to 473 K. 9.3x9.8 nm^2, V=+611.3 mV, I=+0.430 nA. A (3x2) net is superimposed on the STM image. The grid is generated by two vectors: the blue one measures 3 short-bridge lattice spacings (7.68Å) along [1-10] and the red one measures 2 long-bridge lattice spacings (7.23 Å) along [001].

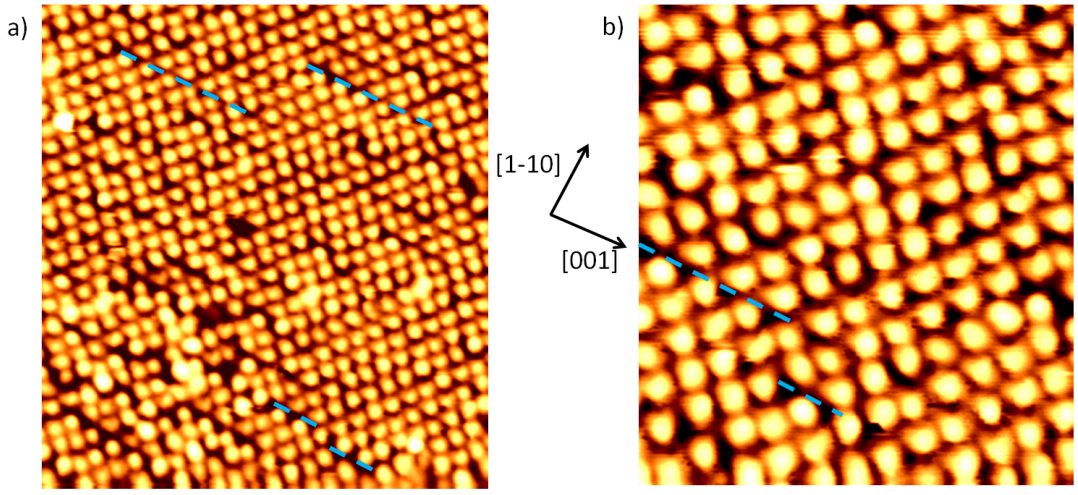

Figure 6.10: STM images acquired on an S-valine adlayer on Cu(110), following annealing at 473 K. a) 13.2x14.2 nm^2, V=+758.0 mV, I=+0.530 nA. b) 6.5x7.2 nm^2, V=+758.0 mV, I=+0.550 nA. The dashed blue lines represent a guide to the eye to indicate local interruptions and wider spacings placed between two molecules or two rows or molecules. The larger spacings are mainly found along the [1-10] direction, as also shown in figure 6.8.

6.3 Structural models

The various manners in which adsorbed S-valine molecules are able to populate the Cu(110) surface in a (3x2) fashion are investigated in this section. The rationale underpinning this reasoning is based on previous studies concerning the adsorption of amino acids on the same surface. In particular, the *carboxylate rule* [41, 42] hypothesis, extensively presented in section 4.4 in the study of enantiopure serine on Cu(110), represents the starting point to build the molecular structure.

In general terms, a (3x2) organisation hosting two molecules per unit cell implies a more densely packed molecular arrangement than those found for the enantiomerically pure amino acids proline [32, 36] and serine [43] (see also chapter 4), which adopt proper and skewed (4x2) organisations, respectively. The contraction in area of a unit cell from a (4x2) to a (3x2) on Cu(110) consists in a reduction equal to 25% (from 74.14 $Å^2$ to 55.60 $Å^2$). This consideration, coupled with the fact that valine molecules feature a significantly larger residual group (see figure 6.1) in comparison with serine, which just possesses a hydroxy-methyl moiety, provides us with the idea of the necessity of an enhanced on-surface packing efficiency.

Formally, the staggering of the surface-bound carboxylate groups, demanded by the *carboxylate rule*, yields one sole kind of carboxylate scaffolds (figure 6.11). It is assumed here that the tridentate adsorption geometry adopted by S-valine on Cu(110) sees the deprotonated carboxylate moiety placed across the short-bridge site of the underlying surface, as it happens with all the amino acids adsorbed on Cu(110). The two possible carboxylate scaffolds (figure 6.11a,b) possess rotational symmetry, property that, coupled with the 2-fold symmetry of the surface, renders the two models identical. Thus only the scaffold depicted in figure 6.11a will be taken into account, with the certainty of not neglecting any other possible models. Being the (3x2) unit cell populated with two S-valine molecules, these are generally non-equivalent. This means that the scaffolds labelled with different numbers (1 or 2) in figure 6.11 belong to molecules that have in principle different geometries (e.g. footprints).

The extended (3x2) structures can be built on this basis, in a procedure that is analogous to the one used for the assembly of enantiopure serine (section 4.4). Firstly, the possible combinations in terms of footprint for the molecule in position 1 are searched (figure 6.12a-d). Taking into account both the rotamers that the λ and the δ footprints can give rise to, and excluding those situation in which a surface atom is coordinated to more than one adsorbed molecule, two possible positions are found for the S-valine molecule in position 1 (figure 6.12a,c). These two geometries, possessing opposite footprint chirality, are indicated with the capital letters A and B. With the same reasoning, two possible geometries for the S-valine molecule in position 2 are found (figure 6.12f,h), again with differing footedness: these are denoted with C and D. It is noted that no

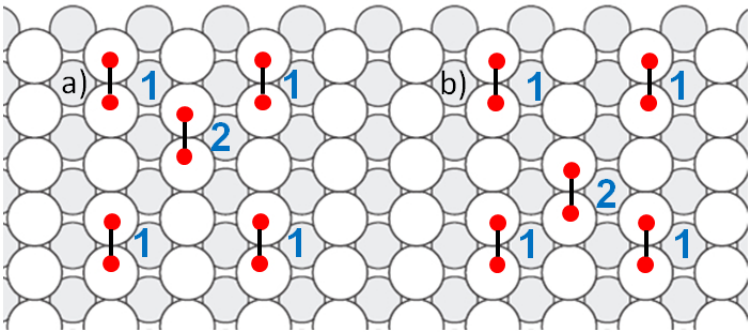

Figure 6.11: a,b) The two possible carboxylate scaffolds permitted by the *carboxylate rule*, that allows only long-range organisations in which carboxylate involved in adsorption are staggered [41, 42] (see figure 4.13a). The adsorption through carboxylate is rendered here with the representation of the oxygen atoms, sketched with red circles and connected with a black line, solely. The numbers 1 and 2 indicate the two positions in the unit cell that can host inequivalent S-valine conformers. The two scaffolds are rotamers.

asymmetries in the number of λ or δ allowed footprints is observed. This is a direct result of the absence of chirality in the unit cell. A chiral unit cell, conversely, would be likely to introduce a bias in the number of possible footprints with a given chirality, as in the case of enantiopure serine on Cu(110) (see section 4.4).

The definition of the geometries A and B for the molecule in position 1 and C and D for the molecule in position 2 is the basis for the population of the (3x2) unit cell at the footprint level. The simple combination of the allowed footprints yields the models shown in figure 6.13. Two models (figure 6.13a,d) are homochiral in footedness, while the other two (figure 6.13b,c) are heterochiral. However, it is noted that the models underlined in green in figure 6.13b and 6.13c are completely equivalent, since, also considering the symmetry of the substrate, they are rotamers.

Further considerations can be drawn on the three remaining structures, which are depicted in figure 6.14. These are obtained by placing eight molecules in the (3x2) arrangement, to provide the reader with a wider picture of the footprint distribution for each model. It is noted that the two models featuring homochiral footedness, sketched in figure 6.14a,c, present a common feature. As highlighted with black rectangles, there are situations in which two right-angle triangles, as the molecules are sketched, have their hypotenuses in close proximity. At the molecular level, this signifies a non-negligible hindrance. As an example, the DFT calculations performed on the R-serine/Cu(110) system are reminded here (see section 4.5). It has been shown that model IV, which features a similar situation, proves unstable during a DFT relaxation, yielding a final state in which the molecular footprint changes in order to compensate the initial molecular hindrance. In addition, it is noted that valine possesses a relatively large aliphatic residual group, which would render these footprint arrangements very unlikely. In figure 6.14d,e the closeness that two S-valine molecules would experience according to the models depicted in figure 6.14a,c is shown with ball-and-stick

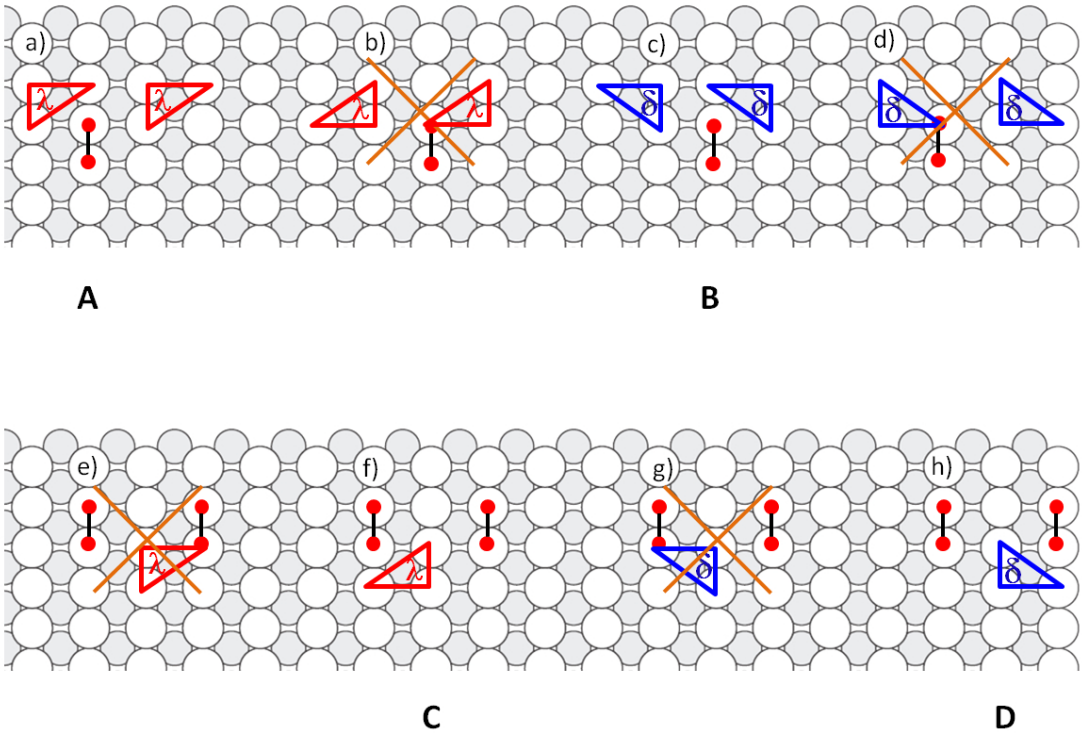

Figure 6.12: a-d) Possible conformers that can be accommodated in position 1. e-f) Possible conformers that can be accommodated in position 2. The situations in which a surface atom is coordinated to atoms belonging to multiple adsorbed molecules are disregarded and crossed out in orange. The footprints of the conformers are indicated with red and blue right-angle triangles in the cases of λ and δ footprints, respectively. The allowed molecular positionings (a,c,f,h) are renamed with the capital letters A, B, C and D, respectively.

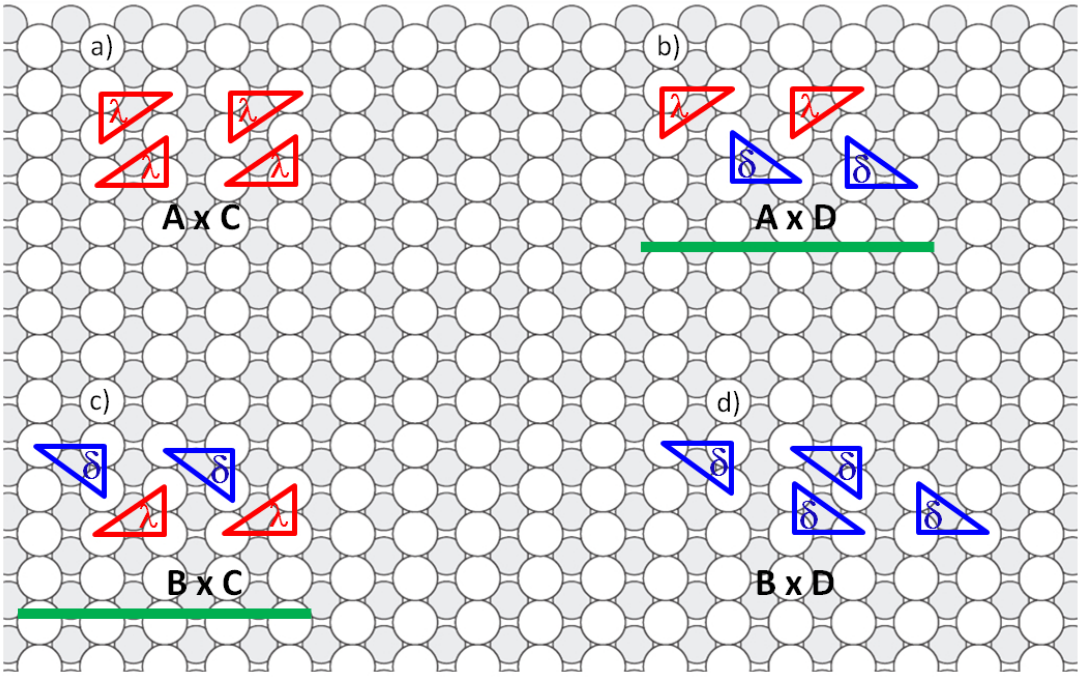

Figure 6.13: a-d) The population of the positions 1 and 2 with the possible conformers, according to the operations A, B, C and D defined in figure 6.12. Green lines underline two rotameric structures that are thus equivalent.

models posed on the (110) surface. These models are not constructed on the basis of any theoretical calculations, but are drawn to render visually the hindrance that these footprint arrangements would imply. In the light of the aforementioned reasons, the homochiral footprint models depicted in figure 6.14a,c are ruled out, thus only one possibility is left, i.e. the homochiral footprint arrangement schematically represented in figure 6.14b. This model will be tested theoretically in the following sections.

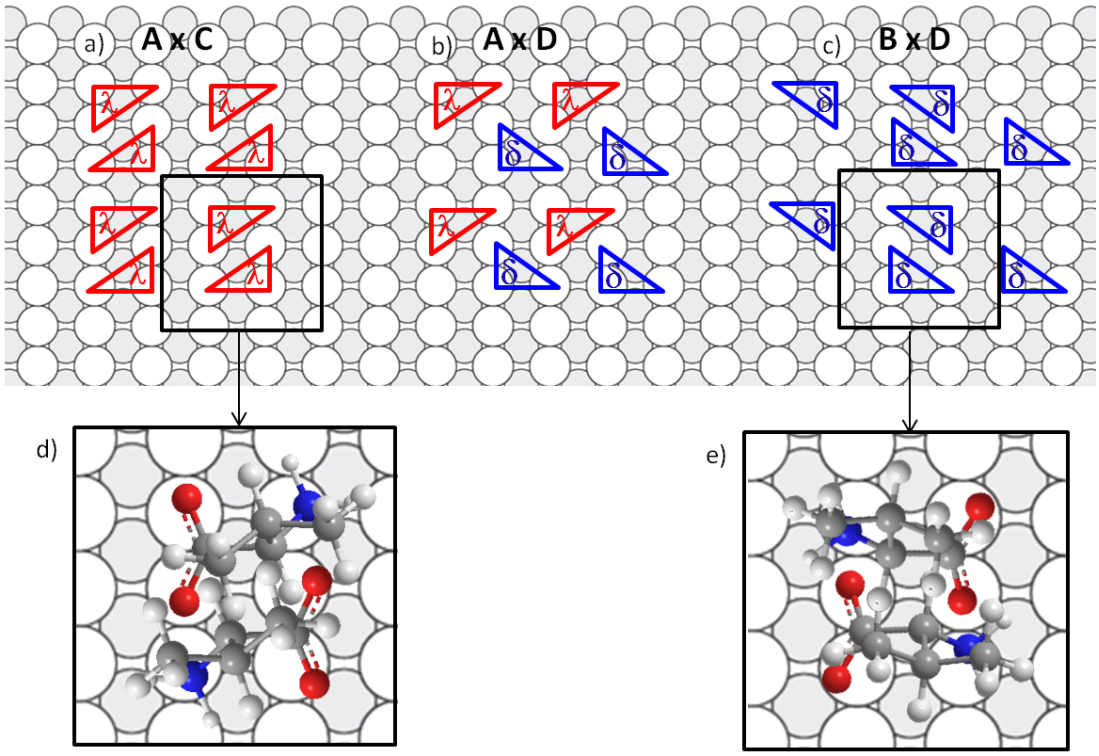

Figure 6.14: a-c) The allowed footedness distributions according to the *carboxylate rule*. The models are constructed placing eight molecules in the (3x2) arrangement. e,d) Molecular representations of the dimers indicated by the black rectangles in a) and c), respectively. Hydrogen atoms are shown in white, oxygen in red, carbon in grey and nitrogen in blue. The structures are not the results of any theoretical calculations.

6.4 Theory

In order to gain a deeper understanding of the nature of the (3x2) molecular assembly adopted by S-valine on the Cu(110) surface, this system has been tested theoretically using DFT with Van der Waals corrections and STM simulations. The main aim of this theoretical study is to ascertain the energetic stability of the overlayer, as well as the level of agreement between the experimental STM images and the simulated ones. The theoretical calculations have been carried out by Dr George Darling at the Surface Science Research Centre, Department of Chemistry, University of Liverpool (UK). The methods utilised for the theoretical study of the system are described in section 6.7 of this chapter.

6.4.1 DFT calculations

Firstly, DFT calculations have taken into account the binding energies associated with a single adsorption event on Cu(110) involving one molecule of S-valine. This procedure is a standard method used to discover the favoured on-surface adsorption geometry at the single-molecule level. As reviewed in the introductory chapter of this thesis (chapter 1), deprotonated amino acids are prone to bind to the Cu(110) surface via the carboxylate and amino groups, giving rise to a three-footed coordination and thus to two possible footprints, *delta* and *lambda*, that are chiral in two dimensions. On this basis, the two possible adsorbed S-valine conformers are placed on the surface and let relax through DFT with Van der Waals corrections, yielding, as a final result, the geometries illustrated in figure 6.15.

It is noteworthy that a significant difference in energy is detectable between the two conformers. The λ conformer (figure 6.15a,c) yields a final energy of -1.944 eV, while the molecule having the mirror-image footprint is calculated to have -1.805 eV (figure 6.15b,d). Their energetic difference, equal to 139 meV, signifies a huge preference for the λ geometry in the case of a single adsorption event of S-valine on Cu(110).

Perhaps surprisingly, however, the most favourable geometry belongs to a conformer that has not been hitherto taken into account. A conformer that sees the carboxylate group bound across the long-bridge site of the Cu(110) surface is found to have an energy of -1.964 eV. In figure 6.16 the top and side-views of this geometry is displayed. According to the spatial distribution of the atoms coordinated with the surface, this conformer is denoted as λ (or *pseudo*-λ), albeit this footprint classification has been created for amino acids whose on-surface carboxylate bonding takes place at the short-bridge site of the (110) surface.

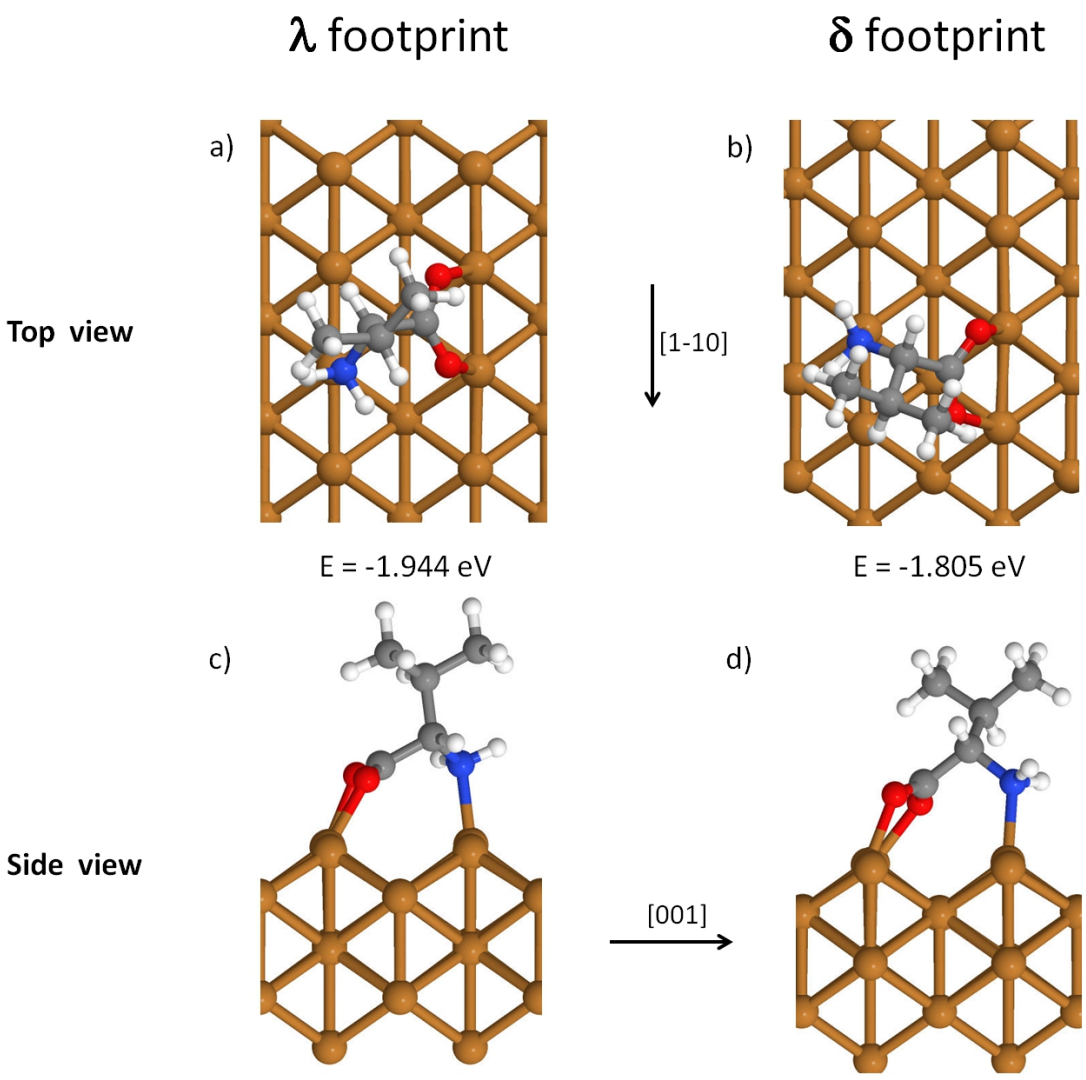

Figure 6.15: a,c) Top- and side-views of the λ conformer, respectively. b,d) Top- and side-views of the δ conformer, respectively. The final energies obtained as a result of the DFT relaxations of both the adsorbers are indicated in figure.

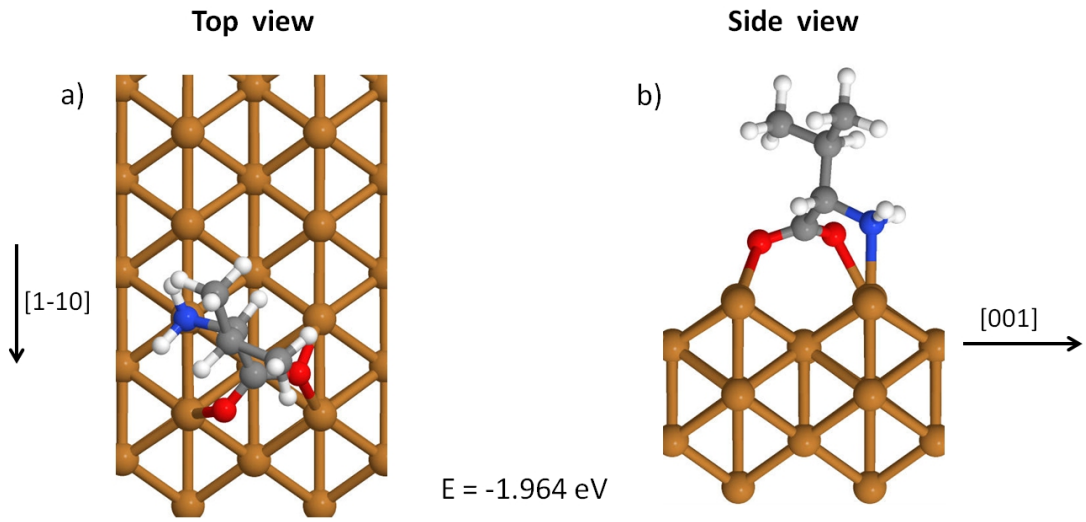

Figure 6.16: a,b) Top- and side-views of the *pseudo*-λ conformer, which features an adsorption geometry in which the carboxylate moiety is coordinated across the long-bridge site of the (110) surface, i.e. with the OCO molecular plane approximately parallel to the [001] direction. The energy possessed by this conformer after DFT relaxation is denoted in the figure.

Despite the favourable energy possessed by the latter conformer, it is unlikely that it can play a role in the long-range (3x2) arrangement of S-valine on Cu(110). As visible in figure 6.16a, in fact, one of the two oxygen atoms of the carboxylate moiety adopts a partial displacement along the [1-10] surface direction, which results in a double coordination of this oxygen with two distinct copper atoms. The resulting geometry, which can be considered almost quadridentate, though not strictly a μ_4 coordination, is not compatible with a (3x2) molecular organisation. Furthermore, a hypothetical (3x2) repeat composed of at least one *pseudo*-λ conformer, as the one represented in figure 6.16, would see an uninterrupted distribution of coordinated carboxylate moieties along the short bridge sites. In other words, every single copper atom of certain rows running along the [001] direction would participate in the coordination with ad-molecules. The latter situation is unfavoured on the basis of the repulsive interactions that take place between deprotonated oxygen atoms and of the possible surface stress that can be induced by unstaggered carboxylate coordination, similarly to the forbidden carboxylate scaffolds according to the *carboxylate rule*. For these reasons the long-range (3x2) arrangement constituted by S-valine molecules coordinated via their carboxylate group to long-bridge sites is disregarded.

The extended structure of the sole possible (3x2) geometry that has been hypothesised so far, i.e. the structure schematically displayed in figure 6.14b, which possesses conformers with alternating footprints, has been the subject of a DFT calculation, whose final outcome is portrayed in figure 6.17. The top-view of this structure, shown in figure 6.17a, allows us to see how the molecules are arranged in a strict heterochiral distribution in terms of footedness. This confirms that the starting footprint geometry, as schematically portrayed in figure 6.14b, proves stable over the DFT relaxation.

The final energy calculated for the (3x2) structure is equal to -2.396 eV per molecule. This value is higher, in modulus, if compared to the energy of all the single conformers calculated (figures 6.15 and 6.16), indicating that the organisation in a (3x2) arrangement gives stability to the system, if the energy at the single molecule level is taken into account. The side-view portrayed in figure 6.17b, in which the observer looks along the [1-10] surface direction, shows that all the molecules adopt an up-right position, with their isopropyl moieties oriented away from the surface independently of their footprint chirality. This generates a symmetry that is in contrast, for instance, with the behaviour of enantiopure proline on Cu(110), in which different footprints yield very distinct molecular geometries (see reference [32] and section 1.7.2). Another interesting feature noticeable in the DFT-relaxed structure consists in the fact that oxygen atoms belonging to the same carboxylate moiety of a given molecule show an asymmetric positioning with respect to the [1-10] direction, or in other words, an imaginary line connecting these two atoms is not parallel to the surface close-packed direction. This characteristic is common to both the footprints that the molecule adopts (figure 6.17a) and is consistent with the presence of a weak adsorption peak at 1614-1616 cm^{-1} in the RAIRS investigation, due to the $\nu_{as}(OCO^{-})$ asymmetric stretch (see figure 6.3 and table 6.1).

In order to have an additional term of comparison, the energy of a S-valine overlayer composed of molecules with λ footedness, which is the most favoured in the event of a single adsorption, has been calculated. Given that molecules with homogeneous footedness cannot populate a (3x2) unit cell, as shown in figures 6.14d,e, a c(4x2) structure is taken as a model for this hypothetical arrangement. This is schematically represented and indicated with a black arrow in figure 6.21b. Its DFT-relaxed molecular distribution proves stable (image not shown), and gives, as a result, a final energy equal to -2.243 eV per molecule, a value which indicates that a c(4x2) organisation with homochiral footprints is sensibly unfavourable with respect to the (3x2) organisation with heterochiral footprints.

In order to gain a deeper understanding of the driving forces that lead to the formation and stabilisation of the (3x2) arrangement of S-valine on Cu(110), this is further analysed in figure 6.18. This kind of analysis requires the comprehension of the intermolecular interactions that occur between the adsorbed molecules. Typically, amino

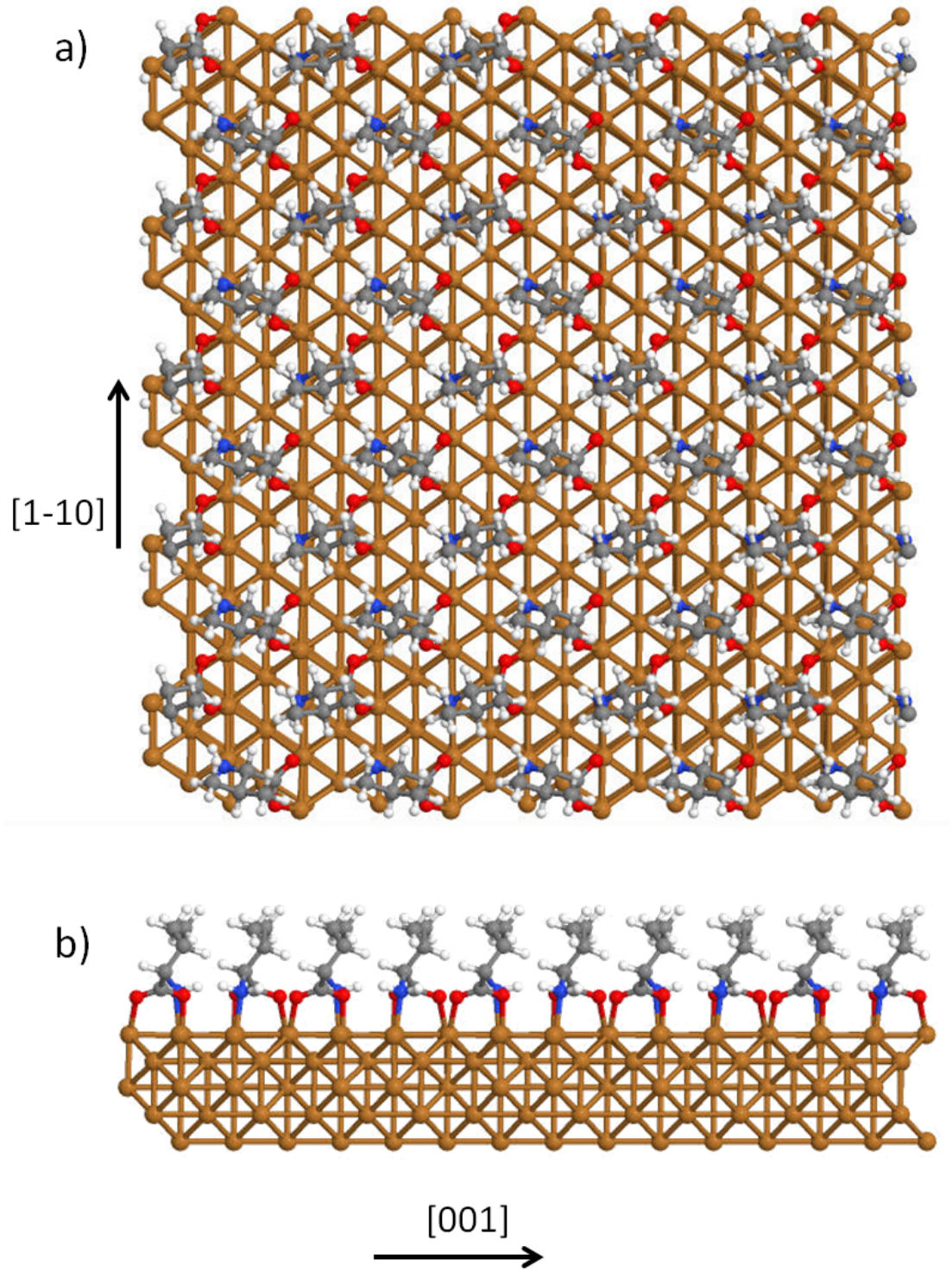

Figure 6.17: a,b) Top- and side-views of the DFT relaxed (3x2) structure possessing alternating footprints, respectively. This organisation is characterised by an energy of -2.396 eV per molecule.

acids are able to give rise to assemblies with long-range order on the Cu(110) surface in light of the hydrogen bonds that can be established between moieties belonging to adjacent molecules (see for example references [31, 32, 43, 44]). In particular, strong hydrogen bonds, which provide the system with the most significant contribution to its stability, take place between a hydrogen atom and a hetero-atom placed at a distance smaller than a spatial threshold. In the case of hydrogen bonds established between hydrogen and oxygen (O–H), this threshold is set to 2.2 Å [45, 46]. As it is shown in figure 6.18, all the four carboxylate oxygen atoms of the two conformers are involved in hydrogen bonds. Specifically, the oxygen atoms belonging to the λ conformer are placed at 1.97 Å and and 1.91 Å from an amino and a methyl hydrogen atom belonging to the δ molecule, respectively. Furthermore, the latter conformer sees the interaction of one of its carboxylate oxygen atoms with a methyl hydrogen atom of the λ conformer, at a distance of 1.88 Å. The three aforementioned hydrogen bonds belong to the *strong* category [45, 46], and explain the energetic stability of the (3x2) overlayer of S-valine molecules on Cu(110). The additional hydrogen bond present, occurring between a carboxylate oxygen atom of the δ conformer and a hydrogen atom bonded to the skeletal stereocentre of the λ conformer, might be considered *weak*, given that the atoms involved are positioned at 2.65 Å away from each other. This bond represents a further, however minor, contribution to the energetics of the entire supramolecular structure.

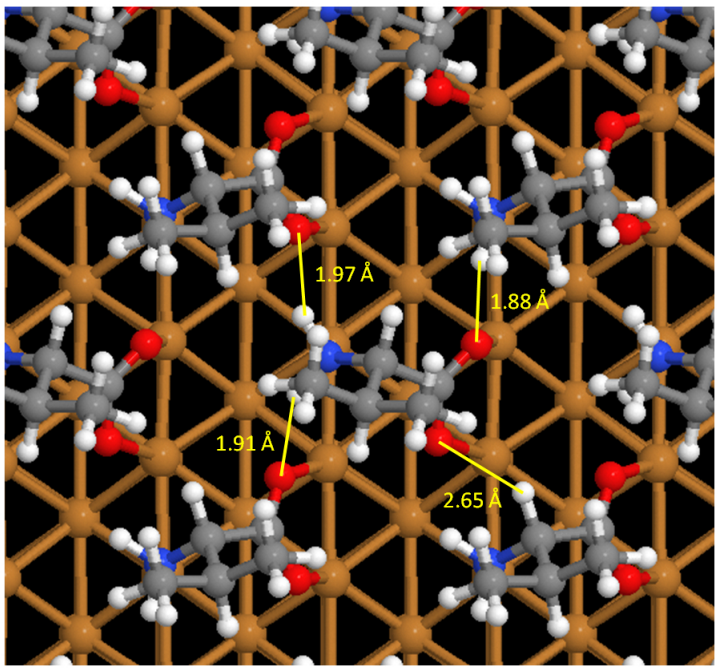

Figure 6.18: The inter-molecular hydrogen bonds that are thought to take place between carboxylate oxygens atoms and hydrogen atoms belonging to a different conformer, indicated with yellow lines. The distances that separate the atoms involved in the interaction are indicated in the figure.

6.4.2 STM simulations

The most favourable long-range organisation adopted by S-valine on Cu(110), indicated to possess a (3x2) unit cell as a result of experimental and theoretical investigations (see sections 6.2 and 6.4) has been the subject of simulations aiming at establishing a possible agreement between the simulated images and the STM images acquired experimentally. In figure 6.19 a gallery of simulations of STM images displaying the appearance of the (3x2) structure is depicted. The images are displayed at different bias voltages, and are obtained according to the methods described in section 6.7. The *x,y,z* scales are indicated for each picture, as well as the average tip-sample distances at which each simulations is performed (z_{mean}). For the images 6.19a,b,c,d bias voltages of -1, -0.25, +0.25 and +1 V are applied, respectively. It is noticeable that in all cases the two conformers λ and δ give rise to distinct shapes and orientations of the intensities. This aspect is more accentuated in the images of figure 6.19b,c,d while the simulation in figure 6.19a yields conformers with more rounded shapes. In every case, an apparent dimerisation seems to take place, manifested by the asymmetric position of the central molecule when any (3x2) unit cell is taken into account. Finally, no significant asymmetries in the apparent height of the two conformers are detected.

On the basis of the available data, the next steps consists of a direct comparison between the experimental and the simulated STM images. The STM image presented in 6.20a, collected at a bias voltage of +1095.6 mV, presents features possessing different shapes. In particular, there are zones in which the STM signals produced by molecules placed along two consecutive rows running along the [001] direction are alternated. This is indicated with the light blue triangles possessing different orientation in figure 6.20a. This becomes clearer in the magnification of figure 6.20c, where the molecules in the first row produce asymmetric signals, approximately with a triangular shape, with a faint protrusion at the top left. The molecules of the second row, conversely, possess an STM appearance with a faint protrusion pointing at its bottom left. This experimental image is compared to the simulated ones that have been calculated at positive voltages, in order to have a more reliable comparison between experiment and theory. In both cases, the λ and δ conformers give rise to signals with a distinct orientation. On this basis, the footprint chirality is tentatively assigned to the molecules investigated in the experimental image of figure 6.20c. It is stressed here, however, that this absolute assignment is speculative, given that the correspondence between experimental and simulated shapes produced by the single conformers is not straightforward. It is however clear that alternating shapes are present, and we propose that the (3x2) model featuring alternating homochiral footprints holds valid for the achiral phase of S-valine on Cu(110), at least with a local nature. This, in fact, does not encompass the whole sample, as for example in the area highlighted with a green rectangle in figure 6.20a. The hypothesised reasons for these breaks are discussed in the following section.

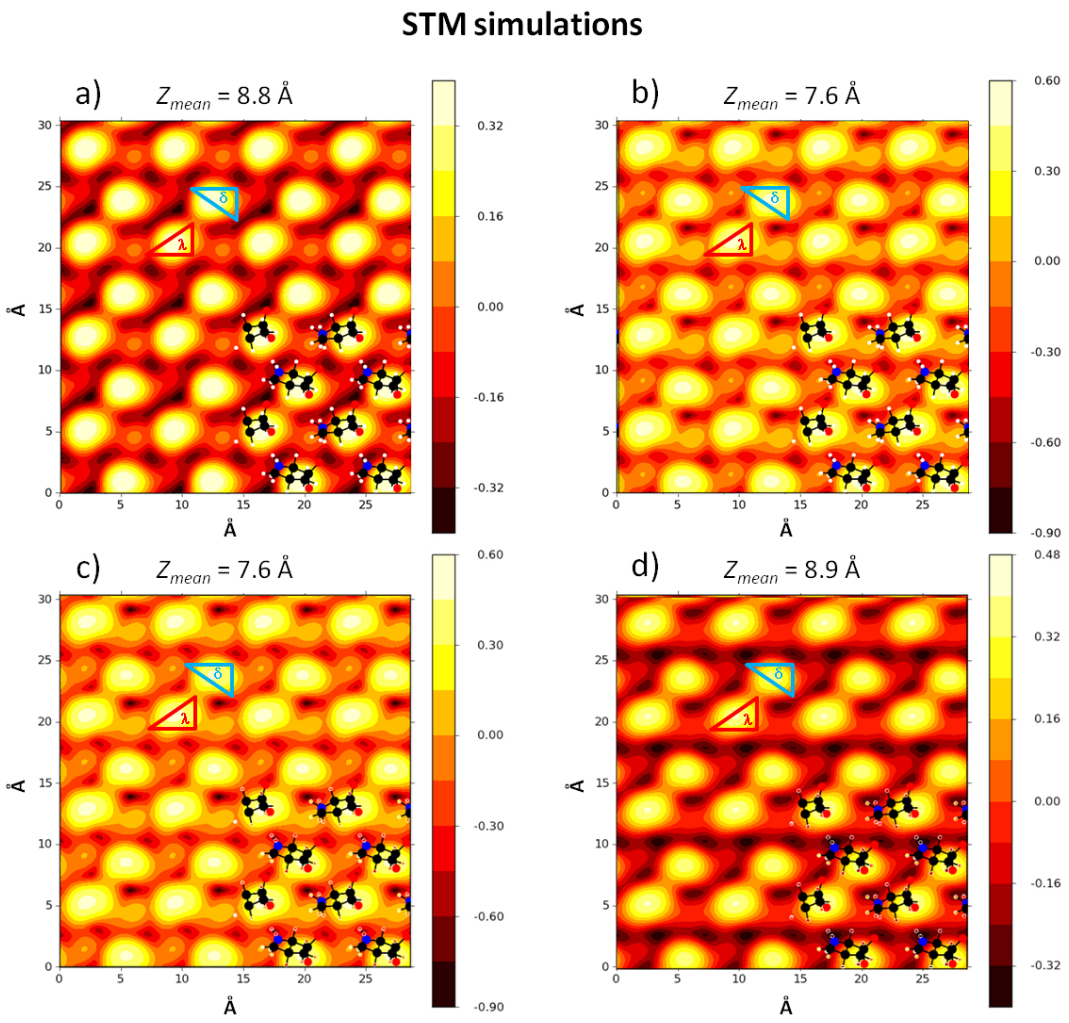

Figure 6.19: a-d) Simulated STM images calculated on the (3x2) structure of S-valine on Cu(110). The x,y distances are reported on the axes in Å, while the z scale is indicated next to each image. The z_{mean} field displayed at the top of each image denotes the average tip-sample distance for the relevant simulation. The λ and δ conformers are also indicated with the right-angle triangles convention. a) V=-1000 mV. b) V=-250 mV. c) V=+250 mV. d) V=+1000 mV.

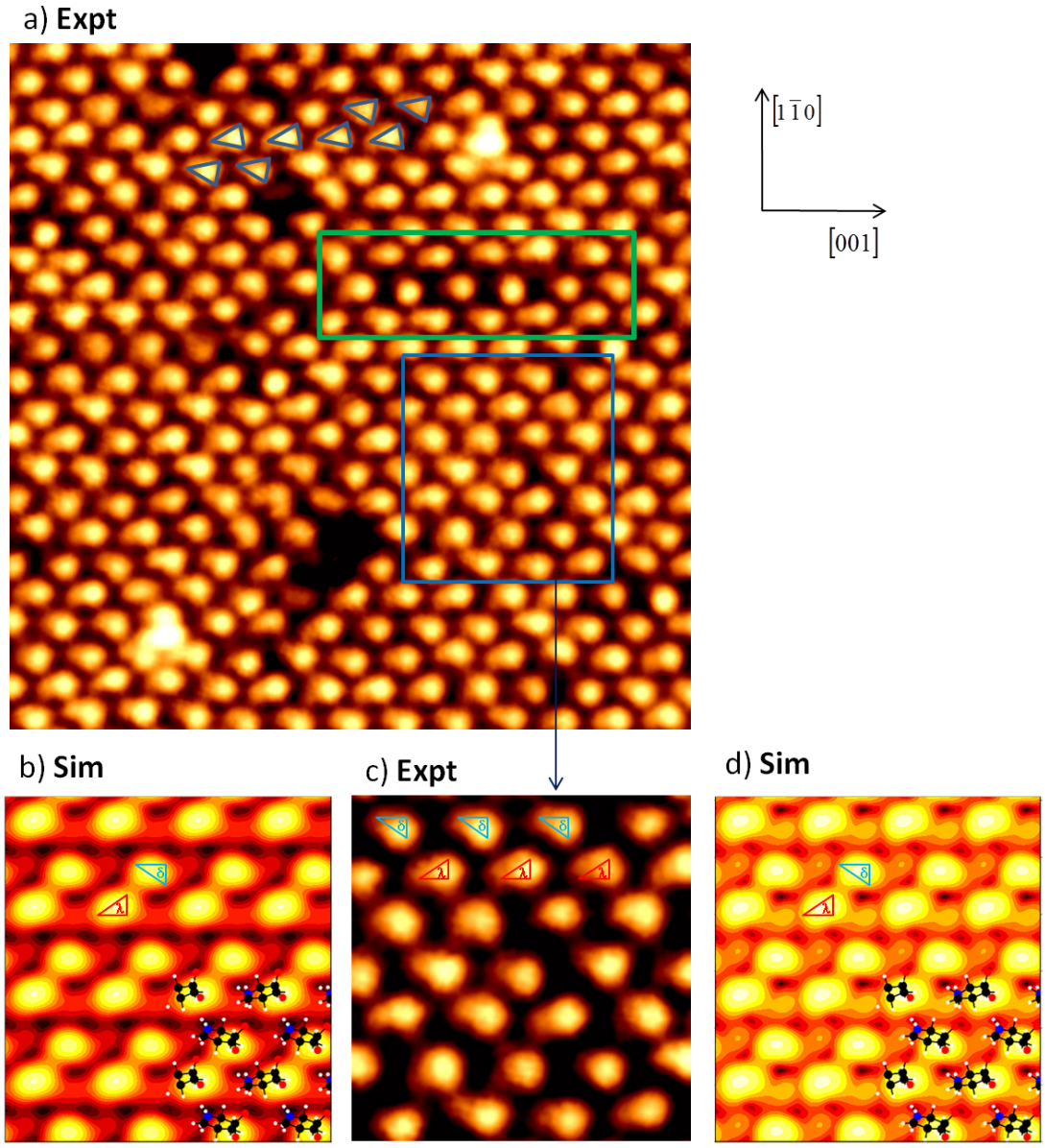

Figure 6.20: a) Experimental STM image acquired on the high-temperature phase of S-valine on Cu(110). Sample annealed at 473 K. 9.34x9.39 nm^2, V=+1095.6 mV, I=+0.720 nA. The light-blue triangles denote features with different shapes. The green rectangle highlights an area in which the (3x2) arrangement seems interrupted. b) Simulated STM image. 3.0x3.0 nm^2, V=+1000 mV, as in figure 6.19d. c) Insight of the image in a) with enhanced colour scale contrast, as indicated by the square selection. 3.0x3.0 nm^2. The molecular footprints denoted with δ and λ are tentatively assigned here. d) Simulated STM image. 3.0x3.0 nm^2, V=+250 mV, as in figure 6.19c. For each image, the high-symmetry surface directions are placed as indicated in figure.

6.5 Hypotheses on the origin of the irregularity of the (3x2) organisation

So far, it has been proposed, on the basis of the experimental data and with the support of theoretical calculations, that the achiral phase adopted by S-valine on Cu(110) after annealing up to 473 K consists, mainly, of a (3x2) arrangement characterised by heterochiral footprints. Nevertheless, as it has been hitherto noted throughout this chapter, this geometry does not persist over the long-range of the Cu(110) surface (see for instance the STM image in figure 6.9 and the LEED patterns in figure 6.5). This phenomenon has been encountered previously in the study of the adsorption of enantiopure and racemic alanine on the same surface [37]. The alanine/Cu(110) system has since then been the subject of recent experimental studies aimed at explaining this long-range loss of registry between the surface lattice and the adsorbates [39, 40]. The authors of these works used LEED in combination with Fast Atom Diffraction (FAD) to probe the (3x2) organisation of enantiopure and racemic alanine on Cu(110). They propose that the electron scattering has a convoluted contribution from a specific part of the molecule, the methyl moieties, which are displaced with respect to the periodicity of the molecule as a whole, to give rise to a centred c(nx2) arrangement, with $n \sim 3.2$. This specific contribution coming from the dangling methyl groups of the alaninate conformer is thus suggested to be responsible for the distortion in the LEED patterns. This geometry also implies a change of the sequence of the chiral footprints and an overall lower coverage, which would explain the absence of long-range periodicity in the alanine/Cu(110) system [40].

This reasoning could be also applied to the (3x2) organisation of S-valine on Cu(110), given that the isopropyl moieties of the residual group might represent independent scattering centres that give significant contribution to the LEED pattern, provided that a molecular rearrangement which locally breaks the (3x2) periodicity takes place. This has been shown to occur in the S-valine/Cu(110) system (see for instance figures 6.8 and 6.8). On the basis of the results presented herein, some causes for the local break of a strict (3x2) arrangement are proposed, as it happens for instance in the regions delimited by dashed blue lines along the [001] surface direction in figure 6.10.

One possible cause of the local loss of registry might be due to the presence of rotational domains, in which areas containing molecules in a (3x2) arrangement with heterochiral footprints, with the exception of the boundary between the two rotational domains. This possible phenomenon, i.e. the presence of rotational domains, is similar to the interpretation proposed by Seifert and co-workers for the case of alanine on Cu(110) [40]. A possible boundary between two rotational domains is schematically represented in figure 6.21a. Another possibility sees the local presence of a c(4x2) unit cell, as schematically represented in figure 6.21b, which is larger than a (3x2) unit

and thus would imply a higher local inter-molecular spacing. Finally, the possibility of sporadic occurrences of conformers coordinated via the carboxylate moiety to the long-bridge site of the Cu(110) surface cannot be excluded (figure 6.21c, in which this conformer is represented with a filled red triangle), given the favourable energy that this geometry possesses when a single adsorption event is taken into account (see figure 6.16).

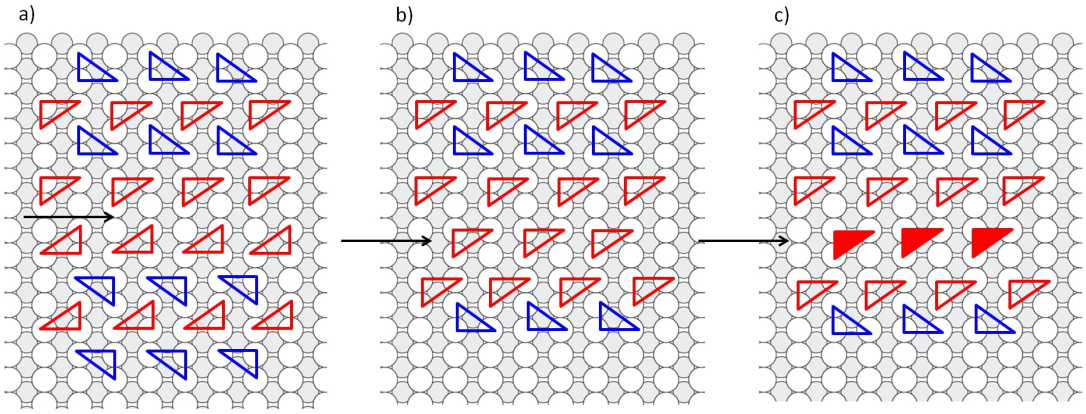

Figure 6.21: Hypotheses on the causes of the local interruptions of the (3x2) organisation of S-valine on Cu(110). Red and blue triangles represent λ and δ conformers, respectively. Filled triangles represent conformers coordinated with the carboxylate group across the long-bridge site. a) Rotational (3x2) domains. b) Occurrence of a (4x2) unit cell. c) Occurrence of the conformer having the carboxylate across the long-bridge surface site.

The hypothesis illustrated in figure 6.21a, corresponding to the presence of rotational (3x2) domains, is corroborated further via the direct comparison between some (3x2) units in the same image. Figure 6.22a features an additional STM image of the achiral phase of S-valine on Cu(110). The area indicated with a blue rectangle is then magnified in figure 6.22b: within this, two (3x2) units are highlighted by dashed green and red rectangles. These units are in proximity of each other, specifically they are six close-packed lattice spacings apart. In both cases, the STM intensity originated from the central molecule adopts an eccentric position with respect to the rectangle representing the unit cell. This effect is predicted in the STM simulations at all bias voltages considered (see images in figure 6.19). Interestingly, the central molecules within the unit cells delimited by the green and red rectangles produce signals placed towards the bottom and the top of the rectangles, respectively. For comparison, the magnification of the STM simulation carried out at a positive bias voltage (figure 6.19d) is displayed in figure 6.22c,d. In the latter case the image is rotated by 180°, i.e. it represents the STM simulation performed on the rotational isomer of the (3x2) structure whose simulations

are presented in figure 6.19. The similarities of the distribution of intensities within the green rectangles in figures 6.22b,c and within the red rectangles in figures 6.22b,d may thus lead to hypothesise the presence of rotameric (3x2) unit cells close to each other, confirming the absence of a long-range extension of a pure (3x2) organisation.

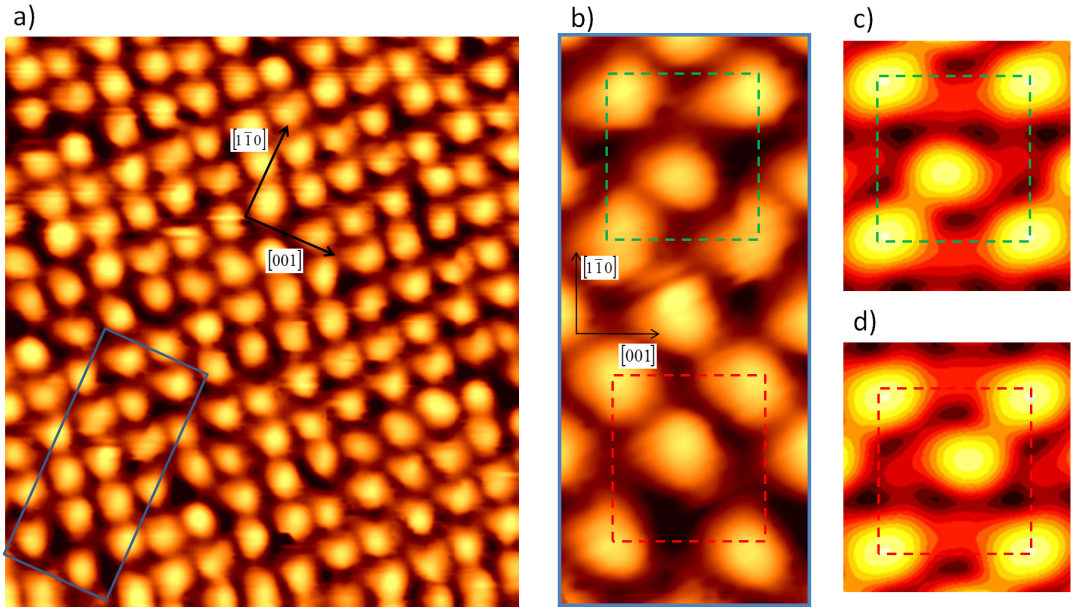

Figure 6.22: a) STM image collected on the achiral phase of S-valine on Cu(110) after annealing at 473 K. 6.5x7.2 nm^2, V=+758.0 mV, I=+0.550 nA. b) Inset as indicated by the blue rectangle in a). 1.4x3.1 nm^2. The image is rotated in order to have the [1-10] direction in a vertical position. The dashed green and red rectangles highlight two (3x2) units that are two unit cells far apart along the [1-10] direction. c) Inset of the STM simulation displayed in figure 6.19d, performed at a bias voltage of +1000 mV. d) Same as c), after the application of a 180° rotation.

6.6 Conclusion

In this chapter the achiral organisation of S-valine of Cu(110), which is formed on the surface once that the sample is annealed to 473 K is systematically investigated by means of experimental techniques and theoretical calculations. The RAIRS results confirm the integrity of the adlayer once this is converted from the as-dosed chiral organisation to the achiral one through a thermal treatment. This chiral-achiral conversion is then followed via LEED and STM: both techniques show the progressive disappearance of the chiral arrangement, until the achiral phase remains the sole molecular organisation on the surface. Furthermore, both STM and LEED studies show that this phase possesses a (3x2) periodicity, albeit with irregularities, as testified by the measurements in STM images and the presence of a distortion of some of the generated diffraction spots.

The possible models compatible with the adsorption of S-valine on Cu(110) with a (3x2) periodicity are then constructed, yielding one sole possibility due to the packing efficiency required. This model, which possesses a heterochiral footprint distribution, is tested theoretically through DFT with Van der Waals corrections, which give a stable geometry with all the oxygen atoms involved in inter-molecular hydrogen bonds. Moreover, the STM simulations produced are able to locally reproduce the experimental images, corroborating the idea of having areas in which the molecular footprints follow a strict alternating distribution.

Finally, the origin of the spatial breaks that cause the mismatch with a perfect (3x2) periodicity is discussed on the basis of experimental studies performed on the alanine/Cu(110) system [39, 40] and following a reasoning that sees the interruption of the (3x2) long range order with rotational domain boundaries, different unit cells and the presence of diverse conformers.

6.7 Methods section

The RAIRS investigations have been performed in the RAIRS chamber (section 3.4.1), whereas the STM characterisations have been carried out with the Specs STM (section 3.4.2). The LEED patterns have been acquired on both the aforementioned UHV chambers. S-valine (purity $> 98\%$) is bought from Sigma Aldrich and used without further purification. The molecular source is held in a glass crucible, wrapped in a tantalum wire with a diameter of 0.25 mm, with which the crucible is resistively heated. A current of 0.72 A is required to induce the sublimation of S-valine molecules, with a temperature of the crucible of 363 K, approximately. In order to achieve the achiral phase, the sample is annealed resistively typically to 473 K. The sample temperature is controlled via a thermocouple attached to the UHV manipulator holding the crystal, as described in section 5.4.

All the theoretical calculations were done with VASP (Vienna Ab-initio Simulation Package) [47, 48] using a cut-off energy of 400 eV with the atom cores represented using the PAW method. The optB88-vdw exchange-correlation functional [49, 50] was used, containing Van der Waals corrections. The binding energies of single molecules were calculated in a 5x3 supercell of a slab consisting of 5 Cu layers having three layers fixed, with a 7x6x1 k-point set. Calculations for the smaller 3x2 unit cell required a larger 10x10x1 k-point set to achieve a comparable density of k-points. For the production of the STM simulations the Tersoff-Hamann approximation [51] was used, as implemented by Lorente and Persson [52].

References for chapter 6

[1] J. Elemans, I. De Cat, H. Xu, and S. De Feyter, "Two-dimensional chirality at liquid-solid interfaces," *Chemical Society Reviews*, vol. 38, no. 3, pp. 722–36, 2009.

[2] M. Heitbaum, F. Glorius, and I. Escher, "Asymmetric heterogeneous catalysis," *Angewandte Chemie (International ed. in English)*, vol. 45, no. 29, pp. 4732–62, 2006.

[3] T. Bürgi and A. Baiker, "Heterogeneous enantioselective hydrogenation over cinchona alkaloid modified platinum: mechanistic insights into a complex reaction," *Accounts of Chemical Research*, vol. 37, no. 11, pp. 909–17, 2004.

[4] H.-U. Blaser, H.-P. Jalett, M. Müller, and M. Studer, "Enantioselective hydrogenation of α-ketoesters using cinchona modified platinum catalysts and related systems: A review," *Catalysis Today*, vol. 37, no. 4, pp. 441–463, 1997.

[5] A. Baiker, "Progress in asymmetric heterogeneous catalysis: Design of novel chirally modified platinum metal catalysts," *Journal of Molecular Catalysis A: Chemical*, vol. 115, no. 3, pp. 473–493, 1997.

[6] Y. Izumi, "Modified Raney Nickel (MRNi) Catalyst: Heterogeneous Enantio-Differentiating (Asymmetric) Catalyst," *Advances in Catalysis*, vol. 32, p. 215, 1983.

[7] G. Webb and P. Wells, "Asymmetric hydrogenation," *Catalysis Today*, vol. 12, no. 2-3, pp. 319–337, 1992.

[8] V. Humblot, S. Haq, C. Muryn, W. A. Hofer, and R. Raval, "From Local Adsorption Stresses to Chiral Surfaces: (R,R)-Tartaric Acid on Ni(110)," *Journal of the American Chemical Society*, vol. 124, no. 3, pp. 503–510, 2002.

[9] I. L. Garzón, M. R. Beltràn, G. Gonzàlez, I. Gutierrez-Gonzàlez, K. Michaelian, J. A. Reyes-Nava, and J. I. Rodriguez-Hernàndez, "Chirality, defects, and disorder in gold clusters," *The European Physical Journal D*, vol. 24, no. 1-3, pp. 105–109, 2003.

[10] C. Noguez and I. L. Garzón, "Optically active metal nanoparticles," *Chemical Society Reviews*, vol. 38, no. 3, pp. 757–71, 2009.

[11] C. Gautier and T. Bürgi, "Chiral gold nanoparticles," *Chemphyschem*, vol. 10, no. 3, pp. 483–92, 2009.

[12] S. M. Barlow and R. Raval, "Nanoscale insights in the creation and transfer of chirality in amino acid monolayers at defined metal surfaces," *Current Opinion in Colloid and Interface Science*, vol. 13, pp. 65–73, 2008.

[13] X. Zhao, Z. Gai, R. Zhao, W. Yang, and T. Sakurai, "Adsorption of glycine on Cu(001) and related step faceting and bunching," *Surface Science*, vol. 424, no. 2-3, pp. L347–L351, 1999.

[14] X. Zhao, R. Zhao, and W. Yang, "Adsorption of alanine on Cu(001) studied by scanning tunneling microscopy," *Surface Science*, vol. 442, no. 2, pp. L995–L1000, 1999.

[15] X. Zhao, R. G. Zhao, and W. S. Yang, "Scanning Tunneling Microscopy Investigation of L-Lysine Adsorbed on Cu(001)," *Langmuir*, vol. 16, no. 25, pp. 9812–9818, 2000.

[16] X. Zhao, "Fabricating Homochiral Facets on Cu(001) with L-lysine," *Journal of the American Chemical Society*, vol. 122, no. 50, pp. 12584–12585, 2000.

[17] A. G. Mark, M. Forster, and R. Raval, "Direct visualization of chirality in two dimensions," *Tetrahedron*, vol. 21, no. 9-10, pp. 1125–1134, 2010.

[18] P. Fürst and P. Stehle, "What are the essential elements needed for the determination of amino acid requirements in humans?," *The Journal of Nutrition*, vol. 134, no. 6 Suppl, pp. 1558S–1565S, 2004.

[19] H. A. McManus and P. J. Guiry, "Recent developments in the application of oxazoline-containing ligands in asymmetric catalysis," *Chemical Reviews*, vol. 104, no. 9, pp. 4151–202, 2004.

[20] J. R. Cronin, "Enantiomeric Excesses in Meteoritic Amino Acids," *Science*, vol. 275, no. 5302, pp. 951–955, 1997.

[21] M. Levine, C. S. Kenesky, D. Mazori, and R. Breslow, "Enantioselective synthesis and enantiomeric amplification of amino acids under prebiotic conditions," *Organic Letters*, vol. 10, no. 12, pp. 2433–6, 2008.

[22] M. Klussmann, H. Iwamura, S. P. Mathew, D. H. Wells, U. Pandya, A. Armstrong, and D. G. Blackmond, "Thermodynamic control of asymmetric amplification in amino acid catalysis," *Nature*, vol. 441, no. 7093, pp. 621–3, 2006.

[23] I. Rubinstein, G. Clodic, G. Bolbach, I. Weissbuch, and M. Lahav, "Racemic β-sheets as templates for the generation of homochiral (isotactic) peptides from aqueous solutions of (RS)-valine or -leucine N-carboxy-anhydrides: relevance to biochirogenesis," *Chemistry - A European Journal*, vol. 14, no. 35, pp. 10999–11009, 2008.

[24] A. Commeyras, H. Collet, L. Boiteau, J. Taillades, O. Vandenabeele-Trambouze, H. Cottet, J.-P. Biron, R. Plasson, L. Mion, O. Lagrille, H. Martin, F. Selsis, and M. Dobrijevic, "Prebiotic synthesis of sequential peptides on the Hadean beach by a molecular engine working with nitrogen oxides as energy sources," *Polymer International*, vol. 51, no. 7, pp. 661–665, 2002.

[25] D. Hafenbradl, M. Keller, G. Wächtershäuser, and K. Stetter, "Primordial amino acids by reductive amination of α-oxo acids in conjunction with the oxidative formation of pyrite," *Tetrahedron Letters*, vol. 36, no. 29, pp. 5179–5182, 1995.

[26] H. Moshe, M. Vanbel, V. K. Valev, T. Verbiest, D. Dressler, and Y. Mastai, "Chiral thin films of metal oxide," *Chemistry - A European Journal*, vol. 19, no. 31, pp. 10295–301, 2013.

[27] H. Moshe, G. Levi, D. Sharon, and Y. Mastai, "Atomic layer deposition of enantioselective thin film of alumina on chiral self-assembled-monolayer," *Surface Science*, vol. 629, pp. 88–93, 2014.

[28] S. Barlow and R. Raval, "Complex organic molecules at metal surfaces: bonding, organisation and chirality," *Surface Science Reports*, vol. 50, no. 6-8, pp. 201–341, 2003.

[29] M. L. Támara, *Factors controlling enantiomer-selective amino acid adsorption on mineral and metal surfaces*. PhD thesis, University of Liverpool (UK), 2009.

[30] J. Williams, S. Haq, and R. Raval, "The bonding and orientation of the amino acid l-alanine on Cu{110} determined by RAIRS," *Surface Science*, vol. 368, no. 1-3, pp. 303–309, 1996.

[31] S. Barlow, K. Kitching, S. Haq, and N. Richardson, "A study of glycine adsorption on a Cu{110} surface using reflection absorption infrared spectroscopy," *Surface Science*, vol. 401, no. 3, pp. 322–335, 1998.

[32] M. Forster, M. S. Dyer, M. Persson, and R. Raval, "Probing conformers and adsorption footprints at the single-molecule level in a highly organized amino acid assembly of (S)-proline on Cu(110)," *Journal of the American Chemical Society*, vol. 131, no. 29, pp. 10173–81, 2009.

[33] I. Nakagawa, R. Hooper, J. Walter, and T. Lane, "Infrared absorption spectra of metal-amino acid complexes - III - Infrared spectra and normal vibrations of metal-valine chelates," *Spectrochimica Acta*, vol. 21, no. 1959, pp. 1–14, 1965.

[34] S. G. Stepanian, I. D. Reva, E. D. Radchenko, and L. Adamowicz, "Combined matrix-isolation infrared and theoretical DFT and ab initio study of the nonionized valine conformers," *The Journal of Physical Chemistry A*, vol. 103, no. 22, pp. 4404–4412, 1999.

[35] L. Atanasoska, J. Buchholz, and G. Somorjai, "Low-energy electron diffraction study of the surface structures of adsorbed amino acid monolayers and ordered films deposited on copper crystal surfaces," *Surface Science*, vol. 72, no. 1, pp. 189–207, 1978.

[36] E. Mateo Marti, S. Barlow, S. Haq, and R. Raval, "Bonding and assembly of the chiral amino acid S-proline on Cu(110): the influence of structural rigidity," *Surface Science*, vol. 501, no. 3, pp. 191–202, 2002.

[37] S. Haq, A. Massey, N. Moslemzadeh, A. Robin, S. M. Barlow, and R. Raval, "Racemic versus enantiopure alanine on Cu(110): an experimental study," *Langmuir*, vol. 23, no. 21, pp. 10694–700, 2007.

[38] S. Barlow, S. Louafi, D. Le Roux, J. Williams, C. Muryn, S. Haq, and R. Raval, "Polymorphism in supramolecular chiral structures of R- and S-alanine on Cu(110)," *Surface Science*, vol. 590, no. 2-3, pp. 243–263, 2005.

[39] J. Seifert, M. Busch, E. Meyer, and H. Winter, "Surface Structure of Alanine on Cu(110) Studied by Fast Atom Diffraction," *Physical Review Letters*, vol. 111, no. 13, p. 137601, 2013.

[40] J. Seifert, M. Busch, E. Meyer, and H. Winter, "Surface structure of alanine on Cu(110) via grazing scattering of fast atoms and molecules," *Physical Review B*, vol. 89, no. 7, p. 075404, 2014.

[41] M. Forster, M. S. Dyer, M. Persson, and R. Raval, "Assembly of Chiral Amino-Acids at Surfaces from a Single Molecule Perspective: Proline on Cu(110)," *Topics in Catalysis*, vol. 54, no. 1-4, pp. 13–19, 2011.

[42] M. Forster and R. Raval, "Simple Rules Steer Complex Chiral Organisations on Surfaces : Amino-acids on Cu(110)," *in preparation*.

[43] T. Eralp, A. Shavorskiy, Z. V. Zheleva, G. Held, N. Kalashnyk, Y. Ning, and T. R. Linderoth, "Global and local expression of chirality in serine on the Cu{110} surface," *Langmuir*, vol. 26, no. 24, pp. 18841–51, 2010.

[44] A. Kühnle, T. R. Linderoth, B. Hammer, and F. Besenbacher, "Chiral recognition in dimerization of adsorbed cysteine observed by scanning tunnelling microscopy," *Nature*, vol. 415, no. 6874, pp. 891–3, 2002.

[45] G. Desiraju and T. Steiner, *The Weak Hydrogen Bond*. Oxford University Press, 2001.

[46] M. Forster, M. S. Dyer, M. Persson, and R. Raval, "2D random organization of racemic amino acid monolayers driven by nanoscale adsorption footprints: proline on Cu(110)," *Angewandte Chemie (International ed. in English)*, vol. 49, pp. 2344–2348, 2010.

[47] G. Kresse and J. Hafner, "Ab initio molecular dynamics for liquid metals," *Physical Review B*, vol. 47, no. 1, pp. 558–561, 1993.

[48] G. Kresse and J. Furthmüller, "Efficient iterative schemes for ab initio total-energy calculations using a plane-wave basis set," *Physical Review B*, vol. 54, no. 16, pp. 11169–11186, 1996.

[49] J. Klimeš, D. R. Bowler, and A. Michaelides, "Chemical accuracy for the van der Waals density functional," *Journal of Physics: Condensed Matter*, vol. 22, no. 2, p. 022201, 2010.

[50] J. Klimeš, D. R. Bowler, and A. Michaelides, "Van der Waals density functionals applied to solids," *Physical Review B*, vol. 83, no. 19, pp. 1–13, 2011.

[51] J. Tersoff and D. R. Hamann, "Theory and Application for the Scanning Tunneling Microscope," *Physical Review Letters*, vol. 50, no. 25, pp. 1998–2001, 1983.

[52] N. Lorente and M. Persson, "Theoretical aspects of tunneling-current-induced bond excitation and breaking at surfaces," *Faraday Discussions*, no. 117, pp. 277–290, 2000.

Chapter 7

On-surface inception of chirality in the self-assembly of achiral biomolecules: adenine on Cu(110)

7.1 Introduction

The nitrogenous bases are important bioactive molecules, being constituents of the cellular nucleic acids. Their fundamental role is manifested through the interactions between bases belonging to different polynucleotides that stabilise the structure of double-stranded DNA, the genetic repository in every living organism, and are thus responsible for the mechanisms that govern the cell division processes and the reproduction of life from one generation to the next [1]. Furthermore, defects and damages that involve a chemical modification of nucleic acid bases [2], or a mismatch in the base-base pairing mechanism [3], are often responsible for the formation and the development of tumoral cells, thus nucleobases and nucleoside analogues have been proposed for the treatment of cancer [4].

Although nucleic acid bases are achiral molecules, their main biochemical activities take place in stringently chiral environments. Examples of these include their covalent bond (*glycosidic bond*) with single-chirality D-ribose and 2-deoxy-D-ribose, respectively, in the structures of RNA and DNA, biopolymers that also possess a strictly chiral helicity, and the interactions with single-handed amino acids in the protein biosynthesis processes, in which the amino acylation of the D-ribose group in RNA represents a crucial step [5, 6].

The nucleobase adenine has received specific attention in view of its possible role in the development of life, as adenine is a pentamer of hydrogen cyanide (see figure 7.1). In fact, HCN is thought to have been widely present in the primitive Earth atmosphere [7]. It was demonstrated for the first time that it is possible to obtain adenine, albeit with

a small yield of 0.5%, by simply heating highly concentrated solutions of HCN at 350 K for few days [8, 9]. Since then, the polymerisation of HCN to give adenine has been achieved in various experimental conditions [10–12] and thermodynamic pathways have been proposed [13].

The chemical behaviour of nucleic acid components in non-biochemical environments, via the study of model systems, is the subject of a specific branch of research aimed at fully understanding the mechanisms that underpin their bioactivity. In this sector, the creation of hybrid systems constituted of inorganic and organic elements has received particular interest recently, thanks to the possibility of achieving the synthesis of biocompatible materials [14–16]. In addition, 2D confined nucleic acid bases are interesting in terms of their electronic properties, since the precise electronic characterisation of the relevant nucleobases could lead to the development of a faster method for DNA sequencing [17–19]. For all these reasons, the adsorption of thymine, adenine, cytosine, guanine and uracil, the biochemically relevant nitrogenous bases, on single-crystal metallic surfaces has been studied via diverse and complementary surface science techniques and theoretical calculations, with the objective of revealing their chemical form, properties of assembly and molecule-molecule and molecule-substrate interactions. For the recent literature on this field see the references [18, 20–36]and for a detailed review see the reference [37].

The adsorption of adenine, whose structure is presented in figure 7.1 with the classic atomic numbering, at surfaces has been studied consistently since the STM-based work published in the 90s by Tanaka and collaborators [27], in which the authors illustrated the unidimensional self-assembly of adenine on the Cu(111) surface in chains composed of adenine dimers(see also references [21, 38]). Moreover, the same authors reported a hexagonal pattern [39] for the same system. A superstructure constituted by adenine pairs has also been observed on the Au(111) surface by means of STM [40, 41]. Furthermore, the existence of chiral domains upon self-assembly of adenine molecules on highly oriented pyrolytic graphite has been reported at the solid-liquid interface [42].

On the Cu(110) surface, adenine has been shown, via STM and LEED characterisations, to self-organise into chains upon annealing (430 K). The chains have mirroring elongations along the surface directions ($\pm$1, 2), as shown in figure 7.2b. At high coverages, a 2D crystal structure is formed, with chiral domains having (1 $\pm$2, 6 0) unit cells (figure 7.2a). Each building unit of the chains, on the basis of its dimensions in STM images, is judged to be composed of adenine dimers, i.e. two adenine molecules in proximity. Furthermore, each dimer has been shown to possess an internal C_2 rotational symmetry property [44]. This is a clear example of surface-induced chiral organisation, a well known phenomenon that sees the interaction between an achiral molecule and the substrate atoms as the symmetry-breaking factor that effectively introduces local chirality, while, overall, the system is racemic [45, 46]. In addition to this 2D chiral

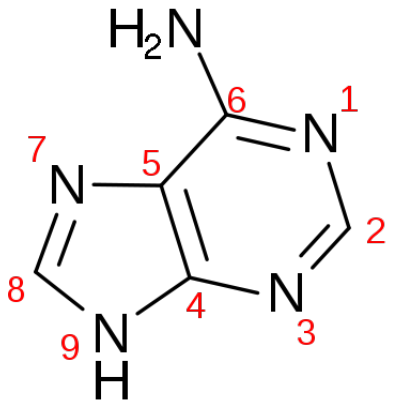

Figure 7.1: Chemical structure of the 9(H) adenine tautomer, that is the most stable in the gas phase [43].

behaviour, this system has shown a further chiral recognition property towards the subsequent adsorption of chiral biomolecules. Namely, the amino acid phenylglycine with a given chirality adsorbs on the Cu(110) surface in a position located next to an adenine chain with a specific direction, while the same phenomenon occurs if both the chiralities of the adenine chain and of the incoming phenylglycine molecules are inverted [47, 48]. In other words, the adenine chains on Cu(110) have been demonstrated to manifest enantiospecific recognition properties towards the chiral resolution of phenylglycine in two dimensions.

This peculiar property has rendered the adenine/Cu(110) system a prototype for the study of chiral recognition phenomena at metallic interfaces, with the subsequent publications of several experimental and theoretical studies having the objective of achieving a comprehensive understanding of the chemical form of the adsorbate, the mutual interactions between adenine molecules within the chiral chains and the driving forces that lead to this molecular organisation [49–58].

Notwithstanding the considerable amount of literature dedicated to this system, significantly divergent models have been proposed, and several aspects are still debated. X-ray-based spectroscopic studies [54, 57] agree on the fact that adenine molecules adsorb intact on the surface, and also no signs of molecular fragmentation are observed upon annealing up to 430 K, as reported in the original work [44]. However, a deprotonation upon adsorption at the N(9) site has also been proposed [49, 50]. With regards to the molecular orientation, a controversy has arisen as a consequence of two different RAIRS studies performed on the adenine/Cu(110) system. McNutt and collaborators have proposed a significantly tilted molecular orientation of adenine molecules, which gives origin to a strong IR adsorption band at 1626 cm^{-1}, corresponding to the in-plane scissoring vibration of the amino group, along with several weaker peaks in the spectral range 1133-1468 cm^{-1}, that are attributed to molecular motions coplanar with the molecular rings [50] (figure 7.3a). Conversely, Yamada and co-workers have ob-

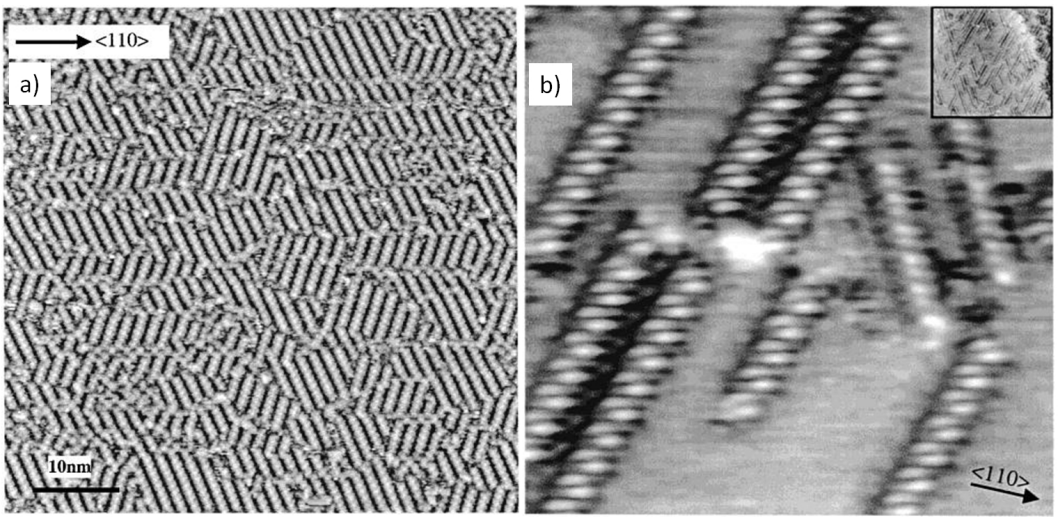

Figure 7.2: a) Chiral domains of adenine on Cu(110) at saturation coverage, upon annealing up to 430 K, with unit cells (1 ±2, 6 0). 60x60 nm^2, V=-160 mV, I=-2.38 nA. b) 1D chiral chains of adenine on Cu(110) along the (±1, 2) directions, obtained after annealing up to 430 K. 10x10 nm^2, V=-10000 mV, I=-0.63 nA. Both images are reproduced after reference [44].

served these signals only for sample coverages greater than one monolayer, and have not detected any significant IR absorption peaks at sub-monolayer coverages, a result which indicates a flat orientation of adenine molecules upon adsorption on the metallic surface [51] (figure 7.3b).

A basically flat-lying molecular geometry has also been proposed on the basis of experimental [54] and theoretical studies [44, 52–55, 58]. In an attempt to solve these conflicting views, Feyer and collaborators [57] have suggested, by means of a XPS and NEXAFS study supported with DFT, a coverage-dependent adsorption geometry, with the adenine molecular plane parallel and at an angle greater than 55° with respect to the Cu(110) surface at sub-monolayer and saturation coverage, respectively. Additionally, the footprint of the molecule, i.e. the individuation of those atoms that are in contact with the surface, is debated. Chen and co-workers proposed, in their original paper, a coordination through the amino moiety, and a stabilisation of the dimers via mutual hydrogen-bonding between the N(3) and N(9)H groups (figure 7.4) [44]. This contact geometry has been subsequently suggested in theoretical studies [52, 56], but also the N(7) site has been proposed as a simultaneous contact point [55, 57, 58]. Other authors have suggested a double contact through the imine N(1) and the amine $N(6)H_2$ at high coverages [57], or through the N(3) and dehydrogenated N(9) atoms [50].

The effect of annealing, which has been shown to induce the formation of chiral adenine chains, has been discussed in terms of vibrational spectroscopy by McNutt and collaborators: the authors indicate the emergence of a disorder-order transition, as the reason for a sharpening of the vibrational peaks associated with the amino group,

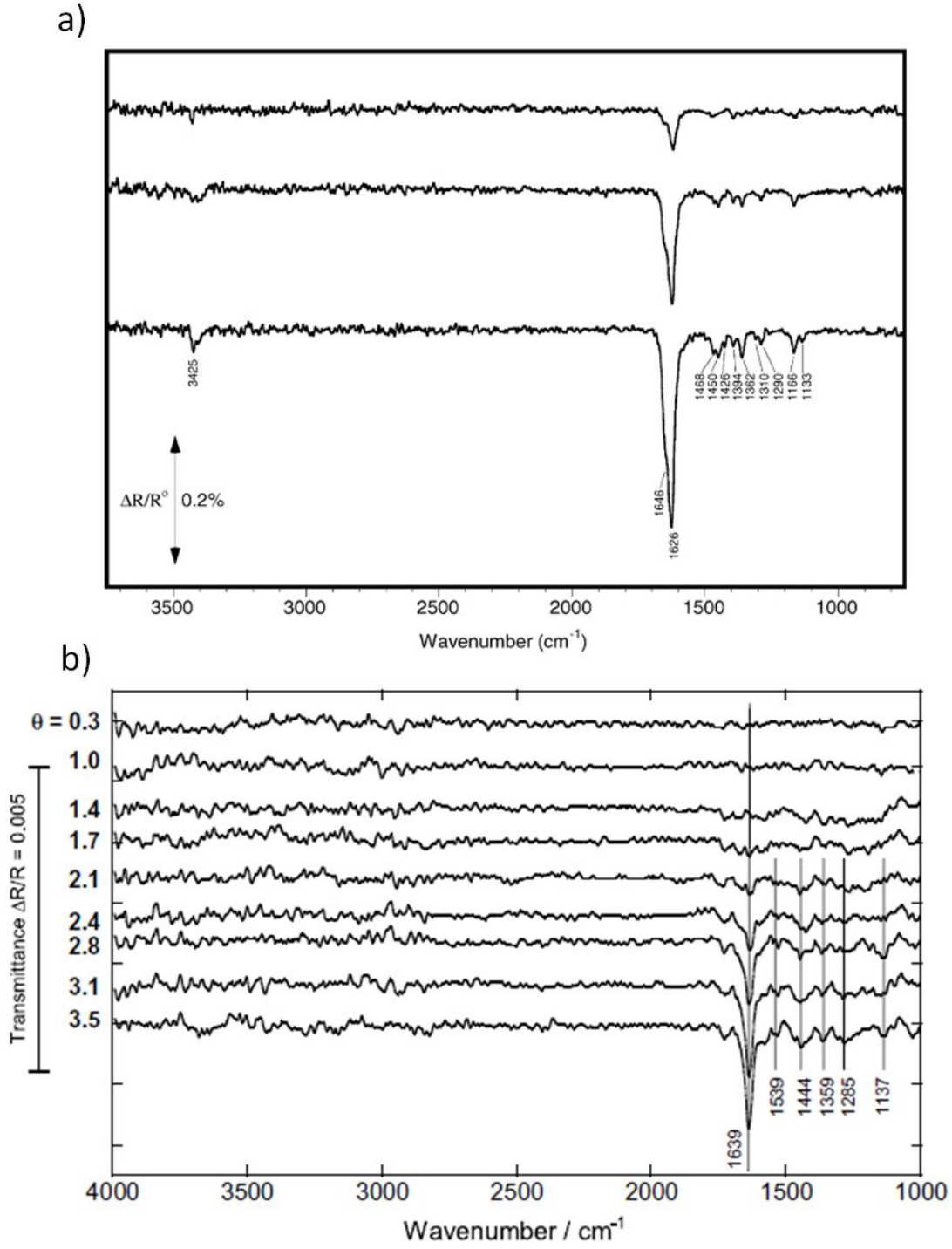

Figure 7.3: a) RAIR spectra acquired on as-dosed adenine on Cu(110) in the submonolayer regime. The maximum coverage achieved is 0.6 ML. Reproduced from [50]. b) RAIR spectra acquired on as-dosed adenine on Cu(110) for coverages ranging from 0.3 to 3.5 ML. Reproduced from [51].

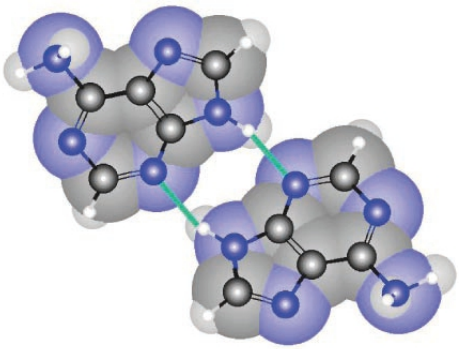

Figure 7.4: The geometry of an adenine dimer on the Cu(110) surface, according to Chen and co-workers [44]. The hydrogen bonds between N(9)H and N(3) involved in the stabilisation of the dimer are indicated. Reproduced from [47]. Colour code: hydrogen = white, carbon = grey, nitrogen = blue.

which, in this model, is reputed to be involved in the formation of inter-molecular hydrogen bonds [49, 50]. Zhang and co-workers [58] have also studied the effect of thermal treatment of the sample, via STM and DFT with corrections for Van der Waals interactions. They observe the formation of stable adenine dimers in meta-stable chiral chains at room temperature. The effect of an annealing step up to 373 K is thus proposed to induce the rotation of 90° of the whole chains, with the achievement of the phase observed previously by Chen and collaborators [44]. This high-temperature phase is composed of meta-stable dimers in stable chains, on the basis of the lower energy that the as-deposited dimers possess [58].

The present work consists of an STM characterisation of the behaviour of adenine on Cu(110). It is stressed that the achievement of a complete description of the molecular geometries is not attempted, because of the little chemical sensitivity that STM investigations provide. Nevertheless, STM represents a useful tool when the aim of the research is to describe the behaviour of adsorbed molecules in terms of their tendency to form supramolecular structures. A multitude of phases are observed when the parameters related to the sample preparation are varied. In this chapter, the different supramolecular organisations will be denoted with capital letters A, B, C, D and E. This indication will be used throughout the text of this chapter.

A low-order molecular assembly (phase A) is detected in as-deposited samples, along with dimer chains pointing in the (±4, 1) direction (phase B). The latter organisation has been observed previously [58]. Successive intermediate annealing processes, ranging from approximately 323 K to 373 K, induce the disruption of the as-deposited phases, yielding the progressive on-surface formation of other molecular organisations, which include an achiral molecular distribution placed along the close-packed surface direction (phase C) and the formation of isolated chiral adenine dimers (phase D) which are proposed to embody the building units that break the symmetry on the surface, leading

to the rise of a final chiral assembly. Further annealing up to 423 K causes the chiral dimers to assemble in chains, with chiral selectivity, to give rise to the chain-like phase observed experimentally previously (phase E) [44]. The latter organisation is thus proposed to be the thermodynamically favoured phase adopted by adenine on Cu(110). In figure 7.5 a schematic diagram of the supramolecular phases that are observed as a function of the annealing temperature of the sample is presented. Further details on the individual phases are presented in the experimental sections of this chapter.

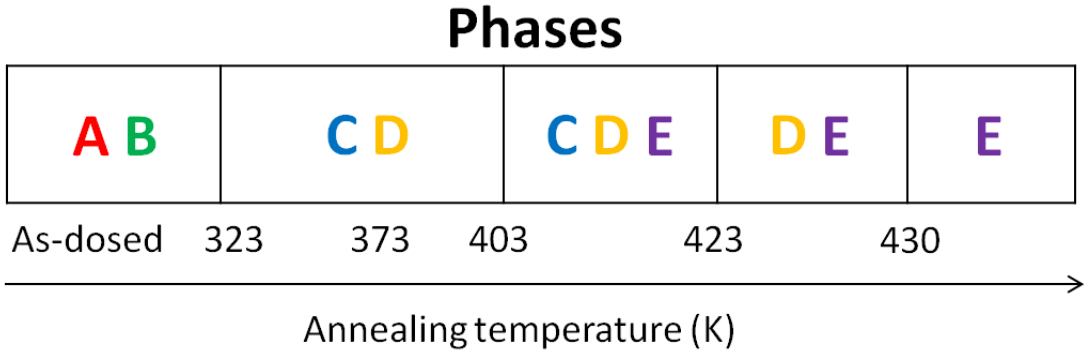

Figure 7.5: Phase diagram indicating the presence of the organisational phases A, B, C, D and E as a function of the annealing temperature. The scale of the annealing temperature is not linear. It is noted that the phase E alone, found at annealing temperatures higher than 430 K, is not found in the data presented herein, but it is inferred from reference [44]. For the details on the single phases see text in this and the following sections.

Finally, on the basis of the results presented herein, the isolated adenine dimers (phase D), whose formation is proposed to take place on the surface, are considered chiral nuclei from which a more extended chiral supramolecular assembly manifests itself, thanks to additional lateral interactions that are established between dimers with homogeneous handedness. This proposed path towards the formation of unidirectional chiral chains is discussed and compared with previously suggested mechanisms [56, 58].

7.2 Experimental results

7.2.1 STM on as-deposited samples

The adsorption of adenine on Cu(110) at room temperature and its subsequent characterisation via STM lead to the images displayed in figure 7.6. Whereas a significant disorder of the molecular arrangement is observed, in agreement with the RAIRS results published previously [50] and the lack of observation of a LEED pattern in as-dosed samples [44], some indications of the formation of clusters with local periodicity can be deduced. It is worth noting that two distinct molecular phase are observed and are denoted with the letters A and B in figure 7.6. Phase A denotes a rather disordered molecular organisation (red arrows in figure 7.6b,c), with a preferential direction of growth loosely placed along the [1-10] surface direction. Phase B, to which green ar-

rows point in figure 7.6b,c, corresponds to a locally chiral organisation which has been observed in a previous experimental and theoretical study published by Zhang and co-workers [58]. The authors of this paper claim that this chiral arrangement (figure 7.6d) consists of metastable chains composed of stable dimers, on the basis of theoretical calculations. Interestingly, the chains are elongated along the (±4, 1) surface directions, exactly at a right-angle with respect to the chiral chains observed originally by Chen and co-workers [44], which are placed along the (±1, 2) directions. The authors thus affirm that it is possible to induce the rotation of the whole chiral chains via an annealing process to 373 K. However, it will be shown in the following subsections that the formation of chiral chains along the (±1, 2) directions sees intermediate and more complex phase changes. Finally, it is noted that the STM intensities produced by adenine molecules belonging to the phases A and B are very distinct in the tunneling conditions used to produce the images of figure 7.6a-c. A much lower intensity, in particular, is associated with the molecules organised into phase B. The significance of this effect is unknown, however different intermolecular networks of interactions in the two phases, which would then give rise to distinct distributions of electron densities, can be hypothesised.

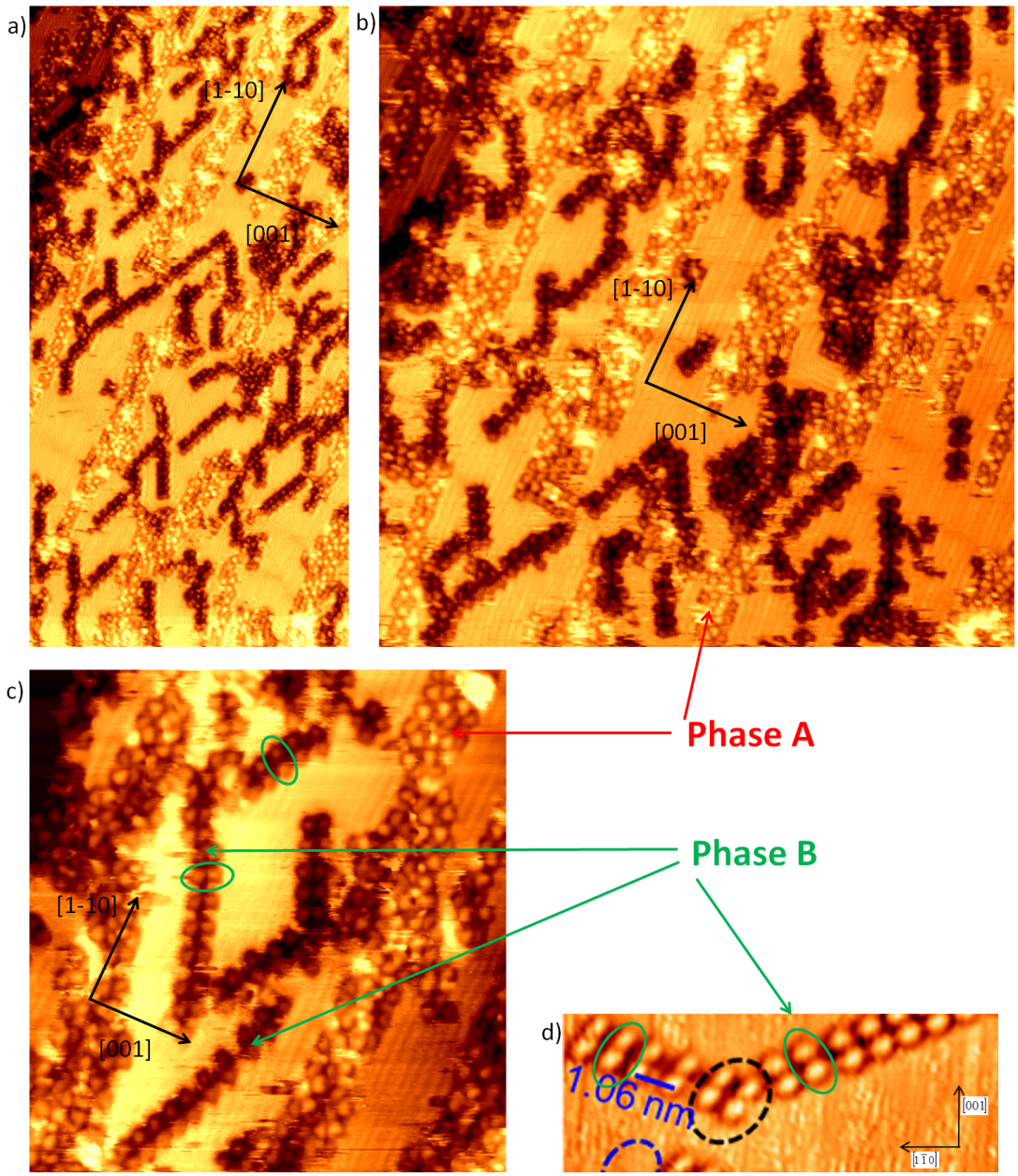

Figure 7.6: a-c) STM images acquired on the as-deposited adenine adlayer on Cu(110). a) 34.1x68.4 nm^2, V=+1317.1 mV, I=+1.060 nA. b) 40.9x41.3 nm^2, V=+1317.1 mV, I=+0.920 nA. c) 20.4x21.4 nm^2, V=+1317.1 mV, I=+0.830 nA. Two phases, labelled A and B are clearly visible, and are indicated with red and green arrows, respectively, in b) and c). d) The chiral chains observed by Zhang and collaborators, image adapted from reference [58]. In c) and d) green ovals highlight adenine dimers. In each STM image, the surface directions are indicated.

7.2.2 STM on samples annealed to intermediate temperatures

The thermal treatment of the sample whose STM images are presented in figure 7.6a-c yields novel molecular organisations, which are indicated with light blue and yellow arrows in figure 7.7a,b and are termed phase C and phase D, respectively. Profound differences characterise these two phases. Specifically, phase C sees a long range molecular organisation which is distributed along the [1-10] directions in rows, in which the STM signals of each adenine molecule is distinguished. Conversely, phase D is constituted by sparsely distributed single clusters, circled in yellow in the STM images of figure 7.7. It is finally noted that the sample presented in figure 7.7a has undergone a post-deposition annealing to 323 K, while the sample in figure 7.7b has been annealed to 373 K: no significant differences in the distribution of the molecular phases has been observed in this range of temperatures.

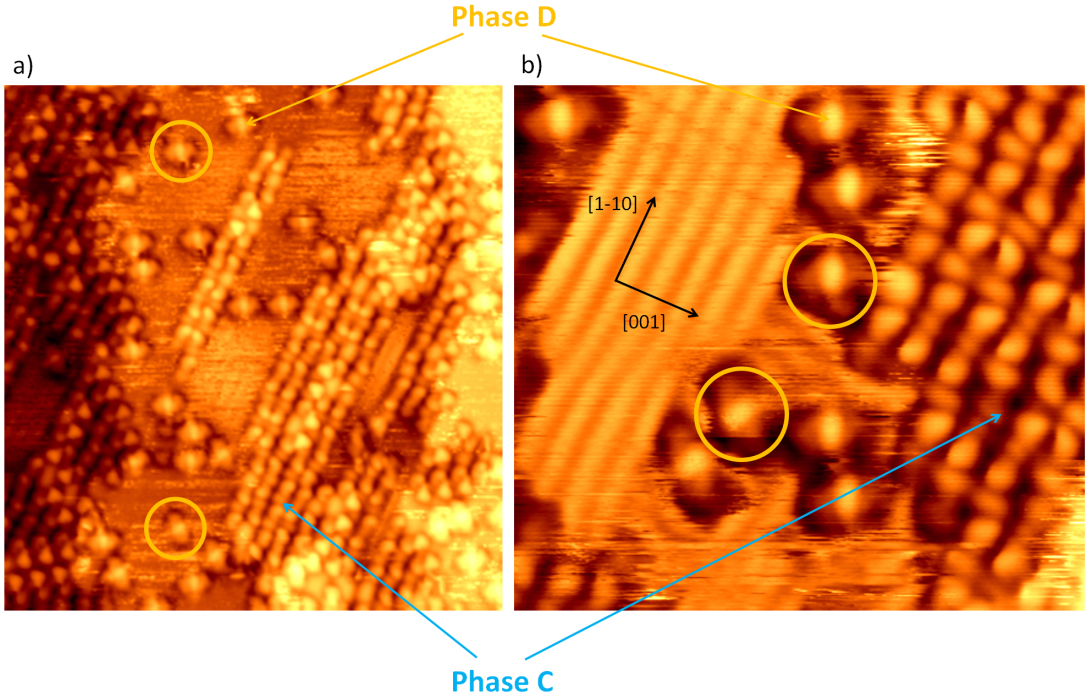

Figure 7.7: a) STM image collected on an adenine adlayer on Cu(110), following post-deposition annealing to 323 K. 20.4x21.4 nm^2, V=-1400.4 mV, I=-1.100 nA. b) STM image collected on an adenine adlayer on Cu(110), following post-deposition annealing to 373 K. 9.5x8.5 nm^2, V=+1238.7 mV, I=+0.550 nA. Phase C and phase D are indicated with light blue and yellow arrows, respectively. The yellow circles highlight the isolated clusters that are formed in phase D.

A more in-depth analysis of the STM images related to phase C formed by alanine on Cu(110) reveals new insights into this molecular arrangement. In figure 7.8a,b the same STM image is displayed, albeit with different contrasts in the false-colour scale rendering. It can be seen that the imaging of single adenine molecules appears in a variety of manners. Features with elongated shapes, highlighted with ovals in

figure 7.8a,b, are visible. Their elongations are roughly orientated along the [001] surface direction, and possess a lower intensity with respect to surrounding features, which also possess a defined direction of elongation (triangles in figure 7.8b) along non-symmetric surface directions. Larger elements, such as the one highlighted with a circle, are also present. The analysis of the line profile along a molecular row placed in the close-packed direction (figure 7.8c) also testifies the irregularities in the distribution of intensities of the STM signals. The multitude of ways in which adenine molecules in phase C are imaged renders the interpretation of STM images extremely difficult, since no obvious connection can be made between the appearance of the single features with the actual conformation of a given adsorbed molecule. In order to achieve this, further experimental investigations and possibly theoretical calculations would be necessary.

A clearer picture can be deduced with regards to phase D. Elements with two different and mirroring orientations are present, as circled in yellow in figure 7.9a. The two types of mirror-image orientations are highlighted in the close-up STM image in figure 7.9b. These entities are constituted by a central bright zone, with two lobes with lower intensity that are placed laterally. Contiguously to these, an area with depleted signal is present (see line profile drawn in figure 7.9c). On the basis of the dimensional analysis, these features comprise two adenine molecules, i.e. an adenine dimer. In the line profile shown in figure 7.9c, for instance, the longitudinal measurement, with the exclusion of the part with the decreased tunneling conductivity, yields a value of 1.22 nm, which is compatible with the measurement of two adenine molecules positioned in close proximity of each other. The detection of isolated single chiral adenine dimers on the Cu(110) surface represents an unprecedented result and constitutes the direct observation of the temperature-led symmetry-breaking phenomenon that induces the achiral molecule adenine to adopt a chiral supramolecular organisation on Cu(110). Although a chiral phase is observed in as-deposited samples (phase B), these are readily disrupted as a result of a gentle thermal treatment which gives origin to the achiral phase C and to the chiral dimers of phase D.

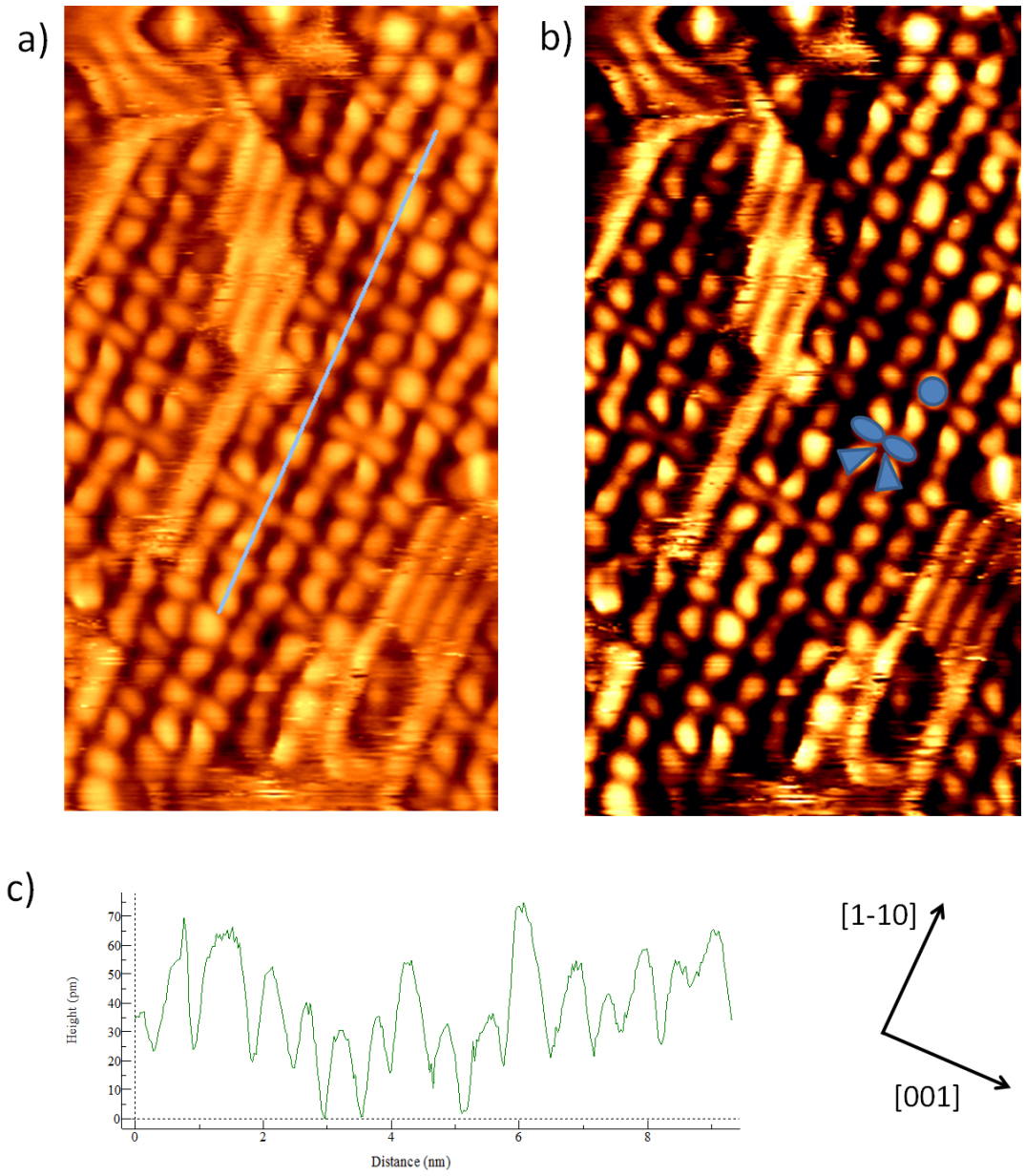

Figure 7.8: a-b) STM images of phase C formed by adenine on Cu(110). Sample annealed at 373 K. The image is reproduced twice, with an enhanced false-colour contrast in b). 7.7x14.2 nm^2, V=+1238.7 mV, I=+0.560 nA. The light blue ovals, circles and triangles superimposed on image in b) sketch the different shapes in which adenine molecules are imaged. c) Line profile measured across the line indicated in a).

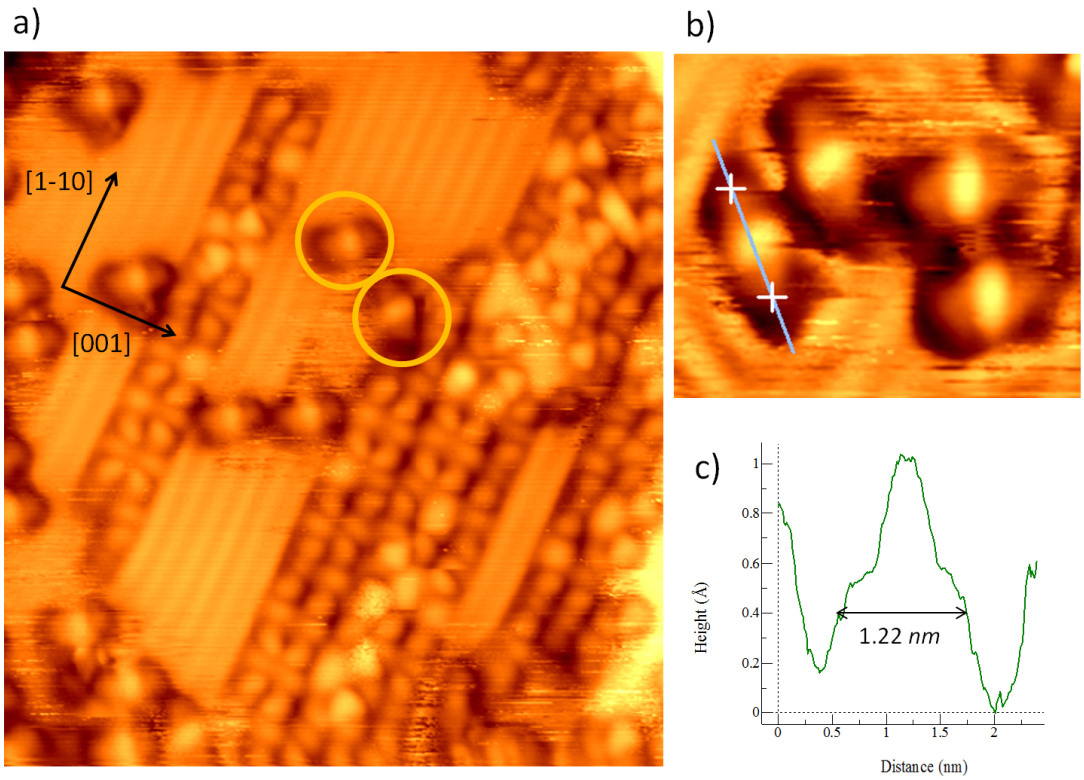

Figure 7.9: a-b) STM images of phase D formed by adenine on Cu(110), after annealing at 373 K. a) 13.2x14.2 nm^2, V=+1129.7 mV, I=+1.040 nA. Two possible orientations of the clusters are visualised. A sample of each type is circled in yellow. b) 4.3x3.6 nm^2, V=+1238.7 mV, I=+0.540 nA. Close-up image showing two pairs of clusters with both orientations in proximity. c) Line profile measured across the line indicated in b).

7.2.3 STM on samples annealed to the final temperature

When the sample is annealed up to higher temperatures, the chiral chains observed by Chen and collaborators [44] for the first time are formed on the surface and are termed phase E in this chapter. The conversion process to phase E does not appear to be sharp and abrupt. In the STM image portrayed in figure 7.10a, for instance, the phases C, D and E coexist on the same sample, which has been annealed to 403 K. Specifically, the achiral phase C is seen on the surface, as indicated by the blue arrow. There is a significant presence of isolated adenine dimers belonging to phase D (yellow arrow), but interestingly, the emergence of chains composed of adenine dimers is clear, as denoted by the purple arrow. It is noted here that the number of chains observed at this annealing temperature (403 K) is limited, as well as the length that the chains possess. For example, in figure 7.10a, the longest molecular chain that is detected (circled in purple) is composed of four adenine dimers.

Once the thermal treatment of the sample is brought up to 423 K (figure 7.10b), the disappearance of the achiral phase C is noticeable. Molecules are largely arranged in chiral chains, as expected after this temperature of annealing [44]. Furthermore, the chains seem to be composed of a larger number of dimeric units: the chains circled in purple are made of six adenine dimers, as an example. However, even at this annealing temperature, single adenine dimers remain sparsely distributed on the surface. Some of them are circled in yellow in figure 7.10b.

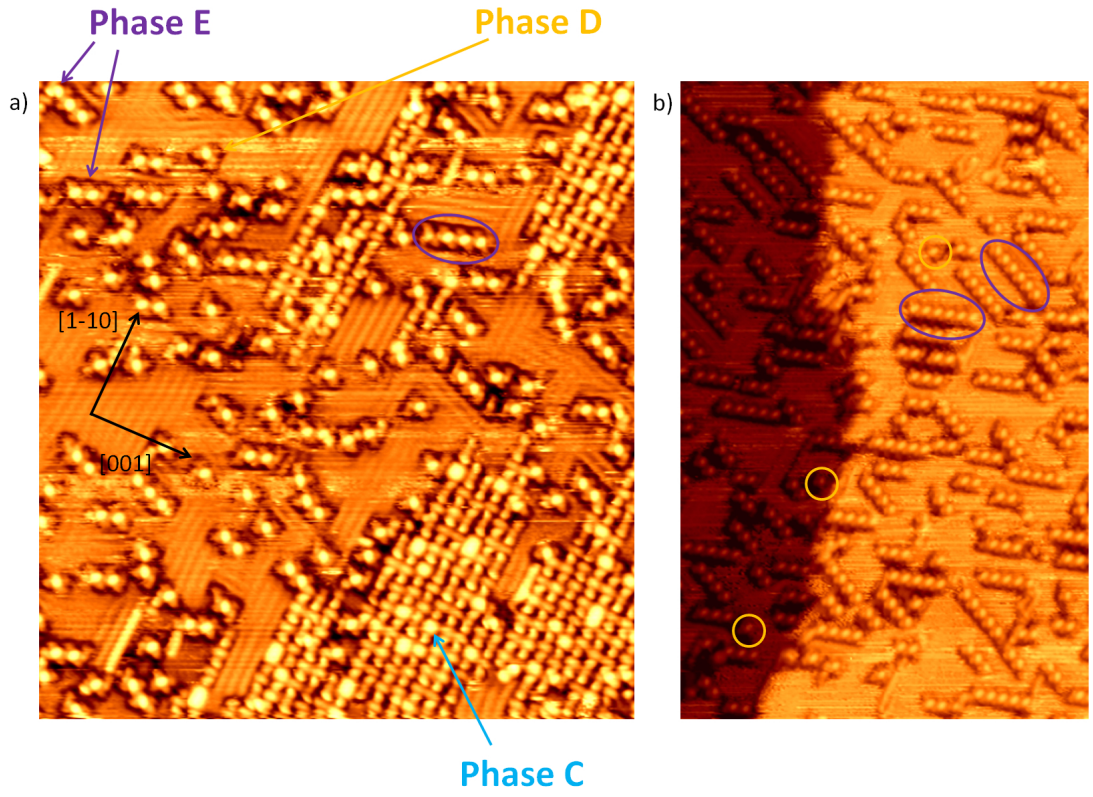

Figure 7.10: a) STM image of adenine on Cu(110), following annealing at 403 K. 27.2x29.1 nm^2, V=+911.2 mV, I=+0.720 nA. The coexistence of phases C, D and E is indicated through light blue, yellow and purple arrows, respectively. The purple oval encircles an adenine chain (phase E) consisting of four dimers. b) STM image of adenine on Cu(110), following annealing at 423 K. 26.4x41.2 nm^2, V=+999.1 mV, I=+1.720 nA. Yellow circles highlight some isolated adenine dimers (phase D). Purple ovals highlight adenine chains (phase E), with opposite chiralities, each containing six adenine dimers.

7.3 Discussion and proposed mechanism for the formation of the chiral chains

The simultaneous presence of the two phases D and E on the same sample, as revealed, for instance, in the STM images of figure 7.10, allows a direct visual comparison between the isolated dimers and their assembly into chains. The handed units of phase D, once created, maintain a specific chirality on the surface and are subsequently induced to form chiral assemblies possessing a longer range, i.e. the chiral chains of phase E. These are thus proposed to be formed on the Cu(110) surface through lateral interactions that are established between dimers that are homochiral in terms of their adsorption-induced handedness. The shape and orientation of the isolated dimers, in fact, remain unchanged during their assembly into chains, as visible in the magnified STM image of figure 7.11. The orientation of the dimers, calculated as the orientation of the longitudinal axis of their STM elongated features, is at an angle of approximately $\pm 45°$ with respect to the [001] surface direction. The same orientation is found for the dimers included in a chain (see figure 7.11, in which both chiralities are visible). The latter aspect is a confirmation of the fact that the adenine dimers, once created in their chiral conformation, retain their handedness when they assemble into chains, without any detectable modifications of their orientation with respect to the underlying surface. The construction of the chains, in other words, appears to take origin by a simple spatial translation of dimers already formed on the surface, as a result of novel lateral interactions that are induced by a further thermal treatment.

Simulated STM images on the adenine/Cu(110) chain system have been presented in the literature in combination with DFT calculations [56, 58]. In both publications the authors have essentially concurred with the study published by Chen and co-workers [44, 47] in terms of the molecular geometry of adenine in the chain structure (phase E), with a model that sees the interaction between two members of a dimer mediated by hydrogen bonds between the N(9)H and the N(3) groups (see figure 7.4). Preuss and co-workers have published simulated constant height STM images (figure 7.12a), which thus do not reflect the experimental conditions of previously published [44] and data presented herein. Although the C_2 rotational symmetry is preserved, the extremely detailed molecular structure present in the simulated image is too unrealistic to be utilised in a direct comparison with experimental results. The simulation performed by Zhang and collaborators (figure 7.12b) produces, instead, a more reasonable image in terms of the signal generated by a tip-molecule convoluted interaction. The direct comparison between this simulation and an experimental image presented herein (figure 7.12c) is possible. In both images, a C_2 symmetry property is recognisable. Furthermore, a net elongation of the dimers along a direction placed roughly at 45° with respect to the [001] surface direction is observed. The experimental image, however,

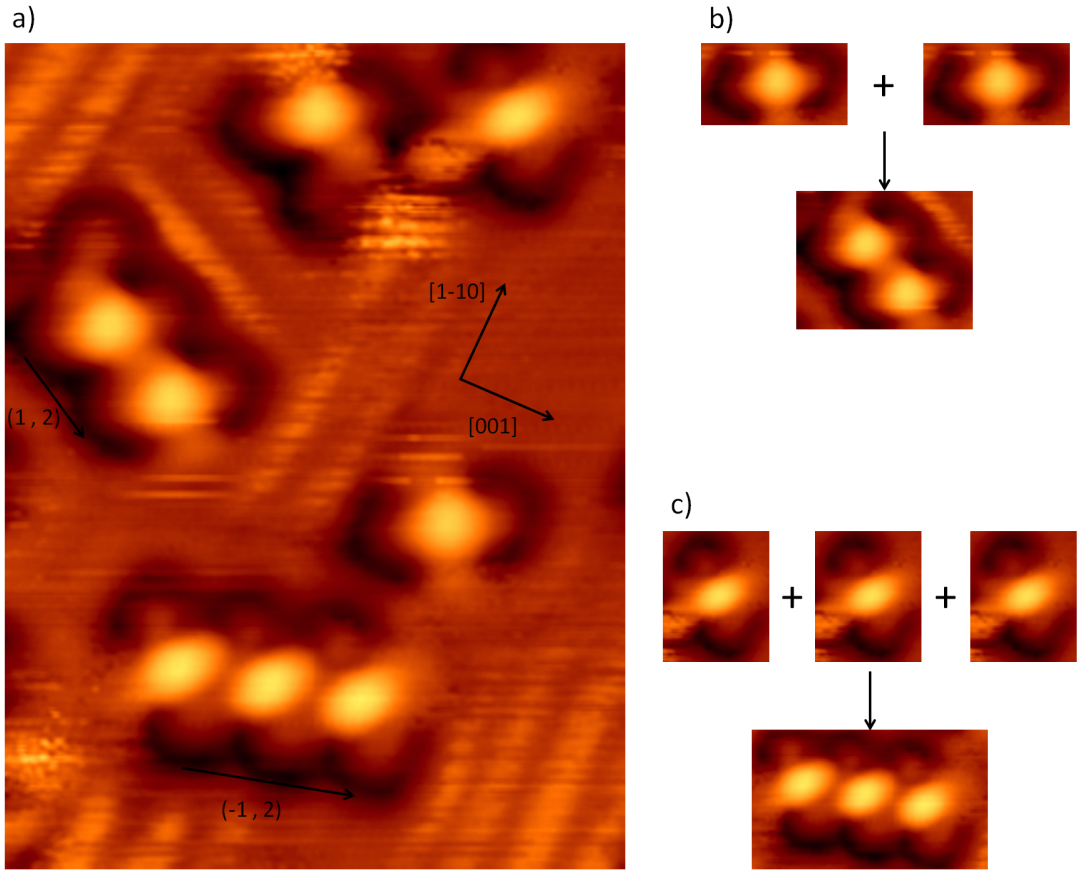

Figure 7.11: a) Magnification of an STM image of adenine on Cu(110), following annealing at 423 K. 5.1x7.3 nm^2, V=+734.8 mV, I=+1.080 nA. The image features the coexistence of adenine dimers in the phases D and E. Both chiralities are represented. b,c) Schematic representation of the formation of the chiral chains of phase E through the addition of building blocks represented by dimers in phase D. The modes of growth along the (1,2) and (-1,2) surface directions are represented, respectively.

shows three-lobe features with a much clearer high intensity region in the central part of the dimers, whereas in the simulation two-lobe features, with internal structure, are visible. The simulated images available in the literature are however not sufficient for a validation of a specific model through experimental STM. A systematic theoretical study over all the possible dimeric structures, complemented with STM simulations for each of them, could provide more information on the validity of the molecular models hypothesised so far.

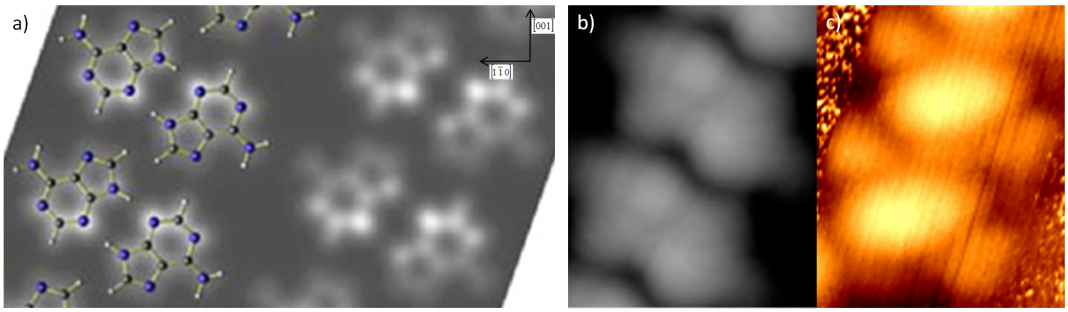

Figure 7.12: a,b)Simulated STM images on the most favoured structure for the adenine chains according to reference [56] and reference [58], respectively. a) Constant-height mode. V=-10000 mV. b) Constant-current mode. V=-100 mV. c) Magnification of an experimental STM image of this work (phase E), for comparison. 1.5x1.8 nm^2, V=-1277.1 mV, I=-0.790 nA.

In conclusion, a pathway for the formation of the chiral supramolecular structure of adenine on Cu(110) is proposed. Initially, adenine molecules adsorb on the surface in two distinct phases (A and B). Upon step-wise annealing processes, the two initial phases disappear, and the emergence of two additional phases is detected (C and D). The latter consists of dimerised adenine molecules which thus give rise to mirroring units, considered the manifestation of the inception of their stable organisational chirality. Upon further sample annealing, the dimers interact laterally with dimers that possess the same chirality to produce unidirectional chiral chains. This mechanism of formation partially agrees with the one proposed by Preuss and collaborators [56], who highlighted the importance of the prior formation of adenine dimers. However, they suggested that this process takes place in the gas phase, i.e. prior to the adsorption on Cu(110). They did so by decomposing the calculated adsorption energy per molecule in a chain into the contributions, or energy gains, provided by intra-dimer hydrogen bonding, inter-dimer hydrogen bonding and adsorption on the surface. The authors showed that the most significant energetic contribution (>60%) to the stabilisation of the system is given by the hydrogen bonds that are established within a dimer, i.e. between the N(9)H and the N(3) moieties of two adenine molecules, according to the structural model that they propose. The energy gain upon adsorption on the surfaces is computed to give more than 30% of the total stabilisation energy, while the remaining part is attributed to the hydrogen bonds that are formed between different dimers

in a chain [56]. In this work the importance that the intra-dimer interactions possess in comparison with the inter-dimer ones is confirmed. However, a surface-mediated dimerisation is herein proposed on the basis of the available experimental STM images, process that coincides with the on-surface symmetry-breaking nucleation of chiral units which then give rise to a more extended chiral organisation.

7.4 Conclusion

The behaviour of the biologically relevant nucleobase adenine upon adsorption on a Cu(110) single crystal is herein investigated experimentally by means of the sole STM technique. A step-wise thermal treatment of the samples induces the emergence of diverse phases whose formation is temperature controlled and irreversible. The phases are discussed in terms of the chiral manifestations that arise at local and global scales, and the priority of formation of chiral features are highlighted. A discussion upon the orientation of single molecules and the relevant intermolecular forces that drive the molecular assembly, aspects that are still debated in the literature, is not attempted, due to the nature of the investigating technique. The as-dosed samples show the formation of two distinct phases, of which one arranged into chiral chains (phase B), as observed previously [58] and one achiral (phase A) possessing a slight preference of adenine molecules to align along the Cu(110) close-packed direction. Following a thermal treatment of the sample up to 373 K, two new phases (C and D) emerge, with the simultaneous disappearance of the phases A and B. Phase C features adenine molecules, that are imaged singularly, positioned in rows running along the [1-10] surface direction, thus with an achiral organisation. In contrast, phase D sees the formation of isolated pairs of adenine molecules, with two well defined mirroring orientations on the surface. This newly found arrangement represents a clear example of the formation of single-point chirality elements, an example of 0D chirality [59], which locally break the symmetry of the underlying surface. Adenine molecules might be prochiral upon a simple adsorption event, i.e. they may adopt a chiral footprint as soon as they adsorb on the surface, however it is the temperature induced local interactions between two adenine molecules that play a role in the formation of locally chiral units at the supramolecular level. These constitute the nucleation seeds for more extensive 1D chiral structures [44], as it is shown when the samples are annealed to higher temperatures (423 K). Chen and collaborators have also shown that in highly covered samples extended chiral domains are obtained (see figure 7.2). The combination of these results testifies the importance of the variety of the chiral supramolecular organisations that the achiral biomolecule adenine gives rise to on the Cu(110) surface. In particular, all the dimensionalities of the chiral organisations, from 0D to 2D [59] are observed in this system, with the adenine dimers acting as chiral seeds for longer-range molecular assemblies with the same chirality.

The direct comparison between isolated dimers and chains substantiate the assumption that the chains are formed as a result of the lateral interactions that occur between adenine dimers possessing homogeneous on-surface chirality. The high-resolution STM images of adenine chains could provide the basis for future theoretical calculations, in particular STM simulations, with the aim of establishing the geometry and the orientations of single adenine molecules in dimers and chains. This would also give an insight into the intermolecular forces that have priority in the symmetry breaking phenomena at local and global scales. In this respect, the importance of the on-surface formation of adenine dimers prior to the organisation in chains is proposed. This is a partial confirmation of a theoretical study previously published [56], which, however, predicted that the dimerisation occurs in the gas phase.

7.5 Methods section

The STM experiments described in this chapter have been carried out exclusively by means of the Specs STM 150 Aarhus, described in section 3.4.2 of this thesis. The sublimation of adenine molecules, purchased from Sigma-Aldrich (purity $\geq 99\%$), has been induced by applying a current of 0.70 A to the tantalum wire wrapped around the glass crucible containing the molecular source, which is estimated to have reached a temperature of 385 K during the sublimation. Finally, the thermal treatments of the sample, when performed, are carried out via resistive heating, with a temperature control as described in section 5.4.

References for chapter 7

[1] J. D. Watson and F. H. C. Crick, "Molecular Structure of Nucleic Acids: A Structure for Deoxyribose Nucleic Acid," *Nature*, vol. 171, no. 4356, pp. 737–738, 1953.

[2] D. E. Barnes and T. Lindahl, "Repair and genetic consequences of endogenous DNA base damage in mammalian cells," *Annual Review of Genetics*, vol. 38, pp. 445–76, 2004.

[3] R. R. Iyer, A. Pluciennik, V. Burdett, and P. L. Modrich, "DNA mismatch repair: functions and mechanisms," *Chemical Reviews*, vol. 106, no. 2, pp. 302–23, 2006.

[4] C. M. Galmarini, J. R. Mackey, and C. Dumontet, "Nucleoside analogues and nucleobases in cancer treatment," *The Lancet Oncology*, vol. 3, no. 7, pp. 415–424, 2002.

[5] J. C. Lacey and D. W. Mullins, "Experimental studies related to the origin of the genetic code and the process of protein synthesis - A review," *Origins of Life*, vol. 13, no. 1, pp. 3–42, 1983.

[6] J. Martyn Bailey, "RNA-directed amino acid homochirality," *FASEB journal*, vol. 12, no. 6, pp. 503–7, 1998.

[7] P. H. Abelson, "Chemical events on the primitive Earth," *Proceedings of the National Academy of Sciences of the United States of America*, vol. 55, no. 6, pp. 1365–1372, 1966.

[8] J. Oró, "Synthesis of adenine from ammonium cyanide," *Biochemical and Biophysical Research Communications*, vol. 2, no. 6, pp. 407–412, 1960.

[9] J. Oró, "Mechanism of synthesis of adenine from hydrogen cyanide under possible primitive earth conditions," *Nature*, vol. 191, pp. 1193–1194, 1961.

[10] R. A. Sanchez, J. P. Ferris, and L. E. Orgel, "Studies in prebiotic synthesis. IV. Conversion of 4-aminoimidazole-5-carbonitrile derivatives to purines," *Journal of Molecular Biology*, vol. 38, no. 1, pp. 121–128, 1968.

[11] R. F. Shuman, W. E. Shearin, and R. J. Tull, "Chemistry of hydrocyanic acid. 1. Formation and reactions of N-(aminomethylene)diaminomaleonitrile, a hydrocyanic acid pentamer and precursor to adenine," *Journal of Organic Chemistry*, vol. 44, no. 25, pp. 4532–4536, 1979.

[12] A. Voet and A. Schwartz, "Prebiotic adenine synthesis from HCN - Evidence for a newly discovered major pathway," *Bioorganic Chemistry*, vol. 12, no. 1, pp. 8–17, 1983.

[13] D. Roy, K. Najafian, and P. von Ragué Schleyer, "Chemical evolution: the mechanism of the formation of adenine under prebiotic conditions," *Proceedings of the National Academy of Sciences of the United States of America*, vol. 104, no. 44, pp. 17272–17277, 2007.

[14] J. P. García-Terán, O. Castillo, A. Luque, U. García-Couceiro, G. Beobide, and P. Román, "Molecular Recognition of Protonated Cytosine Ribbons by Metal-Oxalato Frameworks," *Crystal Growth & Design*, vol. 7, no. 12, pp. 2594–2600, 2007.

[15] J. Navarro and B. Lippert, "Simple 1:1 and 1:2 complexes of metal ions with heterocycles as building blocks for discrete molecular as well as polymeric assemblies," *Coordination Chemistry Reviews*, vol. 222, no. 1, pp. 219–250, 2001.

[16] A. D. Richards and A. Rodger, "Synthetic metallomolecules as agents for the control of DNA structure," *Chemical Society Reviews*, vol. 36, no. 3, pp. 471–83, 2007.

[17] J. MacNaughton, A. Moewes, and E. Z. Kurmaev, "Electronic structure of the nucleobases," *The Journal of Physical Chemistry B*, vol. 109, no. 16, pp. 7749–7757, 2005.

[18] S. Kilina, S. Tretiak, D. Yarotski, J.-X. Zhu, N. Modine, A. Taylor, and A. Balatsky, "Electronic Properties of DNA Base Molecules Adsorbed on a Metallic Surface," *The Journal of Physical Chemistry C*, vol. 111, no. 39, pp. 14541–14551, 2007.

[19] A. C. Rajan, M. R. Rezapour, J. Yun, Y. Cho, W. J. Cho, S. K. Min, G. Lee, and K. S. Kim, "Two dimensional molecular electronics spectroscopy for molecular fingerprinting, DNA sequencing, and cancerous dna recognition," *ACS Nano*, vol. 8, no. 2, pp. 1827–1833, 2014.

[20] D. J. Frankel, Q. Chen, and N. V. Richardson, "Formation of hydrogen-bridged cytosine dimers on Cu(110)," *The Journal of Chemical Physics*, vol. 124, no. 20, 2006.

[21] M. Furukawa, H. Tanaka, and T. Kawai, "The role of dimer formation in the self-assemblies of DNA base molecules on Cu(111) surfaces: A scanning tunneling microscope study," *The Journal of Chemical Physics*, vol. 115, no. 7, pp. 3419–3423, 2001.

[22] W. H. Li, W. Haiss, S. Floate, and R. J. Nichols, "In-situ infrared spectroscopic and scanning tunneling microscopy investigations of the chemisorption phases of uracil, thymine, and 3-methyl uracil on Au(111) electrodes," *Langmuir*, vol. 15, no. 14, pp. 4875–4883, 1999.

[23] T. Nakagawa, H. Tanaka, and T. Kawai, "Two-dimensional self-assembly of uracil molecules on Cu(111) surfaces: a low-temperature STM study," *Surface Science*, vol. 370, no. 1, pp. L144–L148, 1997.

[24] R. Otero, M. Schöck, L. M. Molina, E. Lægsgaard, I. Stensgaard, B. Hammer, and F. Besenbacher, "Guanine quartet networks stabilized by cooperative hydrogen bonds," *Angewandte Chemie (International ed. in English)*, vol. 44, no. 15, pp. 2270–2275, 2005.

[25] S. Rapino and F. Zerbetto, "Modeling the stability and the motion of DNA nucleobases on the gold surface," *Langmuir*, vol. 21, no. 6, pp. 2512–2518, 2005.

[26] M. Rocco, R. Dudde, K.-H. Frank, and E.-E. Koch, "Angle-resolved photoemission from uracil and thymine adsorbed on Cu(110)," *Chemical Physics Letters*, vol. 160, no. 4, pp. 366–370, 1989.

[27] H. Tanaka, T. Nakagawa, and T. Kawai, "Two-dimensional self-assembly of DNA base molecules on Cu(111) surfaces," *Surface Science*, vol. 364, no. 2, pp. L575–L579, 1996.

[28] W. Xu, R. E. A. Kelly, R. Otero, M. Schöck, E. Lægsgaard, I. Stensgaard, L. N. Kantorovich, and F. Besenbacher, "Probing the hierarchy of thymine-thymine interactions in self-assembled structures by manipulation with scanning tunneling microscopy," *Small*, vol. 3, no. 12, pp. 2011–2014, 2007.

[29] F. Allegretti, M. Polcik, and D. Woodruff, "Quantitative determination of the local structure of thymine on Cu(110) using scanned-energy mode photoelectron diffraction," *Surface Science*, vol. 601, no. 17, pp. 3611–3622, 2007.

[30] M. Furukawa, H. Fujisawa, S. Katano, H. Ogasawara, Y. Kim, T. Komeda, a. Nilsson, and M. Kawai, "Geometrical characterization of pyrimidine base molecules adsorbed on Cu(1 1 0) surfaces: XPS and NEXAFS studies," *Surface Science*, vol. 532-535, pp. 261–266, 2003.

[31] D. C. Jackson, D. A. Duncan, W. Unterberger, T. J. Lerotholi, D. Kreikemeyer-Lorenzo, M. K. Bradley, and D. P. Woodruff, "Structure of cytosine on Cu(110): A scanned-energy mode photoelectron diffraction study," *The Journal of Physical Chemistry C*, vol. 114, no. 36, pp. 15454–15463, 2010.

[32] F. Kalkan, M. Mehlhorn, and K. Morgenstern, "A switch based on self-assembled thymine," *Journal of Physics: Condensed Matter*, vol. 24, no. 39, p. 394010, 2012.

[33] A. McNutt, S. Haq, and R. Raval, "High temperature phase of the DNA base thymine on Cu(110): a resonance delocalised bonding system," *Surface Science*, vol. 502-503, pp. 185–192, 2002.

[34] R. Otero, M. Lukas, R. E. A. Kelly, W. Xu, E. Lægsgaard, I. Stensgaard, L. N. Kantorovich, and F. Besenbacher, "Elementary structural motifs in a random network of cytosine adsorbed on a gold(111) surface," *Science*, vol. 319, no. 5861, pp. 312–315, 2008.

[35] O. Plekan, V. Feyer, S. Ptasińska, N. Tsud, V. Cháb, V. Matolín, and K. C. Prince, "Photoemission study of thymidine adsorbed on Au(111) and Cu(110)," *The Journal of Physical Chemistry C*, vol. 114, no. 35, pp. 15036–15041, 2010.

[36] I. Temprano, G. Thomas, S. Haq, M. S. Dyer, E. G. Latter, G. R. Darling, P. Uvdal, and R. Raval, "1D self-assembly of chemisorbed thymine on Cu(110) driven by dispersion forces," *The Journal of Chemical Physics*, vol. 142, no. 10, p. 101916, 2015.

[37] L. Liu, D. Xia, L. H. Klausen, and M. Dong, "The self-assembled behavior of DNA bases on the interface," *International Journal of Molecular Sciences*, vol. 15, no. 2, pp. 1901–14, 2014.

[38] M. Furukawa, H. Tanaka, and T. Kawai, "Formation mechanism of low-dimensional superstructure of adenine molecules and its control by chemical modification: a low-temperature scanning tunneling microscopy study," *Surface Science*, vol. 445, no. 1, pp. 1–10, 2000.

[39] M. Furukawa, H. Tanaka, and T. Kawai, "Scanning tunneling microscopy observation of two-dimensional self-assembly formation of adenine molecules on Cu(111) surfaces," *Surface Science*, vol. 392, no. 1-3, pp. L33–L39, 1997.

[40] R. E. Kelly, W. Xu, M. Lukas, R. Otero, M. Mura, Y.-J. Lee, E. Lægsgaard, I. Stensgaard, L. N. Kantorovich, and F. Besenbacher, "An investigation into the interactions between self-assembled adenine molecules and a Au(111) surface," *Small*, vol. 4, no. 9, pp. 1494–500, 2008.

[41] M. Lukas, R. E. A. Kelly, L. N. Kantorovich, R. Otero, W. Xu, E. Lægsgaard, I. Stensgaard, and F. Besenbacher, "Adenine monolayers on the Au(111) surface: structure identification by scanning tunneling microscopy experiment and ab initio calculations," *The Journal of Chemical Physics*, vol. 130, no. 2, p. 024705, 2009.

[42] W. Mamdouh, M. Dong, R. E. A. Kelly, L. N. Kantorovich, and F. Besenbacher, "Coexistence of homochiral and heterochiral adenine domains at the liquid/solid interface," *The Journal of Physical Chemistry B*, vol. 111, no. 42, pp. 12048–52, 2007.

[43] C. Plützer and K. Kleinermanns, "Tautomers and electronic states of jet-cooled adenine investigated by double resonance spectroscopy," *Physical Chemistry Chemical Physics*, vol. 4, no. 20, pp. 4877–4882, 2002.

[44] Q. Chen, D. J. Frankel, and N. V. Richardson, "Self-Assembly of Adenine on Cu(110) Surfaces," *Langmuir*, vol. 18, no. 8, pp. 3219–3225, 2002.

[45] K.-H. Ernst, "Molecular chirality in surface science," *Surface Science*, vol. 613, pp. 1–5, 2013.

[46] J. Elemans, I. De Cat, H. Xu, and S. De Feyter, "Two-dimensional chirality at liquid-solid interfaces," *Chemical Society Reviews*, vol. 38, no. 3, pp. 722–36, 2009.

[47] Q. Chen and N. V. Richardson, "Enantiomeric interactions between nucleic acid bases and amino acids on solid surfaces," *Nature Materials*, vol. 2, no. 5, pp. 324–8, 2003.

[48] S. Blankenburg and W. Schmidt, "Long-Range Chiral Recognition due to Substrate Locking and Substrate-Adsorbate Charge Transfer," *Physical Review Letters*, vol. 99, no. 19, p. 196107, 2007.

[49] A. McNutt, *Structural studies of the adsorption of the nucleic acid bases on Cu(110)*. PhD thesis, University of Liverpool (UK), 2002.

[50] A. McNutt, S. Haq, and R. Raval, "RAIRS investigations on the orientation and intermolecular interactions of adenine on Cu(110)," *Surface Science*, vol. 531, no. 2, pp. 131–144, 2003.

[51] T. Yamada, K. Shirasaka, A. Takano, and M. Kawai, "Adsorption of cytosine, thymine, guanine and adenine on Cu(110) studied by infrared reflection absorption spectroscopy," *Surface Science*, vol. 561, no. 2-3, pp. 233–247, 2004.

[52] M. Preuss, W. Schmidt, and F. Bechstedt, "Coulombic Amino Group-Metal Bonding: Adsorption of Adenine on Cu(110)," *Physical Review Letters*, vol. 94, no. 23, p. 236102, 2005.

[53] W. Schmidt, K. Seino, M. Preuss, A. Hermann, F. Ortmann, and F. Bechstedt, "Organic molecule adsorption on solid surfaces: chemical bonding, mutual polarisation and dispersion interaction," *Applied Physics A*, vol. 85, no. 4, pp. 387–397, 2006.

[54] M. Furukawa, T. Yamada, S. Katano, M. Kawai, H. Ogasawara, and A. Nilsson, "Geometrical characterization of adenine and guanine on Cu(110) by NEXAFS, XPS, and DFT calculation," *Surface Science*, vol. 601, no. 23, pp. 5433–5440, 2007.

[55] E. Rauls, S. Blankenburg, and W. Schmidt, "DFT calculations of adenine adsorption on coin metal (110) surfaces," *Surface Science*, vol. 602, no. 13, pp. 2170–2174, 2008.

[56] M. Preuss and F. Bechstedt, "Self-assembly of adenine-dimer chains on Cu(110): Driving forces from first-principles calculations," *Surface Science*, vol. 602, no. 9, pp. 1643–1649, 2008.

[57] V. Feyer, O. Plekan, K. Prince, F. Šutara, T. Skála, V. Cháb, V. Matolín, G. Stenuit, and P. Umari, "Bonding at the organic/metal interface: Adenine to Cu(110)," *Physical Review B*, vol. 79, no. 15, p. 155432, 2009.

[58] Y. Y. Zhang, Y.-L. Wang, L. Meng, S. B. Zhang, and H.-J. Gao, "Thermally Controlled Adenine Dimer Chain Rotation on Cu(110): The Critical Role of van der Waals Interactions," *The Journal of Physical Chemistry C*, vol. 118, no. 12, pp. 6278–6282, 2014.

[59] R. Raval, "Chiral expression from molecular assemblies at metal surfaces: insights from surface science techniques," *Chemical Society Reviews*, vol. 38, no. 3, pp. 707–21, 2009.

Conclusions and future work

In this thesis the diverse chiral manifestations expressed by selected amino acids and the nucleobase adenine on the Cu(110) surface are investigated by means of experimental surface science techniques with the support of theoretical calculations.

The collection of STM images with single-molecule resolution has been crucial in obtaining a deeper understanding of the molecular position within the known unit cell of R-serine on Cu(110) (chapter 4). The direct comparison between these experimental images with the simulated ones, along with the energetic calculations that have been performed, allows one to propose a homochiral footprint distribution. However, on the basis of the energetics, a heterochiral arrangement cannot be excluded. In order to gain a complete picture on this system, additional experimental characterisations might be useful. LEED-IV investigations, for instance, would give insights into the atomic positioning within the unit cell.

The tracking of chirality at the single molecule level has been also fundamental in the study of the adsorption of racemic serine on Cu(110). In addition to the previously reported tendency to on-surface chiral resolution, which is proposed to be the energetically favoured state, additional properties of chiral recognition are detected. Metastable states, that are thus protected in a local energetic minimum, are detected for the first time, in which the emergence of serine trimers is clear. These trimers possess heterogeneous molecular chirality, specifically a serine dimer with a given chirality interacts with a single molecule with differing handedness. The competition of kinetic and thermodynamic effects in the chiral recognition between serine molecules in racemic ratio on the Cu(110) surface is on this basis highlighted.

In chapter 6 the high-temperature achiral phase adopted by the enantiopure amino acid S-valine on Cu(110) is characterised. On the basis of STM and LEED investigations, an arrangement with a (3x2) periodicity is proposed. Within this, the comparison between experimental and simulated STM images permits one to propose an alternating distribution at the footprint level. This organisation, however, clearly shows irregularities and mismatches with the underlying copper surface, as previously reported for the (3x2) organisation of alanine on the same surface. The origin of this is unknown, however diverse hypotheses might be brought forward. These include the local occurrence of molecules with carboxylate adsorption at the long-bridge site of

the (110) surface, the presence of rotational domains or a local (4x2) arrangement to compensate the highly packed S-valine adlayer. Further investigations on the nature of these discrepancies from the "true" (3x2) organisation would be needed, although the intrinsic challenges presented by the local nature of the defects would be a significant obstacle. The next step would consist in the systematic study of the behaviour of racemic valine on Cu(110), with regards to the chiral recognition phenomena taking place at the molecular and footprint levels.

As a final remark, it is worth noting a general trend displayed by amino acid on the Cu(110) surface. Those enantiopure amino acids that adopt an achiral (nx2) organisation, such as glycine, alanine, proline and valine in its high-temperature phase, display an alternation in the footedness distribution, i.e. the unit cell is populated with two molecules possessing opposite footprint chiralities. Enantiopure serine, in contrast, adopts a strictly chiral organisation and is proposed herein to possess a homochiral footprint distribution, albeit a heterochiral arrangement cannot be totally excluded. Furthermore, racemic alanine and proline have been shown to form random solid solutions of molecular chiralities on Cu(110), while maintaining a strict heterochiral footprint arrangement. In the case of racemic serine, instead, the thermodynamically preferred state is the racemic conglomerate, i.e. the chiral resolution of the two enantiomers.

It would be interesting to expand the knowledge on the behaviour of enantiopure and racemic amino acids on Cu(110), in order to check whether these links between the organisational chirality and the footprint distribution with the behaviour of the correspondent 2D crystalline structure holds true for different systems.

Finally, with regards to the STM study on the adsorption of the achiral nitrogenous base adenine on Cu(110), a mechanism of chiral nucleation is proposed. On the basis of the STM images collected the central role played by the single adenine dimers in the breaking of the symmetry of the underlying surface is highlighted. In this way, it is noted that adsorbed adenine molecules are able to give rise to supramolecular chiral organisations from 0D to 2D, fact that renders this system interesting for additional theoretical and experimental studies. The number of different organisational phases detected, however, implies intrinsic difficulties. This is an aspect that needs to be taken into account when, for instance, averaging experimental techniques are used, thus any future result needs to be correlated with a specific molecular phase formed by adenine on Cu(110).

As a general consideration on the systems studied, it stressed that potential phenomena involving the reconstruction of the Cu(110) surface upon molecular adsorption are not taken into account. The role that this effect plays could be investigated via different techniques, for example by means of Surface X-Ray Diffraction (SXRD).

Finally, as a possible future plan of investigation, it is recommendable to study the adsorption of the same organic molecules on a different substrate. In this respect it would be interesting to introduce a crystal in which the surface symmetry is maintained and the material is changed. With the use, for instance, of a Ag(110) surface, the extent to which chiral manifestations of selected organic molecules on a less reactive surface could be investigated.